Technische Universität München
Lehrstuhl E23 für Technische Physik
Walther-Meißner-Institut für Tieftemperaturforschung
der Bayerischen Akademie der Wissenschaften

Magnetization dynamics in coupled magnetic systems

Stefan Horst Klingler

Vollständiger Abdruck der von der Fakultät für Physik der Technischen Universität München zur Erlangung des akademischen Grades eines

Doktors der Naturwissenschaften

genehmigten Dissertation.

Vorsitzender:	Prof. Dr. Wilhelm Zwerger
Prüfer der Dissertation:	1. Prof. Dr. Sebastian T.B. Goennenwein
	2. Prof. Dr. Christian Back

Die Dissertation wurde am 10.12.2018 bei der Technischen Universität München eingereicht und durch die promotionsführende Einrichtung am 20.03.2019 angenommen.

Stefan Horst Klingler

Magnetization dynamics in coupled magnetic systems

Dissertation, April 9, 2019

Reviewers: Prof. Dr. Sebastian T.B. Goennenwein and Prof. Dr. Christian Back

Technische Universität München

Lehrstuhl E23 für Technische Physik

Walther-Meißner-Institut für Tieftemperaturforschung

der Bayerischen Akademie der Wissenschaften

Walther-Meißner-Straße 8

85748 and Garching

Abstract

This thesis aims at the investigation of magnetization dynamics in coupled magnetic systems using broadband ferromagnetic resonance and Brillouin light scattering techniques. We observe and characterize the coupling and relaxation mechanisms between magnons and electrons in semiconductors, magnons and magnons in magnetic heterostructures, and magnons and photons in photonic resonators. Our findings will help to utilize the electron spin degree of freedom in novel spintronic devices.

Kurzfassung

Diese Dissertation beschäftigt sich mit der Untersuchung der Magnetisierungsdynamik in gekoppelten magnetischen Systemen unter Verwendung breitbandiger ferromagnetischer Resonanz und Brillouin-Lichtstreutechniken. Wir beobachten und charakterisieren die Kopplungs- und Relaxationsmechanismen zwischen Magnonen und Elektronen in Halbleitern, Magnonen und Magnonen in magnetischen Heterostrukturen und Magnonen und Photonen in photonischen Resonatoren. Unsere Ergebnisse werden dabei helfen, den Spin-Freiheitsgrad des Elektrons in neuen spintronischen Bauteilen zu nutzen.

Contents

Introduction

1

Our everyday life is strongly influenced by a big stream of data. Mobile applications, the internet of things and cloud computation not only allow for a fast data communication between all clients, they all require electrical energy, mass storage and the ability to process data.

The modern information technology which is based on complementary metal-oxide semiconductors (CMOS), is facing new challenges, which are not only relevant to technical enthusiasts, but for the big data society. According to Moore's law an exponential increase of the processing speed was predicted in the late 1960's [1]. However, only thirty years later the clock speed of CMOS based processors started to stagnate. The solution to this problem was to increase the number of transistors per chip, which goes along with a downscaling of the transistors. However, this process is bound by physical limitations. For example, the Shannon-von Neumann-Landauer entropy [2] predicts a minimal switching energy at room temperature, which limits the transistor size to about 1.5 nm, due to the Heisenberg uncertainty principle [3]. In addition, solving this problem would not remove the linear calculation limitations, which come into play for exponential problems, like finding the shortest path between several destinations, for transportation of cargo (travelling salesman problem) or public transport with shared autonomous cars. For this, we require the application of quantum technology [4, 5].

On the other hand, mass storage faces similar problems. The feature size of the bits needs to be reduced in order to keep the device size small. This is indeed a macroscopic problem in the world of big data centers, where a doubling of the storage density results in a data center, which needs about half the space. However, with the realization of a single atom data storage [6] the end of the downscaling process seems to be within reach.

In the field of modern information technology, we thus require an alternative to CMOS technology, at some point in the future. One candidate to overcome several limitations of the CMOS technology is the field of spintronics, which sparked a lot of attention and research after the awarding of the Nobel-Prize to Albert Fert and Peter Grünberg in 2007 for the discovery for the giant magnetoresistance effect (GMR) [7–10]. In spintronics, we utilize the spin degree of freedom, not only the charge freedom of the electron. This leads for example to the change of the electric resistance of a magnetic bilayer, in dependence on the relative bilayer magnetization direction (GMR). In the field of magnonics the pure spin-degree of freedom is utilized in the framework of spin waves, which allow for a parallel processing of data, with high clock speeds and a feature size limitation, which is

in the order of the lattice constant of the magnet. In this field, the ferrimagnetic insulator yttrium iron garnet (YIG) has numerous applications due to its low intrinsic Gilbert damping and large spin-wave propagation length [11]. It is used as prototypical material in various experiments [12–16] and is indispensable for microwave technology. We therefore mainly focus on this material in this thesis.

However, spintronic devices are not likely to replace all of the devices based on CMOS technology in the near future. Nevertheless, a combination of spintronics and CMOS is an exciting challenge as the application of the GMR effect in hard disk drives has shown. This thesis therefore aims at the investigation of coupling mechanisms between magnons and electrons in semiconductors, magnons and magnons in magnetic heterostructures, and magnons to photonic resonators. With these effects, it is possible to combine the best of two worlds, as they can be understood as read- and write operations between different data systems.

The thesis is organized as follows. In Chapter 2, we give the theoretical background, which includes the description of the ferromagnetic resonance using the Landau-Lifshitz-Gilbert equation and the dissipation processes in ferromagnetic materials. We furthermore present the FMR technique, and a generic experimental FMR measurement setup. Finally, we discuss the origin of our measurement signals, and show that we have direct access to the ac magnetic susceptibility through FMR experiments.

In Chapter 3, we report on the spin pumping mechanism in a generic ferromagnet/semiconductor system, here, permalloy/doped silicon samples. We introduce the theory of the spin pumping mechanism with which we can describe the transport of angular momentum from the magnetic spin system into silicon semiconductors. We present the FMR experiments, and investigate the efficiency of the spin injection into silicon in dependence on the silicon doping and the permalloy thickness.

In Chapter 4, we investigate the Gilbert damping of an yttrium iron garnet sphere. First, we derive the magnetostatic mode spectrum of the ferromagnetic insulator, and discuss the implications of a mode pattern on two-magnon scattering processes. Second, we present the experimental results where we find a record low Gilbert damping parameter for all magnetostatic modes, but different two-magnon scattering contributions. Third, theoretical calculations reveal the dominant influence of the two-magnon scattering at the interface of the sphere.

In Chapter 5, we investigate the dynamic magnetization coupling of two ferromagnets using spin currents and exchange coupling. In the first section, we extend the spin pumping theory from Chap. 3 to a ferromagnet 1/normal metal/ferromagnet 2 system, here yttrium iron garnet/copper/cobalt. We derive an expression for the dynamic susceptibility, together with a simplified macro spin model. The latter is used to discuss the influence of the different torques on the yttrium iron garnet and cobalt mode dispersions. In the experimental section, we find the excitation of spin waves with wavelength down less than 100 nanometers,

which is a first step towards exchange magnonics. We model and discuss our observations in the framework of our modified spin pumping theory.

In Chapter 6, we present our results on the strong coupling between magnons and photons in YIG/cavity hybrid systems. This effect can be employed for the up- and down-conversion of quantum signals between microwave and optical frequencies. We first introduce the magnon-photon coupling mechanism, and subsequently present the used split-ring resonator and the Brillouin light scattering measurement setup. In our experiments, we find the formation of a magnon-photon hybrid when the dispersions of the YIG and the SRR coincide.

Finally, we summarize the obtained experimental results in Chap. 7, and give an outlook to further exciting experiments.

Broadband Ferromagnetic Resonance

2

In 1946, Griffiths discovered an anomalous high-frequency resistance of ferromagnetic metals, when he studied the permeability of ferromagnetic films with microwaves with wavelengths between 1 cm to 3 cm as a function of the applied magnetic field [17]. It turned out that the features in the resistance curves shift with the used resonator wavelength, where the shift is in the order of the gyromagnetic ratio. As an explanation for this observation, Griffiths suggested a resonant absorption of the microwave field by the magnetic dipoles. As we know today, this indeed is the correct picture and marks the discovery of the ferromagnetic resonance absorption.

The resonant absorption of microwave energy in ferromagnets (or more generally in exchange-coupled systems) is known as ferromagnetic resonance (FMR), similar to electron spin resonance of paramagnetic electron spins, or nuclear magnetic resonance (NMR) which is successfully applied in a broad field of natural and medical sciences. The FMR plays a key-role in the field of spintronics and magnonics, as the dynamic properties of a ferromagnetic material determine important parameters such as magnetization switching timescales in hard disks or spin-torque random access memory and the propagation behavior of spin waves for microwave signal processing [18].

The theory of ferromagnetic resonance is of great importance for this thesis, as all presented results are based on dynamic magnetic excitations. In this chapter we thus review the underlying theory of ferromagnetic resonance absorption, and put the different chapters into the context our experiments.

In the first part of this chapter, we introduce the concept of the effective field, and the equation of motion of the magnetization, called the Landau-Lifshitz-Gilbert equation (LLG). We furthermore introduce the Gilbert damping mechanism and the understanding of inhomogeneous line broadenings. In the second part of this chapter, we present experimental realizations of broadband ferromagnetic resonance spectroscopy using a lock-in amplifier and a vector network analyzer (VNA), including quantitative expressions for the signal strength. In the third part of this chapter, we discuss experimentally induced damping mechanisms, such as radiative and eddy-current damping.

2.1 Theoretical Background

2.1.1 The Effective Field

To determine the properties of a dynamic magnetization precession in a ferromagnet, we need to summarize all energy contributions, which influence the orientation of the magnetization in an external magnetic field. The total magnetic energy E_{tot} normalized to the volume V and the saturation magnetization M_{s} is called the the total energy density $\varepsilon_{\mathrm{tot}} = E_{\mathrm{tot}}/(VM_{\mathrm{s}})$ and reads [19]:

$$\varepsilon_{\mathrm{tot}} = \varepsilon_{\mathrm{stat}} + \varepsilon_{\mathrm{dyn}} + \varepsilon_{\mathrm{ex}} + \varepsilon_{\mathrm{d}} + ..., \tag{2.1}$$

where $\varepsilon_{\mathrm{stat}}$ is the normalized energy density of the magnetization in a static magnetic field $\boldsymbol{H}$, $\varepsilon_{\mathrm{dyn}}$ is the normalized energy density contribution from a time dependent magnetic field $_{\mathrm{dyn}}$, $\varepsilon_{\mathrm{ex}}$ is the normalized exchange energy density and ε_{d} is the normalized demagnetization energy density. The latter two are discussed in some more detail below. We define the effective magnetic field as [19]:

$$\mu_0 \boldsymbol{H}_{\mathrm{eff}} = -\nabla_{\boldsymbol{M}} \varepsilon_{\mathrm{eff}}, \tag{2.2}$$

where

$$\nabla_{\boldsymbol{M}} = \left(\frac{\partial}{\partial m_x}, \frac{\partial}{\partial m_y}, \frac{\partial}{\partial m_z} \right) \tag{2.3}$$

is the gradient along the magnetization unit vector $\boldsymbol{M} = (m_x, m_y, m_z)$. In the following, we discuss the most important contributions to the effective magnetic field.

2.1.1.1 Exchange Field

The exchange field originates from the exchange energy in the magnet, which arises from spin-spin-interactions and the Pauli principle - it can thus only be understood based on quantum mechanics [20]. The exchange energy in the magnet scales with the so-called exchange integral J, which is the overlap of the electron wave functions, and thus decreases rapidly with increasing spatial spin separation [21]. The exchange energy of two spins reads [21]:

$$E_{\mathrm{ex},ij} = -2J\boldsymbol{S}_i \cdot \boldsymbol{S}_j. \tag{2.4}$$

For $J > 0$ a parallel alignment of the spins is favored, whereas for $J < 0$ an antiparallel alignment of the spins is preferred (ferromagnetic and antiferromagnetic coupling, respectively). Although the exchange integral gives a very clear picture of the origin of the exchange interaction, there are various other types of indirect exchange, where the electron wave functions do not overlap directly. In the case of

superexchange an oxygen atom couples the spin orientations of adjacent electrones via its atomic orbital, whereas in the case of RKKY interaction conduction electrons in standing electron waves mediate the exchange [20]. However, most importantly we study the direct exchange in this thesis, as this is the dominant mechanism in our experiments.

When the angle φ_{ij} between the spins is small, we can express the exchange energy as [22]:

$$\begin{aligned} E_{\mathrm{ex},ij} &= -2JS_iS_j\cos\left(\varphi_{ij}\right) = -2JS_iS_j\left(1-\frac{\varphi_{ij}^2}{2}+\mathcal{O}\left(\varphi^3\right)\right) \\ &= JS_iS_j\varphi_{ij}^2 - \underbrace{2JS_iS_j\left(1+\mathcal{O}\left(\varphi^3\right)\right)}_{\text{constant}}. \end{aligned} \tag{2.5}$$

Here we have first used the definition of the scalar product $\boldsymbol{S}_i\boldsymbol{S}_j = S_iS_j\cos(\varphi_{ij})$ with a subsequent Taylor expansion of the cos-function for small angles φ_{ij} between the spins. Equation (2.5) consists of a constant term, which is the source of a spontaneous magnetic order in the solid state, and a term which depends on the angle φ_{ij}^2. The latter shows the influences of spin textures on the exchange energy, such as domain walls or spin waves. In a ferromagnetic system, every pair of spins, which is not aligned in parallel, increases the exchange energy of the system. As we are only interested in this part for the discussion of magnetization dynamics, we neglect the constant term below.

Next, we want to derive an expression for φ_{ij} an follow Ref. [19]. From the scalar product and the Taylor expansion, we already know:

$$\varphi_{ij}^2 = 2\left(1-\frac{\boldsymbol{S}_i\cdot\boldsymbol{S}_j}{S_iS_j}\right) = 2(1-\boldsymbol{u}_i\cdot\boldsymbol{u}_j), \tag{2.6}$$

where $\boldsymbol{u}_i$ and $\boldsymbol{u}_j$ are the unit vectors of the spins. In the approximation the angles φ_{ij} are very small, and thus only change slightly between the lattice sites $\boldsymbol{r}_i$ and $\boldsymbol{r}_j$. We approximate $\boldsymbol{u}_j$ with a Taylor expansion in the coordinates of the lattice [19]:

$$\begin{aligned} \boldsymbol{u}_j = \boldsymbol{u}_i &+ \frac{\partial\boldsymbol{u}_i}{\partial x}x_j + \frac{\partial\boldsymbol{u}_i}{\partial y}y_j + \frac{\partial\boldsymbol{u}_i}{\partial z}z_j \\ &+ \frac{1}{2}\left(\frac{\partial^2\boldsymbol{u}_i}{\partial x^2}x_j^2 + \frac{\partial^2\boldsymbol{u}_i}{\partial y^2}y_j^2 + \frac{\partial^2\boldsymbol{u}_i}{\partial z^2}z_j^2\right) + \ldots \end{aligned} \tag{2.7}$$

Here, we have shifted the reference frame into the spin at $\boldsymbol{r}_i$, with which we can rewrite Eq. (2.5). As the exchange interaction requires the spin wave functions to overlap, we restrict our sum to the nearest neighbor terms [19]:

$$\begin{aligned} E_{\mathrm{ex},i} =& JS^2 \sum_{j\in nn} 2(1-\boldsymbol{u}_i\cdot\boldsymbol{u}_j) \\ =& -JS^2 \sum_{j\in nn} \left(\boldsymbol{u}_i \frac{\partial^2 \boldsymbol{u}_i}{\partial x^2} x_j^2 + \boldsymbol{u}_i \frac{\partial^2 \boldsymbol{u}_i}{\partial y^2} y_j^2 + \boldsymbol{u}_i \frac{\partial^2 \boldsymbol{u}_i}{\partial z^2} z_j^2 \right). \end{aligned} \tag{2.8}$$

Here, we used that all terms which are linear in x_j, y_j and z_j sum up to zero. E.g., for every spin at x_j there is an opposite energy contribution from the spin at $-x_j$. Note that the constant terms $\boldsymbol{u}_i^2 = 1$ vanish as well. Furthermore, we have assumed a distribution of equal spins in the lattice $S_i = S_j = S$ To simplify Eq. (2.8), we assume a cubic crystal structure with a lattice constant a. In such a structure we find [19]:

$$\sum_{j\in nn} x_j^2 = \sum_{j\in nn} y_j^2 = \sum_{j\in nn} z_j^2 = 2a^2, \tag{2.9}$$

which allows us to write:

$$E_{\mathrm{ex},i} = -2JS^2a^2\boldsymbol{u}_i\Delta\boldsymbol{u}_i, \tag{2.10}$$

where $\Delta = \partial^2/\partial x^2 + \partial^2/\partial y^2 + \partial^2/\partial z^2$ is the Laplace operator. Hence, the sum of Eq. (2.8) over the number of atomic pairs in a unit cell n yields the expression for the exchange density:

$$\varepsilon_{\mathrm{ex}} = \frac{1}{2V}\sum_{i=1}^{n} E_{\mathrm{ex},i} = -A_{\mathrm{ex}}\boldsymbol{u}_i\Delta\boldsymbol{u}_i. \tag{2.11}$$

Here, $A_{\mathrm{ex}} = JnS^2a^2/2V$ is the exchange constant, which is for yttrium iron garnet (YIG) in the order of $3.7\times10^{-12}\,\mathrm{pJ/m}$ [23]. As we want to use the units of magnetization, we replace the unit vector of the spin moment by the magnetization $\boldsymbol{u} \to \boldsymbol{M}$:

$$\varepsilon_{\mathrm{ex}} = -A_{\mathrm{ex}}\boldsymbol{M}\Delta\boldsymbol{M} = DM_{\mathrm{s}}\boldsymbol{M}\Delta\boldsymbol{M}/2. \tag{2.12}$$

Here, $D = 2A_{\mathrm{ex}}/M_{\mathrm{s}}$ is the exchange stiffness constant, which is for YIG in the order of $5.25\times10^{-17}\,\mathrm{Tm}^2$ [23].

2.1.1.2 Demagnetization field

The demagnetization field $\boldsymbol{H}_d$ arises from dipole-dipole interactions in the magnet, and thus couples the orientations of the magnetic moments over macroscopic distances. As all magnetic moments contribute to the dipolar energy, we find a vanishing dipolar interaction for infinite and homogeneous magnetized samples. However, for finite or inhomogeneous magnetized samples the dipolar interaction plays a major role, as shown below.

The dipole-dipole interaction between two magnetic moments $\boldsymbol{\mu}_i$ and $\boldsymbol{\mu}_j$ at the positions $\boldsymbol{r}_i$ and $\boldsymbol{r}_j$ with the distance $\boldsymbol{r} = \boldsymbol{r}_i - \boldsymbol{r}_j$ reads [24]:

$$E_\mathrm{d} = -\mu_0 \left(\frac{3\,(\boldsymbol{r}\cdot\boldsymbol{\mu}_i)\,(\boldsymbol{r}\cdot\boldsymbol{\mu}_j)}{r^5} - \frac{\boldsymbol{\mu}_i\cdot\boldsymbol{\mu}_j}{r^3} \right). \tag{2.13}$$

It is practically impossible to sum Eq. (2.13) over all combinations of i and j to obtain an expression for the dipolar energy in the magnetic sample. We thus use the Maxwell equations in the magnetostatic approximation to derive the demagnetization field directly [25]:

$$\nabla \times \boldsymbol{H}_d = 0, \tag{2.14}$$

$$\nabla \cdot \boldsymbol{B} = \nabla \cdot (\mu_0 \boldsymbol{H}_\mathrm{d} + \mu_0 M_\mathrm{s} \boldsymbol{M}) = 0. \tag{2.15}$$

As the rotation of $\boldsymbol{H}_\mathrm{d}$ vanishes, we can introduce a magnetic potential which satisfies [25]:

$$\boldsymbol{H}_\mathrm{d} = -\nabla\psi. \tag{2.16}$$

Together with the second Maxwell equation, we obtain the Poisson equation of magnetostatics [25]:

$$\Delta\psi = \nabla \cdot M_\mathrm{s}\boldsymbol{M} \equiv -\rho. \tag{2.17}$$

Here, $\rho = -\nabla \cdot M_\mathrm{s}\boldsymbol{M}$ is the effective magnetic charge density which creates the demagnetization field. The solution of the Poisson equation is a Poisson integral [25]:

$$\psi = -\frac{1}{4\pi} \int \frac{\nabla' \cdot M_\mathrm{s}\boldsymbol{M}(\boldsymbol{r}')}{|\boldsymbol{r} - \boldsymbol{r}'|} d^3r' \tag{2.18}$$

which can be separated into two contributions for the case of a finite sample volume [25]:

$$\psi = -\frac{1}{4\pi} \int_V \frac{\rho}{|\boldsymbol{r} - \boldsymbol{r}'|} d^3r' + \frac{1}{4\pi} \int_{\partial V} \frac{\sigma}{|\boldsymbol{r} - \boldsymbol{r}'|} d^2r'. \tag{2.19}$$

The first term denotes the magnetic volume charge, which is created by inhomogeneities of the sample magnetization, e.g. domain walls. The second term denotes the magnetic surface charge, which arises if the magnetization is not parallel to the surface of the sample $\sigma = \boldsymbol{n} \cdot M_\mathrm{s}\boldsymbol{M}$, where $\boldsymbol{n}$ is the surface normal. In the case of a homogeneous magnetized sample, only magnetic surface charges create the demagnetization field.

The energy density of the demagnetization field is defined as [20]:

$$\varepsilon_\mathrm{d} = -\frac{1}{2}\mu_0 M_\mathrm{s}\boldsymbol{M} \cdot \boldsymbol{H}_\mathrm{d} = \frac{1}{2}\mu_0 \boldsymbol{H}_\mathrm{d}^2. \tag{2.20}$$

It is easy to see that a demagnetization field always increases the energy density of the system. In order to reach the magnetic ground state, it is necessary to decrease the demagnetization energy by means of a closed magnetic flux. This leads to the formation of magnetic domains [20].

We can express the demagnetization field in an arbitrarily shaped sample using a demagnetization tensor [26]:

$$\boldsymbol{H}_\mathrm{d} = -\tilde{\boldsymbol{\mathcal{N}}} \cdot M_\mathrm{s}\boldsymbol{M}, \tag{2.21}$$

where

$$\tilde{\boldsymbol{\mathcal{N}}} = \begin{pmatrix} \mathcal{N}_{x'x'} & \mathcal{N}_{x'y'} & \mathcal{N}_{x'z'} \\ \mathcal{N}_{y'x'} & \mathcal{N}_{y'y'} & \mathcal{N}_{y'z'} \\ \mathcal{N}_{z'x'} & \mathcal{N}_{z'y'} & \mathcal{N}_{z'z'} \end{pmatrix}. \tag{2.22}$$

For general ellipsoids [27] the demagnetization tensor only consists of diagonal elements $\mathcal{N}_{ij} = 0$ with $\mathcal{N}_{x'x'} + \mathcal{N}_{y'y'} + \mathcal{N}_{z'z'} = 1$. The latter means, that the sum of the longitudinal demagnetization fields along the direction of $\boldsymbol{M}$ has the amplitude of the saturation magnetization [28].

In Tab. 2.1 the diagonal elements of the demagnetization tensor are shown for three sample shapes. Note that we express the demagnetization factors in a coordinate system, which is oriented along the symmetry axes of the ellipsoids. For a thin film which has the film normal parallel to the z'-axis, the only non-vanishing demagnetization component lies along the z'-direction (cf. Fig. 2.1) and has a magnitude $\mu_0 H_\mathrm{d} = -\mu_0 M_\mathrm{s}$. Hence, we must apply a magnetic field strength of $\mu_0 H = \mu_0 M_\mathrm{s}$ parallel to the film normal in order to overcome the demagnetization field and to turn the sample's magnetization out of the film plane. Without an external magnetic field, the sample's magnetization will align in the film plane to reduce the stray field energy in Eq. (2.20). In a spherical sample in contrast the demagnetization field is isotropic $H_\mathrm{d} = -M_\mathrm{s}/3$ in all directions.

Shape	$\mathcal{N}_{x'x'}$	$\mathcal{N}_{y'y'}$	$\mathcal{N}_{z'z'}$
sphere	1/3	1/3	1/3
film (film normal parallel to z'-axis)	0	0	1
cylinder (long axis along z'-axis)	1/2	1/2	0

Tab. 2.1. – Diagonal elements of the demagnetization tensor for various sample shapes, adapted from Ref. [29]

Furthermore, we can express the demagnetization energy density in terms of the demagnetization tensor using Eq. (2.20) and Eq. (2.21):

$$\varepsilon_\mathrm{d} = \frac{1}{2} M_\mathrm{s} \mu_0 \boldsymbol{M} \cdot \tilde{\boldsymbol{\mathcal{N}}} \cdot \boldsymbol{M}, \tag{2.23}$$

which simplifies the expressions for the demagnetization field tremendously.

2.1.2 Magnetization Dynamics - Macrospin Model

The magnetization dynamics in the solid state is a collective phenomenon, where the magnetic moments precess with a certain phase relation around the direction of the effective field. The case of a uniform precession phase is referred to as ferromagnetic resonance. The case where we have a non-uniform precession with a finite phase shift between adjacent spins is called a spin wave. In the following, we motivate the undamped Landau-Lifshitz equation, which describes this precessional motion. We then introduce the Landau-Lifshitz-Gilbert equation, which adds a phenomenological, viscous damping to the equation of motion. From the latter case, we also derive the expressions for the ferromagnetic resonance frequencies for arbitrary sample orientation.

2.1.2.1 Landau-Lifshitz-Gilbert Equation

The energy of a magnetic moment $\boldsymbol{\mu}_\mathrm{m}$ in an effective field is given by [20]:

$$E = -\boldsymbol{\mu}_\mathrm{m} \mu_0 \boldsymbol{H}_\mathrm{eff}, \tag{2.24}$$

where $\boldsymbol{H}_\mathrm{eff}$ is the effective magnetic field, introduced in Chap. 2.1.1. In the static case, the magnetic moment aligns parallel to the direction of the external field [20]. However, for deviations from the equilibrium position a torque $\boldsymbol{D}$ arises [29]:

$$\boldsymbol{D} = -\boldsymbol{\mu}_\mathrm{m} \times \boldsymbol{H}_\mathrm{eff}. \tag{2.25}$$

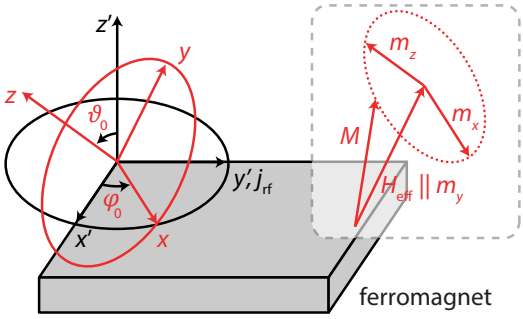

Fig. 2.1. – Coordinate system of a ferromagnetic film. The film normal is parallel to the z'-axis of the reference frame. However, if we apply a magnetic field under a certain angle (ϑ_0, φ_0) to the z'-axis, we have to rotate the demagnetization tensor accordingly. Inset: The magnetization precesses around the direction of the effective field.

The magnetic moment starts to precess around the direction of the effective field with a certain frequency ω, which is calculated below. The magnetic moment is connected to the total angular momentum $\boldsymbol{J}$ [29]:

$$\boldsymbol{\mu}_\mathrm{m} = -\gamma \boldsymbol{J}, \tag{2.26}$$

where $\gamma = g\mu_\mathrm{B}/\hbar$ is the gyromagnetic ratio. From this we derive the equation of motion:

$$\boldsymbol{D} = \frac{\partial \boldsymbol{J}}{\partial t} = \frac{1}{\gamma}\frac{\partial \boldsymbol{\mu}_\mathrm{m}}{\partial t} = -\boldsymbol{\mu}_\mathrm{m} \times \mu_0 \boldsymbol{H}_\mathrm{eff}, \tag{2.27}$$

where we have used that the torque equals the time derivative of the angular momentum. For the observation of an ensemble of magnetic moments, we summarize over the magnetic moments per unit volume, which leads to the Landau-Lifshitz equation [29–31]:

$$\frac{\partial \boldsymbol{M}}{\partial t} = -\gamma \boldsymbol{M} \times \mu_0 \boldsymbol{H}_\mathrm{eff}. \tag{2.28}$$

The Landau-Lifshitz equation describes the precessional motion of the magnetization around the effective magnetic field, which is shown in the inset of Fig. 2.1. The cone angle of the precession is constant, as no dissipation term is included in Eq. (2.28). The energy dissipation can be included using a phenomenological damping term, which leads to the Landau-Lifshitz-Gilbert equation [31, 32]:

$$\frac{\partial \boldsymbol{M}}{\partial t} = -\gamma \boldsymbol{M} \times \mu_0 \boldsymbol{H}_\mathrm{eff} + \alpha \boldsymbol{M} \times \frac{\partial \boldsymbol{M}}{\partial t}. \tag{2.29}$$

Here, α is the Gilbert damping parameter [32]. As the damping term is proportional to $\partial \boldsymbol{M}/\partial t$, we speak about a viscous damping.

2.1.2.2 Ferromagnetic Resonance

A solution of the linearized LLG yields the fundamental ferromagnetic resonance frequencies and linewidths for an arbitrarily shaped sample [29–31, 33]. For this we take the total magnetic free energy density normalized by the saturation magnetization, which reads:

$$\varepsilon_{\text{tot}} = -\mu_0(\boldsymbol{H} + \boldsymbol{H}_{\text{dyn}}) \cdot \boldsymbol{M} + \frac{1}{2}\mu_0 M_s \boldsymbol{M} \cdot \tilde{\boldsymbol{\mathcal{N}}} \cdot \boldsymbol{M} - \frac{D}{2}\boldsymbol{M}\Delta\boldsymbol{M}, \tag{2.30}$$

where we have already added a dynamic magnetic field $\boldsymbol{H}_{\text{dyn}}$, which produces small time-dependent perturbations from the magnetization's equilibrium position. The external magnetic field is applied in an arbitrary direction, with respect to the x', y', z'-laboratory frame. The aforementioned relation is only valid in the primed-system, as the demagnetization tensor is written in this system. Note that in a real system we need to take also the dipolar interaction between the spins into account [34]. However, we can neglect this interaction here, as this thesis mainly deals with the $k = 0$ FMR mode where the dipolar energy vanishes.

We can apply magnetic fields in any orientation with respect to the primed sample system. Without loss of generality, we introduce a new coordinate system, where the static part of the magnetization points along the y-direction, and the dynamic parts of the magnetization can be found in the m_x, m_z-components. In this coordinate system, the dynamic and static parts of the magnetization decouple [30]:

$$\boldsymbol{M} = \begin{pmatrix} m_x(t) \\ 0 \\ m_z(t) \end{pmatrix} + \begin{pmatrix} 0 \\ m_y \\ 0 \end{pmatrix}. \tag{2.31}$$

The demagnetization field of an ellipsoid depends on the angles between the magnetization and its symmetry axes. If we rotate the sample in the magnetic field around ϑ_0 and φ_0 (such as the in-plane and out-of-plane directions of a magnetic film), this can be mathematically accomplished by a rotation of the demagnetization tensor, as the entries $\mathcal{N}_{ii}$ are bound to the fixed sample shape.

To build our rotation matrix we use the Euler angles [35]. For this we first rotate our primed-system around the angle φ_0 around the z'-axis:

$$\tilde{\boldsymbol{\mathcal{U}}}_{z'} = \begin{pmatrix} \cos(\varphi_0) & \sin(\varphi_0) & 0 \\ -\sin(\varphi_0) & \cos(\varphi_0) & 0 \\ 0 & 0 & 1 \end{pmatrix}, \tag{2.32}$$

and second, we rotate the primed-system around the angle ϑ_0 around the x'-axis:

$$\tilde{\boldsymbol{\mathcal{U}}}_{x'} = \begin{pmatrix} 1 & 0 & 0 \\ 0 & \cos(\vartheta_0) & \sin(\vartheta_0) \\ 0 & -\sin(\vartheta_0) & \cos(\vartheta_0) \end{pmatrix}. \tag{2.33}$$

A rotation of a vector in our primed-system $\boldsymbol{r}'$ of the samples ellipsoid into the system of our magnetization $\boldsymbol{r}$ is obtained using:

$$\boldsymbol{r} = \tilde{\boldsymbol{\mathcal{U}}} \cdot \boldsymbol{r}' \tag{2.34}$$

with

$$\begin{aligned} \tilde{\boldsymbol{\mathcal{U}}} &= \tilde{\boldsymbol{\mathcal{U}}}_{x'} \cdot \tilde{\boldsymbol{\mathcal{U}}}_{z'} \\ &= \begin{pmatrix} \cos(\varphi_0) & \sin(\varphi_0) & 0 \\ -\cos(\vartheta_0)\sin(\varphi_0) & \cos(\vartheta_0)\cos(\varphi_0) & \sin(\vartheta_0) \\ \sin(\vartheta_0)\sin(\varphi_0) & -\cos(\varphi_0)\sin(\vartheta_0) & \cos(\vartheta_0) \end{pmatrix}. \end{aligned} \tag{2.35}$$

Using this transformation matrix, the m_x-component is always in the x'-y'-plane, whereas the m_z-component is either in the x'-y'-plane or perpendicular to it, depending on the angle ϑ_0.

The free energy density of a sample with an anisotropic demagnetization tensor in an arbitrarily oriented magnetic field then reads:

$$\begin{aligned} \varepsilon_{\text{tot}} = &-\mu_0(\boldsymbol{H}(\vartheta_0, \varphi_0) + \boldsymbol{H}_{\text{dyn}}(\vartheta_0, \varphi_0)) \cdot \boldsymbol{M} \\ &+ \frac{1}{2}\mu_0 \boldsymbol{M} \cdot \tilde{\boldsymbol{\mathcal{N}}}(\vartheta_0, \varphi_0) \cdot \boldsymbol{M} - \frac{D}{2}\boldsymbol{M}\Delta\boldsymbol{M}, \end{aligned} \tag{2.36}$$

where $\tilde{\boldsymbol{\mathcal{N}}}(\vartheta_0, \varphi_0) = \tilde{\boldsymbol{\mathcal{U}}}^{-1} \cdot \tilde{\boldsymbol{\mathcal{N}}} \cdot \tilde{\boldsymbol{\mathcal{U}}}$, and $\boldsymbol{H}_{\text{dyn}}(\vartheta_0, \varphi_0) = \tilde{\boldsymbol{\mathcal{U}}} \cdot \boldsymbol{H}_{\text{dyn}}$. Note that our dynamic magnetic field can always be described in the same coordinate system as the sample, as we do not rotate our samples relative to the excitation field. By using Eq. (2.36) in Eq. (2.2) we obtain the effective field, which we put into the Landau-Lifshitz-Gilbert equation (2.29). We linearize the Landau-Lifshitz-Gilbert equation around $m_x = m_z = 0$ as we only treat small magnetization perturbations and sort the remaining expressions in terms of the dynamic magnetization components. We furthermore assume that the deviations from the equilibrium orientation are small so that $m_y \approx 1$ and $m_x, m_z \ll m_y$ and we identify H as the applied magnetic static field strength. This yields for the dynamic magnetization:

$$M_{\text{s}} \begin{pmatrix} m_x \\ m_z \end{pmatrix} = \tilde{\chi} \begin{pmatrix} h_x \\ h_z \end{pmatrix} \tag{2.37}$$

where

$$\tilde{\chi} = \frac{\mu_0 M_s}{\chi_{xx}^{-1}\chi_{zz}^{-1} - \chi_{xz}^{-1}\chi_{zx}^{-1}} \begin{pmatrix} \chi_{zz}^{-1} & -\chi_{xz}^{-1} \\ -\chi_{zx}^{-1} & \chi_{xx}^{-1} \end{pmatrix} \tag{2.38}$$

is the Polder susceptibility tensor with the entries:

$$\begin{aligned} \chi_{zz}^{-1} =& - D_s k_z^2 - \mu_0 H - \frac{1}{2}\mu_0 M_s (N_{y'y'} + N_{z'z'}) + \frac{i\alpha\omega}{\gamma} \\ &+ \mu_0 M_s \left(N_{y'y'} \cos^2(\vartheta_0) + N_{z'z'} \sin^2(\vartheta_0)\right) \cos^2(\varphi_0) \\ &+ \mu_0 M_s \left(N_{x'x'} \sin^2(\varphi_0) + \frac{1}{2}(N_{y'y'} - N_{z'z'}) \cos(2\vartheta_0)\right) \end{aligned} \tag{2.39}$$

$$\chi_{xz}^{-1} = \mu_0 M_s (N_{z'z'} - N_{y'y'}) \cos(\vartheta_0) \sin(\vartheta_0) \sin(\varphi_0) - \frac{i\omega}{\gamma} \tag{2.40}$$

$$\chi_{zx}^{-1} = \mu_0 M_s (N_{z'z'} - N_{y'y'}) \cos(\vartheta_0) \sin(\vartheta_0) \sin(\varphi_0) + \frac{i\omega}{\gamma} \tag{2.41}$$

$$\begin{aligned} \chi_{xx}^{-1} =& - D_s k_z^2 - \mu_0 H + \frac{i\alpha\omega}{\gamma} \\ &+ \mu_0 M_s (-N_{x'x'} + \frac{1}{2} N_{y'y'} + \frac{1}{2} N_{z'z'}) \cos(2\varphi_0) \\ &+ \frac{1}{2}\mu_0 M_s (N_{y'y'} - N_{z'z'}) \cos(2\vartheta_0) \cos(2\varphi_0) \end{aligned} \tag{2.42}$$

In Fig. 2.2 (a) we plot the real and imaginary part of χ_{xx} for an out-of-plane magnetized film as a function of the applied microwave frequency for a fixed magnetic field. From the signal χ_{xx} we obtain a resonant behavior, which is associated with a certain resonance frequency and linewidth. We can easily determine the resonance frequency ω_{res}, and the full-width at half-maximum $\Delta\omega$ from the plot. However, it is also possible to calculate the resonance frequencies and linewidths. For this we set the determinant of the inverse susceptibility to zero:

$$\det\left(\tilde{\chi}^{-1}\right)|_{\omega=\omega_{res}} = \chi_{xx}^{-1}\chi_{zz}^{-1} - \chi_{zx}^{-1}\chi_{xz}^{-1}|_{\omega=\omega_{res}} = 0. \tag{2.43}$$

Hereby, the real part of the solution gives the resonance frequency, whereas the imaginary part gives the linewidth, which is determined by the Gilbert damping parameter. In the following, we want to investigate the ferromagnetic resonance conditions of two important sample shapes, which are used in this thesis.

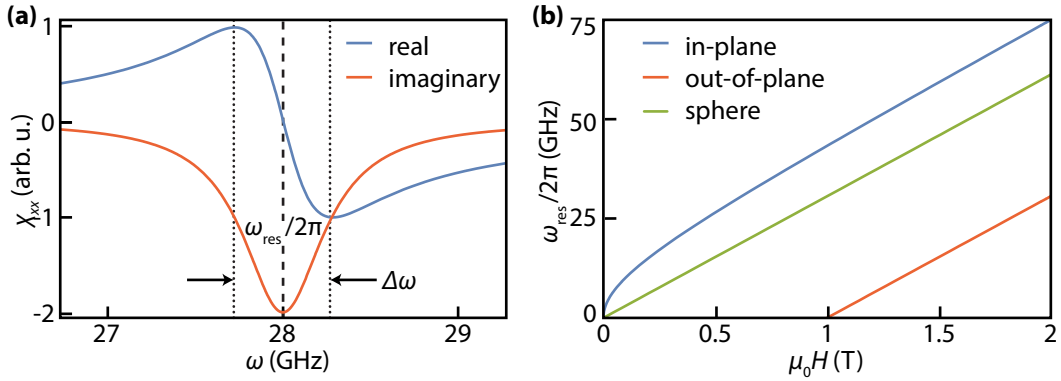

Fig. 2.2. – (a) Real and imaginary part of χ_{xx} calculated for $\mu_0 M_s = 1\,\mathrm{T}$, $\gamma = 28\,\mathrm{GHz/T}$, and a fixed magnetic field of $\mu_0 H = 2\,\mathrm{T}$ for an out-of-plane magnetized film. (b) Resonance conditions for different sample shapes and magnetization orientations.

2.1.2.3 Ferromagnetic Slabs

To calculate the ferromagnetic resonance frequencies of a film with the demagnetization factors given in Tab. (2.1), we assume an in-plane rotation of $\varphi_0 = 0$, hence the magnetic field can be applied in- and out-of-the film plane by a variation of ϑ_0. By using Eq. (2.43) we then obtain:

$$\begin{aligned}\omega_{\mathrm{res}} =& \frac{1}{2}\gamma\Big[4D_s^2k_z^4 + 2D_sk_z^2\mu_0(4H - M_s) \\ &+ \mu_0 M_s\left(\cos(2\vartheta_0)\left(6D_sk_z^2 + 6\mu_0 H - 2\mu_0 M_s\right) + \mu_0 M_s\cos(4\vartheta_0)\right) \\ &+ \mu_0^2\left(4H^2 - 2HM_s + M_s^2\right)\Big]^{1/2}\end{aligned} \tag{2.44}$$

We obtain the so-called Kittel equation for in-plane magnetized films for $\vartheta_0 = 0$ [23, 29]:

$$\omega_{\mathrm{res}}^{\mathrm{ip}} = \gamma\sqrt{\left(\mu_0 H + D_s k^2\right)\left(\mu_0 H + D_s k^2 + \mu_0 M_s\right)}, \tag{2.45}$$

whereas we find the well-known case for out-of-plane magnetized films for $\vartheta_0 = \pi/2$ [23, 29]:

$$\omega_{\mathrm{res}}^{\mathrm{oop}} = \gamma\left(\mu_0 H + D_s k^2 - \mu_0 M_s\right). \tag{2.46}$$

Both cases are shown in Fig. 2.2 (b) as blue and orange lines for $k = 0$. The resonance frequencies of the in-plane case are always higher than for the out-of-plane case, as the demagnetization field increases the effective field in the in-plane case, whereas it decreases the effective field for the out-of-plane case. We furthermore restrict the plot of the out-of-plane magnetized case to the part of Eq. (2.46) where $H > M_s$. For $H < M_s$ the magnetization is not aligned parallel

to the applied magnetic field due to demagnetization effects, which requires a numeric treatment of Eq. (2.43) in this intermediate regime.

2.1.2.4 Ferromagnetic Spheres

A ferromagnetic sphere with the demagnetization factors given in Tab. (2.1) has the resonance frequencies [29]:

$$\omega_{\text{res}} = \gamma \left(\mu_0 H + D_s k^2 \right) . \tag{2.47}$$

This resonance condition is independent of any demagnetization effects and any angle of the external static field. If we neglect the exchange interaction, the ferromagnetic resonance frequency only depends on the gyromagnetic ratio of the material, which allows to determine this parameter with a very high accuracy [36, 37]. The resonance condition is shown in Fig. 2.2 (b) as a green line.

2.2 Spin Waves

In ferromagnetic resonance all spins precess in phase. However, there are also excitations, where adjacent spins have a non-vanishing phase relation, so called spin waves. In this case again all spins precess with the same frequency, but the phase difference between adjacent spin determines a wavelength. The quanta of a spin wave is the magnon, which carries a spin of $\hbar$ and is thus a bosonic quasi particle. The finite wavelength (and thus the finite wavevector) together with a non-vanishing group velocity allow for information transport using spin waves [18]. This can be achieved by encoding information in the spin-wave phase [13, 38–41], or in the spin-wave amplitude [12, 14, 18, 42].

As for a spin wave not all spins precess in phase, we get locally different effective fields, which are due to dynamic demagnetization and exchange fields. Taking these effects into account, leads to a complex spin-wave manifold, where the spin-wave dispersion depends on the angle between the wave vector and the magnetization, the magnetic field, and material parameters. The complex spin-wave manifold delivers also the opportunity for $k = 0$ ferromagnetic resonances to scatter into excitations with $k \neq 0$, which makes it an important variable when we discuss the damping effects, e.g. in Chap. 4.

Kalinikos and Slavin have calculated the general spin-wave dispersion relations to be [34]:

$$\omega(k) = \gamma \sqrt{(\mu_0 H + D_s k^2)(\mu_0 H + D_s k^2 + \mu_0 M_s F_{nn}(k_\parallel, \phi, d))}. \tag{2.48}$$

Here, ω is the resonance frequency, k is the wavevector, H is the applied magnetic field, D_s is the exchange stiffness, d is the thickness of the magnetic film, ϕ is the angle between the magnetization and the wavevector. The in-plane wavevector is

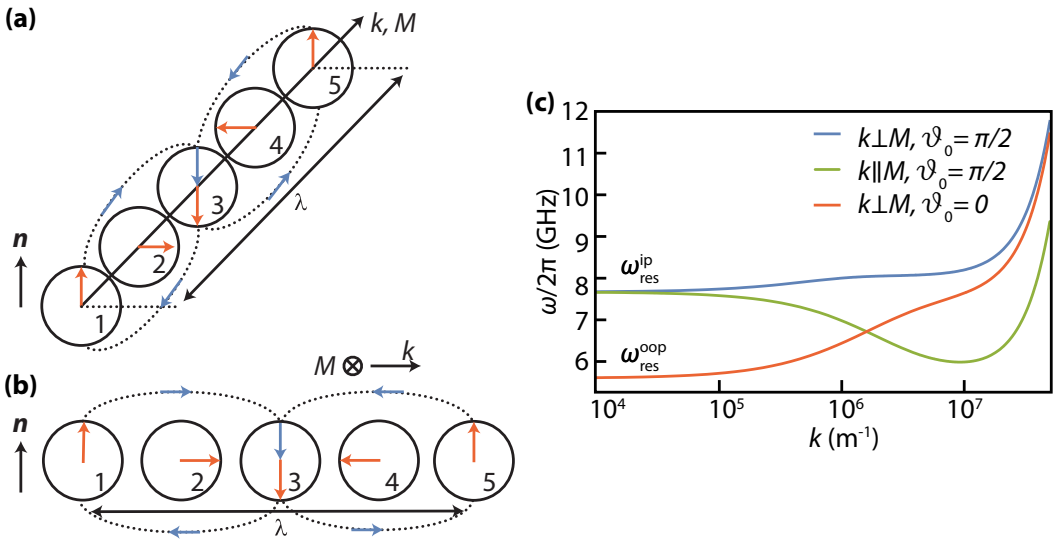

Fig. 2.3. – Dynamic magnetization components and stray fields for (a) backward volume waves, and (b) magnetostatic surface waves, adapted from Ref. [43]. (c) Spin-wave dispersion relations for backward volume (green), magnetostatic surface (blue) and forward volume (orange) waves.

given by $k_{\parallel}^2 = (n\pi/d)^2 - k^2$, where the term including the mode number n gives the wavevector of the standing spin wave over the film thickness. The factor F_{nn} is the matrix element which contains the dipole-dipole interaction of the dynamic magnetization of the n-th standing spin wave, which dominantly influences the dispersion relations. For the important case of $n = 0$ and hence $k_{\parallel} = k$, the dipole-dipole element is given by [34]:

$$F_{00}(k,\phi,d) = 1 + P_{00}(k)(1 - P_{00})\left(\frac{\mu_0 M_s}{\mu_0 H D_s k^2}\right)\sin(\phi)^2 - P_{00}\cos(\phi)^2, \qquad (2.49)$$

with

$$P_{00}(k) = 1 - \frac{1 - e^{-kd}}{kd}. \qquad (2.50)$$

We can now discuss the dispersion relations for three important cases [30, 34].

2.2.1 Backward Volume Waves

For in-plane magnetized films, where the wavevector is parallel to the magnetization direction, we are in the case of so called backward volume waves, where the wave propagates in the volume of the film [11]. The dynamic magnetization configuration for a point in time is shown in Fig. 2.3 (a) as red arrows. The dynamic magnetization produces a magnetic stray field, shown as blue arrows, when it points parallel to the film normal $\boldsymbol{n}$. When the spin-wave wavelength decreases, the stray fields become smaller, as the opposing dynamic magnetizations get closer to each other, which reduces the magnetic flux.

The dispersion relation is given by [11, 30, 34]:

$$\omega = \gamma \sqrt{(D_s k^2 + \mu_0 H)\left(D_s k^2 + \mu_0 H + \mu_0 M_s \frac{1 - e^{-dk}}{dk}\right)}, \tag{2.51}$$

which is plotted as green line in Fig. 2.3 (c) for $\mu_0 H = 0.2\,\mathrm{T}$, $\mu_0 M_s = 0.175\,\mathrm{T}$ and $D_s = 5.3 \times 10^{-17}\,\mathrm{Tm}^2$. We find indeed, that the frequency decreases with increasing wavevector, as predicted by the above picture. This is the reason we speak of backward volume waves, as the group velocity $v_g = \partial\omega/\partial k < 0$.

However, for large wavevectors the frequency increases rapidly with increasing wavevectors, due to exchange interactions.

2.2.2 Magnetostatic Surface Waves

For in-plane magnetized films, where the wavevector is perpendicular to the magnetization direction, we are in the case of magnetostatic surface waves. For magnetostatic surface waves the dynamic magnetization components are shown for a point in time in Fig. 2.3 (b). As known from the backward volume waves, a decrease of the wavelength reduces the dynamic stray fields. However, two adjacent dynamic magnetization vectors point antiparallel to each other (e.g. arrow 2 and 4), which increases the energy of the system [43]. The latter effect counteracts the reduction of the magnetic stray fields. We furthermore find, that the dynamic stray fields are parallel to the dynamic magnetization on the top side of the film, whereas the dynamic magnetization and the dynamic stray fields are antiparallel on the bottom side of the film. This illustrates, that the surface spin waves have a larger amplitude at one side of the film.

The dispersion relation for these waves is given by [11, 30, 34]:

$$\omega = \gamma \sqrt{(D_s k^2 + \mu_0 H)(D_s k^2 + \mu_0 H + \mu_0 M_s) + \frac{\mu_0^2 M_s^2}{4}(1 - e^{-2dk})}, \tag{2.52}$$

which is plotted as blue line in Fig. 2.3 (c). As the slope of the dispersion is positive for all wavevectors, all group velocities are positive as well.

At this point we want to emphasize that the spin-wave dispersion is obviously highly anisotropic, as we get different dispersion relations for different angles of wave propagation. This can lead to various scattering effects, when the propagation direction of the spin wave is changed [38]. However, it was successfully shown that the spin waves can effectively be steered by utilizing Snell's law for spin-wave dispersions [44], or by the application of thermal gradients [45].

2.2.3 Forward Volume Waves

When the magnetic film is magnetized parallel to the film normal and the wavevector lies in the film plane, the dynamic magnetization does not produce any magnetic stray field. In this case the spin-wave dispersion is isotropic (as all in plane wavevectors are perpendicular to the magnetization). The advantage of isotropic spin waves is that they can easily be guided around curves and bends, and that scattering effects into other modes are not possible [13].

The dispersion relation of these waves is given by [11, 30, 34]:

$$\omega = \gamma \sqrt{(D_s k^2 + \mu_0 H)\left(D_s k^2 + \mu_0 H + \mu_0 M_s \left(1 - \frac{1 - e^{-dk}}{dk}\right)\right)}, \tag{2.53}$$

which is plotted as orange line in Fig. 2.3 (c).

2.2.4 Exchange Waves

As motivated above an isotropic dispersion relation is favored for the application of spin waves in devices, as it easily allows for the utilization of spin waves in two dimensional structures, as they are not influenced by scattering effects. However, it is not always possible to tilt the magnetization out of the film plane, when only a limited external magnetic field exists which is smaller than the saturation magnetization. In this case one has to overcome the limitations of the dipole-dipole interaction in Eq. (2.48), which is the case for large wavevectors: $D_s k \gg \mu_0 M_s F_{pp}(k_\parallel, \phi, d))$. This limit can be found also in Fig. 2.3 (c), when the exchange interaction starts to dominate the different dispersion relations above $k > 10^7\,\mathrm{m}^{-1}$. In this limit the dispersion relation reduces to:

$$\omega(k) = \gamma(\mu_0 H + D_s k^2), \tag{2.54}$$

which is independent of the in-plane propagation angle ϕ. The dispersion increases quadratically with the wavevector, which leads to a group velocity $v_g \propto k$. Hence the information transport is faster for smaller wavelengths (larger k).

2.3 Damping Models

We here introduce the Gilbert damping mechanism, which is important for all experiments conducted in this thesis. We additionally include a discussion of the inhomogeneous line broadening which is an indicator for the sample quality (homogeneity and roughness), which is of great importance for Chap. 4. Furthermore, we introduce extrinsic damping contributions, which stem from the coupling between the samples and the experimental setup, which is required for Chap. 3.

2.3.1 Gilbert Damping

The Gilbert damping describes a viscous relaxation of the ferromagnetic resonance. By a measurement of the Gilbert damping parameter we gain information about the spin-wave lifetime. Different intrinsic damping mechanisms resulting in Gilbert damping have been proposed, such as the scattering of magnons with phonons [37, 46–48], where the magnon loses energy to the lattice. This phenomenon can ultimately be traced back to the spin-orbit interaction [49]. Furthermore, magnons can lead to inter- and intraband excitations by magnon-electron scattering [50]. Last but not least magnons can scatter with other magnons which leads to a manifold of multi-magnon scattering processes [36, 46, 51–59]. Another Gilbert-like damping mechanism is the creation of eddy currents in metallic ferromagnets or conducting substrates. Such eddy current damping is not present in ferromagnetic insulators. An eddy current can also be created in the metallic coplanar waveguide or the microwave cavity, which excites the ferromagnetic resonance. In this case, one speaks about radiative damping. Both phenomena are discussed in detail in Chap. 2.5. Furthermore, Gilbert-like damping can arise due to the creation of spin currents, known as the spin pumping mechanism. This damping requires an additional metallic layer adjacent to the ferromagnet. The spin current, which is created by the ferromagnetic resonance, is then absorbed in the metal. A detailed discussion can be found in Chap. 3.1.

In the following we show the connection of the Gilbert damping to the spin-wave lifetime, and derive an import expression for the resulting resonance linewidth. As can be seen from the Landau-Lifshitz-Gilbert equation (2.29), a transition from the undamped LLG to the damped LLG is achieved by using the transition:

$$\omega \rightarrow \omega - i\alpha\omega \tag{2.55}$$

in the susceptibility tensor. Hence, the damping is always given by $\mathrm{Im}\left[\omega_{\mathrm{res}}\right]$ as stated before in Chap. 2.1.2.2. Using the transition to complex frequencies leads to an exponential decay of the magnetization precession, e.g.:

$$m_x \rightarrow m_x \mathrm{e}^{-i\omega t}\mathrm{e}^{-\alpha\omega t}, \tag{2.56}$$

where we can connect a relaxation rate $1/t_{\mathrm{e}}$ of the magnetic excitation with the Gilbert damping, where t_{e} is the time in which the spin-wave amplitude drops to $1/\mathrm{e}$:

$$1/t_{\mathrm{e}} = \alpha\omega_{\mathrm{res}} = \Delta\omega/2. \tag{2.57}$$

In the last step, we have used a Fourier transformation that connects the relaxation time with the full width at half maximum $\Delta\omega$ in the frequency space. We furthermore obtain the important relation:

$$\Delta\omega = 2\alpha\omega_{\mathrm{res}}, \tag{2.58}$$

which describes a linear dependence of the resonance linewidth on the resonance frequency. However, in many experiments the linewidth of the FMR resonance is only available in the magnetic field space. In this case the linewidth is given by $\mathrm{Im}\,[H_{\mathrm{res}}]$, from which we obtain [60]:

$$\mu_0\Delta H = \frac{2\omega\alpha}{\gamma}. \tag{2.59}$$

A conversion between the resonance linewidth in field and frequency space is given by using the following relation for small linewidths:

$$\frac{\Delta\omega}{\Delta H} \rightarrow \left.\frac{\partial\omega}{\partial H}\right|_{\omega=\omega_{\mathrm{res}}}. \tag{2.60}$$

Equation (2.58) and Eq. (2.59) are the so called Gilbert damping relations.

2.3.2 Inhomogeneous Line Broadening

The Gilbert damping mechanism is not the only mechanism that increases the linewidth of the resonance. Experimentally, one often finds an extrapolated non-zero linewidth ΔH_0 for vanishing frequency, which is called the inhomogeneous line broadening:

$$\mu_0\Delta H = \frac{2\omega\alpha}{\gamma} + \mu_0\Delta H_0. \tag{2.61}$$

As the inhomogeneous line broadening varies with the sample quality, like grain size and surface roughness [48, 61] this process is considered to be an extrinsic damping. An important mechanism for the inhomogeneous line broadening are two-magnon scattering processes. In general, a two-magnon scattering process is described by the scattering of an incident magnon with wavevector $\boldsymbol{k}$ into a magnon state $\boldsymbol{k}'$:

$$\boldsymbol{k}' = \boldsymbol{k} + \boldsymbol{q}. \tag{2.62}$$

The conservation of energy requires that the incident and scattered magnon oscillate with the same frequency [62]:

$$\omega(\boldsymbol{k}) = \omega(\boldsymbol{k}'). \tag{2.63}$$

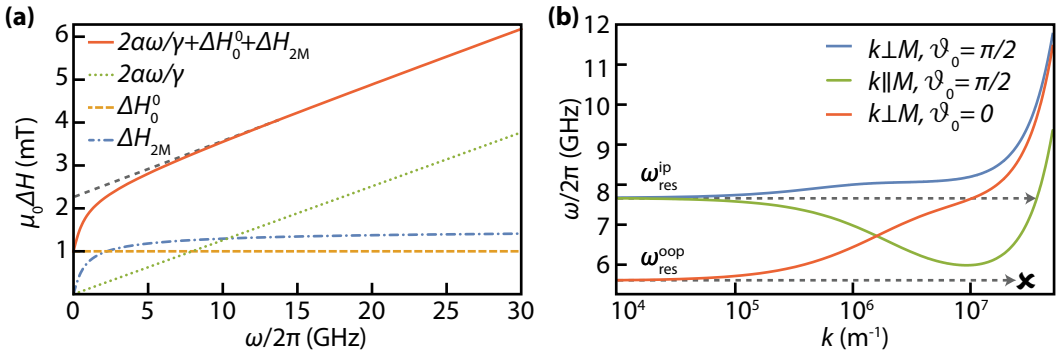

Fig. 2.4. – (a) Linewidth contributions as a function of excitation frequency. (b) Spin wave frequency as a function of the in-plane wavevector for different geometries.

Hereby the scattering is mediated by the magnetic potential of the inhomogeneities [55], which depends on the uniaxial anisotropy energy, and the spatial dimensions and shape of the inhomogeneities.

For the case of an in-plane magnetized magnetic film the linewidth due to two-magnon scattering processes is approximately given by [54, 63]:

$$\mu_0 \Delta H_{2\mathrm{M}} = \mu_0 \Gamma \arcsin \sqrt{\frac{\sqrt{\omega^2 + (\omega_\mathrm{M}/2)^2} - \omega_\mathrm{M}/2}{\sqrt{\omega^2 + (\omega_\mathrm{M}/2)^2} + \omega_\mathrm{M}/2}}, \tag{2.64}$$

where $\omega_\mathrm{M} = \gamma \mu_0 M_\mathrm{s}$. Figure 2.4 (a) shows the linewidth evolution from Eq. (2.64) as a function of the microwave frequency due to the two-magnon scattering for $\mu_0 M_\mathrm{s} = 0.175\,\mathrm{T}$ and $\mu_0 \Gamma = 1\,\mathrm{mT}$ (blue, dash-dotted line). We find a steep increase of the linewidth for small frequencies, but a fast saturation above $\omega/2\pi = 5\,\mathrm{GHz}$ towards the saturation value:

$$\mu_0 \Delta H_{2\mathrm{M}}^{\infty} = \lim_{\omega \to \infty} \mu_0 \Delta H_{2\mathrm{M}} = \frac{\pi \mu_0 \Gamma}{2}. \tag{2.65}$$

Above the saturation frequency, the two-magnon scattering contribution looks almost frequency-independent. The pure Gilbert-like part from Eq. (2.58) is shown as a green, dotted line for $\alpha = 0.01$, and denoted as $2\alpha\omega/\gamma$. It is a linear function of the microwave frequency. We further include a constant frequency offset of $\mu_0 \Delta H_0^0 = 1\,\mathrm{mT}$, which includes all other frequency independent linewidth contributions. The sum of all linewidth contributions is shown as orange, solid line:

$$\mu_0 \Delta H_\mathrm{tot} = \frac{2\alpha\omega}{\gamma} + \mu_0 \Delta H_{2\mathrm{M}} + \mu_0 \Delta H_0^0. \tag{2.66}$$

We find for frequencies below $\omega/2\pi = 5\,\mathrm{GHz}$ a steep increase which stems from the two-magnon scattering effects. For frequencies above $\omega/2\pi = 5\,\mathrm{GHz}$ we observe a linear increase as known from the Gilbert damping. The experimentally observed linewidth evolution is thus a superposition of two different damping

effects. However, if we fit a linear function to the linewidth evolution, the slope is given by the Gilbert damping parameter in good approximation, whereas the offset is given by $\Delta H_0 = \Delta H_{2M} + \Delta H_0^0$. We will refer to ΔH_0^0 as the inhomogeneous line broadening in the following.

However, we can switch off the two-magnon scattering effects by magnetizing the film parallel to the surface normal. In Fig. 2.4 (b) we show the spin-wave dispersions for different magnetization angles and propagation directions. The dispersions from Chap. 2.2 are plotted for $\mu_0 M_s = 0.175\,\mathrm{T}$, $D_s = 5.3 \times 10^{-17}\,\mathrm{Tm}^2$ and $d = 1\,\mu\mathrm{m}$, which are typical values for YIG [23]. For an in-plane excited magnon at ω_{res}^{ip} and $k = 0$ a scattering event is possible into a $\boldsymbol{k} \neq 0$ magnon at the same frequency. The reason for this is the complex spin-wave dispersion relation which depends on the demagnetization fields created by the dynamic magnetization [34]. However, for an out-of-plane excited magnon at ω_{res}^{oop} and $k = 0$, such a scattering effect is not possible. The dynamic magnetization components lie in the film plane and do not create any dynamic demagnetization fields. Thus, the spin-wave dispersion is isotropic, when the film is magnetized out-of-plane, and thus the two-magnon scattering effects are switched off. If an in-plane linewidth which exceeds the out-of-plane linewidth is observed experimentally, two-magnon scattering effects are likely the origin of this observation [64].

Note that in magnetic spheres we always create magnetic stray fields, as the demagnetization tensor is isotropic. Hence, we always find a wave vector in which we can scatter under the conservation of energy, cf. Fig. 4.3(a). Here, the two magnon scattering effects can only be reduced by improving the sample quality.

2.4 Experimental Methods

In this section, we present our lock-in broadband ferromagnetic resonance setup, and we discuss the origin of the measurement signal. A discussion of the vector network analyzer-based setup is given below in Chap. 2.4.3.

A sketch of a generic room-temperature broadband ferromagnetic resonance setup is shown in Fig. 2.5 (a). It consists of a three parts, firstly, the electromagnet, secondly, the coplanar waveguide for the creation of dynamic magnetic field, thirdly, the measurement group, for the excitation and detection of the ferromagnetic resonance.

For this thesis we used an water-cooled electromagnet consisting of an iron yoke and a pair of pole shoes. The electromagnet is operated using a bipolar Danfysik 9100 power supply, which is limited to a output voltage of $V_{out} = 60\,\mathrm{V}$, which results in a maximum current through the coils of the electromagnet of about $I_{max} = 70\,\mathrm{A}$. The pole shoes of the electromagnet are designed in a Helmholtz-like configuration in order to guarantee for a homogeneous static magnetic field in which the samples are placed. We use two pairs of pole shoes with different diameters in this thesis. With a pole shoe diameter of $a = 3\,\mathrm{cm}$ we have a field

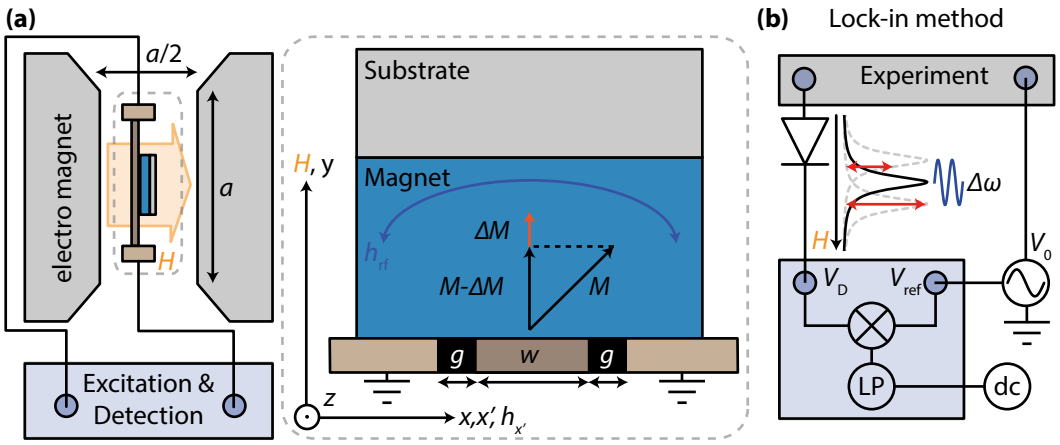

Fig. 2.5. – (a) Experimental setup for the broadband FMR measurement using the lock-in method. The samples are place face down onto the coplanar waveguide, where the microwave field of the CPW excites the ferromagnetic resonance. The out-of-plane magnetization angle is $\vartheta_0 = \pi/2$. Note that due to the in-plane rotation angle of $\varphi_0 = 0$ the x-axis and the x'-axis of the sample and the CPW coincide. (b) Sketch of the Lock-in method.

limitation of about $|\mu_0 H| \leq 2.9\,\mathrm{T}$, whereas we reach a maximum field of about $|\mu_0 H| \leq 2.25\,\mathrm{T}$ with a pole shoe diameter of $a = 5\,\mathrm{cm}$.

The samples were placed face down on the conductor of a coplanar waveguide (CPW), which was located between the pole shoes of the electromagnet. A CPW is an antenna structure which consists of a center conductor strip with a width w and adjacent ground electrodes in distance g to the center conductor [65]. The center conductor and the ground electrodes consist of a special silver alloy, which is deposited and patterned on a dielectric substrate. In order to enable a microwave transmission in a broad frequency range between $\omega/2\pi = 0\,\mathrm{GHz}$ and $\omega/2\pi = 43.5\,\mathrm{GHz}$, the coplanar waveguide is impedance matched to a standard microwave circuit impedance of $Z_0 = 50\,\Omega$. In this thesis we use a coplanar waveguide with $w = 300\,\mu\mathrm{m}$. The details of the CPW can be found in Ref. [66].

If a microwave current is injected into the CPW, an oscillating magnetic field will emerge around the center conductor due to Ampere's law. When the microwave frequency matches the resonance condition given by Eq. (2.43) for a certain applied magnetic field (or vice versa) this results in an oscillating torque on the samples magnetization and hence the excitation of the ferromagnetic resonance.

2.4.1 Principle of Reciprocity

We now address the FMR detection scheme [60, 67]. The precession of the magnetization in resonance above the CPW creates an oscillating magnetic flux in the center conductor, which leads to an inductive voltage due to Faraday's law. This inductive voltage is the signal used to detect FMR. To obtain an expression for the inductive voltage of the sample in the CPW, we use the principle of reciprocity, which says that we can replace the magnetization of the sample by a current loop, which generates the same flux [68]. The flux Φ generated by the transverse magnetization in the CPW is then given by [68, 69]:

$$\Phi = \frac{\mu_0}{I} \int_{V_{\text{sample}}} \boldsymbol{H}' M_s \boldsymbol{M}' dV, \tag{2.67}$$

where $\boldsymbol{H}'$ and $\boldsymbol{M}$ is the dynamic magnetic field and the dynamic magnetization in the coordinate system of the CPW. In this coordinate system we can express the magnetic driving field distribution by the Karlqvist equations [70] using $\boldsymbol{H}' = (h_{x'}, 0, h_{z'})$. Note that we have here assumed, that the microwave current in the CPW flows along the y' direction. The field strength can be calculated using the Karlqvist equations [70]:

$$h_{x'}(x', z') = -\frac{h_0}{\pi} \left(\arctan\left(\frac{w/2 + x'}{z'} \right) + \arctan\left(\frac{w/2 - x'}{z'} \right) \right) \tag{2.68}$$

$$h_{z'}(x', z') = \frac{h_0}{2\pi} \log\left(\frac{z'^2 + (w/2 + x')^2}{z'^2 + (w/2 - x')^2} \right), \tag{2.69}$$

where $h_0 = I/2w$, $I = \sqrt{P/Z_0}$ and P is the applied microwave power. The magnetic driving fields can be approximated for samples, which are much thinner than the width of the center conductor (for $z \ll w$) [68]:

$$h_{x'}(x', z') = h_0 \left(\Theta\left(x' + w/2\right) - \Theta\left(x' - w/2\right) \right) \tag{2.70}$$

$$h_{z'}(x', z') = \frac{h_0}{2\pi} \log\left(\frac{(w/2 + x')^2}{(w/2 - x')^2} \right), \tag{2.71}$$

Here Θ is the Heaviside step function. Note that the $h_{z'}$ vanishes, if we are in the center of the center conductor $x' = 0$. We now assume a uniform mode profile of the dynamic magnetization over the sample thickness, and the flux becomes [71]:

$$\begin{aligned}\Phi &= \frac{\mu_0 M_\mathrm{s}}{I} \int_{V_\mathrm{sample}} \boldsymbol{H}' \boldsymbol{M}'(t) dV \\ &= \frac{\mu_0 M_\mathrm{s}}{I} \int_{V_\mathrm{sample}} \boldsymbol{H}' \cdot \left(\mathcal{U}^{-1} \boldsymbol{M} \right) dV \\ &= \frac{\mu_0 M_\mathrm{s}}{I} \int_{V_\mathrm{sample}} \left(h_{x'} m_{x'} + h_{z'} m_{z'} \right) dV \\ &= \frac{\mu_0 M_\mathrm{s}}{2} dl m_{x'}.\end{aligned} \tag{2.72}$$

Note that we have used in the second line, that the dynamic magnetization points only along the x- and y- axis, which leads to $m_{x'} = m_x \cos(\varphi_0) + m_z \sin(\vartheta_0) \sin(\varphi_0)$, $m_{y'} = m_x \sin(\varphi_0) - m_z \sin(\vartheta_0) \cos(\varphi_0)$ and $m_{z'} = m_z \cos(\vartheta_0))$. In the fourth line we have neglected the $h_{z'}$ field as stated above and performed the integration, where d and l are the thickness and the length of the sample, respectively.

For the sample fixed coordinate system we now obtain the inductive voltage, which is created by the magnetization precession:

$$V_\mathrm{ind} = -\frac{\partial \Phi}{\partial t} = i\omega \frac{\mu_0 M_\mathrm{s}}{2} dl m_{x'}(t) \propto \chi_{x'x'} h_{x'}. \tag{2.73}$$

We find, that the inductive voltage depends on the geometry of the sample above the center conductor and the saturation magnetization. The inductive voltage furthermore increases with increasing microwave frequency, but most importantly inductive voltage depends on the $x'-$component of the magnetization. This comes from the principle of reciprocity, as we have only a sensitivity for the x'-component due to our assumptions. We hence have direct access to the dynamic susceptibility via the inductive voltage of the ferromagnetic resonance.

To gain more information about the dynamic magnetization process we rewrite the expression above in the coordinate system of the magnetization:

$$V_\mathrm{ind} = i\omega \frac{\mu_0 M_\mathrm{s}}{2} dl m_x (\cos(\varphi_0) + \eta \sin(\vartheta_0) \sin(\varphi_0)) \propto \chi_{xx}, \tag{2.74}$$

where we have introduced the ellipticity factor $\eta = m_z / m_x$, where the magnetization components have a phase shift of $\pi/2$. Note that we obtain a vanishing inductive voltage for an in-plane rotated sample ($\vartheta = 0$), where the center conductor is aligned perpendicular to the external field ($\varphi = \pi/2$). This is in full agreement with our experimental experiences.

2.4.2 Lock-In Amplifier Measurements

In our measurement setup in Fig. 2.5 (b) we employ a lock-in technique to investigate the ferromagnetic resonance. Our excitation group consists of a Rhode & Schwartz SMF100A microwave source, which is connected to the CPW. The detection group consists of a microwave diode, which rectifies the microwave currents, and a Zurich Instruments MFLI lock-in amplifier. In our lock-in experiments, we keep the microwave frequency fixed, and we sweep the external field. In the section below, we want to quantify the measurement signal.

The lock-in detection is a heterodyne detection method, where the signal is periodically modulated with a certain amplitude. The lock-in amplifier recognizes the modulation frequency and records the change of a voltage signal at that frequency. This results in a low-noise detection, as the bandwidth using this homodyning technique is only several Hertz wide, as shown below.

2.4.2.1 Frequency Modulation

In most of the experiments performed in this thesis, we use a frequency-modulation method, where we change the microwave excitation frequency periodically:

$$\omega' = \omega + \omega^* \sin\left(\Omega t + \varphi_{\text{sig}}\right). \tag{2.75}$$

Here, ω is the center frequency, ω^* is the frequency modulation depth, and $1/\Omega$ is the period of the frequency modulation. It is convenient to introduce here the phase φ_{sig}, which allows to compensate the phase accumulation due to the electrical length of the microwave cables from the output of the microwave source to the input of the lock-in amplifier. We assume that the modulation depth is small in comparison to the linewidth of the resonance, and $\Omega \ll \omega$, so that we expect a linear response of the susceptibility to the periodic modulation. We can then expand the susceptibility of our measurement signal, where we in the following neglect the index of $\chi_{x'x'}$:

$$\begin{aligned}\chi(\omega') &= \chi(\omega')\big|_{\omega'=\omega} + \left.\frac{\partial\chi}{\partial\omega'}\right|_{\omega'=\omega}(\omega' - \omega) \\ &= \chi(\omega')\big|_{\omega'=\omega} + \left.\frac{\partial\chi}{\partial\omega'}\right|_{\omega'=\omega}\omega^* \sin\left(\Omega t + \varphi_{\text{sig}}\right).\end{aligned} \tag{2.76}$$

2.4.2.2 Square-Law Detection

The measurement signal after the CPW is rectified with a microwave diode. The microwave diode is a square-law detector where the rectified output voltage is proportional to the square of the input voltage:

$$V_{\mathrm{D}} \propto V_{\mathrm{in}}^2 = (V_{\mathrm{BG}} + V_{\mathrm{ind}})^2 = V_{\mathrm{BG}}^2 + 2V_{\mathrm{BG}}V_{\mathrm{ind}} + V_{\mathrm{ind}}^2. \tag{2.77}$$

Here, we have used that the voltage input of the square-law detector is the sum of a background voltage and the inductive voltage. Note that the square-law detector includes a low-pass filter, so that the high-frequency component of the excitation frequency ω vanishes. The background voltage V_{BG} is proportional to the slope of the frequency transmission characteristic of the CPW. As $V_{\mathrm{ind}} \ll V_{\mathrm{BG}}$ we only have to take the linear terms of V_{ind} into account.

2.4.2.3 Homodyning Technique

The voltage signal of the diode is multiplied in the lock-in amplifier [72] using a reference voltage $V_{\mathrm{ref}} = V_{\mathrm{ref},0} \sin(\Omega' t + \varphi_{\mathrm{ref}})$. Here, $V_{\mathrm{ref},0}$ is the amplitude of the reference signal, $1/\Omega'$ is the period of the reference signal, and φ_{ref} is the internal reference phase of the lock-in amplifier. This reference voltage either stems from the lock-in itself, or is delivered from the microwave source, however, in each case it is useful to use the same reference clock for both instruments. We obtain:

$$\begin{aligned} V_{\mathrm{D}} V_{\mathrm{ref}} \approx & (V_{\mathrm{BG}}^2 + 2V_{\mathrm{BG}}V_{\mathrm{ind}}) V_{\mathrm{ref},0} \sin\left(\Omega' t + \varphi_{\mathrm{ref}}\right) \\ \propto & (V_{\mathrm{BG}}^2 + 2V_{\mathrm{BG}}\chi(\omega')) V_{\mathrm{ref},0} \sin\left(\Omega' t + \varphi_{\mathrm{ref}}\right) \\ = & \left(V_{\mathrm{BG}}^2 V_{\mathrm{ref},0} + 2V_{\mathrm{BG}}\, \chi(\omega')\big|_{\omega'=\omega}\right) V_{\mathrm{ref},0} \sin\left(\Omega' t + \varphi_{\mathrm{ref}}\right) \\ & + V_{\mathrm{BG}} V_{\mathrm{ref},0} \left.\frac{\partial \chi}{\partial \omega'}\right|_{\omega'=\omega} \omega^* \cos\left((\Omega - \Omega')t + \varphi_{\mathrm{sig}} - \varphi_{\mathrm{ref}}\right) \\ & + V_{\mathrm{BG}} V_{\mathrm{ref},0} \left.\frac{\partial \chi}{\partial \omega'}\right|_{\omega'=\omega} \omega^* \cos\left((\Omega + \Omega')t + \varphi_{\mathrm{sig}} + \varphi_{\mathrm{ref}}\right). \end{aligned} \tag{2.78}$$

In the second step we used the inductive voltage from Eq. (2.73), whereas we used the developed susceptibility from Eq. (2.76) in the third step. We find two fast oscillating terms with Ω' and $\Omega + \Omega'$, and a slowly oscillating term $\Omega - \Omega'$. In the experiment we have used the same frequency for the modulation and the reference signal $\Omega = \Omega'$, which results in a dc-component of the multiplied signal which contains all the measurement information. To increase the signal we have to phase-match the reference and signal phase $\varphi_{\mathrm{sig}} = \varphi_{\mathrm{ref}}$, which can be accomplished automatically by the lock-in amplifier. Note that the lock-in contains two phase-sensitive inputs, which are shifted by $\pi/2$, so that we are able to record

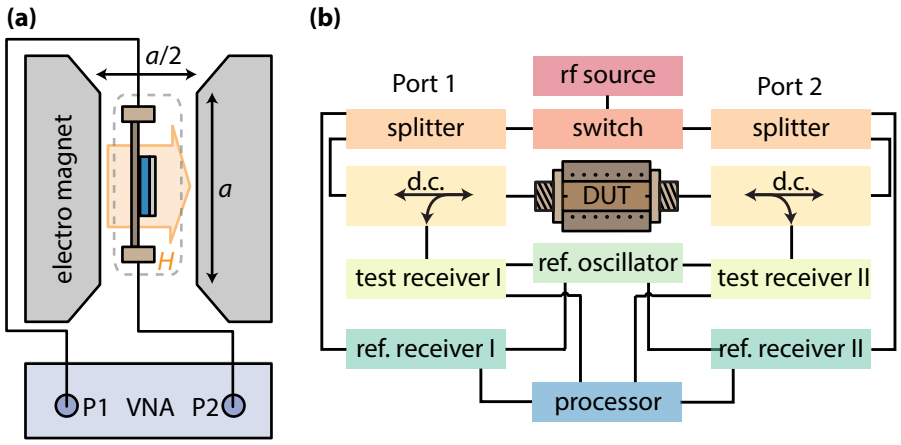

Fig. 2.6. – (a) Experimental setup for the VNA-based broadband FMR measurement. (b) Sketch of the VNA working principle.

a signal even if $\varphi_{\mathrm{sig}} - \varphi_{\mathrm{ref}} = \pi/2$. After a low-pass filtering of the multiplied signal we obtain:

$$V_{\mathrm{dc}} \propto \mathrm{e}^{i\varphi_\chi} \left| \frac{\partial \chi}{\partial \omega'} \right|_{\omega'=\omega} . \tag{2.79}$$

Here, we have introduced the phase of the resonance φ_χ, which is given by $\tan \varphi_\chi = \mathrm{Im}[\partial_{\omega'}\chi]/\mathrm{Re}[\partial_{\omega'}\chi]$. As we measure only the real part of our V_{dc}, we can fit the ferromagnetic resonances using:

$$V_{\mathrm{dc}}^{\mathrm{fit}} = A + B\mu_0 H + Z\cos(\varphi + \varphi_\chi) \left| \frac{\partial \chi_{x'x'}}{\partial \omega'} \right|_{\omega'=\omega} , \tag{2.80}$$

where we have to use the appropriate susceptibility functions. We furthermore replaced the proportionality with a small linear field dependent background, based on the real scaling parameters A, B and Z, and a fitting phase ϕ.

In summary, we can use a lock-in amplifier to measure the frequency-derivative of the dynamic magnetic susceptibility. We can then fit Eq. (2.80) to our homodyned measurement signal and extract the resonance field and the resonance linewidth of the measured resonance.

2.4.3 Vector Network Analyzer Measurements

In addition to our lock-in amplifier-based setup, we also use an Agilent N5242A PNA-X vector network analyzer-based setup for the detection of the FMR. The vector network analyzer setup consists of three devices, as shown in Fig. 2.6 (a). The electromagnet and the CPW which were already introduced. The vector network analyzer (VNA) is discussed in this section, as VNA measurements are used and discussed in Chap. 4 and Chap. 5. The VNA combines the aforementioned excitation and detection group in one device.

The VNA is used to characterize a device under test (DUT, in our case the CPW with the sample) by using scattering parameters:

$$S_{ij} = \left.\frac{V_i^-}{V_j^+}\right|_{V_k^+=0 \text{ for } k\neq j} = \frac{|V_i^-|}{|V_j^+|}e^{i\varphi}. \tag{2.81}$$

The scatter S-parameters are defined as the voltage wave ratio of the reflected voltage wave V_i^- from port i to the incident voltage wave V_j^+ from port i. In the second step we introduced the phase φ of the signal. In Fig. 2.6 (b) we sketch the operation principle of the VNA. In a first step, the microwave signal from an internal microwave source is switched towards port 1 or port 2. Without loss of generality, we only discuss the signal path through port 1, as it is similar for port 2. The microwave signal is split and directed towards a reference receiver (ref. receiver I) and a directional coupler (d. c.). The directional coupler again splits the signal path and the microwave travels towards a test receiver I but also towards the device under test, where we induce an inductive voltage with the ferromagnetic resonance as shown previously. Behind the DUT, the modified rf signal is guided towards the test receiver II by a directional coupler. The modified signal at the test receiver II is now compared in a processor to the undisturbed signal at the reference receiver I using a reference oscillator, which is the same for all receivers. From the relative amplitudes and phases one can now calculate the transmission and the reflection coefficients.

In general, the change of the transmitted signal with applied microwave frequency between the port 1 and port 2 is given by [71]:

$$\Delta S_{21} = \frac{S_{21} - S_{21}^0}{S_{21}^0}, \tag{2.82}$$

where S_{21} is the measured scattering parameter, and S_{21}^0 is the background signal, which contains all losses in the system, e.g. from the microwave cables or reflection losses. If we assume that we have a $Z_0 = 50\,\Omega$ impedance matched rf circuit, including the DUT, then the change of the transmission is given by [71]:

$$\Delta S_{21} = \frac{1}{2}\left(\frac{-i\omega L_0}{Z_0 + i\omega L_0}\right) \approx \frac{-i\omega L_0}{2Z_0}. \tag{2.83}$$

For this we have assumed a simple voltage divider model, where the inductance of the sample L_0 is in parallel with the impedance Z_0 of the rf circuit. The inductance is given using the flux from Eq. (2.72) [71]:

$$L_0 = \frac{\Phi}{I} = \frac{\mu_0 M_s}{4wh_0} dl m_x'(t) \tag{2.84}$$

Note that this expression is completely equivalent to the equations given in Ref. [71] for a uniform magnetization precession and a uniform dynamic magnetic field.

We can further simplify this expression for a CPW orientation along $\varphi_0 = 0$. In this case, the normal of the CPW is parallel to the external static magnetic field in the out-of-plane orientation, whereas the center conductor is parallel to the external field in the in-plane orientation. The inductance then reads [71]:

$$L_0 = \frac{\mu_0 M_s}{4w} dl \chi_{x'x'}, \tag{2.85}$$

and the measurement signal is given by [71]:

$$S_{21} = \Delta S_{21} S_{21}^0 + S_{21}^0 = S_{21}^0 - S_{21}^0 \frac{i\omega}{2Z_0} L_0 = S_{21}^0 - iCe^{i\varphi} \chi_{x'x'}. \tag{2.86}$$

The VNA measurements performed in this thesis were all conducted using frequency sweeps at fixed field. The VNA traces then contains the fingerprint of the magnetic resonance. As stated above the parameter S_{21}^0 contains a background signal from the CPW and the microwave cables. As these losses are frequency dependent, we have to model a frequency dependent microwave background $S_{21}^0 = A + B\omega$, where A and B are complex scaling parameters.

We can now perform a fit of Eq. (2.86) to our measured scatter parameters. From the fits we can then extract the magnetic susceptibility, the resonance frequency, and the linewidth of the resonance.

2.5 Experimentally Induced Damping

The precessing magnetization above the CPW induces an ac voltage in the center conductor due to Faraday's law, as shown in the previous sections. However, for the magnetization this is accompanied with a loss of energy, and thus a broadening of the linewidth. As the inductive voltage increases with increasing microwave frequency, we expect a Gilbert-like damping contribution to the total linewidth. This process is called radiative damping and should be present in all measurements.

Furthermore, we can also induce eddy-currents in metallic ferromagnetic samples and conducting substrates due to the time-varying magnetic flux. This process is independent from the excitation method, but vanishes in insulating ferromagnets and substrates. In the following we want to give quantitative expressions for both damping mechanisms, which is of crucial importance for the discussion of our results of Chap. 3.1.

2.5.1 Radiative Damping

As we have seen in Chap. 2.4.1 the magnetization precession is accompanied with an inductive voltage V_{ind}. This leads to an average radiative power dissipation:

$$P_{\mathrm{rad}} = V_{\mathrm{ind}} I_{\mathrm{ind}} = \frac{V_{\mathrm{ind}}^2}{Z_0} = -\frac{\omega^2}{Z_0} \mu_0^2 d^2 l^2 \langle m_{x'}(t)^2 \rangle \tag{2.87}$$

As shown in Ref. [67] we can use this expression to obtain the radiative damping contribution for a uniform precession [67]:

$$\alpha_{\mathrm{rad}} = \frac{1}{16} \frac{\eta \gamma M_{\mathrm{s}} \mu_0^2 dl}{Z_0 w} = C_{\mathrm{rad}} d. \tag{2.88}$$

Here, η is a correction factor for non-uniform modes. Equation (2.88) shows that the radiative damping depends on the sample and waveguide dimensions. In the second step we have absorbed all parameters into the prefactor C_{rad}. Hence, radiative damping is always present in our FMR measurements. We especially have to take radiative damping into account when we investigate the damping of a sample set, where the thickness is varied.

2.5.2 Eddy Current Damping

For the derivation of the eddy current damping, we take the total flux passing through the metallic film [67]:

$$\frac{\partial \Phi}{\partial t} = \frac{\mu_0 M_{\mathrm{s}}}{2} dl \frac{\partial m_{x'}(t)}{t}. \tag{2.89}$$

where ld is basically the area which is permeated by the flux. Again, we obtain from Ref. [67] the eddy-current damping contribution:

$$\alpha_{\mathrm{EC}} = \frac{C}{16} \frac{\gamma \mu_0^2 M_{\mathrm{s}} d^2}{\rho} = C_{\mathrm{EC}} d^2, \tag{2.90}$$

where C is a phenomenological parameter which accounts for non-uniform eddy-currents in the layer and ρ the resistivity of the film. In the second step we have absorbed all parameters into the prefactor C_{EC}. In total, we expect an enhancement of the Gilbert parameter for thick films and small substrate resistivities owing to Eddy currents.

3 Spin Pumping in Permalloy/Silicon Heterostructures

Spin injection into semiconductors was intensively studied in recent years in the hope to utilize the long spin relaxation time of single spins in semiconductors [73] for spin-based (quantum) information processing. Moreover, the gate tunability of carrier density, and thus of spin in semiconductors could allow to realize spin metal-oxide-semiconductor field-effect-transistors (MOSFETs). Finally yet importantly, the coupling of spin angular momentum to semiconductor properties opens a wide range of possible applications where spintronic and magnonic functionality can be integrated with CMOS technology.

A central problem for spin injection from FM metals into semiconductors is the conductance mismatch [74,75] between the metals (used for the spin injection) and the semiconductors. In simple terms, the spin injection efficiency into the semiconductor depends on the ratio σ_{SC}/σ_{FM}, where σ_{SC} and σ_{FM} are the conductivity of the semiconductor and the ferromagnet, respectively. As the conductivity of the ferromagnet is typically orders of magnitude larger than the conductivity of the semiconductor, the spin injection is very inefficient [76]. However, this limitation can be overcome by FM/TMR/SC stacks [75,77,78], where the TMR tunnel barrier acts as a spin-dependent resistance. Another very attractive option is the spin pumping mechanism [79,80], where angular momentum is transferred from a magnetic excitation to an adjacent layer. As spin pumping does not require the application of an electric current across the ferromagnet/semiconductor interface, it is not harnessed by conductance mismatch problems. Subsequently, spin injection via spin pumping into semiconductors was achieved independent on the conductivity mismatch between the layers of the heterostructures [81–85]. While the method was initially used in metallic multilayer systems, it was later implemented to inject spin currents into semiconductors [81,86], normal metals [87] and nowadays topological insulators [88–91] and ferromagnetic insulators [92], (cf. Chap. 5). Recently, we have utilized this method to achieve spin injection even into a two dimensional electron gas, which emerges between a 5 nm thick $LaAlO_3$ layer and a $SrTiO_3$ substrate [93]. However, to date there was no systematic study of the spin pumping based spin injection as a function of the resistivity of the underlying semiconductor channel.

In this chapter, we study the Gilbert damping parameter in permalloy/silicon heterostructures using broadband ferromagnetic resonance spectroscopy, which is a measure for the spin pumping efficiency. In the first part of the chapter we

present a short introduction to the theory of spin pumping. In the subsequent experimental section, we present the used FMR setup, and determine the Gilbert damping parameter of the Py as a function of the Si doping concentration, hence the Si resistivity. We observe an increase of the Gilbert damping in the Py (considering Py films with the same thickness) with increasing Si resistivity. In the second part of the experiments, we measure the Gilbert damping as a function of the Py thickness, whereas the Si resistivity is fixed. We observe a strong increase of the Gilbert damping with decreasing Py thickness, which evidences the interfacial nature of the spin pumping process and thus is an important confirmation of our interpretation. Furthermore, we do not find any increased Gilbert damping Py/Si samples with an insulating interlayer between the metal and the semiconductor. Our observations can be consistently explained with an enhanced spin pumping efficiency into Si with a low resistivity.

Some of the figures and parts of the text in this chapter have been published in R. Ohshima, S. Klingler, S. Dushenko, Y. Ando, M. Weiler, H. Huebl, T. Shinjo, S.T.B. Goennenwein, M. Shiraishi, *Spin injection into silicon detected by broadband ferromagnetic resonance spectroscopy*, Applied Physics Letters **110**, 182402 (2017).

3.1 Spin Pumping in a FM/NM System

According to Refs. [95,96] the spin pumping mechanism can be thought of as an analogy to an Archimedes' screw pump. The screw pump rotates mechanically and transports a certain amount of a fluid per revolution from one reservoir to the other. The spin pump, in analogy, can be though of as the magnetization precession, which transports angular momentum from one reservoir, the ferromagnet, to the other, the normal metal. As no net charge current but only a spin current is required to transport angular momentum, the spin pump is also operational in ferromagnetic insulators, such as YIG.

In a ferromagnetic resonance experiment, we feed angular momentum to the ferromagnet, as we excite a FMR mode, see Chap. 2.1.2.2. This results in an accumulation of (non-equilibrium) spin angular momentum in the ferromagnet. If we now bring a normal metal close to the ferromagnet, the spin accumulation can flow and relax into the normal metal via a spin current, which transports the spins away from the interface. Hence, the spin pumping mechanism is a loss of angular momentum of the ferromagnet. The creation of spin currents into an adjacent normal metal is accompanied with an increase of the Gilbert damping parameter of the ferromagnet [94,97–100], see Chap. 2.3. This makes broadband ferromagnetic resonance a suitable tool to detect the spin pumping effect. Another method to measure this relaxation mechanism is the electrically detected spin pumping [101–107]. For this a normal metal is required on top of the ferromagnet, which converts the spin current into a charge current via the inverse spin Hall effect, which can then be measured with a voltmeter.

In the following, we want to give a quantitative description of the spin pumping mechanism. The spin current which is pumped by a metallic ferromagnet is given by [79, 108, 109]:

$$\boldsymbol{I}_\mathrm{s} = \frac{\hbar}{4\pi}\left(A_\mathrm{r}\left(\boldsymbol{M}\times\frac{\partial \boldsymbol{M}}{\partial t}\right) - A_\mathrm{i}\frac{\partial \boldsymbol{M}}{\partial t}\right), \tag{3.1}$$

where $A_\mathrm{r}, A_\mathrm{i}$ are interfacial scattering parameters given by [108]:

$$A_\mathrm{r} = \frac{1}{2}\sum_{mn}|r^{\uparrow}_{mn} - r^{\downarrow}_{mn}|^2 + |t^{\uparrow}_{mn} - t^{\downarrow}_{mn}|^2, \tag{3.2}$$

$$A_\mathrm{i} = \mathrm{Im}\left[\sum_{mn}\left(r^{\uparrow}_{mn}r^{\downarrow *}_{mn} + t^{\uparrow}_{mn}t^{\downarrow *}_{mn}\right)\right], \tag{3.3}$$

where r_{mn} and t_{mn} are the reflection and transmission coefficients for spin-up ($\uparrow$) and spin-down ($\downarrow$) electrons and m, n are labels of the electron modes at the Fermi energy. The sum of Eq. (3.2) and Eq. (3.3) yields:

$$A_\mathrm{r} + iA_\mathrm{i} = \sum_{mn}\left(\delta_{mn} - r^{\uparrow}_{mn}r^{\downarrow *}_{mn}\right) - \sum_{mn}t^{\uparrow}_{mn}t^{\downarrow *}_{mn} = G^{\uparrow\downarrow} - T^{\uparrow\downarrow}, \tag{3.4}$$

where δ_{nm} is the Kronecker delta, $G^{\uparrow\downarrow} = \sum_{mn}\left(\delta_{mn} - r^{\uparrow}_{mn}r^{\downarrow *}_{mn}\right)$ is the complex interfacial spin mixing conductance and $T^{\uparrow\downarrow} = \sum_{mn} t^{\uparrow}_{mn}t^{\downarrow *}_{mn}$ is the complex transmission matrix [79]. If the ferromagnetic film is thicker than the transverse spin-coherence length $d > \pi/(k^{\uparrow}_\mathrm{F} - k^{\downarrow}_\mathrm{F})$, where $k^{\uparrow\downarrow}_\mathrm{F}$ are the spin-dependent Fermi wavevectors, the transmission matrix $T^{\uparrow\downarrow}$ vanishes as the spins dephase before they reach the interface [108]. Hence, the spin transport typically is governed by the reflection coefficients: $A_\mathrm{r} = \mathrm{Re}\left[G^{\uparrow\downarrow}\right]$ and $A_\mathrm{i} = i\mathrm{Im}\left[G^{\uparrow\downarrow}\right]$. This spin current across the FM/NM interface can thus be written as [79]:

$$\boldsymbol{I}_\mathrm{s} = \frac{\hbar}{4\pi}\left(\mathrm{Re}\left[G^{\uparrow\downarrow}\right]\boldsymbol{M}\times\frac{\partial \boldsymbol{M}}{\partial t} - \mathrm{Im}\left[G^{\uparrow\downarrow}\right]\frac{\partial \boldsymbol{M}}{\partial t}\right). \tag{3.5}$$

As detailed in literature, in many of the systems the imaginary part of the spin mixing conductance is either much smaller that the real part, or vanishes completely [79]. Thus, we neglect $\mathrm{Im}\left[G^{\uparrow\downarrow}\right]$ in the following. However, in Chap. 5 we will find a mechanism in magnetic heterostructures where this simplification seems not to be adequate.

Note that the model of the spin mixing conductance above is only valid for conducting magnets, as the $g^{\uparrow\downarrow}$ depends on the transmission and reflection coefficients of the conduction electrons at the ferromagnetic metal/normal metal interface. For a ferromagnetic insulator (FI)/normal metal (NM) heterostructures the situation is different, as no conduction electrons are present in the FI to transport spin angular momentum. However, the basic description of a spin current in Eq. (3.5) still holds, and a conversion of magnetic excitations into a

spin current in adjacent normal metal layers can be observed, see for example Refs. [97, 110, 111]. The spin mixing conductance is in this case related to a magnon current-spin current conversion at the interface [112], where the spin torque is mediated via the localized ion moments in the ferromagnetic insulator via local-moment exchange fields [112, 113]. Qualitatively one can understand this conversion as an annihilation of an excited magnon with angular momentum $\hbar$ in the FI at the FI/NM interface. The magnon transfers its angular momentum by a spin flip of a conduction electron in the NM (or vice versa). This creates a non-equilibrium spin accumulation which diffuses in the normal metal, and hence creates a spin current [112]. Surprisingly, the amplitude of the spin mixing conductance is in insulating yttrium iron garnet/normal metal/platinum of the same order of magnitude ($g^{\uparrow\downarrow} \approx 10^{19}\,\mathrm{m}^{-2}$) as in ferromagnetic metal/platinum heterostructures ($g^{\uparrow\downarrow} \approx 5 \times 10^{19}\,\mathrm{m}^{-2}$) [103, 114].

As already briefly mentioned above, the dissipation of a spin current into a normal metal shows up as a Gilbert-like damping of the ferromagnetic resonance. To derive the spin pumping damping, we take the pumped spin current as the total spin angular momentum, which dissipates [43, 62]:

$$\frac{\partial \boldsymbol{S}}{\partial t} = -\boldsymbol{I}_\mathrm{s} \tag{3.6}$$

where the total spin momentum is related to the total magnetic moment M_tot via $\gamma \boldsymbol{S} = -M_\mathrm{tot}\boldsymbol{M}$ [62]. Using $M_\mathrm{tot} = M_\mathrm{s} V$ we obtain a useful expression for the spin pumping damping:

$$\frac{\partial \boldsymbol{M}}{\partial t} = \frac{\gamma}{M_\mathrm{tot}}\boldsymbol{I}_\mathrm{s} = \frac{\gamma}{M_\mathrm{s} d}\frac{\hbar}{4\pi}\mathrm{Re}\left[g^{\uparrow\downarrow}\right]\boldsymbol{M} \times \frac{\partial \boldsymbol{M}}{\partial t}. \tag{3.7}$$

Here, $V = Ad$ is the volume of the magnet, A is the interface area, d denotes the thickness and $g^{\uparrow\downarrow} = G^{\uparrow\downarrow}/A$ is the normalized interfacial spin mixing conductance. We find from Eq. (3.7) that a magnet with a small total magnetization is more sensitive to a loss of angular momentum due to spin pumping, as a thin ferromagnet has less magnetic moments than a thick ferromagnet of the same material. Equation (3.7) is a torque equation, which has the same symmetry as the Gilbert damping, see Chap. 2.3. It is thus clear that the spin pumping mechanism can be detected by a change of the Gilbert damping parameter. For the case when all spins are absorbed in the adjacent metal we can write the increase of the Gilbert damping parameter as:

$$\alpha_\mathrm{sp} = \frac{\gamma}{M_\mathrm{s} d}\frac{\hbar}{4\pi}\mathrm{Re}\left[g^{\uparrow\downarrow}\right]. \tag{3.8}$$

In general a material might not absorb all of the spin current, but would emit it back to the pumping ferromagnet. This phenomenon is know as spin

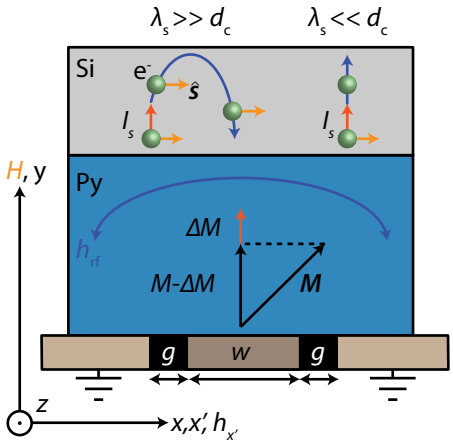

Fig. 3.1. – In ferromagnetic resonance, the magnetization M pumps a spin current I_s (red arrow) with a certain spin polarization (orange arrow) from the Py into the adjacent Si layer. For a long spin diffusion length λ_s the spin current is reflected back (shown as blue arrow), where the spin polarization is conserved (this is not the case for interfaces with spin-flip scattering). In total, the ferromagnet does not lose any angular momentum, when the spin current enters the ferromagnet again. In this case the Gilbert damping is not increased. However, for a short spin diffusion length, the spin current relaxes in the Si layer, which is a loss of angular momentum for the ferromagnet. In this case the Gilbert damping parameter is increased.

backflow [108], which can be considered in terms of an effective spin mixing conductance [114–116]:

$$g_{\text{eff}}^{\uparrow\downarrow} = \eta g^{\uparrow\downarrow}, \tag{3.9}$$

where

$$\eta = \left(1 + 2g^{\uparrow\downarrow}\rho\lambda_s \frac{e^2}{h} \coth \frac{d_c}{\lambda_s}\right)^{-1}. \tag{3.10}$$

Here, d_c the thickness of the conductor (metal) and λ_s the spin-diffusion length in the conductor and ρ is the resistivity of the normal metal.

In summary, the spin pumping process can be observed in ferromagnetic resonance experiments of FM/NM heterostructures. As the ferromagnet pumps angular momentum to the adjacent metal by the magnetization precession, we find an increase of the Gilbert damping parameter. As spin pumping is an interfacial process, thin ferromagnetic films are strongly affected by the loss of angular momentum, which make them suitable for such experiments.

We now come back to the spin pumping mechanism in semiconductors, where the following conditions, sketched in Fig. 3.1, should be fulfilled in order to achieve a large spin injection efficiency from the FM to the semiconductor: (i) trivially, mobile charge carriers should be present adjacent to the ferromagnet (where we here now take the semiconductor as the metal). In Fig. 3.1 the mobile charge carriers are depicted as electrons, shown in green. In our case, we vary the

conductivity of the Si layer by doping. (ii) The spin diffusion length should be small in comparison to the thickness of the conductor, so that an efficient relaxation of the spin current in the semiconductor is achieved. If the adjacent semiconductor has a long spin diffusion length, this would lead to a large spin accumulation close to the interface, which generates a large diffusive spin backflow in the direction opposite to the spin pumping current [109]. This spin backflow effectively cancels out the spin pumping current in systems with a long spin relaxation time, such that the spin pumping contribution to the Gilbert damping parameter becomes small of even vanishes if λ_s is large.

3.2 Experimental Methods

3.2.1 Sample Preparation

To investigate the spin pumping mechanism from ferromagnetic Py samples into Si three different sets of samples were prepared by R. Ohshima in the group of M. Shiraishi, Osaka, Japan. A first set of samples is produced to check the dependence of the Gilbert damping on the doping concentration and thus the resistivity of the Si samples. For this 7 nm-thick Py films are deposited by electron beam evaporation on top of various Si substrates. The sample size is $1 \times 1\,\mathrm{cm}^2$ throughout, but the resistivities of the substrates change in a range from $10^{-3}\,\Omega$cm to $10^{3}\,\Omega$cm owing to doping with phosphor atoms. The oxidized surface of the Si substrates is removed using 10 % hydrofluoric acid (HF) prior to the Py evaporation. This results in a direct contact of the Py with the doped substrates, without the influence of an insulating interlayer. The list of the used samples can be found in Tab. 3.1.

A second set of samples is prepared in order to investigate the dependence of the Gilbert damping parameter on the Py thickness. For this a P-doped SOI substrate is used with a fixed resistivity, for which we found the largest value for the Gilbert damping parameter in our experiments, see Tab. 3.1. SOI is the abbreviation for silicon-on-insulator, and describes a technique where a thin silicon layer is separated from the bulk silicon substrate by an oxide interlayer.

In a third set of samples, we intentionally decided to insert an insulating interlayer between the 7 nm-thick Py films and various substrates. The task of these control samples is to check whether there is an influence of eddy current damping from the substrates, that could jeopardize our interpretations. As eddy current damping changes the Gilbert damping parameters very similar to spin pumping, it is a problematic experimental artifact. Since, the spin pumping mechanism should be suppressed upon the introduction of insulating non-magnetic interlayers of sufficient thickness [92, 117, 118], this set of samples should only exhibit eddy current damping effects in addition to the intrinsic Py damping. The interlayers are prepared by evaporation of 2 nm of Ti and 3 nm of Al on the non-treated

substrates, with a subsequent oxidation for one day at ambient conditions. For the Al layer the process was repeated three times ($3 \times 1\,\mathrm{nm}$), as Al is self-passivating for a surface thickness of about 2 nm [119]. After the oxidation step the Py films are evaporated on top of the insulating layers. The list of the used control samples is also shown in Tab. 3.1.

3.2.2 Lock-In FMR Measurements

The lock-in amplifier FMR measurements were already introduced together with the used FMR setup (cf. Chap. 2.4.2 and Fig. 2.5). The samples are placed face down on the center conductor of a coplanar waveguide (CPW), which is located between the pole shoes of the electromagnet. Here, were use the pole show pair with $a = 3\,\mathrm{cm}$, which allows to apply external magnetic field of almost 3 T, where the saturation magnetization of Permalloy is in the order of $\mu_0 M_\mathrm{s} = 1\,\mathrm{T}$. In this way we have a theoretical frequency limitation (cf. Eq. (2.46)) of about 50 GHz, which is already higher than the available frequency range of the microwave source ($\omega/2\pi < 40\,\mathrm{GHz}$). The static magnetic field is applied perpendicular to the surface ($\vartheta_0 = \pi/2, \varphi_0 = 0$), as this prevents additional two-magnon scattering processes [120] (cf. Chap. 2.3.2). Note that in this configuration the y-axis is parallel to the z'-axis of the magnetic film, see Fig. 2.1.

In our measurement configuration, the resonance condition is given by the out-of-plane Kittel equation (2.46), where we neglect any exchange fields $H_\mathrm{ex} = 0$:

$$\omega_\mathrm{res}^\mathrm{oop} = \gamma\mu_0 \left(H - M_\mathrm{eff}\right). \tag{3.11}$$

The latter assumption is justified, as we do not observe any standing spin-wave modes in our samples, i.e. $k = 0$. Note, that we have introduced an effective magnetization $M_\mathrm{eff} = M_\mathrm{s} - H_\mathrm{ia}$, where $H_\mathrm{ia} \propto 1/d$ is the interfacial anisotropy field, which is inversely proportional to the thickness of the magnetic field [121, 122].

We use the Gilbert damping model, which phenomenologically models the viscous damping of the magnetic resonance. As detailed in Chap. 2.3, one then obtains a linear relation between the full width at half maximum ΔH of the resonance and the applied microwave frequency $\omega/2\pi$, the so-called Gilbert damping equation (2.66) [123]:

$$\mu_0 \Delta H = \mu_0 \Delta H_0 + \frac{2\alpha\omega}{\gamma} \tag{3.12}$$

Here, $\mu_0 \Delta H_0$ corresponds to the inhomogeneous line broadening as discussed in Chap. 2.3.2. The Gilbert damping parameters α consists of the intrinsic damping α_0,

Name	Doping density (cm^{-3})	Structure (nm)	Substrate resistivity (Ωcm)	α (10^{-3})	Re $[g^{\uparrow\downarrow}]$ ($10^{18}\,m^{-1}$)
Py/P-doped SOI	6.5×10^{19}	Py(7)/Si(100)/SiO_2(200)/Si	1.3×10^{-3}	10.7	5.7
Py/Sb-doped Si	1×10^{19}	Py(7)/Si	5×10^{-3}	9.3	2.3
Py/N-doped Si	1×10^{19}	Py(7)/Si	1×10^{-1}	9.5	2.6
Py/SOI	1×10^{15}	Py(7)/Si(100)/SiO_2(200)/Si	4.5	9.0	1.3
Py/P-doped Si	1×10^{13}	Py(7)/Si	1×10^{3}	8.7	0.5
Py/SiO_2	-	Py(7)/SiO_2(500)/Si	-	8.5	-
Py/Quartz	-	Py(7)/Si	-	8.6	-
Py/AlO_x/P-doped SOI	6.5×10^{19}	Py(7)/AlO_x(3)/ Si(100)/SiO_2(200)/Si	1.3×10^{-3}	8.5	-
Py/AlO_x/Sb-doped Si	1×10^{13}	Py(7)/AlO_x(3)/ Si	1.0×10^{3}	8.5	-
Py/AlO_x/SiO_2	-	Py(7)/AlO_x(3)/ SiO_2(500)/Si	-	8.8	-
Py/TiOx/P-doped SOI	6.5×10^{19}	Py(7)/TiO_x(2)/ Si(200)/SiO_2(300)/Si	1.3×10^{-3}	7.5	-
Py/TiO_x/P-doped Si	1×10^{13}	Py(7)/TiO_x(2)/ Si	1.0×10^{3}	7.9	-
Py/TiO_x/SiO_2	-	Py(7)/TiO_x(2)/ SiO_2(500)/Si	-	7.8	-
Py/P-doped SOI	6.5×10^{19}	Py(5)/Si(100)/SiO_2(200)/Si	1.3×10^{-3}	11.4	
		Py(7)/Si(100)/SiO_2(200)/Si		9.7	
		Py(10)/Si(100)/SiO_2(200)/Si		7.9	
		Py(15)/Si(100)/SiO_2(200)/Si		7.7	12
		Py(30)/Si(100)/SiO_2(200)/Si		7.8	
		Py(50)/Si(100)/SiO_2(200)/Si		8.0	
		Py(80)/Si(100)/SiO_2(200)/Si		8.0	

Tab. 3.1. – List of the used samples.

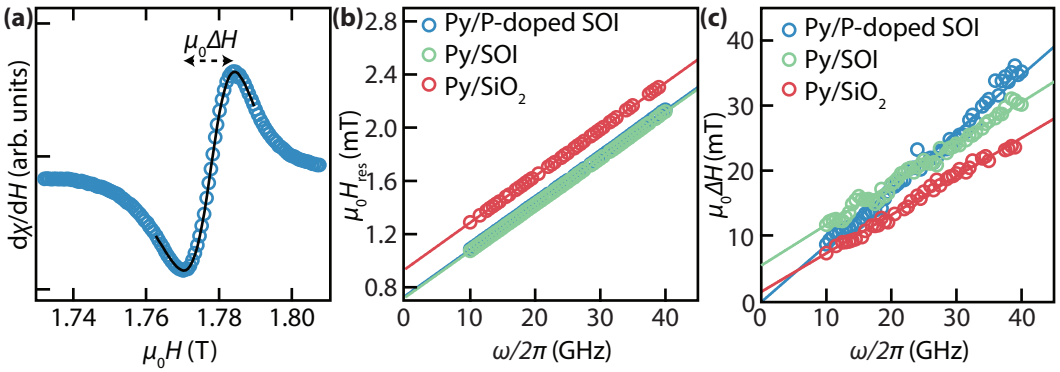

Fig. 3.2. – (a) typical ferromagnetic resonance spectrum of a 7 nm-thick Py film on a P-doped SOI substrate at $\omega/2\pi = 30\,\mathrm{GHz}$ (symbols). The black line shows the fitting curve. (b) Resonance field versus applied frequency for various samples with a Py thickness of 7 nm. (c) Linewidth as a function of applied frequency. The slope of the Py/P-doped SOI sample is increased in comparison to the Py/SOI and Py/SiO_2 samples.

the radiative damping α_{rad}, the eddy-current damping α_{EC} from Eq. (2.90), and the spin pumping damping α_{sp} from Eq. (3.8):

$$\alpha = \alpha_0 + \alpha_{\mathrm{sp}} + \alpha_0\mathrm{rad} + \alpha_{\mathrm{EC}} = \alpha_0 + \frac{\gamma}{M_s d}\frac{\hbar}{4\pi}\mathrm{Re}\left[g^{\uparrow\downarrow}\right] + C_{\mathrm{rad}}d + C_{\mathrm{EC}}d^2 \quad (3.13)$$

When we use the material parameters of Py ($\eta = 1$ (uniform precession), $\gamma/2\pi = 28\,\mathrm{GHz/T}$, $\mu_0 M_s = 1\,\mathrm{T}$, $Z_0 = 50\,\Omega$, $w = 300\,\mu\mathrm{m}$, $d \approx 10\,\mathrm{nm}$ and l=10 mm) we obtain from Eq. (2.88) that $\alpha_{\mathrm{rad}} \approx 0.1 \times 10^{-3}$, which is small compared to the intrinsic Py Gilbert damping parameter of permalloy $\alpha_0 \approx 6.5 \times 10^{-3}$ [67]. We can thus neglect the influence of radiative damping processes here.

3.3 Experimental Results

3.3.1 Silicon-Resistivity Dependence

Figure 3.2 (a) shows a typical lock-in FMR measurement of the 7 nm-thick Py on P-doped SOI sample (symbols). The microwave frequency is $\omega/2\pi = 30\,\mathrm{GHz}$ and the field is swept over the resonance field H_{res}. A single FMR line was observed here, but for frequencies below $\omega/2\pi = 10\,\mathrm{GHz}$ several modes were found in the resonances. This can be explained with a non-parallel alignment of the magnetization to the external field, and the formation of domains (not shown). The black line shows a fit of Eq. (2.80) to the data. More specifically, we use the susceptibility of a ferromagnetic film Eq. (2.38) with $\vartheta_0 = \pi/2$, $\varphi_0 = 0$ and $\mathcal{N}_{x'x'} = \mathcal{N}_{y'y'} = 0$ and $\mathcal{N}_{z'z'} = 1$ and thus fit:

$$V_{\mathrm{dc}}^{\mathrm{fit}} = A + B\mu_0 H + Z\cos(\varphi + \varphi_\chi)\left|\frac{\partial\chi}{\partial\omega'}\right|_{\omega'=\omega}, \quad (3.14)$$

with

$$\left.\frac{\partial\chi}{\partial\omega'}\right|_{\omega'=\omega} = \frac{1}{2}\gamma\mu_0 M_s \left(\frac{1-i\alpha}{(-i\alpha\omega - \gamma\mu_0(M_s - H) + \omega)^2} - \frac{1+i\alpha}{(i\alpha\omega + \gamma\mu_0(M_s - H) + \omega)^2} \right). \tag{3.15}$$

to the data. In order to obtain values for the linewidth ΔH and the resonance field H_{res}, we make the transitions: $\mu_0 M_s \rightarrow \mu_0 H_{res} - \omega/\gamma$ and $\alpha \rightarrow \mu_0 \Delta H \gamma/(2\omega)$, according to the Kittel- and Gilbert damping- equations.

3.3.1.1 Gilbert Damping

Figure 3.2 (b) shows the extracted resonance fields as a function of the applied microwave frequency for the Py/P-doped SOI, Py/SOI and Py/SiO_2 samples, where the Py thickness is 7 nm throughout. We fit the Kittel equation (3.11) to the data, from which we extract the g-factor and M_{eff}. Using $\gamma = g\mu_B/\hbar$, the extracted g-factors were estimated to be 2.049(1), 2.051(1), and 2.038(1) for the Py/P-doped SOI, Py/SOI and Py/SiO_2 samples, respectively. These values fit very good to previously reported values for Py films between $g = 2.0$ and $g = 2.17$, see Ref. [121] and references therein. The extracted effective magnetizations were estimated to be 0.732 T, 0.724 T and 0.935 T for the Py/P-doped SOI, Py/SOI and Py/SiO_2 samples, respectively. The reason for the discrepancy of M_{eff} to the bulk magnetization of Py ($\mu_0 M_s = 1\,T$, [67, 121]) is the shape anisotropy, which will be discussed below. We find that the effective magnetization of the Py/SiO_2 sample is increased in comparison to the other samples. This is attributed to the an inter-diffusion/inter-mixing of the Fe and Ni from the permalloy with the Si of the substrate [124, 125]. This is also the reason for a slightly different g-factor.

Figure 3.2 (c) shows the extracted linewidths as a function of the applied microwave frequency for the Py/P-doped SOI, Py/SOI and Py/SiO_2 samples. We find that the linewidth of all samples follow a linear function, as expected for Gilbert-like damping mechanisms. However, we also find that the slope of the Py/P-doped SOI sample is increased in comparison to the other samples. A fit of the Gilbert damping relation Eq. (3.12) to the data sets allows to extract the Gilbert damping parameters and the inhomogeneous line broadenings. The Gilbert damping parameters were estimated to be 10.7×10^{-3}, 9.0×10^{-3} and 8.5×10^{-3} for the Py/P-doped SOI, Py/SOI and Py/SiO_2 samples, respectively, where the accuracy of the Gilbert damping parameter is limited by the scattering of the data points. The Gilbert damping parameter of the 7 nm-thick Py films is determined in a similar fashion as above from Py/SiO_2 and Py/Quartz samples, as no spin pumping contributions are expected for these insulating samples ($\alpha = \alpha_0$). We find as Gilbert damping parameters $\alpha_0 = 8.5 \times 10^{-3}$ and $\alpha_0 = 8.6 \times 10^{-3}$, for the Py/$SiO_2$ and Py/Quartz samples respectively, which fits nicely into the range of previously reported damping parameters of Py films between 7×10^{-3}

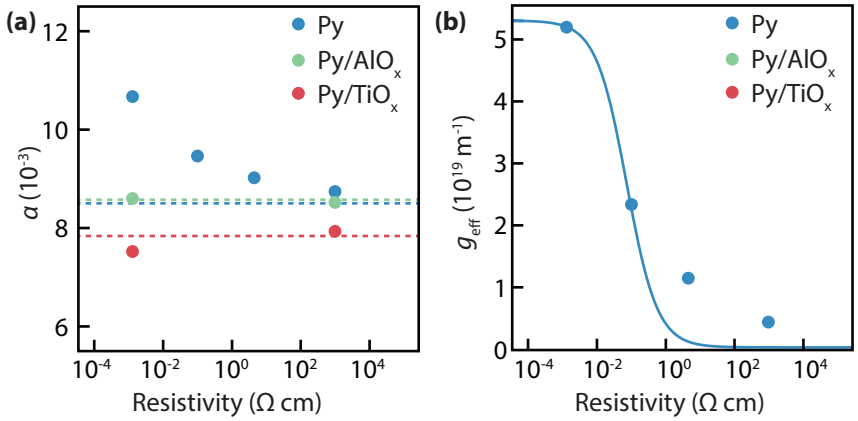

Fig. 3.3. – (a) Gilbert damping parameter as a function of the substrate resistivity. We observe a decrease of the Gilbert damping with increasing resistivity. (b) Effective spin mixing conductance as a function of the substrate resistivity. The blue line is a fit of Eq. (3.9) to the data.

and 9×10^{-3} for various thicknesses [67, 126]. When we compare the damping parameters of the samples with the conducting Si substrates with those for the insulating Si substrates, we find a decrease of the Gilbert damping with resistivity. We take this as a first hint that the spin pumping efficiency is suppressed with increasing substrate resistivity. However, in order to draw a robust conclusion, we must first address the impact of radiative and eddy current damping contributions.

3.3.1.2 Influence of Radiative Damping

Although, we have discussed that the influence of the radiative damping should be negligibly small, we now use our experimental data to verify this assumption. In order to determine the influence of a radiative damping into the Si substrate, we measure the linewidth evolution of Py/AlOx/Si and Py/TiOx/Si samples for various Si substrate resistivities. In those samples the insulating interlayer between the Py and the Si substrate should block any spin current, such that the Gilbert damping contribution from spin pumping vanishes ($\alpha_{sp} = 0$). However, the radiative damping process should persist in those samples. The eddy current damping process is the same for those samples due to the same Py thickness. We find Gilbert damping parameters of $\alpha = 8.8 \times 10^{-3}$ and $\alpha = 7.5 \times 10^{-3}$ for the Py/AlOx/Si and Py/TiOx/Si samples, respectively, independent of the Si resistivity. These damping parameters are in agreement with the extracted damping parameters for the Py/SiO_2 ($\alpha_0 = 8.5 \times 10^{-3}$) and the Py/Quartz ($\alpha_0 = 8.6 \times 10^{-3}$) samples. We can thus exclude any radiative damping into the Si substrate as origin of the decreasing Gilbert damping with increasing resistivity.

3.3.1.3 Variation of the Spin-Mixing Conductance

Figure 3.3 summarizes the experimental findings of various material parameters as a function of the substrate resistivity. Figure 3.3 (a) shows the Gilbert damping as a function of the substrate resistivity for various sample stacks. We find approximately a logarithmic decrease of the Gilbert damping with the substrate resistivity (blue symbols). This result is in agreement with the notion that the spin pumping requires the presence of free charge carriers in the system, which dissipate the angular momentum. Hence, the spin pumping is more efficient in the substrates with a small substrate resistivity. This goes along with to observation that the electron spin resonance linewidth increases with increasing substrate resistivity due to impurity spin-orbit interaction [127]. Hence, the samples with a large doping concentration lead to a shorter spin relaxation time and hence a shorter spin diffusion length (cf. Tab. 3.1). As a short spin diffusion length allows for an efficient dissipation of angular momentum, we expect an increased spin pumping efficiency for the samples with high doping concentration and small resistivity. The dashed lines in Fig. 3.3 (a) show the average values of the Gilbert damping of the Py/AlOx/Si and Py/TiOx/Si samples (green and red symbols, respectively), whereas the average Gilbert damping of the Py/SiO_2 and Py/Quartz samples is shown as blue, dashed line. Note that all measured samples without any insulating barrier show an increased Gilbert damping parameter, we attribute this observation to an enhanced spin pumping efficiency.

In order to quantify the influences of the resistivity on the damping, we calculate the spin mixing conductance using Eq. (3.8), as shown in Fig. 3.3 (b). For this we denote the spin pumping damping as $\alpha_{sp} = \alpha - \alpha_0$, where we use $\alpha_0 = 8.5 \times 10^{-3}$ from the Py/SiO_2 sample. The effective spin mixing conductance follows Eq. (3.9), where we take $g^{\uparrow\downarrow}$ and λ_s as free fit parameters. Unfortunately the relaxation mechanism of the spin current in the p-doped SOI is unclear and there are basically two mechanisms: (i) Elliot-Yaffet (EY) scattering [128,129] which is a spin-flip scattering process, where the spin-diffusion length in proportional to the conductivity of the semiconductor [130]. We can thus introduce a resistance: $\rho_{EY} = A_{EY}/\rho$, where A_{EY} is a scaling factor. (ii) D'yakonov-Perel (DP) scattering, which is a associated with a dephasation process of the conduction electron in effective magnetic fields during propagation. For the DP process the spin-diffusion length is independent on the conductivity [130]. Hence the DP resistance reads $\rho_{DP} = A_{DP}$, where A_{DP} is a scaling factor. We use Matthiessen's rule [131] to determine the total resistance due to both scattering mechanisms, which reads $\rho_{tot} = \rho_{EY} + \rho_{DP}$. We now use that the scattering time $\tau \propto 1/\rho_{tot}$, where the scattering time is connected to a scattering length via a constant A, which has the units of a velocity. We can thus write the spin-diffusion length as:

$$\lambda_s = \frac{A}{\rho_{tot}} = \frac{1}{A^*_{DP} + A^*_{EY}/\rho}, \tag{3.16}$$

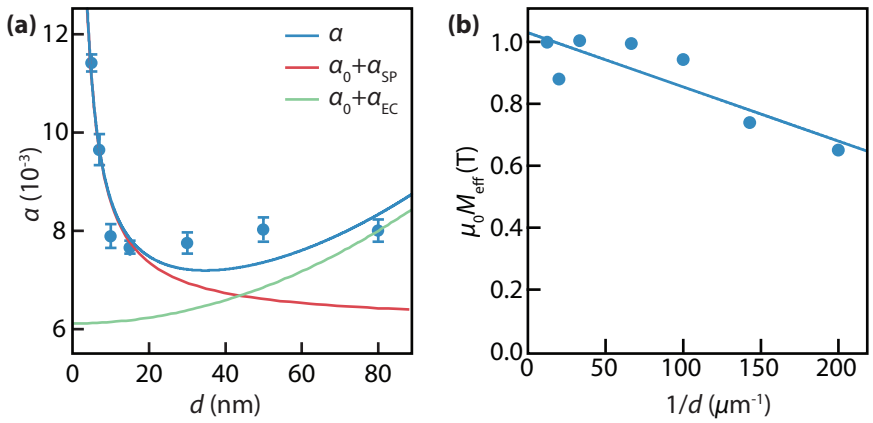

Fig. 3.4. – (a) Gilbert damping parameter as a function of the substrate resistivity. We observe a decrease of the Gilbert damping with increasing resistivity. (b) Gilbert damping parameter of the Py/P-doped SOI samples with various Py thicknesses. A decrease of the Gilbert damping is observed with increasing Py layer thickness in quantitative agreement with the spin pumping theory.

where we have absorbed the total scaling factor A into $A^*_{\mathrm{DP}} = A^{/}_{\mathrm{DP}} A$ and $A^*_{\mathrm{EY}} = A^{/}_{\mathrm{EY}} A$. A fit of Eq. (3.9) is shown as solid line in Fig. 3.3 (b). We find a good agreement between the theoretical model and our experimental values, although the theoretical spin mixing conductance should decrease faster with increasing substrate resistivity. From the fit we find $g^{\uparrow\downarrow} = 5.27 \times 10^{19}\,\mathrm{m}^{-2}$, which is of comparable magnitude to FI/NM and FM/NM samples [103, 114]. We furthermore find that $A^*_{\mathrm{DP}} = 3.5 \times 10^{12}\,\mathrm{m}^{-1}$, whereas we find for $2 \times 10^{-4}\,\mathrm{m}^{-1} < A^*_{\mathrm{EY}}/\rho < 2.5 \times 10^{2}\,\mathrm{m}^{-1}$, which might indicate a dominant D'yakonov-Perel scattering process. However, with the aforementioned values we find a constant spin-diffusion length of $\lambda_{\mathrm{s}} = 2.8 \times 10^{-13}\,\mathrm{m}$, which is unphysically small. We note that we use three free parameters for four data points in our fitting model, which might cause dramatic errors. Nevertheless, we draw the conclusion that the used model of the spin mixing conductance and the spin backflow at least describe qualitatively the behavior of the effective spin mixing conductance and the Gilbert damping of permalloy films of semiconductor substrates.

3.3.2 Permalloy-Thickness Dependence

To draw robust conclusion about the spin pumping and eddy current damping, we vary the permalloy thickness, as both damping processes are affected by this important sample property. We thus now address the dependence of the Gilbert damping parameter on the Py thickness. Figure 3.4 (a) shows the Py thickness dependence of the Gilbert damping parameter for the Py/P-doped SOI samples.

We find a fast decrease of the Gilbert damping with increasing Py thickness. The dataset is fitted using Eq. (3.12) and Eq. (3.13):

$$\alpha = \alpha_0 + \frac{\gamma}{M_s d}\frac{\hbar}{4\pi}\mathrm{Re}\left[g^{\uparrow\downarrow}\right] + C_{\mathrm{rad}} d + C_{\mathrm{EC}} d^2, \tag{3.17}$$

which is shown by the blue line. For this we use $C_{\mathrm{rad}} = 0$, α_0 and C_{EC} are free parameters, as well as the spin mixing conductance $g^{\uparrow\downarrow}$. All other material parameters were extracted above from the fit of the Kittel equation. We, again, find an excellent agreement between theory and experimental observations. We extract an intrinsic damping parameter of $\alpha_0 = 6.1 \times 10^{-3}$, a spin mixing conductance $g^{\uparrow\downarrow} = 1.2 \times 10^{19}\,\mathrm{m}^{-2}$ and $C_{\mathrm{EC}} = 2.9 \times 10^{11}\,\mathrm{m}^{-2}$. The intrinsic damping parameter extracted does not contain any eddy current damping contribution and is thus directly comparable to the intrinsic Gilbert damping parameter given in [67], $\alpha_0 = 6.5 \times 10^{-3}$. In comparison to the chapter above, we find a slightly decreased spin-mixing conductance. As can be seen from Tab. 3.1, we find also a smaller Gilbert damping for the 7 nm-thick permalloy film in this sample set. We thus argue that the different growth conditions lead to slightly different spin-mixing conductances. However, also the value extracted here is in the scatter of previously reported values for $g^{\uparrow\downarrow}$, see Ref. [114]. The red line shows the spin pumping contribution to the total damping. As expected from $\alpha_{\mathrm{sp}} \propto 1/d$ the spin pumping is dominant for small Py thicknesses. In contrast, the eddy current damping contribution (shown as green line) scales as $\alpha_{\mathrm{EC}} \propto d^2$ for large Py thicknesses. As evident from Fig. 3.4, eddy current damping is negligible for $d < 20\,\mathrm{nm}$. In particular, for Py films with a thickness of $d = 7\,\mathrm{nm}$, spin pumping damping dominates. We conclude that the eddy current damping in our samples, especially at $d = 7\,\mathrm{nm}$, is negligibly small. Hence, we can attribute the damping dependence on resistivity and Py thickness observed in the 7 nm-thick Py film samples entirely to the spin pumping effect.

Figure 3.4 (b) shows the thickness-dependence of the extracted saturation magnetization. We find a linear decrease of the magnetization with $1/d$, which is due to a small interfacial anisotropy [121, 122, 132]. From the y-intercept we find the bulk magnetization to be $\mu_0 M_s^{\mathrm{bulk}} = 1.03\,\mathrm{T}$ which fits very well to previously reported values ($\mu_0 M_s = 1.02\,\mathrm{T}$) [121].

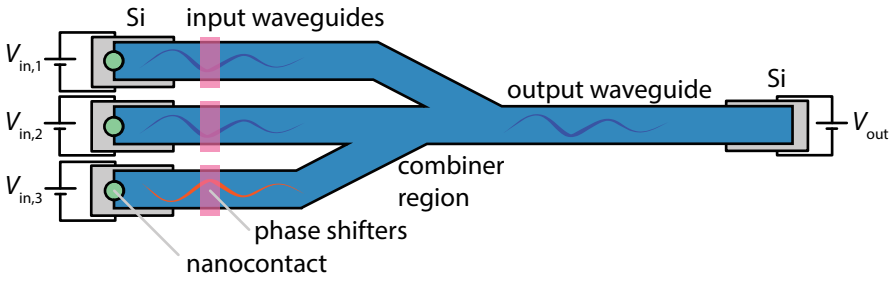

Fig. 3.5. – CMOS compatible magnon majority gate. The permalloy majority gate is placed on a silicon substrate. Spin waves are excited in the input waveguides using spin torque nanooscillators and the phase of the waves is modified with phase shifters. The spin waves propagate and interfere in the combiner region, where only the majority phase enters the output waveguide. In the output waveguide the spin-wave excitation is converted back to a voltage signal in the silicon due to spin pumping and inverse spin Hall effect. Figure adapted from Ref. [13]

3.4 Conclusion

In conclusion, we study the Gilbert damping in Py/Si heterostructures for different substrate resistivities. On the one hand, we find that the Gilbert damping parameter of the Py films decreases with increasing substrate resistivity. We attribute this effect to the decreasing density of charge carriers, which are responsible for the dissipation of angular momentum. This can be understood at least qualitatively in the spin pumping picture. On the other hand, we observe an increase of the Py damping for decreasing Py film thickness for a fixed substrate resistivity. This dependence is expected for the spin pumping effect, since spin pumping in an interface process.

The results presented in this chapter show that spin angular momentum can be transferred to semiconductors by means of spin pumping. This in in agreement with previous studies of spin pumping into Si [83, 86], GaAs [81, 84, 133, 134] and Ge [85] substrates. However, the presented study shows the first systematic variation of the spin pumping efficiency with the substrate resistivity. Furthermore, we take additional radiation and eddy-current damping effects into account, which have to be considered in real applications.

This technique opens a new way to exploit magnetization dynamics and generate pure spin currents in semiconductor devices. For example our findings could be used in CMOS compatible magnonic structures and network. This would allow to process information in, e.g., spin-wave based majority gates [13, 14, 38], which could lead to a downscaling of the actual logic architecture in a CMOS chip. In Fig. 3.5 the setup of such an majority gate is sketched. It consists of three input waveguides, where spin waves are launched using spin torque nanooscillators [135, 136]. For this the dc-current from the surrounding CMOS architecture is used through Si contacts. The spin waves are phase shifted by phase shifters [137–139], where the logical bit is encoded in the waves phase. In

the combiner region the three input waveguides are merged together where the waves interfere. The output spin wave in the output waveguide propagates with the majority phase of the input waves. The signal is then converted into an voltage signal using the inverse spin Hall effect. This can be accomplished either using a Pt interlayer [114, 140, 141] between the Py output waveguide and the Si substrate, or using the inverse spin Hall effect of silicon itself [82].

4 Gilbert Damping in an Yttrium Iron Garnet Sphere

In the previous chapter we have introduced the standard FMR procedure for the characterization of magnetic samples. We furthermore have seen that we can use spin currents to couple the magnetic excitation to an extrinsic bath, to transport and utilize the (non-equilibrium) angular momentum. The Gilbert damping parameter α hereby reflects the strength of magnetization damping. Detailed knowledge about the magnitude of α in different materials is very important, as magnetization damping limits the life time of the magnetic excitations (magnons or spin waves). A material which became famous for its low intrinsic damping is the ferrimagnetic insulator yttrium iron garnet (YIG), which exhibits the smallest Gilbert damping value at room temperature reported so far (results discussed in this chapter). This makes YIG spheres the prototypical material for the fabrication of microwave filters and oscillators [142, 143]. In absolute numbers, in YIG the linewidths of 1 MHz at 10 GHz excitation frequency can be achieved, which refers to a spin-wave lifetime in the order of micro-seconds. In order to achieve a high applicability of ferromagnetic materials, spherical samples are used, as the ferromagnetic resonance frequencies are independent of the magnetization direction and the shape and size of the sphere.

The crystalline structure of YIG is shown [144–146] in Fig. 4.1. The Fe^{3+}-ions are located either in an octahedral site or a tetrahedral site, whereas the yttrium ions Y^{3+} are sitting in sites with dodecahedral symmetry. On the corners of the different sites we find oxygen O^{2-}-ions which couple the magnetic moments of the Fe^{3+}-ions by super exchange, which leads to an antiferromagnetic alignment of the iron moments. YIG has a cubic crystal structure with unit cell size of 1.25 nm, and contains twenty Fe^{3+}-ions (8 octahedral and 12 tetrahedral), in two antiferromagnetically coupled sublattices [11]. However, the different net magnetic moment of the different sublattices causes YIG to be a ferrimagnet, but not an antiferromagnet. The Curie temperature of YIG is about 550 K [147], it has a room temperature saturation magnetization of $\mu_0 M_s = 0.18\,\mathrm{T}$ [147, 148] and an exchange stiffness of $D_s = 5.25 \times 10^{-17}\,\mathrm{Tm}^2$ [23].

Although YIG emerged to be an omnipresent material in magnetization dynamics research and microwave applications, there is no systematic broadband study of the magnetic excitations and the magnetization damping in YIG spheres. One type of magnetic excitations in YIG spheres are magnetostatic modes (MSMs) which resemble standing spin-wave patterns within the sphere. However, for the MSMs we can neglect any exchange field contributions, as their occurrence can be fully described by dipolar interaction. This is in general not the case for standing

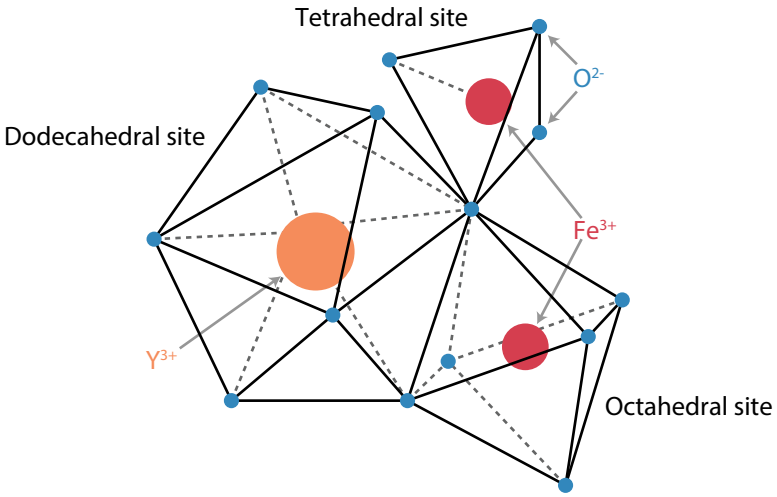

Fig. 4.1. – Crystalline structure of yttrium iron garnet. The iron ions in the octahedral and tetrahedral sites are coupled antiferromagnetically via super exchange via the oxygen ions. Figure adapted from Ref. [144].

spin waves, as discussed in Chap. 5. The linewidth of MSMs in YIG spheres has been studied at a few fixed frequencies in the past [48, 57, 149], however, the respective contributions of intrinsic Gilbert damping and inhomogeneous line broadening to the total linewidth in YIG spheres was missing. In particular, it is not evident from the literature, whether different MSMs feature one and the same or different (and mode dependent) Gilbert damping [30, 150]. In this chapter, we report on a systematic broadband FMR measurement multiple magneto static modes [151–153] for a 300 μm diameter YIG sphere.

The chapter is organized as follows: In the first part of this chapter, we introduce the magneto-static mode spectrum of a ferromagnetic sphere. For this we solve the Maxwell equations in the sphere and find various modes which fulfill the boundary conditions. Second, we sketch the physical background of the two-magnon scattering mechanism of the different magnetostatic modes in the sphere. Third we present the used experimental setup and the data evaluation which is required for a smart background reduction. Finally, we describe and discuss the experimental observations. We identify the individual MSMs via their characteristic dispersion relations and the corresponding mode number tuples (nmr) are assigned. The linewidth analysis shows that all MSMs share the same Gilbert damping parameter $\alpha = 2.7(5) \times 10^{-5}$ irrespective of their mode index. However, the inhomogeneous line broadening markedly differs between the observed MSMs. This finding can be described with two-magnon scattering processes of the MSMs into the spin-wave manifold, mediated by surface and volume defects.

Some of the figures and parts of the text in this chapter have been published in S. Klingler, H. Maier-Flaig, C. Dubs, O. Surzhenko, R. Gross, H. Huebl, S.T.B.

Goennenwein, M. Weiler, *Gilbert damping of magnetostatic modes in a yttrium iron garnet sphere*, Applied Physics Letters **110**, 092409 (2017).

4.1 Magnetostatic Modes in Spheres

In the following, we derive an expression for the mode profiles of standing spin waves in a magnetic sphere, called magnetostatic modes (MSMs). This section follows the description of Ref. [152]. We use the magnetostatic approximation, where we neglect all retardation effects regarding the long spin-wave wavelength limit. In the magnetostatic limit and without exchange coupling the Maxwell equations read:

$$\nabla \times \boldsymbol{H} = 0, \tag{4.1}$$

$$\nabla \cdot \boldsymbol{B} = \nabla \cdot \mu_0 \left(\boldsymbol{H} + M_\mathrm{s} \boldsymbol{M} \right) = 0. \tag{4.2}$$

Note, that M_s is the saturation magnetization, whereas $\boldsymbol{M}$ is the magnetization unit vector. As the rotation of the magnetic field vanishes, we can introduce a magnetic potential ψ for which we find:

$$\boldsymbol{H} = \nabla \psi. \tag{4.3}$$

We use analogously to Chap. 2.1.1.2 the definition of the magnetostatic potential;

$$\nabla^2 \psi + \nabla \cdot M_\mathrm{s} \boldsymbol{M} = 0, \tag{4.4}$$

which describes the behavior of the magnetic field and the magnetization according to the Maxwell equations. Furthermore, we take the magnetization to obey the Landau-Lifshitz-Gilbert equation, see Chap. 2.1.2.1. For simplicity's sake, we here neglect the magnetic Gilbert damping, as it only has a minor influence on the magnetic mode shape and the resonance frequencies. More specifically, we take $\alpha\omega \ll \omega$:

$$\frac{\partial \boldsymbol{M}}{\partial t} = \gamma \mu_0 \left(\boldsymbol{M} \times \boldsymbol{H}_\mathrm{eff} \right). \tag{4.5}$$

A solution of the LLG of a spherical ferromagnet is given by Eq. (2.38), for $\mathcal{N}_{x'x'} = \mathcal{N}_{y'y'} = \mathcal{N}_{z'z'} = 1/3$ which we rewrite here in Cartesian coordinates as:

$$M_\mathrm{s} \begin{pmatrix} m_x \\ m_z \end{pmatrix} = \begin{pmatrix} \chi_{xx} & \chi_{xz} \\ \chi_{zx} & \chi_{zz} \end{pmatrix} \begin{pmatrix} h_x \\ h_z \end{pmatrix} = \begin{pmatrix} \kappa & -i\nu \\ i\nu & \kappa \end{pmatrix} \begin{pmatrix} \frac{\partial \psi}{\partial x} \\ \frac{\partial \psi}{\partial z} \end{pmatrix}, \tag{4.6}$$

where we have used:

$$\kappa = \Omega_H / \left(\Omega_H^2 - \Omega^2 \right), \tag{4.7}$$

$$\nu = \Omega / \left(\Omega_H^2 - \Omega^2 \right), \tag{4.8}$$

$$\Omega_H = \mu_0 H_{\text{eff}} / \mu_0 M_s, \tag{4.9}$$
$$\Omega = \omega / \gamma \mu_0 M_s, \tag{4.10}$$

together with the definition of the scalar potential from Eq. (4.3). The effective field is given by $H_{\text{eff}} = H - M_s/3 + H_{\text{ani}}$, where H_{ani} is the anisotropy field.[1] Note that solving $\Omega_H^2 - \Omega^2 = 0$ yields the fundamental resonance frequency given in Eq. (2.47). With Eq. (4.6) the expression for the magnetostatic potential Eq. (4.4) reads:

$$(1+\kappa)\left(\frac{\partial^2\psi}{\partial x^2} + \frac{\partial^2\psi}{\partial y^2}\right) + \frac{\partial^2\psi}{\partial z^2} = 0, \tag{4.11}$$

which is also called the Walker equation [151]. The solutions of the Walker equation are called magnetostatic modes.

To solve Eq. (4.11) we have to consider two boundary conditions at the interface. Firstly, we find that the Walker equation reduces to Laplace's equation $\nabla^2\psi = 0$ outside of the sphere as $\boldsymbol{M} = 0$ and thus $\kappa = 0$. In this case Eq. (4.11) is solved by using spherical coordinates (r, ϑ, φ), which yields:

$$\begin{aligned}\psi_{\text{out}} =& r^n P_n^m(\cos(\vartheta)) \left[A_n^m \cos(m\varphi) + iB_n^m \sin(m\varphi)\right] \\ &+ \frac{1}{r^{n+1}} P_n^m(\cos(\vartheta)) \left[D_n^m \cos(m\varphi) + iF_n^m \sin(m\varphi)\right],\end{aligned} \tag{4.12}$$

where $P_n^m(\cos(\vartheta))$ are Legendre polynomials, r is the distance to the spheres center and A_n^m, B_n^m, C_n^m and D_n^m are complex coefficients which are given in explicitly in Ref. [152]. The angles ϑ and φ are given in spherical coordinates by:

$$\begin{aligned}x &= r\sin(\vartheta)\sin(\varphi), \\ y &= r\sin(\vartheta)\sin(\varphi), \\ z &= r\cos(\vartheta)\end{aligned} \tag{4.13}$$

The general solution inside the sphere is more complicated, as the magnetization does not vanish. According to Ref. [152] we use elliptical coordinates (ζ, η, ϕ) the solution reads:

$$\psi_{\text{int}} = P_n^m(\xi) P_n^m(\cos(\eta)) \left[G_n^m \cos(m\phi) + iH_n^m \sin(m\phi)\right], \tag{4.14}$$

where G_n^m and H_n^m are unknown complex coefficients, and η and ξ are implicitly given by the relations:

$$x = R_0\sqrt{-\kappa}\sqrt{1-\xi^2}\sin(\eta)\cos(\phi),$$

[1] We have assumed here, that the anisotropy field is parallel to the demagnetization field. In a more general theory the anisotropy field can have a certain direction with spatial symmetries, which can be expressed by an anisotropy tensor, similar to the demagnetization tensor introduced in Chap. 2.1.1.2.

$$
\begin{aligned}
y &= R_0\sqrt{-\kappa}\sqrt{1-\xi^2}\sin(\eta)\sin(\phi), \\
z &= R_0\sqrt{\frac{\kappa}{1+\kappa}}\xi\cos(\eta).
\end{aligned}
\tag{4.15}
$$

Here, R_0 is the radius of the sphere. By comparison of Eqs. (4.13) and (4.15) one finds at the interface $r = R_0$ the relations:

$$
\begin{aligned}
\vartheta_0 &= \eta_0, \\
\xi_0^2 &= \frac{1}{\kappa} + 1.
\end{aligned}
\tag{4.16}
$$

From Eqs. (4.1) and (4.2) it follows that the normal component of the magnetic induction and the tangential component of the magnetic field have to be continuous at the sphere's interface. The first boundary condition reads in terms of ψ [154]:

$$
\begin{aligned}
\left.\frac{\partial\psi_{\text{out}}}{\partial r}\right|_{r=R_0} &= \left[1+\kappa\sin^2(\vartheta)\right]\left.\frac{\partial\psi_{\text{int}}}{\partial r}\right|_{r=R_0} \\
&\quad + \frac{\kappa}{a}\sin(\vartheta)\cos(\vartheta)\left.\frac{\partial\psi_{\text{int}}}{\partial\vartheta}\right|_{r=R_0} - \frac{i\nu}{a}\left.\frac{\partial\psi_{\text{int}}}{\partial\phi}\right|_{r=R_0}.
\end{aligned}
\tag{4.17}
$$

The second boundary condition reads then:

$$
\psi_{\text{int}}|_{r=R_0} = \psi_{\text{out}}|_{r=R_0} \tag{4.18}
$$

Eq. (4.17) and Eq. (4.18) can be solved in terms of the variables A_n^m, B_n^m, D_n^m, F_n^m, G_n^m and H_n^m [152].We find that the magnetostatic potential and the dynamic magnetization become extremal for a certain field and frequency combination. The resonance frequencies Ω of the MSMs are obtained by solving the characteristic equation [151–153]:

$$
n + 1 + \xi_0\frac{\mathrm{d}P_n^m(\xi_0)/\mathrm{d}\xi_0}{P_n^m(\xi_0)} \pm m\nu = 0, \tag{4.19}
$$

Note, that ξ_0 and ν are functions of Ω. For example we calculate the dispersion of the $n = 1, m = 1$ mode. For this mode we find $P_1^1(\xi_0) = -\sqrt{1-\xi_0^2}$, and the characteristic equation reads:

$$
\begin{aligned}
0 &= 2 + \frac{\xi_0^2}{-1+\xi_0^2} \pm \nu = 3 + \kappa \pm \nu = 3 + \frac{\Omega_H \pm \Omega}{(\Omega_H^2 - \Omega^2)} \\
&= 3 + \frac{1}{(\Omega_H \mp \Omega)},
\end{aligned}
\tag{4.20}
$$

where we have used the definitions from Eq. (4.16), and Eqs. (4.7)-(4.10). The characteristic equation is solved then solved by:

$$
\Omega = \frac{1}{3} + \Omega_H \Leftrightarrow \omega_{\text{res}}^{110} = \gamma\mu_0(H + H_{\text{ani}}), \tag{4.21}
$$

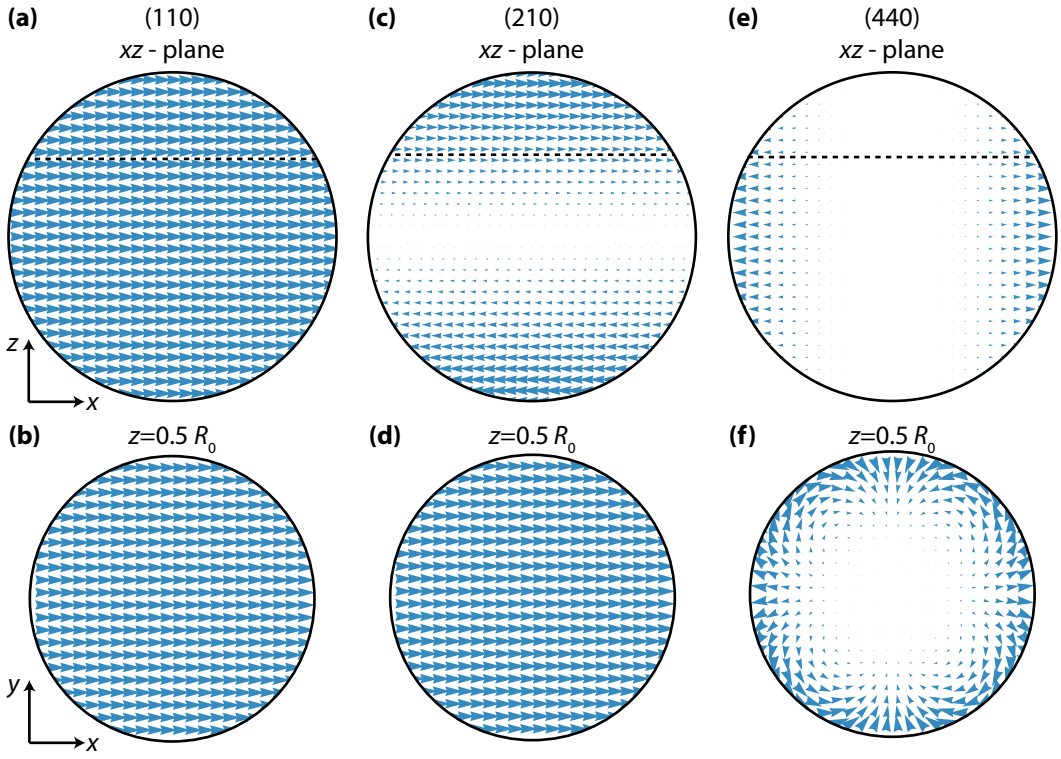

Fig. 4.2. – (a, b) Uniform magnetostatic mode profile of the m_x component of the (110)-mode. (c, d) Magnetostatic mode profile of the m_x component of the (210)-mode. The dynamic magnetization vanishes for $z = 0$. (e, f) Magnetostatic mode profile of the m_x component of the (440)-mode. The dynamic magnetization shows a quadrupolar behavior in the $z = 0.5a$-plane, with a vanishing of all dynamic magnetization components at $x = y = 0$.

where we have neglected the negative solutions for Ω. The equation above is the well known Kittel equation for spheres with an anisotropy field, see Chap. 2.1.2.1. For the (210)-mode we can use the same method, and find using $P_2^1(\xi_0) = -3\xi_0\sqrt{1-\xi_0^2}$:

$$\omega_{res}^{(210)} = \gamma\mu_0\left(H + H_{\text{ani}} - \frac{2}{15}M_s\right), \tag{4.22}$$

The mode profiles of the MSMs have the form of associated Legendre polynomials P_n^m, where the localization of the MSMs at the surface is related to the mode index $n \in \mathbb{N}$ [57]. The index $|m| \leq n$ corresponds to an angular-momentum quantum number of the MSM [155], where the bar above the mode index $\overline{m}$ is used for indices $m < 0$. The index $r \geq 0$ enumerates the solutions of the characteristic equation (4.19) for given n and m for increasing frequencies [152, 156]. In total, each MSM is uniquely identified by the index tuple (nmr). For more information, the review of Ref. [153] is recommended.

Figure 4.2 shows the relative amplitude of the dynamic m_x-component of some magnetostatic modes for a fixed point in time, obtained from Eq. (4.6) using

the internal magnetic potential Eq. (4.14) and the definitions from Eq. (4.16) for $\mu_0 H = 0.5\,\mathrm{T}$, $\mu_0 M_\mathrm{s} = 0.18\,\mathrm{T}$, $\gamma/2\pi = 28\,\mathrm{GHz/T}$ and $\omega/2\pi = 10\,\mathrm{GHz}$. For this we use $G_n^m = H_n^m = 1$, where the first equal sign is used for a circular precession, and the second equal sign to plot a normalized magnetization distribution. We can then write for the m_x component (and analogously the m_y component):

$$M_\mathrm{s} m_x = \left(\kappa \frac{\partial}{\partial x} - i\nu \frac{\partial}{\partial z}\right) P_n^m\left(\xi_0\right) P_n^m\left(\cos(\eta_0)\right) \left[\cos(m\phi) + i\sin(m\phi)\right], \tag{4.23}$$

$$\cos(m\phi) = \mathrm{Re}\left[\frac{(x+iz)^m}{\left(x^2+z^2\right)^{m/2}}\right], \tag{4.24}$$

$$\sin(m\phi) = \mathrm{Im}\left[\frac{(x+iz)^m}{\left(x^2+z^2\right)^{m/2}}\right], \tag{4.25}$$

$$\cos(\eta_0) = \frac{z}{a}, \tag{4.26}$$

where we have used a coordinate transformation from spherical to Cartesian coordinates. We then plot the real part of Eq. (4.23) along the x-axis, and the imaginary part along the z-axis. Note that similar plots are obtained from the dynamic m_z-component.

Figure 4.2 (a) shows the mode profile of the (110)-mode in the x,z-plane, where the length of the arrows is normalized to G_n^m. We find a uniform arrow-length and hence a uniform precession. The same is true for Fig. 4.2 (b), where we calculate the mode profile at $z = 0.5R_0$ (The position is shown as dashed line in Fig. 4.2 (a)). The situation changes for the (210)-mode shown in Fig. 4.2 (c), where we clearly see a change of the magnetization orientation at $z = 0$ in the z-direction. However, in Fig. 4.2 (d) we find at $z = 0.5R_0$ a uniform precession for the (210)-mode. The total magnetization profile is thus a superposition of both, with a vanishing dynamic magnetization in the $z = 0$ plane. In Fig. 4.2 (e) the situation is shown for the (440)-mode in the x,z-plane. We find that the magnetization changes its orientation at $x = 0$ in the x-direction. The dynamic magnetization profile for $z = 0.5R_0$ is shown in Fig. 4.2 (f), where we find a quadrupolar behavior of the dynamic magnetization. In this perspective it becomes clear, that the dynamic M_x-component does not vanish in the $x = 0$ plane, it rather rotates towards the y-direction. Only for $x = y = 0$ we find that the dynamic magnetization vanishes.

4.2 Two-Magnon Scattering in Spheres

In order to discuss the spin-wave manifold in the sphere, we follow Ref. [30] and assume that a plane wave solves the Walker equation, such that we can write $\psi \propto \exp(-i\boldsymbol{kr})$ for the magnetic potential. The Walker equation then reads:

$$(1+\kappa)(k_x^2+k_z^2)+k_y^2=0. \tag{4.27}$$

We furthermore assume that the y-axis is the direction of the external static field. As our system is rotationally symmetrical and we neglect any magneto-crystalline anisotropies here, we only have to have to consider the angle between the wave vector and the y-axis. It is justified to neglect a specific anisotropy field, as it mathematically is an offset to the applied magnetic field. We find for the wave vectors:

$$k_x^2+k_z^2=k^2\sin^2\vartheta, \tag{4.28}$$
$$k_y^2=k^2\cos^2\vartheta \tag{4.29}$$

with which we rewrite the Walker equation into:

$$\kappa\sin^2\vartheta=-1. \tag{4.30}$$

The resonance condition now reads: $\omega=\gamma\mu_0\sqrt{H(H+M_\mathrm{s}\sin^2\vartheta)}$. Obviously, the spin-wave manifold is much more complex than suggested by the simple expression from Eq. (2.47). The reason for this that we now use a more general boundary condition. We additionally introduce the exchange field of the propagating waves by using the transition $\mu_0 H \rightarrow \mu_0 H + D_\mathrm{s}k^2$ and obtain [30]:

$$\omega=\gamma\sqrt{(\mu_0 H+D_\mathrm{s}k^2)(\mu_0 H+D_\mathrm{s}k^2+\mu_0 M_\mathrm{s}\sin^2\vartheta)} \tag{4.31}$$

In Fig. 4.3 (a) we plot the spin-wave dispersions for $\mu_0 H = 0.5\,\mathrm{T}$, $D_\mathrm{s} = 5.3\times 10^{-17}\,\mathrm{Tm}^2$ [23], between $\vartheta_0 = 0$ and $\vartheta_0 = \pi/2$ as a function of the wave vector k. We have chosen an external field of 0.5 T, as this field value is easily achievable in our experiments. We find that in both branches the spin-wave frequency is approximately constant until at about $k = 10^7\,\mathrm{m}^{-1}$ the exchange interaction starts to dominate the dipolar interaction. For higher k-vectors both branches will become degenerate. We then speak of exchange spin waves which are fully isotropic.

As shown in Fig. 4.2, different magnetostatic modes have a different mode profile with a specific dynamic magnetization amplitude at the surface. We thus expect a mode-dependent influence of the two-magnon scattering processes introduced in Chap. 2.3.2 on the inhomogeneous line broadening of the MSMs. The physical reason can be found in the structure of the magnetic sample. Where the YIG sphere has a very homogeneous crystalline structure in its center, it has

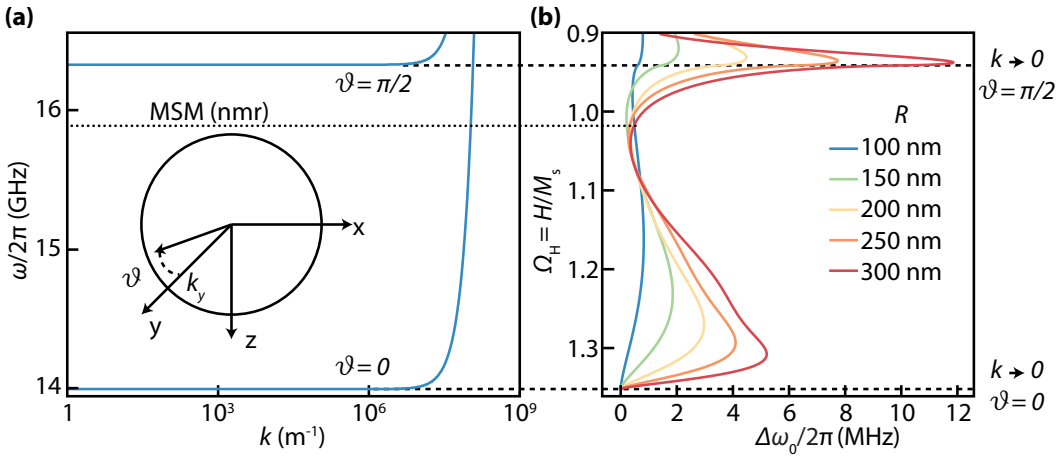

Fig. 4.3. – (a) Spin wave dispersion in a YIG sphere at a field of $\mu_0 H = 0.5\,\mathrm{T}$ for two different angles. (b) Inhomogeneous line broadening as a function of the applied magnetic field, after Ref. [57]. The calculations are performed using Eq. (4.36) for a sphere with a radius $R_0 = 300\mu\mathrm{m}$ for different pit sizes R. The dashed lines mark the top and bottom of the spin-wave spectrum.

pits, scratches, and influences from polishing procedures at the surface. If a magnetic excitation has a large mode amplitude in the spheres center, it is not likely to scatter. However, if the mode has a large amplitude at the surface, it is influenced by the material inhomogeneities, which can lead to two-magnon scattering processes. According to Ref. [157] an imperfection in a volume material can be interpreted as a small spherical cavity in an infinite medium, which creates a scattering potential E_{scatt}:

$$E_{\mathrm{scatt}} = -\mu_0 \frac{1}{2} \int \boldsymbol{H}_c M_\mathrm{s} \boldsymbol{M} d\boldsymbol{r}. \tag{4.32}$$

The scattering potential of the uniform mode into a mode with $k \neq 0$ is given by:

$$E_{\mathrm{scatt}} = F(\boldsymbol{k}, R)(a_0 a_k^\dagger + a_0^\dagger a_k), \tag{4.33}$$

where the prefactor is given by:

$$F(\boldsymbol{k}, R) = 16\pi^2 R^3 (g\mu_\mathrm{B}/2M_\mathrm{s}/V)(3\cos^2\vartheta_k - 1) j_1(kR)/kR, \tag{4.34}$$

where R is the radius of the defect, V is the volume of the sphere, and j_1 is a spherical Bessel function. The operators a_0, a_k are the creation and $a_0^\dagger, a_k^\dagger$ the annihilation operators of the magnons.[2] The line broadening of a uniform magnetic excitation, which is scattered by surface defects, reads:

$$\Delta\omega_{2\mathrm{M}} = \frac{2\pi}{\hbar} \int_0^{k_m} |F(\boldsymbol{k}, R)|^2 \rho_k dk, \tag{4.35}$$

[2] The creation and annihilation operators were introduced by a Holstein-Primakoff transformation, which is beyond the scope of this thesis.

where ρ_k is the density of magnon states at the wave vector k. The final result is given in Ref. [57]:

$$\Delta\omega_{2M} = \gamma \frac{3}{4} \frac{R}{R_0} (\mu_0 M_s)^2 \cdot \int_{u_{min}}^{1} du \frac{\Omega R \left(3u^2 - 1\right)^2}{D_s k \left(4\Omega^2 + (1-u^2)^2\right)^{1/2}} \left(j_1 (kR)\right)^2 \tag{4.36}$$

with,

$$u = \cos(\vartheta), \tag{4.37}$$

$$u_{min} = \begin{cases} \left(\frac{\Omega_H(\Omega_H+1)-\Omega}{\Omega_H}\right)^{1/2}, & \text{for } \Omega^2 \geq \Omega_H(\Omega_H+1) \\ 0, & \text{for } \Omega^2 < \Omega_H(\Omega_H+1) \end{cases}, \tag{4.38}$$

$$k = \left(\frac{\left(4\Omega^2 + (1-u^2)^2\right)^{1/2} - \left(2\Omega_H + (1-u^2)\right)}{2D_s/\mu_0 M_s} \right)^{1/2}. \tag{4.39}$$

In Fig. 4.3 (b) we plot the inhomogeneous line broadening $\Delta\omega_{2M}$ as a function of the applied magnetic field H normalized by the saturation magnetization for various defect sizes. A first important observation is that the inhomogeneous broadening increases with increasing defect size. For a pit radius of 100 nm we find an almost constant linewidth contribution, whereas we find two maxima in the linewidth contribution for larger defect size. This goes along with the notion that a rough sphere surface is likely to increase the two-magnon scattering efficiency. We furthermore find the maxima approximately at the bottom and the top of the spin-wave spectrum. For each MSM at a certain resonance frequency and field (e.g. dashed line), we can read the line broadening from Fig. 4.3 (b).

However, we have found above that the spatial mode distribution is different for modes with different mode indices (nmr). The spatial dependence is not included in the scattering theory, and Eq. (4.36) needs to be modified accordingly. We introduce the factor $F^{(nmr)}$, which represents the ratio of the linewidth of a particular MSM with respect to the uniform precessing (110)-mode [57,149,158,159]:

$$F_{(nmr)} = \langle |m_t|^2 \rangle_{surface} / \langle |m_t^3|^2 \rangle_{volume}, \tag{4.40}$$

where $|m_t|^2 = |m_x|^2 + |m_z|^2$ is the square of the transverse magnetization components, and $\langle\rangle$ denote the surface and volume average. In most cases $F_{(nmr)} = (2n+1)/3$ and independent of r [57].

The total inhomogeneous line broadening then reads [57]:

$$\Delta\omega_0^{(nmr)} = \Delta\omega_{2M} F^{(nmr)} + \Delta\omega_0^0. \tag{4.41}$$

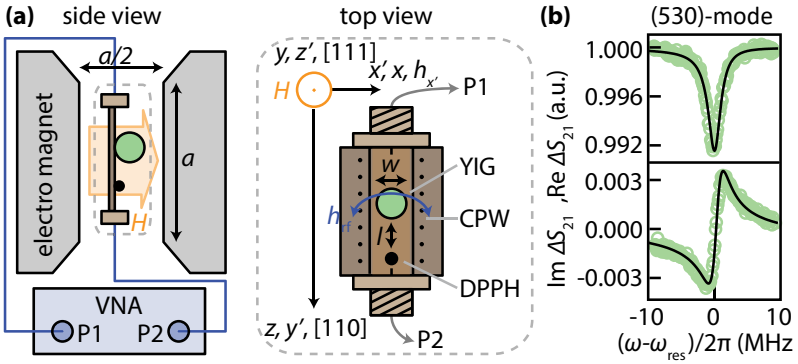

Fig. 4.4. – (a) The CPW with the YIG sphere and the DPPH is positioned in the homogeneous field of an electromagnet. The CPW is connected to port 1 (P1) and port 2 (P2) of a vector network analyzer (VNA). The YIG sphere is placed on top of the center conductor of the CPW with its [111]-axis parallel to the applied magnetic field H_0 in z'-direction. (b) Typical normalized transmission spectrum of the (530)-mode at $\mu_0 H_0 = 0.8\,\mathrm{T}$ (symbols) including a fit to Eq. (4.44) (lines).

The two-magnon scattering processes can be suppressed if a perfectly polished YIG sphere is used, due to the vanishing ability of the system to transfer linear and angular momentum from and to the lattice [57]. The term $\Delta\omega_0^0$ represents a constant contribution to the linewidth in which all other frequency-independent broadening effects are absorbed. A complete discussion of the scattering theory used in this thesis is presented in Ref. [57, 157].

If we now assume a dominant Gilbert-like damping for all MSM modes, the linewidth $\Delta\omega^{(nmr)}$ of a MSM resonance line at a frequency $\omega_{res}^{(nmr)}$ is given by [60], cf. Eq. (2.66):

$$\Delta\omega^{(nmr)} = 2\alpha^{(nmr)}\omega_{\mathrm{res}}^{(nmr)} + \Delta\omega_0^{(nmr)}. \tag{4.42}$$

4.3 Experimental Methods

The YIG crystal used in this chapter is grown in a high temperature solution using the slow cooling method [160] by C. Dubs from Innovent e.V., Jena. The purity of yttrium oxide was 99.9999 % related to the whole rare earth oxides content. The sphere is prepared by grinding and polishing a YIG cube to a diameter of $2R_0 = 300 \pm 10\,\mu\mathrm{m}$ with an asphericity smaller than 1 % and without microscopically detected roughness. A subsequent 4 h annealing process at 950 °C removes strain induced by crystal growth and the rounding-off processes.

Figure 4.4 (a) shows a sketch of the measurement setup. The YIG sphere with a diameter of $2R_0 = 300\,\mu\mathrm{m}$ is placed in a disk shaped Vespel sample holder (diameter 6 mm, not shown), which has a centered hole with a diameter of 350 μm. The sphere in the sample holder is exposed to a static magnetic field in order to align the easy [111]-direction of the YIG crystal [57] parallel to the field direction. The sphere is subsequently fixed in the sample holder using photoresist and the

alignment is confirmed by Laue diffraction, as shown and discussed in more detail in Ref. [66]. Taken together, the Vespel sample holder thus on the one hand simply mechanically holds the small YIG sphere in place. On the other hand, owing to the magnetic field induced alignment, the crystalline orientation of the YIG crystal is now fixed to the sample holder.

The oriented YIG sphere is placed in the middle of the $w = 300\,\mu$m wide center conductor, with the YIG [110]-axis aligned parallel to the long axis of the center conductor of the CPW. However, as stated above, the linewidth of the YIG sphere is very small (1 MHz which is about $35\,\mu$T). For this reason we need a special magnetic field measurement with a very high resolution at the position of the YIG sphere. As a standard Hall probe has a limited field resolution, we additionally glue a pressed crumb of Diphenylpicrylhydrazyl (DPPH) on the center conductor, in distance between the YIG sphere and the DPPH of $l \approx 1\,$cm. We use the DPPH as a spin marker as it has a well known g-factor [161] of $g_{\mathrm{DPPH}} = 2.0036(3)$. The measurement of its paramagnetic resonance frequency:

$$\omega_{\mathrm{DPPH}} = g_{\mathrm{DPPH}} \frac{\mu_{\mathrm{B}}}{\hbar} \mu_0 H^{\mathrm{DPPH}} \tag{4.43}$$

can thus be used as an independent magnetic field reference at the sample position, in addition to Hall probe measurements. The static magnetic field calculated from the DPPH resonance frequency is denoted as H^{DPPH}. The stray field originating from the YIG sphere at the location of the DPPH creates a systematic measurement error of $\delta\mu_0 H_{\mathrm{stray}} \leq 40\,\mu$T, as estimated from considering the YIG sphere as a magnetic dipole. Using this value, we can calculate the YIG g-factor with a very high precision.

We place the CPW between the pole shoes of the electromagnet and use pole shoes with $a = 6\,$cm to ensure a homogeneous applied magnetic field. The measured radial field inhomogeneity in our magnet system creates a systematic field measurement error of $\delta\mu_0 H_{\mathrm{disp}} = 0.3\,$mT for $l = 1\,$cm displacement from the center axis.

For the VNA FMR experiments, already presented in Chap. 2.4.3, we measure the complex scattering parameter S_{21}in a frequency range of $\omega/2\pi \leq 26.5\,$GHz as a function of the applied magnetic field strength. The applied microwave power is $P = -20\,$dBm to avoid non-linear effects causing additional line broadening. We can estimate the driving fields from the Karlqvist equations Eq. (2.68),(2.69), where the field amplitude is given by $\mu_0 h_0 = \mu_0 I/2w$. Using $w = 300\,\mu$m, $I = \sqrt{P/Z_0}$, $P = -20\,$dBm $= 10\,\mu$W, we obtain $\mu_0 h_0 = 1\,\mu$T, which corresponds to a linewidth of $\gamma\mu_0 h_0/2\pi = 26\,$kHz, which is much smaller than the detected resonance linewidth.

In order to eliminate the effect of the frequency dependent background transmission of the CPW, we apply the following measurement protocol: First, we measure S_{21} a fixed field H in a frequency range $\omega_{\mathrm{DPPH}}/2\pi \pm 1\,$GHz. Second, we

measure S_{21} for the same frequency range but at a slightly larger magnetic field $H + \Delta H$, with $\mu_0 \Delta H_0 = 100\,\mathrm{mT}$. Since for this field no YIG and DPPH resonances are present in the observed frequency range, the latter measurement contains the pure background transmission. Third, we calculate the normalized transmission spectra using $\Delta S_{21}^{\star} = S_{21}(H)/S_{21}(H + \Delta H)$, which corrects the magnitude and the phase of the signal. Note that this measurement is equivalent to a common background normalization, where the background is recorded at a certain field value. However, as the field steps in our measurement were very small, the measurement took multiple hours, and the recording of a background spectrum for every field step increased the data quality tremendously, as also slow thermal drifts in the measurement setup were corrected. The background-correction procedure is repeated for all applied magnetic fields. The transmitted magnitude around the resonance can be expressed using Eq. (2.82):

$$\Delta S_{21}(\omega) = \Delta S_{21}^{\star} - 1 = \frac{S_{21} - S_{21}^{0}}{S_{21}^{0}} = \frac{S_{21}^{0} - iCe^{i\phi}\chi_{x'x'} - S_{21}^{0}}{S_{21}^{0}} = \frac{-iCe^{i\phi}\chi_{x'x'}}{S_{21}^{0}}. \quad (4.44)$$

From this we obtain using Eq. (2.86) and Eq. (2.38) the fitting function of our signal:

$$\Delta S_{21} = A + B\omega + \frac{Z}{\left(\omega_{\mathrm{res}}^{(nmr)}\right)^2 - i\omega^2 - i\omega\Delta\omega^{(nmr)}} \quad (4.45)$$

Here, we have additionally introduced A, which is a complex offset parameter, B, which is the slope of a complex linear background and Z, which is a complex scaling parameter that includes all amplitude information from the general susceptibility. Note furthermore, that in our coordinate system $\chi_{xx} = \chi_{x'x'}$, cf. Fig. 2.1. Figure 6.3 (b) exemplary shows the real and imaginary part of ΔS_{21} for the (530)-mode at $\mu_0 H = 0.8\,\mathrm{T}$. In addition, a fit of Eq. (4.44) to the data is shown, which adequately models the shape of the resonances.

4.4 Experimental Results

4.4.1 Magnetostatic Mode Dispersions

Figure 4.5 (a) shows the normalized transmitted magnitude $|\Delta S_{21}|$ as a function of H and $\omega - \omega_{\mathrm{DPPH}}$ on a linear color-coded scale. The frequency axis is chosen relative to the DPPH resonance frequency, so that all modes with a linear dispersion $\omega_{\mathrm{res}}^{(nmr)} \propto H$ appear as straight lines, whereas modes with a non-linear dispersion are curved. Note that the field values displayed on the y-axis represent the magnetic field strength measured with the Hall probe, as this is the raw measurement data. The different modes appearing in the color plot in Fig. 4.5 (a) can be identified in a straightforward manner.

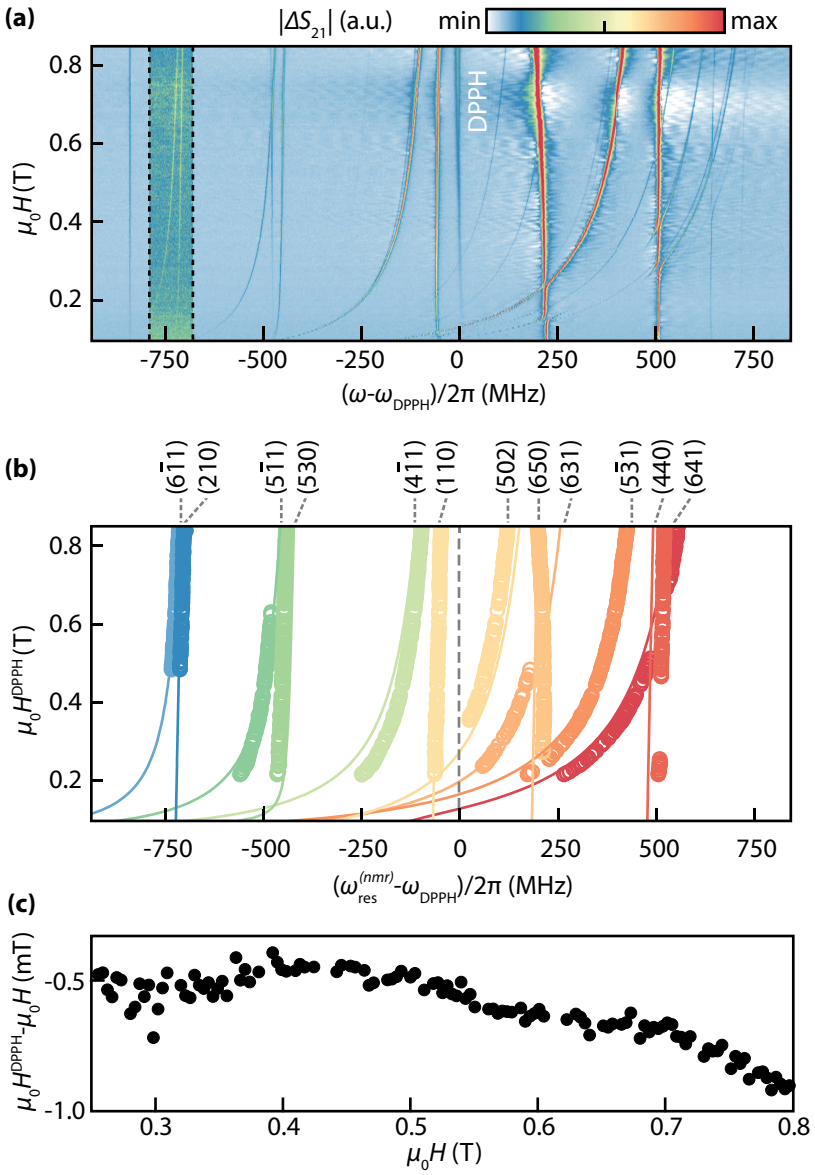

Fig. 4.5. – (a) Normalized transmission magnitude $|\Delta S_{21}|$ plotted versus applied magnetic field $\mu_0 H_0$ and microwave frequency $\omega/2\pi$ relative to the DPPH resonance $\omega_{\mathrm{DPPH}}/2\pi$. The contrast between the dashed lines is stretched for better visibility. (b) Calculated and measured dispersions of various MSMs (lines and open circles, respectively), (c) Deviation of the calculated magnetic field from the DPPH resonance to the measured field as a function of the measured field.

At first, all visible resonances are fitted using Eq. (4.44) in order to extract $\omega_{\mathrm{res}}^{(nmr)}$ and $\Delta\omega^{(nmr)}$. Furthermore, the DPPH resonance line is identified as straight line at $\omega - \omega_{\mathrm{DPPH}} = 0\,\mathrm{MHz}$ and the resonance fields H^{DPPH} are calculated using Eq. (4.43). From our calculation we indeed find an increasing systematic deviation of 1 mT between the measured field and the calculated field from the DPPH resonance, as shown in Fig. 4.5 (c). As the deviation is not constant, the measured

field would cause an error during the YIG g-factor determination. For this reason we will use the calculated DPPH field in the following.

Second, the straight line at about $(\omega - \omega_{\mathrm{DPPH}})/2\pi \approx -60\,\mathrm{MHz}$ is identified as the (110)-mode, as this mode has a linear dispersion:

$$\omega_{\mathrm{res}}^{(110)} = \frac{g_{\mathrm{YIG}}\mu_{\mathrm{B}}}{\hbar}\mu_0\left(H + H_{\mathrm{ani}}\right) \tag{4.46}$$

and a very small frequency offset to the DPPH resonance. Furthermore, we know the dispersion relation for the (210)-mode from Eq. (4.22):

$$\omega_{res}^{(210)} = \frac{g_{\mathrm{YIG}}\mu_{\mathrm{B}}}{\hbar}\mu_0\left(H + H_{\mathrm{ani}} - \frac{2}{15}M_{\mathrm{s}}\right), \tag{4.47}$$

which increases linearly with the applied magnetic field. The frequency offset between the (110)- and the (210)-mode only depends on rather well known material parameters:

$$\frac{\omega_{res}^{(210)} - \omega_{res}^{(110)}}{2\pi} = -\frac{g_{\mathrm{YIG}}\mu_{\mathrm{B}}}{2\pi\hbar}\frac{2}{15}\mu_0 M_{\mathrm{s}} \approx -650\,\mathrm{MHz}. \tag{4.48}$$

We thus can identify the resonance at $(\omega - \omega_{\mathrm{DPPH}})/2\pi \approx -740\,\mathrm{MHz}$ as the (210)-mode. A simultaneous fit of the mode dispersions Eq. (4.46) and Eq. (4.47) to the measured values of $\omega_{\mathrm{res}}^{(110)}$, $\omega_{\mathrm{res}}^{(210)}$ and $\mu_0 H^{\mathrm{DPPH}}$ yields $g_{\mathrm{YIG}} = 2.0054(3)$, $\mu_0 M_{\mathrm{s}} = 176.0(4)\,\mathrm{mT}$ and $\mu_0 H_{\mathrm{ani}} = -2.5(4)\,\mathrm{mT}$. The error of g_{YIG} is given by the systematic error introduced by the field normalization using g_{DPPH}. The errors in $\mu_0 H_{\mathrm{ani}}$ and $\mu_0 M_{\mathrm{s}}$ are given by $\delta\mu_0 H_{\mathrm{disp}} + \delta\mu_0 H_{\mathrm{stray}}$. All values are in good agreement with previously reported material parameters [147, 148, 162–164] for YIG ($g_{\mathrm{YIG}} = 2.005(2)$, $\mu_0 H_{\mathrm{ani}} = -5.7\,\mathrm{mT}$ and $\mu_0 M_{\mathrm{s}} = 180\,\mathrm{mT}$) and, hence, justify the (110)- and (210)-mode assignments.

Third, the complete MSM manifold is computed using the extracted material parameters. The mode numbers of the remaining modes are determined from the characteristic dispersions. Figure 4.5 (b) shows the dispersions of the identified modes as function of $\omega_{\mathrm{res}}^{(nmr)} - \omega_{\mathrm{DPPH}}$ and H^{DPPH}, with very good agreement of theory (lines) and experiment (circles). We might attribute slight deviations between model predictions and data to a non-perfect spherical shape of the sample, which would change the boundary conditions for the magnetization dynamics in the YIG spheroid, and thus the dispersion relations.

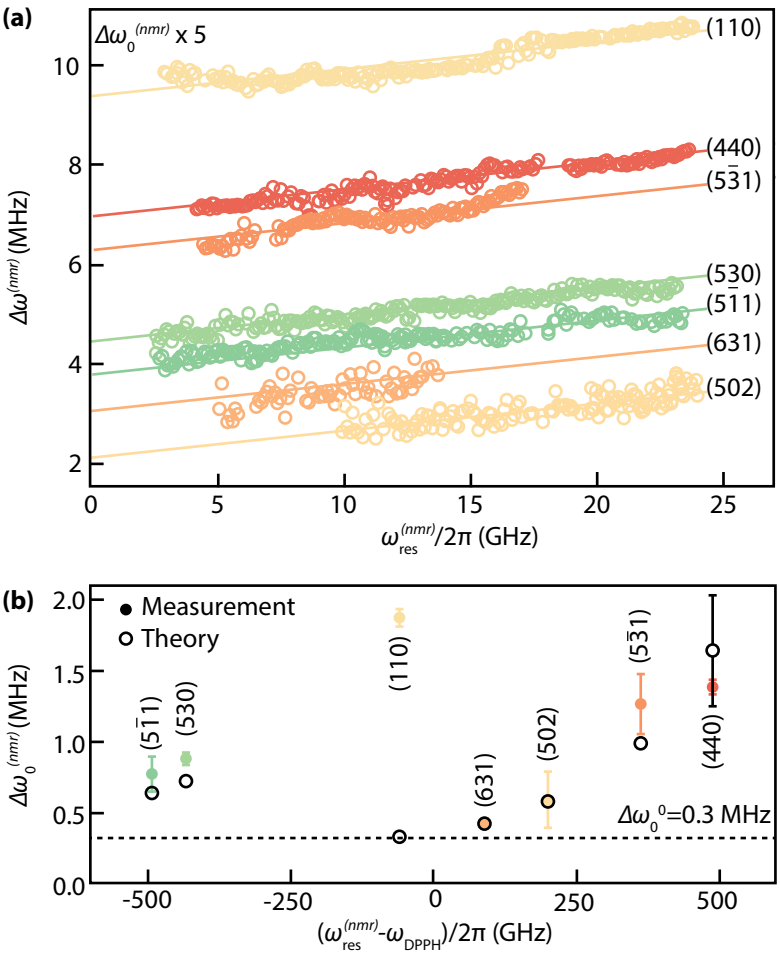

Fig. 4.6. – (a) Linewidth vs. resonance frequency of the measured MSMs. The Gilbert damping of all MSMs is $\alpha = 2.7(5) \times 10^{-5}$ as evident from the same slope of all curves. The inhomogeneous line broadening is different for each MSM. Note that the data points are plotted with an offset proportional to the inhomogeneous line broadening. (b) Inhomogeneous line broadening as a function of $\omega - \omega_{\mathrm{DPPH}}$.

4.4.2 Linewidth Analysis

In Fig. 4.6 (a) the linewidth $\Delta\omega^{(nmr)}$ of each MSM is plotted versus its resonance frequency $\omega_{\mathrm{res}}^{(nmr)}$. We expect a linear relationship between the linewidth and the resonance frequency for a Gilbert-like damping process. The offset $\Delta\omega_0^{(nmr)}$ is magnified by a factor of 5 to emphasize the differences in the inhomogeneous line broadening. Individual fits of all $\Delta\omega^{(nmr)}$ to Eq. (4.42) yield identical slopes for all modes within a small scatter, which is also evident from the linewidth data in Fig. 4.6 (a). Hence, the Gilbert damping parameter and inhomogeneous line broadening are obtained from a simultaneous fit of Eq. (4.42) to the extracted data points. Here, $\alpha^{(nmr)}$ is a shared fit parameter for all MSMs, but the inhomogeneous line broadening $\Delta\omega_0^{(nmr)}$ is fitted separately for each mode. To avoid fitting errors, the linewidth data are disregarded when a mode anti-crossing is observed, since this results in a pronounced change in linewidth [165]. Note that this behavior is a

signature of hybridized excitations as shown and used in Chap. 5. As evident from the solid fit curves in Fig. 4.6 (a) the evolution of the linewidth with resonance frequency of all measured MSMs can be well described with a shared Gilbert damping parameter of $\alpha^{(nmr)} = \alpha = 2.7(5) \times 10^{-5}$, independent of the mode number and the mode intensity. The latter is a strong hint that the radiative damping process has negligible influence on our damping measurement. The error in α is given by the scatter of α from the independent fits. Other groups report Gilbert damping parameters for YIG films [97, 100, 110, 166–169] larger than $\alpha = 6.15 \times 10^{-5}$, whereas for bulk YIG [61, 164, 169] values of around $\alpha = 4 \times 10^{-5}$ are found. Hence, the Gilbert damping parameter obtained here is the smallest experimental value at room temperature reported so far. As the intrinsic damping shown in literature is larger than our reported values, this is a support of our assumption of negligible radiative damping in our experiments. Furthermore, our results are in agreement with the notion that the Gilbert damping parameter is a bulk property, which only depends on intrinsic damping effects.

The question arises, why we observe a linear increase of the linewidth with the resonance frequency, i.e. what the microscopic mechanism behind the viscous damping observed could be. One important relaxation mechanism is the two-magnon-one-phonon scattering process, proposed by Kasuya and LeCraw [46]. In this process the magnon of the ferromagnetic resonance ($k_{m,1} = 0$) scatters under absorption of a phonon ($k_q \neq 0$) into a secondary magnon ($k_{m,2} \neq 0$). For temperatures T between 100 K and 350 K, we obtain $\Delta f \propto Tf$ over the bosonic occupation numbers of the magnon and phonon states [165]. Hence this process is considered to be the physical origin of the phenomenological Gilbert damping in a YIG sphere [37]. Note that we were able to show the Gilbert damping to vary linearly with temperature in a broad temperature range using the same YIG sphere. This observation confirms the assumption of a dominant Kasuya-LeCraw process. The temperature-dependent broadband FMR results have been published in H. Maier-Flaig, S. Klingler, C. Dubs, O. Surzhenko, R. Gross, M. Weiler, H. Huebl, S.T.B. Goennenwein, *Temperature-dependent magnetic damping of yttrium iron garnet spheres*, Physical Review B **95**, 214423 (2017).

However, the inhomogeneous line broadening is indeed different for the various MSMs. Figure 4.6 (b) shows the extracted values for the inhomogeneous line broadening (filled dots) as a function of $\omega_{res}^{(nmr)} - \omega_{DPPH}$. The error bars indicate the variation of the inhomogeneous line broadening between global and individual fits. In order to show the approximate position of the modes in comparison to Fig. 4.5, the x-scale is calculated for a magnetic field strength of $\mu_0 H = 0.5$ T. Additionally, the inhomogeneous line broadenings $\Delta\omega_0^{(nmr)}$ for all modes are calculated using Eq. (4.41). For the calculations of the line broadenings, a pit radius $R = 350$ nm and a constant linewidth contribution of $\Delta\omega_0^0/2\pi = 0.3$ MHz were assumed. Since the calculated $\Delta\omega_{2M}$ are slightly frequency dependent, the average linewidth values for the measured field and frequency range are used and

the standard deviation is indicated by the error bars of the open symbols. For most MSMs the variation is smaller than 10 kHz. Nevertheless, the (440)-mode should show a prominent peak in the linewidth measurement [57] at about $\omega_{\mathrm{res}}^{(440)}/2\pi = 10\,\mathrm{GHz}$ in Fig. 4.6 (a), which is however not observed in the experimental data. Additionally, the (110)-MSM shows a much larger linewidth than expected from the calculations. In a perfect sphere the (110)-mode is degenerate with the (430)-mode [152], but in a real sphere this degeneracy might be lifted. If the difference of the (110)- and (430)-mode frequencies is smaller than the linewidth of the measured resonance, an additional inhomogeneous line broadening is expected. Indeed, a careful analysis of the (110)-MSM line shape reveals a second resonance line in very close vicinity to the (110)-mode, yielding an artificial inhomogeneous line broadening of this mode. Besides these two MSMs, an excellent quantitative agreement between the two-magnon scattering model and experiment is found.

4.5 Conclusion

In conclusion, we perform broadband ferromagnetic resonance experiments on magnetostatic modes in a YIG sphere and we identified various magnetostatic modes. The exceptional data quality allows for an detailed study of the different damping mechanisms in the YIG sphere, namely intrinsic Gilbert damping, and extrinsic damping, which shows up as an inhomogeneous line broadening. A record low Gilbert damping parameter of $\alpha = 2.7(5) \times 10^{-5}$ is found for all MSMs, independent of their mode indices. This is in agreement with the notion that the Gilbert damping is a global material parameter. Due to the high volume of the sphere (in comparison to films) and the low Gilbert damping parameter, YIG spheres are interesting candidates for the application in coupling experiments, similar to those shown in Chap. 6. Furthermore, the inhomogeneous line broadening differs between the various magnetostatic modes, in agreement with the expectations due to two-magnon scattering processes of the magnetostatic modes into the spin-wave manifold. From this we gain important information about the spatial distribution of the magnetic excitations in the sphere, which can be used in quantum coupling experiments, where certain modes should be populated.

However, one could also use these experiments to improve for example the bandwidth of YIG tuned microwave filters [142], where the exact knowledge of the mode dispersions is required and the linewidth is the limiting factor of the filter quality. The inhomogeneous linebroadening of the MSMs can then be used as quality indicator in the production process.

Spin Torques in Coupled YIG/Co Heterostructures

5

As stated in the introduction, the aim of modern spin-wave technology is to encode and transport information using the electron spin-angular momentum [12, 14, 38–41, 170]. To rebuild logic gates the spin waves have to interfere, which requires an effective steering and guiding of the spin waves in the magnetic medium. Spin waves can be guided for example in magnonic waveguides [100] and in domain walls [171], as well as in rather complex two dimensional structures, such as magnonic multiplexer [172, 173] or thermal landscapes [45, 174], where the latter require an exact knowledge of the spin-wave dispersion to manipulate the spin-waves appropriately. For the steering and guiding of spin waves in complex multi-dimensional structures, magnonics based on exchange spin waves is particularly appealing. The spin-wave frequency is dominated for large wave vectors by the isotropic exchange energy term, which leads to an isotropic dispersion relation $\omega \propto \gamma D k^2$. The isotropic dispersion relation of these so called exchange spin waves allows for a uncomplicated guiding of spin waves in multi-dimensional structures, which are necessary for spin-wave signal processing. Recently, we have shown the positive effects of isotropic spin-wave dispersions on the transmission of signals in two dimensional structures [13]. Furthermore, the small wavelength and the large group velocities $v_{gr} = \partial\omega/\partial k \propto k$ promise a fast data transfer and high processing speed.

Unfortunately the excitation of these small wavelength spin waves is challenging. To excite non-uniform magnetization dynamics and propagating spin waves, either the excitation mechanism or the magnetization or both must be non-uniform. Hence, for the excitation of exchange dominated spin waves in a homogeneous magnetized medium, the excitation fields need to be nonuniform on a sub-100 nm length scale. The most common method to excite spin waves is the exploitation of dynamic microwave-frequency magnetic fields, around a antenna, such as an metallic stripline or a coplanar waveguide [141, 175]. The dynamic magnetic fields modulate the magnetization dominantly below the antenna structure, see Chap. 2.4.1. In this case the maximum achievable wave vector of the spin wave is limited by the spatial periodicity of the antenna structure and its dynamic magnetic field. Furthermore, standard striplines have poor efficiency due to high Ohmic losses and impedance mismatch when it comes to downscaling and miniaturization. One can overcome those limitations by using magnon transducers [176], where the generation of an artificial magnetic lattice under the antenna structure leads to an additional k-momentum. In the case of parallel pumping [177, 178], an rf-field with twice the resonance frequency is applied parallel to the magnetization.

In this geometry the microwave photons counteract the magnetic damping and can excite propagating spin waves above a critical threshold power. There are also excitation schemes based on Schlömann resonances, which use the non-uniformity of the demagnetization tensor in a finite sample [179, 180]. This allows to modulate the magnetization in distinct regions of the sample, with global oscillating magnetic fields. In spin-torque oscillator driven devices, spin currents are used to excite a spin-torque nanooscillator [135, 181], where the local dynamic magnetic field can then be coupled into a waveguide system [136]. There are further more exotic spin-wave excitation mechanisms, such as laser-based schemes using pulse trains which exploit local heating and a change of the local anisotropy field [182] or the modulation of the magnetization using the inverse Faraday effect [183] in the laser spot region. Recently, also a generation of spin waves with wave lengths in the 100 nm regime using precessing magnetic vortices was reported [184].

In this chapter we present a new excitation mechanism of exchange spin waves based on exchange and spin torques at the interface of yttrium iron garnet/cobalt (Co) heterostructures. We investigate the heterostructures using a broadband ferromagnetic resonance setup with a coplanar waveguide center conductor width of $w = 300\,\mu$m. We observe an efficient excitation of up to forty perpendicular standing spin waves (PSSWs) with wavelengths down to $\lambda_{\mathrm{PSSW}} \approx 50\,$nm in the YIG layer, together with a hybridization of the YIG PSSWs and the Co FMR line, when the respective resonance frequencies coincide. The hybridization is indicated by avoided crossings of the YIG PSSW and the Co FMR line, which are also observed when a copper (Cu) layer separates the YIG and the Co films. However, the insertion of an insulating AlOx interlayer completely suppresses the excitation of YIG PSSWs. This allows us to exclude dipolar coupling as the origin of the PSSW excitation.

We show that excitation of these exchange spin waves and the hybridization of the YIG and Co resonances is caused by interfacial spin torques in the YIG/Co system. These spin torques couple the YIG and Co magnetization dynamics by microwave frequency spin currents and direct exchange interaction.

Our data are well described by a modified Landau-Lifshitz-Gilbert equation for the Co layer, which includes direct exchange torques and field-like and damping-like torques from mutual spin pumping at the YIG/Co interface. Simulations of our coupled systems reveal the respective influence of the spin toques on the coupling of the different layers. In contrast to the previously observed purely damping-like spin-torques in all-metallic multilayers [185], we find a dominant influence of the field-like torques to the coupling of the YIG and Co.

In the first part of this chapter, we describe the experimental setup, and present and analyze our measurement results. We subsequently introduce a simple macrospin model, based on interfacial exchange interaction and mutual spin pumping, which already contains all salient features of the coupled magnetic system. The full extended theory, which also considers the influence of the non-

uniform magnetization dynamics of the perpendicular standing spin waves is presented in Appendix A. Finally, we use the full theory to simulate the Co susceptibility in the different heterostructures, and discuss the amplitude and signs of the different torques.

Some of the figures and parts of the text in this chapter have been published in S. Klingler, V. Amin, S. Geprägs, K. Ganzhorn, H. Maier-Flaig, M. Althammer, H. Huebl, R. Gross, R.D. McMichael, M.D. Stiles, S.T.B. Goennenwein, M. Weiler, *Spin-torque excitation of perpendicular standing spin waves in coupled YIG/Co heterostructures*, Physical Review Letters **120** (2018).

5.1 Experimental Methods

5.1.1 Sample Preparation

For our investigations we prepared set of four YIG/Co samples, based on commercially available YIG films. The YIG films are grown by liquid-phase epitaxy on a (111)-oriented gallium gadolinium garnet substrate to a YIG thickness of $d_2 = 1\,\mu$m. Each sample is cut to lateral dimensions of $6 \times 5\,\text{mm}^2$ and is cleaned with Piranha etch and subsequently annealed in oxygen at 500 °C for 40 minutes [186]. For the first set of samples a thin Co film is deposited onto the YIG film *in-situ* via electron beam evaporation without breaking the vacuum. These samples have thicknesses of $d_1 = 35\,\text{nm}$ and $d_1 = 50\,\text{nm}$ (samples YIG/Co(35) and YIG/Co(50), respectively). For a second set of samples a Cu layer with a thickness of $d_s = 5\,\text{nm}$ is evaporated on the YIG before a Co film with a thickness of $d_1 = 50\,\text{nm}$ is grown on top of it (YIG/Cu(5)/Co(50)). Finally, a control sample is prepared, where a $d_s = 1.5\,\text{nm}$ thick aluminum (Al) film is sputtered on the YIG with subsequent oxidation. As the aluminum layer thickness is smaller than the average native oxide layer thickness of about 2 nm in aluminum [119], we obtain a fully insulating interlayer. A Co film with a thickness of $d_1 = 50\,\text{nm}$ is subsequently deposited on top of the AlOx layer via electron beam evaporation (YIG/AlOx(1.5)/Co(50)). All samples are capped with a 2.5 nm thick layer of AlOx to prevent oxidation of the Co layer.

5.1.2 Experimental Setup

We measure the dynamic magnetization properties of the YIG/Co samples using the VNA-based broadband ferromagnetic resonance setup at room temperature, presented in Chap. 2.4.3. Figure 5.1 shows a sketch of the measurement setup. The YIG/Co samples are placed on a coplanar waveguide (CPW) with the Co side down. The center conductor of the CPW has a width of $w = 300\,\mu$m. We position the CPW between the $a = 5\,\text{cm}$ pole shoes of the electromagnet. The CPW is connected to port 1 and port 2 (P1 and P2, respectively) of the VNA and the complex-valued transmission of a microwave current S_{21} is measured in a

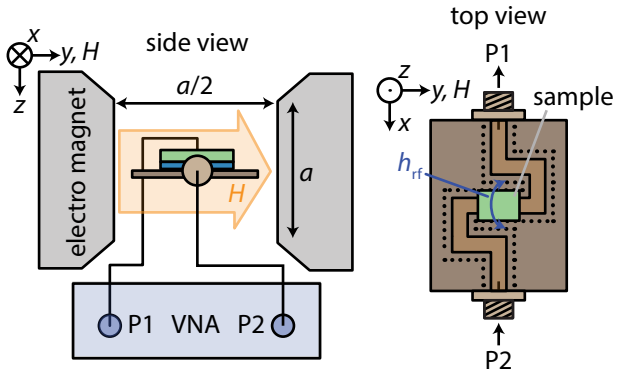

Fig. 5.1. – Sketch of the measurement setup. We place the YIG/Co samples with the Co-side down onto the center conductor of the CPW.

frequency range between $\omega/2\pi = 1\,\mathrm{GHz}$ and $\omega/2\pi = 26.5\,\mathrm{GHz}$ as a function of the magnetic field. When the applied frequency ω matches the resonance condition for a given external magnetic field, microwave power is absorbed, which results in a precession of the magnetization of the sample.

As the transmission signal of the CPW is strongly frequency dependent, we do not show any raw frequency spectra, but the field-derivative of S_{21} [187]. In our measurements, the transmitted microwave signal of the vector network analyzer reads, cf. Chap. 2.4.3:

$$S_{21}(H) = \Delta S_{21}(H) S_{21}^0 + S_{21}^0 \tag{5.1}$$

Here, S_{21}^0 is the field-independent background transmission. Note that a perfect background transmission is achieved for $S_{21}^0 = 1$. The background-corrected field derivative of our measurement signal is now given by [187]:

$$\partial_D S_{21}/\partial H = \frac{1}{S_{21}(H)} \frac{S_{21}(H+\delta H) - S_{21}(H-\delta H)}{\delta H}, \tag{5.2}$$

where δH is a constant field step in our measurement of about 0.5 mT. Note that the differential quotient is rescaled by the central value $S_{21}(H)$ which eliminates background drift.

Below, we simulate $\chi = \chi_{1,xx}$, with:

$$\chi_{1,xx} = \frac{\chi_{1,zz}^{-1}}{\chi_{1,zz}^{-1}\chi_{1,xx}^{-1} - \chi_{1,zx}^{-1}\chi_{1,xz}^{-1}}, \tag{5.3}$$

from which we calculate ΔS_{21} with Eq. (2.83). To compare the simulation results to experimental data, we use Eq. (5.1) with $S_{21}^0 = 1$ and then calculate $\partial_D S_{21}/\partial H$ using the inductance from Eq. (2.85), which yields:

$$\begin{aligned}\partial_D S_{21}/\partial H &= \frac{\Delta S_{21}(H+\delta H) - \Delta S_{21}(H-\delta H)}{(\Delta S_{21}(H)+1)\delta H} \\ &= \frac{d_{\text{tot}} l \mu_0 \omega (\chi_{1,xx}(\delta H + H) - \chi_{1,xx}(H-\delta H))}{\delta H (d_{\text{tot}} l \mu_0 \omega \chi_{1,xx}(H) + 8 i w Z_0)}.\end{aligned} \tag{5.4}$$

5.2 Experimental Results

5.2.1 VNA Measurements

Figure 5.2 (a) shows the background-corrected field-derivative [187] of the VNA transmission spectra $|\partial_D S_{21}/\partial H|$ for the YIG/Co(50) sample as a function of H and ω. We clearly observe two major modes in the color map. The low-frequency mode corresponds to the YIG FMR line, whereas the high-frequency mode corresponds to the Co FMR line. Within the broad Co FMR line, we find several narrow resonances, of which the dispersion is parallel to the YIG FMR. These lines are attributed to the excitation and detection of YIG PSSWs with wavelengths down to 50 nm, as shown in Fig. 5.4. We find avoided crossings between these YIG PSSWs and the Co FMR line (inset), where the splitting is $g_{\text{eff}}/2\pi \leq 200$ MHz. This is a clear indication that the YIG and Co systems are coupled to each other. Furthermore, an additional low-frequency mode with a lower intensity is observed. This line is attributed to an exchange mode of the coupled YIG/Co system, as supported by simulations in Fig. 5.9. Note that our observation is in agreement with previous observations of exchange modes in coupled systems [188–190], although these studies only considered macrospin dynamics for each layer. For all investigated samples with $d_1 = 50$ nm we observe the first Co PSSW at around 22 GHz and $\mu_0 H = 0.1$ T.

Figure 5.2 (b) shows the background-corrected field derivative of the transmission spectra for the YIG/Co(35) heterostructure. Again, we observe the high and the low frequency mode, which correspond to the Co and YIG FMR lines, respectively, together with the exchange mode. The YIG PSSWs form avoided crossings with the Co FMR line as shown in magnification (inset). The frequency splitting has about the same size as found from the YIG/Co(50) heterostructure.

Figure 5.2 (c) shows $|\partial_D S_{21}/\partial H|$ for the YIG/Cu(5)/Co(50) sample as a function of H and ω. Again, we observe the YIG FMR, YIG PSSWs and the Co FMR lines. However, the frequency splitting between the modes is much smaller than for the YIG/Co(50), $g_{\text{eff}} \leq 40$ MHz. This strongly indicates that the coupling efficiency is reduced in comparison to Fig. 5.2 (a,b). We attribute this mainly to the suppression of the static exchange coupling by insertion of the Cu layer. This is also in agreement with the vanishing of the exchange mode.

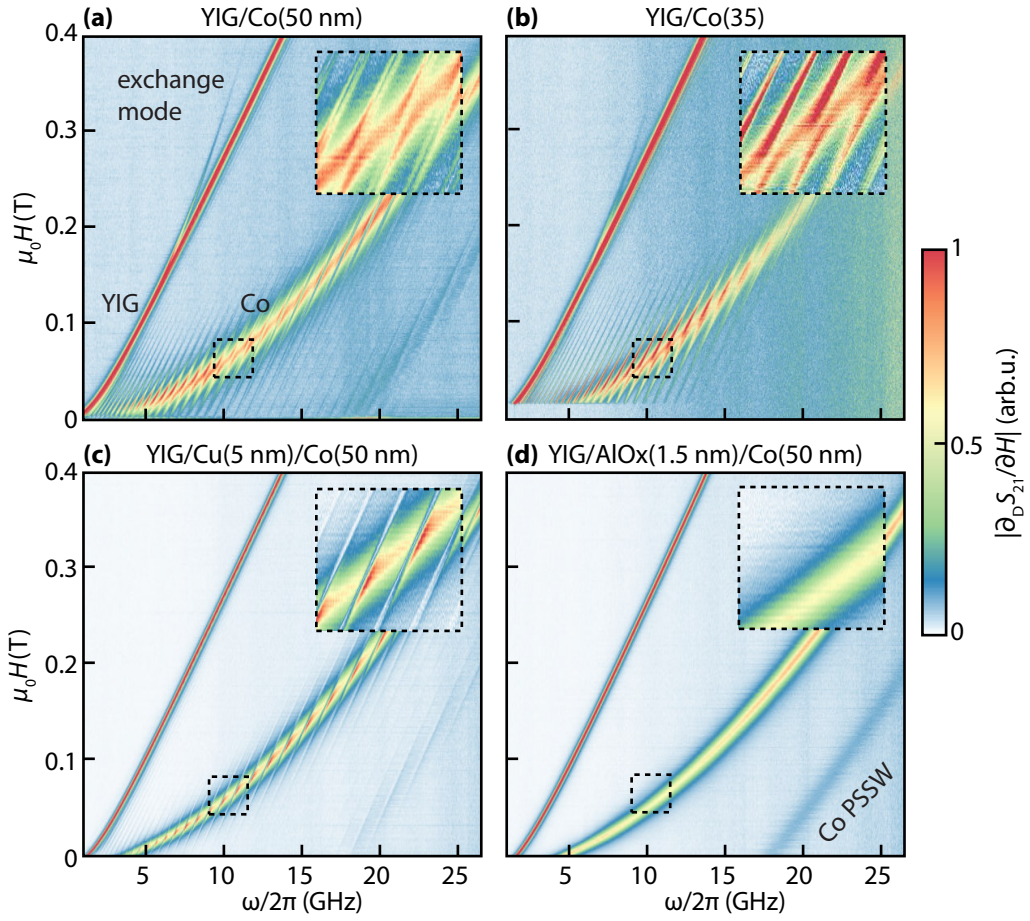

Fig. 5.2. – Field-derivative of the VNA transmission spectra for three different samples as a function of magnetic field and frequency. All samples show two modes corresponding to the YIG (low-frequency mode) and Co (high-frequency mode) FMR lines. We normalized the color scale individually to arbitrary values to allow for direct comparison between the samples. (a) The YIG/Co(50 nm) sample additionally reveals YIG PSSWs and pronounced avoided crossings of the modes for small frequencies. (b) The YIG/Co(35 nm) sample also reveals YIG PSSWs and pronounced avoided crossings of the modes for small frequencies. (c) The YIG/Cu(5 nm)/Co(50 nm) sample also shows the YIG PSSWs, but the frequency splittings of the avoided crossings are much smaller than in (a). (d) The YIG/AlOx(1.5 nm)/Co(50 nm) sample does not show any PSSWs in the Co FMR line, as expected in the YIG and CO are magnetically uncoupled.

Figure 5.2 (d) displays $|\partial_D S_{21}/\partial H|$ for the YIG/AlOx(1.5)/Co(50) sample as a function of H and ω. No YIG PSSWs are observed within the Co FMR line (inset Fig. 5.2 (d)). This provides strong evidence that the insertion of the AlOx layer suppressed the coupling between the YIG and Co magnetization dynamics. An analysis of the Co FMR linewidth (see Chap. 5.2.4) also demonstrates that the insertion of the AlOx layer completely suppresses any coupling between the YIG and Co layers.

From Fig. 5.2, we conclude that any magneto-dynamic coupling is suppressed by insertion of an insulator between the two magnetic layers. This provides strong evidence against a magnetostatic coupling by stray fields, and is in agreement with

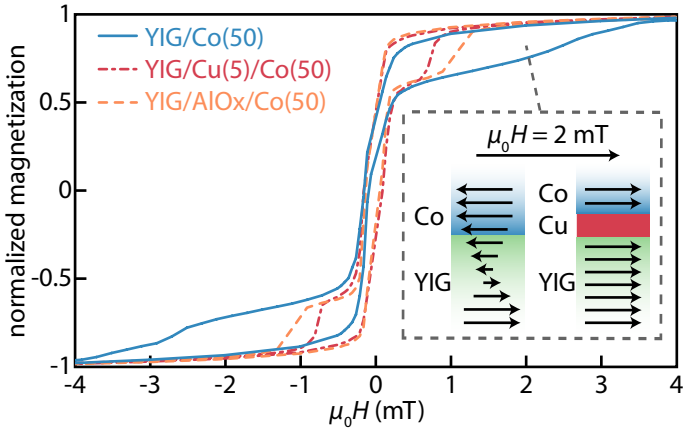

Fig. 5.3. – Normalized magnetic moment in YIG/Co(50) (solid), YIG/Cu(5)/Co(50) (dash-dotted) and YIG/AlOx(1.5)/Co(50) (dashed). The magnetic hysteresis loops of the samples with a Cu or AlOx interlayer reveal a sharp switching of the magnetic moment at the Co coercive field $\mu_0 H_c \approx 1\,\mathrm{mT}$. The YIG/Co sample shows an enhancement of the Co coercive field an a continuous transition to the parallel magnetization state. The inset shows the magnetization distribution in a statically coupled (left) and a statically uncoupled (right) heterostructure at an external magnetic field of $\mu_0 H = 1.5\,\mathrm{mT}$.

a dynamic coupling mediated by spin currents, which can pass through the Cu layer, but are blocked by the AlOx barrier.

5.2.2 SQUID Magnetometry Measurements

Figure 5.3 shows the magnetic hysteresis loops of the YIG/Co samples recorded by Superconducting Quantum Interference Device (SQUID) magnetometry. The hysteresis loop of the YIG/Co(50) sample (shown as solid line in Fig. 5.3) exhibits a sharp switching at the YIG coercive field of about 0.1 mT. However, no sharp switching of the Co layer is visible but a smooth increase of the measured magnetic moment until the bilayer magnetization is saturated. This can be explained by a direct, static exchange coupling between YIG and Co magnetizations (inset), as known from exchange springs [191, 192]. The form of the hysteresis loop suggests an antiferromagnetic coupling, as comparably large magnetic fields are required to force a parallel alignment of the layers. However, without a detailed examination of the remnant state, we cannot rule out any ferromagnetic coupling. Note that the hysteresis curve of the YIG/Co(35) looks similar but is not shown for a better clarity in Fig. 5.3. By inserting a Cu or AlOx layer between the YIG and the Co (dash-dotted and dashed lines in Fig. 5.3) we find a sharp switching at the Co coercive field $\mu_0 H_c \approx 1\,\mathrm{mT}$. This in agreement with the behavior expected for statically uncoupled magnetic layers [193]. However, we still observe a dynamic coupling in Fig. 5.2 (b) in the YIG/Cu(5)/Co(50) sample. Since we find no static exchange coupling between Co and YIG in this sample, the observation of the dynamic coupling requires a different mechanism as the origin of the excitation of the YIG PSSWs.

5.2.3 Determination of the Material Parameters

In Fig. 5.4 (a), an example frequency spectrum is shown for the YIG/Co(50) sample for a fixed field of $\mu_0 H = 0.02\,\mathrm{T}$. Plotted is $|\partial_D S_{21}/\partial H|$ versus applied microwave frequency, and the plot corresponds to a cut along the x-axis in Fig. 5.2 (a). The peak in $|\partial_D S_{21}/\partial H|$ at 2 GHz is attributed to the YIG FMR frequency. At about 6 GHz we find a broad excitation of the Co FMR. Furthermore, we resolve about 40 YIG PSSW resonances. Some of the YIG PSSWs are labeled to guide the reader. In comparison to Ref. [23] we find a drastically increased sensitivity for the YIG PSSWs. Additionally, all PSSWs are equally visible, not only the modes with an odd mode number. We expect this for driving fields, which are strongly inhomogeneous. Such inhomogeneous driving fields cannot stem from the used coplanar waveguide, as the center conductor width is $w = 300\,\mu\mathrm{m}$, which provides homogeneous driving field over the sample thickness of about $1\,\mu\mathrm{m}$.[3]

Figure 5.4 (b) shows the extracted resonance fields as a function of the frequency for the YIG/Co(35) sample using a fit of up to five superimposed Lorentzian resonances. Our algorithm tries to initialize five Lorentzian absorption lines; however, often fewer resonances are sufficient to model our data. We disregard any fits where the relative fitting error in the linewidth is larger than 5 % or the relative error in the resonance fields is larger than 1.5 %. The inset shows a magnification of the field and frequency range marked with the dashed box, and we observe multiple avoided crossings. The frequency splitting g_{eff} is determined using a fit of the coupled harmonic oscillator model of the avoided crossing, see Eq. (6.2).

To obtain the material parameters of the Co layer, we fit the pure Co FMR line which we get by deleting all data points of avoided crossings and YIG PSSWs from the data set, as shown in Fig. 5.4 (c). For the fit, we use the in-plane Kittel equation (2.45):

$$\omega_{\mathrm{res},2} = \gamma\mu_0 \sqrt{H + D_s k^2 \left(H + D_s k^2 + M_s\right)} \tag{5.5}$$

with $k = 0$ for the FMR mode, which yields $\gamma_1/2\pi = 28.7(1)\,\mathrm{GHz/T}$ and $\mu_0 M_{s,1} = 1.91(2)\,\mathrm{T}$, where the number in brackets denotes the error of the last digit. The fit is shown as black line.

To obtain the material parameters of the YIG film, we fit the pure YIG PSSWs using the in-plane Kittel equation (2.45), as shown in Fig. 5.4 (d). For this we assume a fixed saturation magnetization of $\mu_0 M_{s,2} = 0.18\,\mathrm{T}$ [147], as we otherwise get a mutual dependence of $M_{s,2}$ and $D_s k^2 = H_{ex,2}$ during the fit [23]. A global fit, where γ_2 is a shared fit parameter and $H_{ex,2}$ is fitted for each PSSW individually, yields $\gamma_2/2\pi = 27.07(1)\,\mathrm{GHz/T}$. The fits are shown as black lines.

[3] This can also be seen by Eq. (2.71), where the driving fiels is independent of the z'-component for $z' \ll w$.

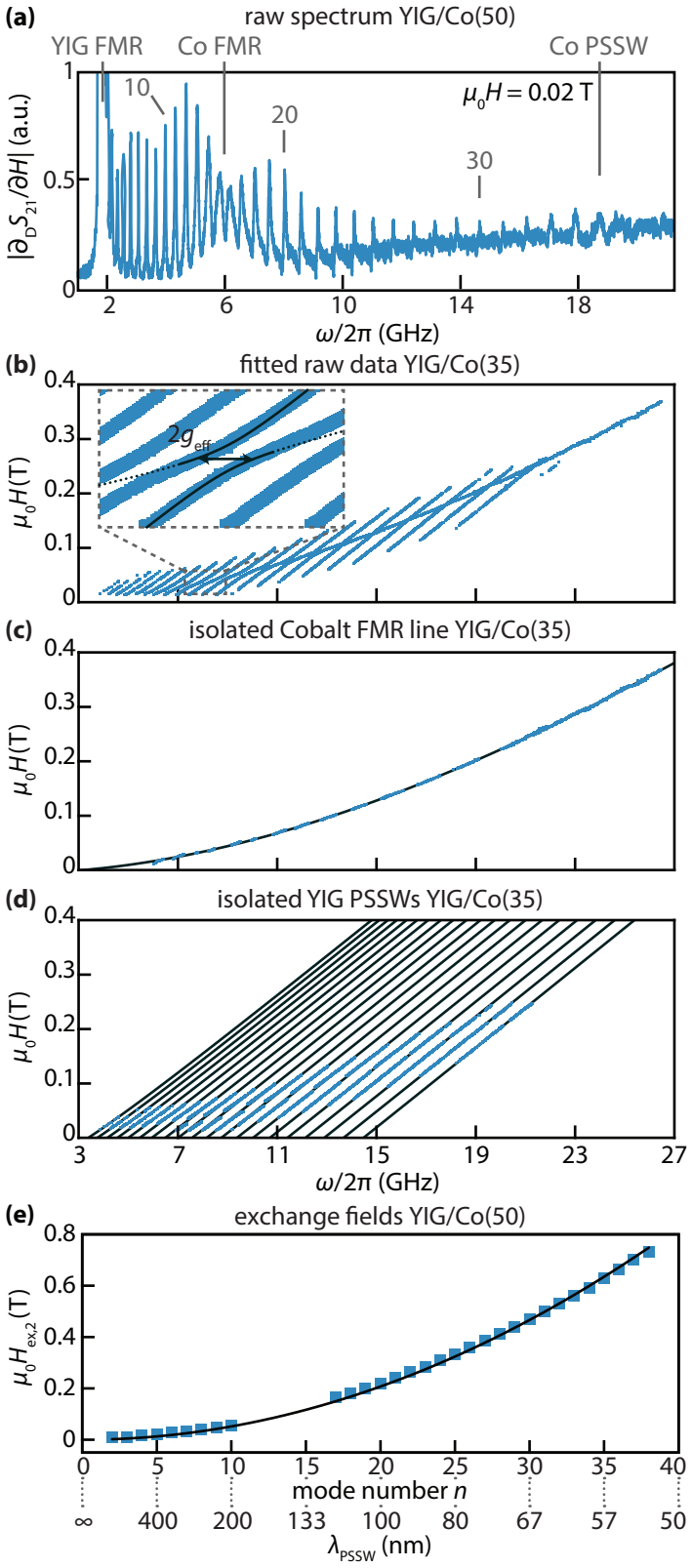

Fig. 5.4. – (a) Example frequency spectrum of the YIG/Co(50) sample at $\mu_0 H = 0.02\,\mathrm{T}$. (b) Fitted raw data resonance fields and frequencies of the YIG/Co(35) sample. (c) Isolated Co FMR line. (d) Isolated YIG PSSWs. (e) The extracted exchange fields of the YIG/Co(50) sample are plotted as a function of the PSSW mode number n.

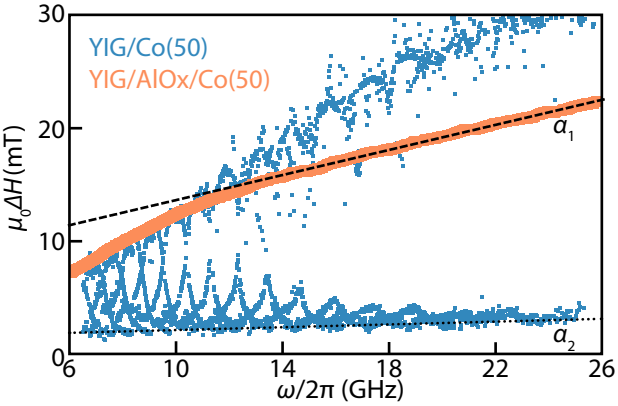

Fig. 5.5. – The linewidth evolution of the YIG/Co(50) and YIG/AlOx(1.5)/Co(50) samples is shown as a function of the excitation frequency. The linewidth of the YIG/AlOx(1.5)/Co(50) sample increases monotonically (orange symbols), without any modulation. The blue symbols show the linewidths of the YIG/Co(50) sample which shows characteristic modulation for every coupled PSSW.

From the extracted resonance fields of each YIG mode, we are able to determine the exchange fields. In Fig. 5.4 (e), the extracted exchange fields are shown as a function of the mode number n. We use the method proposed in Ref. [23] to determine the mode numbering. Having this, we see a quadratic curvature (black) of the exchange field, which is fitted using:

$$\mu_0 H_{\mathrm{ex},2} = D_{\mathrm{s},2} \left(\frac{n\pi}{d_2} \right)^2 . \tag{5.6}$$

From the fit a value of $D_{\mathrm{s},2} = 5.25(2) \times 10^{-17}\,\mathrm{Tm}^2$ is obtained. Using the relation $A_i = D_{\mathrm{s},i} M_{\mathrm{s},i}/2$ we yield $A_2 = A = 3.76\,\mathrm{pJ/m}$. Furthermore, the quadratic increase of the exchange fields with the mode number n and the extracted value of $D_{\mathrm{s},i}$ confirm our assumption that we indeed observe standing spin-wave modes in the YIG film. Note that we only expect minor interfacial corrections to for $H_{\mathrm{ex},2}(k)$ for mixed boundary conditions. If we assume total pinning of the YIG magnetization at both interfaces, we obtain a small deviation of 4 % to the extracted value of $D_{\mathrm{s},2}$.

The fit values of the YIG and the Co film agree very well with the literature values $\gamma_1/2\pi = 29.7\,\mathrm{GHz/T}$, $\mu_0 M_{\mathrm{s}1} = 1.79\,\mathrm{T}$ $\gamma_2/2\pi = 28.06\,\mathrm{GHz/T}$, $D_{\mathrm{s}} = 5.3 \times 10^{-17}\,\mathrm{Tm}^2$ [23, 36, 194, 195] and they are thus taken to be constant throughout for the data analysis.

5.2.4 Damping Analysis

In this section we analyze the linewidth evolution of the YIG/AlOx/Co(50) sample and compare it to the YIG/Co(50) sample. The idea is that a coupling of the YIG and the Co magnetizations should be visible in the linewidth of the

Co and the YIG magnetization, as even a weak coupling opens an additional relaxation channel to the subsystems [102, 196]. This is reflected in the lifetime of the spin-wave resonances and hence the linewidth evolution of the subsystems. In Fig. 5.5 the linewidth evolution of the YIG/Co(50) sample is shown as a function of the excitation frequency (blue symbols). We find for $\omega/2\pi < 14\,\mathrm{GHz}$ a strong modulation of the linewidth. This modulation goes along with the observation of avoided crossings in Fig. 5.2. However, in Fig. 5.5 also the Co linewidth from the YIG/AlOx(1.5)/Co(50) sample (orange symbols) is shown as a function of the excitation frequency. For small frequencies we see a fast increase of the linewidth which flattens out above $\omega/2\pi = 10\,\mathrm{GHz}$. The shape of this linewidth evolution can be understood with Gilbert damping and two-magnon scattering processes, which are expected for an in-plane measurement geometry [51, 59, 197–201], cf. Chap. 2.3.2. There are no additional features that indicate any coupling of the YIG and the Co in the YIG/AlOx(1.5)/Co(50) heterostructure. Hence, we can rule out dynamic stray fields as the origin of the coupling. From the YIG/AlOx(1.5)/Co(50) sample we extract a Gilbert damping parameter α_1 of the Co layer using the Gilbert damping equation [60]:

$$\mu_0 \Delta H_i = \mu_0 \Delta H_{0,i} + \frac{2\omega\alpha_i}{\gamma_i}, \tag{5.7}$$

where ΔH_1 is the Co linewidth and $\Delta H_{0,1}$ the inhomogeneous line broadening of the Co film. The fit is shown as the dashed line in Fig. 5.5 and we obtain an intrinsic Gilbert damping $\alpha_1 = 7.7(1) \times 10^{-3}$ and $\mu_0 \Delta H_{0,1} = 8(1)\,\mathrm{mT}$, where the Gilbert damping agrees well with previous reported values of between $\alpha_1 = 5.2 \times 10^{-3}$ and $\alpha_1 = 7.5 \times 10^{-3}$ [202]. Hence, approximately half of the linewidth of the Co resonance is due to the frequency independent inhomogeneous line broadening. The YIG damping can be estimated in a similar way from the coupled YIG/Co(50) sample, where we take the lower part of the enveloping curve of the blue data points as the YIG linewidth. The fit shown as dotted line in Fig. 5.5 yields $\alpha_2 = 7.2(3) \times 10^{-4}$, which is larger than the damping values from previous reports for $300\,\mu\mathrm{m}$-thick LPE YIG films $\alpha_2 = 0.5 \times 10^{-4}$ [169]. This is denoted to the fact, that we only observe the YIG PSSWs due to the coupling to the Co FMR, which leads to an additional line broadening as shown below. Note furthermore, that the fitted linewidth data stems from about twenty different PSSWs with different wave vectors, which could also lead to an influence of a wave number dependent damping mechanism [177].

5.3 The Simplified Macrospin Model

5.3.1 Derivation of the Macrospin Model

In this chapter we want to introduce a phenomenological model for the observed coupling mechanisms. As the mode profile at the interface of the YIG/Co heterostructures is quite complex, we restrict our model here to the a macrospin model, which only considers a uniform precession of the magnetization in both the YIG and the Co films. This leads to a simplified model with an easy-to-understand susceptibility matrix, which allows us to discuss the influences of the dynamic torques on the coupled system. While the model described below cannot be used for a quantitative analysis of the presented experiments, it can be applied for coupled ferromagnetic heterostructures with film thicknesses in the nanometer range.

In Chap. A.1 and A.2 we derive the full model which contains interfacial torques which lead to mixed boundary conditions at the YIG interfaces. We will find there, that the proposed model here can be reproduced when we neglect any boundary conditions.

We start with the Landau-Lifshitz-Gilbert equation for a homogeneous magnetization precession, introduced in Chap. 2.1.2.1. We furthermore assume that the film lies in the x, y-plane and is magnetized along the $\hat{\boldsymbol{y}}$-direction. The dynamic components of the magnetization are small compared to the saturation magnetization, thus we only consider the linearized part of the LLG. This translates mathematically into $\boldsymbol{M}_i \times \dot{\boldsymbol{M}}_i \rightarrow \hat{\boldsymbol{y}} \times \dot{\boldsymbol{M}}_i$, and the linearized LLG for every layer reads:

$$\dot{\boldsymbol{M}}_i = -\gamma_i \hat{\boldsymbol{y}} \times \left(\mu_0 H_{\mathrm{eff,i}} \boldsymbol{M}_i - \frac{\alpha_i}{\gamma_i} \dot{\boldsymbol{M}}_i \right) \tag{5.8}$$

where we use the effective field:

$$H_{\mathrm{eff,i}} = H + H_{\mathrm{ex,i}} + H_{\mathrm{dyn}} - M_{\mathrm{s,i}} M_{i,z} \hat{\boldsymbol{z}}. \tag{5.9}$$

Note that the exchange field here is included phenomenologically to shift the different FMR curves, in order to simulate the PSSW resonance position. The last term on the right hand side of the equation is the demagnetization field.

We have seen from Eq. (3.7) that the spin current which is pumped out of the ferromagnet from layer i to layer j can be written as:

$$\tau_{\mathrm{loss},i} = \frac{\gamma_i}{M_{\mathrm{s},i} d_i} \frac{\hbar}{4\pi} \left(\mathrm{Re}\left[g^{\uparrow\downarrow} \right] \boldsymbol{M}_i \times \dot{\boldsymbol{M}}_i - \mathrm{Im}\left[g^{\uparrow\downarrow} \right] \dot{\boldsymbol{M}}_i \right). \tag{5.10}$$

However, layer i gains also a torque due to the spin current which is pumped from layer j to layer i. In contrast to the losses, we decrease the damping of the layer i. We can hence write:

$$\tau_{\text{gain},i} = -\frac{\gamma_i}{M_{\text{s},i} d_i} \frac{\hbar}{4\pi} \left(\text{Re}\left[g^{\uparrow\downarrow}\right] \boldsymbol{M}_j \times \dot{\boldsymbol{M}}_j - \text{Im}\left[g^{\uparrow\downarrow}\right] \dot{\boldsymbol{M}}_j \right). \tag{5.11}$$

Note that the gained torque from layer j scales with the saturation magnetization, gyromagnetic ratio and thickness of the layer i. To calculate the total torque, we now use that $\boldsymbol{M}_i$ and $\boldsymbol{M}_j$ are both macrospins which point along the $\hat{\boldsymbol{y}}$-direction. The total torque τ for layer i now reads:

$$\begin{aligned} \tau_i &= \tau_{\text{loss},i} + \tau_{\text{gain},i} \\ &= \frac{\gamma_i}{M_{\text{s},i} d_i} \left(\tau_{\text{D}} \hat{\boldsymbol{y}} \times \left(\dot{\boldsymbol{M}}_i - \dot{\boldsymbol{M}}_j \right) + \tau_{\text{F}} \left(\dot{\boldsymbol{M}}_j - \dot{\boldsymbol{M}}_i \right) \right) \\ &= -\frac{\gamma_i}{M_{\text{s},i} d_i} \left(\tau_{\text{F}} - \tau_{\text{D}} \hat{\boldsymbol{y}} \times \right) \left(\dot{\boldsymbol{M}}_i - \dot{\boldsymbol{M}}_j \right), \end{aligned} \tag{5.12}$$

where we have introduced the field-like torque strength $\tau_{\text{F}} = \frac{\hbar}{4\pi} \text{Im}\left[g^{\uparrow\downarrow}\right]$, as the torque associated with the imaginary part of the spin mixing conductance has the symmetry of a torque from an external magnetic field, and the damping-like torque strength $\tau_{\text{D}} = \frac{\hbar}{4\pi} \text{Re}\left[g^{\uparrow\downarrow}\right]$, as the torque associated with the real part of the spin mixing conductance has the symmetry of a damping term, such as the Gilbert damping. The meaning of Eq. (5.12) is that the magnetization layer i is torqued by an effective spin current, which is the difference between the outgoing and the incident spin current.

Now we turn to the interfacial exchange interaction. The exchange energy of the spin system is given by Eq. (2.4). We now use a similar ansatz to describe the exchange between the magnetic films and we write:

$$\varepsilon_{\text{ex}} = -J \boldsymbol{M}_i \boldsymbol{M}_j, \tag{5.13}$$

which translates to an effective field for the magnetization $\boldsymbol{M}_i$ of:

$$\mu_0 \boldsymbol{H}_{\text{ex},i} = -\nabla_{M_i} (-J \boldsymbol{M}_i \boldsymbol{M}_j) = J \boldsymbol{M}_j. \tag{5.14}$$

The torque becomes now:

$$\tau_{\text{ex},i} = -\gamma_i \boldsymbol{M}_i \times \mu_0 \boldsymbol{H}_{\text{ex},i} = -\gamma_i J \boldsymbol{M}_i \times \boldsymbol{M}_j \tag{5.15}$$

and we find that the magnetization in layer i starts to precess around the magnetization direction of the layer j. The exchange torque thus has the same symmetry as a field-like torque, which is a first hint that the signature of both torques in the

FMR spectrum will look similar. If we linearize the above exchange torque and normalize to the magnetic film thickness and saturation magnetization, we find:

$$\tau_{\mathrm{ex},i} = \frac{\gamma J}{d_i M_{\mathrm{s},i}} \hat{\boldsymbol{y}} \times \left(\boldsymbol{M}_i - \boldsymbol{M}_j \right). \tag{5.16}$$

In the linearized version of the torque we find that the torque is proportional to the difference of the magnetization orientation.

To obtain the full modified macrospin LLG for the coupled system, we now have to introduce the torques from Eq. (5.12) and Eq. (5.16) to the LLG Eq. (5.8):

$$\begin{aligned} \dot{\boldsymbol{M}}_i = &-\gamma_i \hat{\boldsymbol{y}} \times \Bigg(-\mu_0 \left(H + H_{\mathrm{ex,i}} \right) \boldsymbol{M}_i + \mu_0 \boldsymbol{H}_{\mathrm{dyn}} - \mu_0 M_{\mathrm{s,i}} M_{i,z} \hat{\boldsymbol{z}} \\ &- \frac{\alpha_i}{\gamma_i} \dot{\boldsymbol{M}}_i - \frac{J}{M_{\mathrm{s},i} d_i} \left(\boldsymbol{M}_i - \boldsymbol{M}_j \right) \Bigg) \\ &- \frac{\gamma_i}{M_{\mathrm{s},i} d_i} \left(\tau_{\mathrm{F}} - \tau_{\mathrm{D}} \hat{\boldsymbol{y}} \times \right) \left(\dot{\boldsymbol{M}}_i - \dot{\boldsymbol{M}}_j \right). \end{aligned} \tag{5.17}$$

The solution of Eq. (5.17) yields the resonance field (frequency) and the resonance linewidth of each magnetic layer for fixed frequency (field). When all torques vanish ($\tau_{\mathrm{D}} = \tau_{\mathrm{F}} = J = 0$), we obtain the classical picture of two independently precessing macrospins around the direction of their effective fields [29]. For non-vanishing torques, however, the dispersions of the magnetic layers couple. In the following chapter we will discuss the influence of the different torques on the coupling.

5.3.2 Solution of the Macrospin Model

We now solve a set of two LLGs Eq. (5.17) for the Co and the YIG layer using the ansatz:

$$\boldsymbol{M}_i = \hat{\boldsymbol{y}} + (m_{i,x}, 0, m_{i,z}) \exp\left(-i\omega t\right), \tag{5.18}$$

for every magnetic layer. As shown in Chap. 2.1.2.2, we can easily sort the components in Eq. (5.17) according to the dynamic magnetization components. We then obtain a simple matrix expression of the coupled system:

$$\tilde{\boldsymbol{\chi}}^{-1} \cdot \boldsymbol{m} = \boldsymbol{H}_{\mathrm{dyn}}, \tag{5.19}$$

where $\tilde{\boldsymbol{\chi}}^{-1}$ is the inverse susceptibility tensor of the coupled system, $\boldsymbol{m} = (m_{1,x}, m_{1,z}, m_{2,x}, m_{2,z})$ and $\boldsymbol{H}_{\mathrm{dyn}} = (h_x, h_z, h_x, h_z)$. We can identify the different contributions of the torques to the coupled system. When we neglect the exchange

field of the Co layer $H_{\mathrm{ex},1} = 0$, and set $\tau_{\mathrm{F}} = \tau_{\mathrm{D}} = J = 0$, we find the inverse susceptibilities of the uncoupled layers:

$$\tilde{\chi}^{-1}\Big|_{\tau_{\mathrm{F}}=\tau_{\mathrm{D}}=J=0} = \begin{pmatrix} \tilde{\chi}_1^{-1} & 0 \\ 0 & \tilde{\chi}_2^{-1} \end{pmatrix}, \tag{5.20}$$

with

$$\tilde{\chi}_1^{-1} = \begin{pmatrix} -\gamma_1\mu_0(H + M_{\mathrm{s},1}) + i\alpha_1\omega & -i\omega \\ i\omega & -H\gamma_1\mu_0 + i\alpha_1\omega \end{pmatrix} \tag{5.21}$$

and

$$\tilde{\chi}_2^{-1} = \begin{pmatrix} -\gamma_2\mu_0(H + H_{\mathrm{ex},2} + M_{\mathrm{s},2}) + i\alpha_2\omega & -i\omega \\ i\omega & -\gamma_2\mu_0(H + H_{\mathrm{ex},2}) + i\alpha_2\omega \end{pmatrix}. \tag{5.22}$$

To extract the inverse susceptibility entries due to the mutual spin pumping, we have to set all terms to zero, which are not connected to either τ_{F} or τ_{D}. We the obtain:

$$\tilde{\chi}^{-1}\Big|_{H_{\mathrm{eff},i}=\alpha_i=J=0} = \begin{pmatrix} \frac{i\gamma_1\tau_{\mathrm{D}}\omega}{d_1 M_{\mathrm{s},1}} & -\frac{i\gamma_1\tau_{\mathrm{F}}\omega}{d_1 M_{\mathrm{s},1}} & -\frac{i\gamma_1\tau_{\mathrm{D}}\omega}{d_1 M_{\mathrm{s},1}} & \frac{i\gamma_1\tau_{\mathrm{F}}\omega}{d_1 M_{\mathrm{s},1}} \\ \frac{i\gamma_1\tau_{\mathrm{F}}\omega}{d_1 M_{\mathrm{s},1}} & \frac{i\gamma_1\tau_{\mathrm{D}}\omega}{d_1 M_{\mathrm{s},1}} & -\frac{i\gamma_1\tau_{\mathrm{F}}\omega}{d_1 M_{\mathrm{s},1}} & -\frac{i\gamma_1\tau_{\mathrm{D}}\omega}{d_1 M_{\mathrm{s},1}} \\ -\frac{i\gamma_2\tau_{\mathrm{D}}\omega}{d_2 M_{\mathrm{s},2}} & \frac{i\gamma_2\tau_{\mathrm{F}}\omega}{d_2 M_{\mathrm{s},2}} & \frac{i\gamma_2\tau_{\mathrm{D}}\omega}{d_2 M_{\mathrm{s},2}} & -\frac{i\gamma_2\tau_{\mathrm{F}}\omega}{d_2 M_{\mathrm{s},2}} \\ -\frac{i\gamma_2\tau_{\mathrm{F}}\omega}{d_2 M_{\mathrm{s},2}} & -\frac{i\gamma_2\tau_{\mathrm{D}}\omega}{d_2 M_{\mathrm{s},2}} & \frac{i\gamma_2\tau_{\mathrm{F}}\omega}{d_2 M_{\mathrm{s},2}} & \frac{i\gamma_2\tau_{\mathrm{D}}\omega}{d_2 M_{\mathrm{s},2}} \end{pmatrix}. \tag{5.23}$$

To extract the inverse susceptibility entries which stem from the direct exchange coupling, we have to set all terms to zero, which are not connected to J:

$$\tilde{\chi}^{-1}\Big|_{H_{\mathrm{eff},i}=\alpha_i=\tau_{\mathrm{F}}=\tau_{\mathrm{D}}=0} = \begin{pmatrix} -\frac{J\gamma_1}{d_1 M_{\mathrm{s},1}} & 0 & \frac{J\gamma_1}{d_1 M_{\mathrm{s},1}} & 0 \\ 0 & -\frac{J\gamma_1}{d_1 M_{\mathrm{s},1}} & 0 & \frac{J\gamma_1}{d_1 M_{\mathrm{s},1}} \\ \frac{J\gamma_2}{d_2 M_{\mathrm{s},2}} & 0 & -\frac{J\gamma_2}{d_2 M_{\mathrm{s},2}} & 0 \\ 0 & \frac{J\gamma_2}{d_2 M_{\mathrm{s},2}} & 0 & -\frac{J\gamma_2}{d_2 M_{\mathrm{s},2}} \end{pmatrix}. \tag{5.24}$$

The resonance fields H_{res}^* of the coupled system at a fixed excitation frequency ω are obtained for a vanishing determinant of $\tilde{\chi}^{-1}$:

$$0 = \det\tilde{\chi}^{-1}|_{H_0=H_{\mathrm{res}}^*}. \tag{5.25}$$

Note that H_{res}^* is complex, and $\mathrm{Re}\,[H_{\mathrm{res}}^*] \equiv H_{\mathrm{res}}$ contains the resonance fields and $\mathrm{Im}\,[H_{\mathrm{res}}^*] \equiv \Delta H$ contains the linewidth of the resonance.

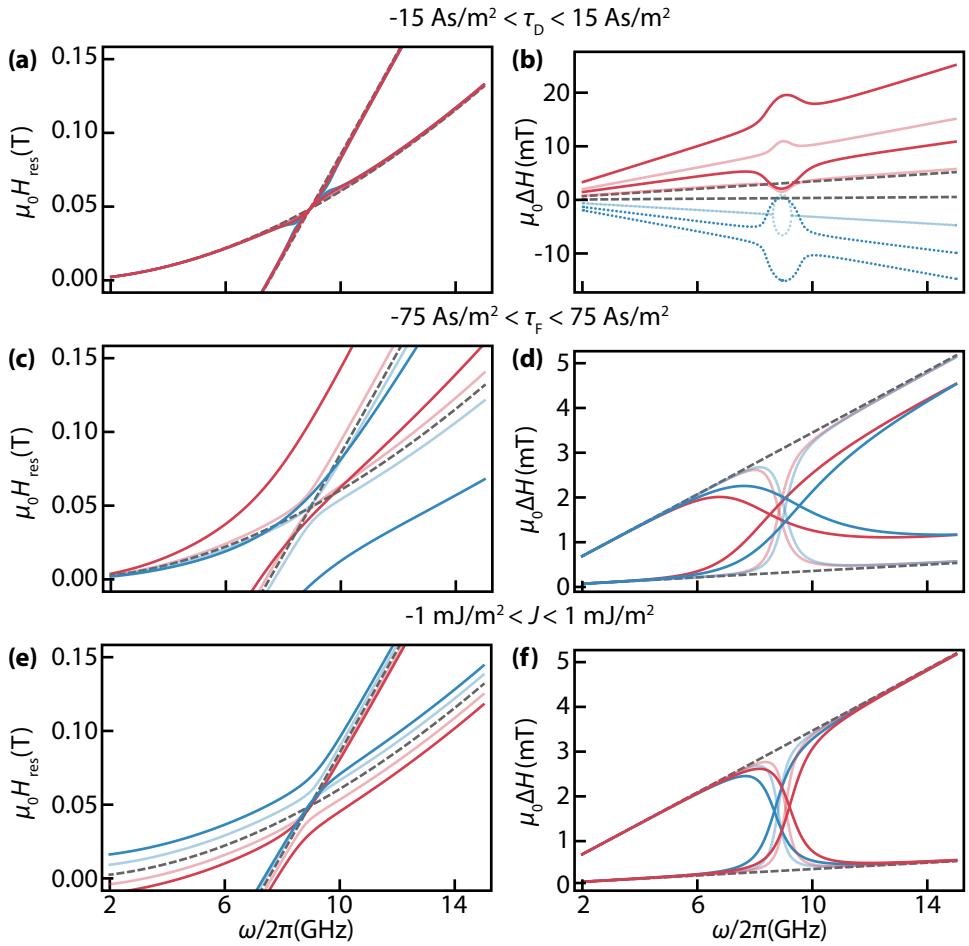

Fig. 5.6. – Influence of the torques on the coupled mode resonance fields and linewidths. (a, b) Dispersions and linewidths for a damping-like torque $-15\,\mathrm{As/m^2} < \tau_\mathrm{D} < 15\mathrm{As/m^2}$. (c, d) Dispersions and linewidths for a field-like torque $-75\,\mathrm{As/m^2} < \tau_\mathrm{F} < 75\,\mathrm{As/m^2}$. (e, f) Dispersions and linewidths for a exchange torque $-1\,\mathrm{mJ/m^2} < \tau_\mathrm{F} < 1\,\mathrm{mJ/m^2}$. The gray dashed lines show the uncoupled cases. The opacity shows the strength of the torques. The low frequency solution of $\det \tilde{\chi}^{-1} = 0$ for a fixed field of Eq. (5.25) is plotted in red, whereas the high frequency solution is plotted in blue.

5.3.3 Influence of the Spin Torques on the Mode Dispersions

To discuss the properties of the coupled system, we plot the dispersions $H_\mathrm{res}(\omega)$ and the linewidths $\Delta H(\omega)$ for $\alpha_1 = 1 \times 10^{-2}$, $\alpha_2 = 1 \times 10^{-3}$, $\mu_0 M_{\mathrm{s},1} = 1.9\,\mathrm{T}$, $\mu_0 M_{\mathrm{s},2} = 0.18\,\mathrm{T}$, $\mu_0 H_\mathrm{ex} = 0.2\,\mathrm{T}$, which would refer to the 20th PSSW in the YIG, $\gamma_1/2\pi = 29\,\mathrm{GHz/T}$, $\gamma_2/2\pi = 28\,\mathrm{GHz/T}$ in Fig. 5.6.

In Fig. 5.6 (a), the calculated resonance field is plotted as a function of the excitation frequency. The influence of τ_D on the dispersions of the coupled system is shown, where the strength of the torque is encoded in the color and opacity of the curves. The opacity gives the absolute value of the torque, whereas we have blue curves for negative torques and red curves for positive torques. As the damping-like torques only have a weak effect on the dispersions for the plotted torque

strengths, all curves lie upon each other. The dashed lines show the uncoupled case. For small frequencies, the YIG and the Co dispersions are uncoupled. As both dispersions enter the coupling regime, the influence of the damping-like torque is rather small and the dispersions remain almost unchanged. However, for large damping-like torques we observe a locking of the mode dispersions. Note that such a frequency locking was observed in all-metallic trilayers [185].

In Fig. 5.6 (b), the influence of the damping-like torque τ_D on the calculated linewidth is shown as a function of the excitation frequency. The background slope is given by the Gilbert damping parameter α_i of each layer (dashed lines), which is modified by mutual spin-pumping when τ_D is changed. When both dispersions enter the coupling regime, the linewidth of the Co increases, while the linewidth of the YIG decreases. This effect becomes stronger with increasing damping-like torque strength in the system (increasingly opaque curves). When the strength of the damping-like torque roughly equals the Gilbert damping of the YIG, we observe a negative linewidth in the simulation. We understand this as a mechanism, which transfers more energy from the Co to the YIG as necessary to compensate the YIG damping, which would result in auto-oscillations in the macrospin model (dotted lines).

In Fig. 5.6 (c), the calculated resonance field is shown as a function of the excitation frequency for various field-like torques τ_F. For vanishing field-like torques, we do not see any effect on the dispersions. However, if τ_F increases the dispersions begin to split up and form an avoided crossing in the coupling region. This effect is known from coupled harmonic oscillators, when a coupled system exchanges energy with a coupling rate g_{eff}, which is the minimal size of the mode splitting, cf. Chap. 6. Figure 5.6 (d) displays again the linewidth as a function of the excitation frequency for various field-like torques. For a vanishing field-like torque, the linewidth remains unchanged, and we observe the pure Gilbert damping behavior for both subsystems (dashed lines). If a small field-like torque occurs, the Co linewidth exhibits a small dip and the YIG linewidth a small peak. For increasing torque strength, the linewidths of both subsystems become equal in the coupling regime. Both resonances have the same linewidth as they practically behave like one hybridized excitation. We furthermore observe a broadening of the transition regime for increasing field-like torques, as we achieve a stronger hybridization of the modes. Furthermore, we reduce the crossing frequency with increasing field-like torque strength.

In Fig. 5.6 (e), the calculated resonance field is shown as a function of the excitation frequency and direct torque strength J. For a vanishing direct coupling (dashed lines), the dispersions remain unchanged. However, for increasing direct coupling we find two effects on the dispersions. Firstly, an avoided crossing of the dispersions as known from the field-like torques, and secondly, a shift of the center of the avoided crossing to higher magnetic fields. Figure 5.6 (f) shows the linewidth evolution as a function of excitation frequency for various direct torque strengths.

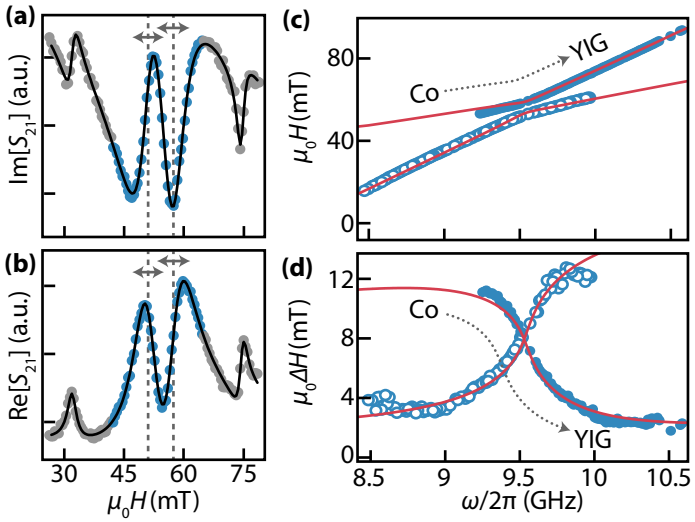

Fig. 5.7. – (a, b) Imaginary and real part of the S_{21} parameter, for a fixed frequency of 9.5 GHz from the YIG/Co(50) sample measurement (symbols). The solid curve is a fit using the sum of complex Lorentz resonances. The dashed lines and arrows indicate the resonance fields and linewidths, which are used in (c, d). The grey data points refer to different avoided crossings. (c, d) Resonance fields and full-width at half-maximum linewidths versus frequency obtained from the YIG/Co(50) sample. The solid lines are fits of the model described by Eq. (5.17).

We obtain the same qualitative behavior as known from the field-like torques. However, the excitation frequency where the linewidths of both subsystems is equal does not change.

The similar look of the direct exchange torques and the field-like torques can be explained using the matrices from Eq. (5.23) and Eq. (5.24). A close look at these matrices reveals, that the entries of the direct exchange torques coincide with entries of the damping-like torques. However, all entries of the spin pumping spin torques contain a factor of i, which leads to a phase shift of $\pi/2$ between the driving field and the magnetization precession. In this case the response of the magnetization to a field-like torque is similar to the response of a direct exchange torque. Note furthermore that the influence of the field-like torques scales linearly with the frequency, whereas the influence of the direct torques is constant.

5.3.4 Fit of the Macrospin Model

Figure 5.7 (a, b) shows the real and imaginary part of $S_{21}(H)$ for the YIG/Co(50) sample for $\omega/2\pi = 9.5\,\mathrm{GHz}$ (closed symbols), together with the obtained fitting curves of the previously mentioned Lorentzian fits (black line), from which we take the resonance fields and linewidths (dashed lines and arrows).

In Fig. 5.7 (c) we plot the obtained resonance fields of the selected resonances of the YIG/Co(50) sample as a function of the frequency for the avoided crossing around 9.5 GHz. We clearly see an avoided crossing of the two dispersions. The Co

FMR mode transitions into a YIG PSSW mode with increasing frequency (closed symbols) and vice versa (open symbols). The dotted arrow also indicates this transformation. In Fig. 5.7 (d), the linewidth is plotted as a function of frequency for the same sample. The closed symbols start in the Co FMR mode with a large linewidth, but in the coupling regime, the linewidth decreases towards that of the YIG PSSW mode. Again, the open symbols follow the reversed behavior. The data from Fig. 5.7 (a, b) are fitted using our model Eq. (5.17). For the fits, we keep $\mu_0 M_{s,2} = 0.18\,\mathrm{T}$, $\gamma_2/2\pi = 27.07(1)\,\mathrm{GHz/T}$, $\gamma_1/2\pi = 28.7(1)\,\mathrm{GHz/T}$ and $\mu_0 M_{s,1} = 1.91(2)\,\mathrm{T}$ constant, cf. Chap. 5.2.3. τ_F, τ_D, J, k, $\alpha_{1,2}$ and H_{ex} are free parameters. We fit both the linewidth and the resonance fields simultaneously in a single model. The resulting fits are shown as solid lines Figs. 5.7 (c, d), and we find a very good agreement between our macrospin model and the experimental data. This demonstrates that the coupling can indeed be modeled as stemming from the combined effects of spin torque and exchange coupling. However, the resulting values for τ_F, τ_D and J are not accurate because the dynamic YIG magnetization is obviously non-uniform. To take the spin-wave character of the YIG excitations into account (and thus obtain accurate results), we now employ the full model discussed in Chap. A.1.

5.4 Simulation Results

5.4.1 Interfacial Spin Torque Model

In this section we want to sketch the full theory model, which includes a finite mode coupling between the YIG and the Co magnetizations at the YIG/Co interface at $z = 0$. The full theory was mainly developed in cooperation with V. Amin, M. D. Stiles, and R. McMichael from the NIST in Gaithersburg, USA, an can be found in its full beauty in Chap. A. We still model the Co magnetization $\boldsymbol{M}_1$ as a macrospin along the y-direction, as in the previous sections. However, the YIG magnetization $\boldsymbol{M}_2(z)$ now depends on the distance z from the YIG/Co interface. We furthermore only calculate the susceptibility of the Co layer to the spin torques, as this already contains all important features of the coupled system. Using this modification, the LLG Eq. (5.17) reads:

$$\begin{aligned}\dot{\boldsymbol{M}}_1 = &-\gamma_1 \hat{\boldsymbol{y}} \times \Bigg[-\mu_0 H \boldsymbol{M}_1 - \frac{\alpha_1}{\gamma_1}\dot{\boldsymbol{M}}_1 - \mu_0 M_{s,1} M_{1,z}\hat{\boldsymbol{z}} \\ &- \frac{J}{d_1 M_{s,1}}(\boldsymbol{M}_1 - \boldsymbol{M}_2(0)) - \mu_0 \boldsymbol{H}_{\mathrm{dyn}}\Bigg] \\ &- \frac{\gamma_1}{d_1 M_{s,1}}\left[(\tau_F - \tau_D \hat{\boldsymbol{y}}\times)(\dot{\boldsymbol{M}}_1 - \dot{\boldsymbol{M}}_2(0))\right].\end{aligned} \tag{5.26}$$

In our model, $\boldsymbol{H}_{\mathrm{dyn}}$ is assumed to be spatially uniform, to reflect the experimental situation where the CPW center conductor width is much larger than either the

YIG or Co thickness, cf. Chap. 2.4.1. The YIG magnetization direction at the YIG/Co interface is given by $\boldsymbol{M}_2(0)$. The YIG magnetization obeys two boundary conditions [203–205]. First, the total torque on the YIG/Co interface at $z = 0$ has to vanish, as the interface has zero volume and hence carries no spin angular momentum:

$$\begin{aligned} 0 =& 2A\hat{\boldsymbol{y}} \times \partial_z \boldsymbol{M}_2(z)|_{z=0} - J\hat{\boldsymbol{y}} \times (\boldsymbol{M}_1 - \boldsymbol{M}_2(0)) \\ &+ (\tau_F - \tau_D \hat{\boldsymbol{y}}\times) \left(\dot{\boldsymbol{M}}_1 - \dot{\boldsymbol{M}}_2(0)\right). \end{aligned} \tag{5.27}$$

Here, A is the exchange constant of YIG. Second, we assume an uncoupled boundary condition at the YIG/substrate interface:

$$0 = 2A\hat{\boldsymbol{y}} \times \partial_z \boldsymbol{M}_2(z)|_{z=d_2}, \tag{5.28}$$

where the torque vanishes as well. The Co susceptibility $\tilde{\boldsymbol{\chi}}_1$ is then derived using the ansatz for the transverse YIG magnetization: $\boldsymbol{m}_2(z,t) = (m_{2,x}(z,t), m_{2,z}(z,t))$:

$$\begin{aligned} \boldsymbol{m}_2(z,t) = \mathrm{Re}\big[& c_+ \boldsymbol{m}_{2+} \cos(k_+ z) \exp(-i\omega t) + \\ & c_- \boldsymbol{m}_{2-} \cos(k_- z) \exp(-i\omega t)\big]. \end{aligned} \tag{5.29}$$

Here, $\boldsymbol{m}_{2\pm}$ are the complex eigenvectors of the uncoupled transverse YIG magnetization, discussed in detail in Chap. A.2.1, $c_\pm$ are complex but yet unknown coefficients, $k_\pm$ are complex wavevectors of the undisturbed YIG films. We find that Eq. (5.29) is a superposition of a propagating wave with a wavevector k_+ and an evanescent wave with an imaginary wavevector k_-. For the latter wave it is clear, that the influence is dominant at the YIG/Co interface at $d = 0$, where the magnetization is coupled. In this way we have introduced an interfacial coupling to our system.

The transverse Co magnetization follows a simple elliptical precession:

$$\boldsymbol{m}_1 = \mathrm{Re}\left[\boldsymbol{m}_{1,0} \exp(-i\omega t)\right] \tag{5.30}$$

where $\boldsymbol{m}_1 = (m_{1,x}, m_{1,z})$, and $\boldsymbol{m}_{1,0} \approx (m_{1,0,x}, m_{1,0,z})$ is a complex precession amplitude. In Chap. A we use the transverse YIG and Co magnetizations in the boundary conditions to find the complex coefficients $c_\pm$. Afterwards these coefficients can be used in the YIG magnetization Eq. (5.29) to determine $\boldsymbol{M}_2(0)$, as shown in Chap. A.2.2. The Co susceptibility $\tilde{\boldsymbol{\chi}}_1$ can be obtained from LLG Eq. (5.26) and is given by Eq. (A.44).

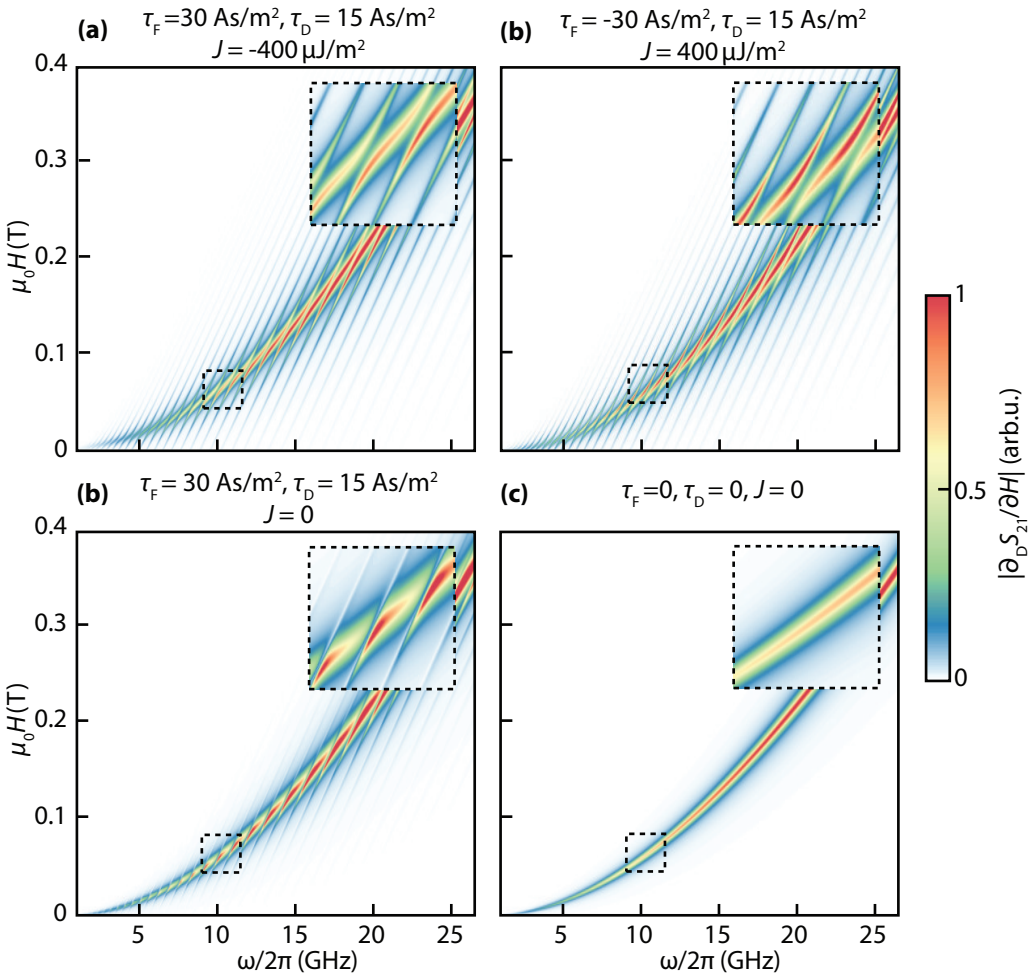

Fig. 5.8. – Calculated $|\partial_D S_{21}/\partial H|$ of the simulated transmission spectra. (a) Simulation of the YIG/Co(50) sample. (b) Simulation of the YIG/Co(35) sample. (c) Simulation of the YIG/Cu(5)/Co(50) sample. (d) Simulation of the YIG/AlOx(1.5)/Co(50) sample.

5.4.2 Comparison to the Experimental Data

Figure 5.8 shows the simulated microwave signal, where we use the full Co susceptibility (Eq. A.44) in the derivative divide formalism $|\partial_D S_{21}/\partial H|$ given in Eq. (5.4). In other words the simulations only show the Co FMR signal including all modifications due to the YIG mode coupling. For all simulations we take the same material parameters, namely $d_1 = 50\,\text{nm}$, $\mu_0 M_{s,1} = 1.91\,\text{T}$, $\alpha_1 = 0.0077$, $\gamma_1 = 28.7\,\text{GHz/T}$ and $d_2 = 1\,\mu\text{m}$, $\mu_0 M_{s,2} = 0.18\,\text{T}$, $A_{ex} = 3.76\,\text{pJ/m}$, $\alpha_2 = 0.00072$, $\gamma_2 = 27.07\,\text{GHz/T}$, as extracted in Chap. 5.2.3, and Chap. 5.2.4. In Fig. 5.8 (a) we show the simulations for the YIG/Co(50) sample using $\tau_F = 30\,\text{As/m}^2$, $\tau_D = 15\,\text{As/m}^2$ and $J = -400\,\mu\text{J/m}^2$. The interfacial exchange constant $J < 0$ models an antiferromagnetic coupling as suggested by the SQUID measurements. We also find that the exchange coupling fields, which can be calculated to be $J/M_{s,1}d_1 = -5.2\,\text{mT}$ and $J/M_{s,2}d_2 = -2.8\,\text{mT}$, fit very good to the external magnetic field, which is necessary to align the YIG and Co magnetizations parallel

($\mu_0 H = 4\,\mathrm{mT}$). The sign of the damping-like torque is required to be positive, as it depends on the real part of the spin mixing conductance of the interface. The simulation reproduces all salient features observed in the experiment, in particular the appearance of the YIG PSSWs and their avoided crossing with the Co FMR line. Note that the simulations do not reproduce the YIG FMR line, as we only simulate the Co susceptibility.

Figure 5.8 (b) shows the simulation for the YIG/Co(35) heterostructure using a negative field-like torque and a ferromagnetic coupling, in contrast to Fig. 5.8 (a), but we obtain a similar color map. However, the intensity asymmetry of the avoided crossings is only reproduced by the aforementioned parameters. The combination of exchange torques with the field-like torques at the $\mathrm{FM_1}|\mathrm{FM_2}$ interface complicates the analysis of the total coupling because both torques affect the coupling in very similar ways. Hence, the signs of the field-like torque and the exchange torque cannot be determined unambiguously for the YIG/Co samples without an interlayer. For more details, see Chap. 5.4.3.

In Fig. 5.8 (c) we show the simulations for the YIG/Cu(5)/Co(50) sample. Here, τ_F and τ_d are unchanged compared to the values used for the YIG/Co(50) sample from Fig. 5.8 (a), but we set $J = 0$, as no exchange coupling was observed in the YIG/Cu(5)/Co(50) sample in the SQUID measurements. The simulation is in excellent agreement with the corresponding measurement shown in Fig. 5.2 (c). The elimination of the static exchange coupling results in a strong reduction of the coupling between the YIG and Co magnetization dynamics. However, the Cu layer is transparent to spin currents mediating the field-like and damping-like torques, as the spin-diffusion length of Cu is much larger than its thickness [206]. We emphasize that a finite field-like torque is necessary to observe the excitation of the PSSWs for vanishing exchange coupling J. Furthermore, the field-like torque is required to be positive to model the intensity asymmetry in the mode branches of the YIG/Cu(5)/Co(50) sample. This becomes evident when comparing Fig. 5.8 (c) with Fig. 5.9 (c).

In Fig. 5.8 (d) we use $\tau_\mathrm{F} = \tau_\mathrm{D} = J = 0$, which reproduces the experimental observation for the YIG/AlOx/Co(50) sample. Importantly, we do not observe any YIG PSSWs in either the experiment or the simulation for this case. In summary, the simulations are in excellent qualitative agreement with the experimental observation of spin dynamics in the coupled YIG/Co heterostructures.

We attribute small quantitative discrepancies between the simulation and the experiment to the fact that we do not take any inhomogeneous linewidth and two-magnon scattering into account. However, the Co linewidth analysis (see 5.2.4) clearly reveals the presence of inhomogeneous broadening and possible contributions from two-magnon scattering to the experimentally observed linewidth. This results in an underestimated linewidth of the Co FMR line, in particular for small frequencies. As $|\partial_\mathrm{D} S_{21}/\partial H|$ is inversely proportional to the linewidths, this results in small quantitative deviations of the simulations and the experimental data.

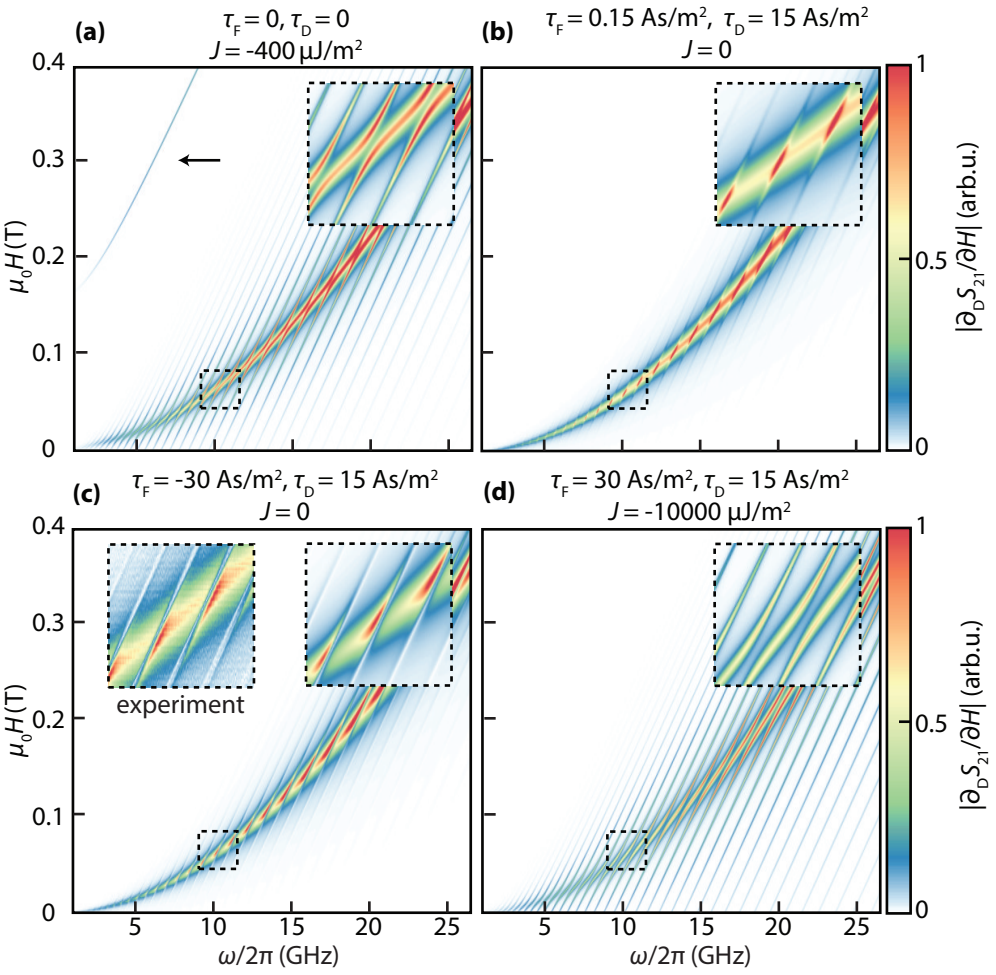

Fig. 5.9. – (a) An exchange coupling can reproduce the exchange mode in the experiment. (b) A dominant damping-like torque results in a mode locking of the YIG and Co resonances. (c) The sing of the field-like torques determines the asymmetry of the color code. We require a positive field-like torque to simulate the YIG/Cu(5)/Co(50) experiments, cf. 5.8 (b). (d) A dominant antiferromagnetic exchange torque produces symmetric avoided crossings.

Furthermore, the exchange modes in Fig. 5.2 (a) are not found in the simulations. We attribute this to the fact that the simulations only represent the Co susceptibility. However, as shown in Fig. 5.9, similar exchange modes can also be found in the Co susceptibility from our simulations.

5.4.3 Simulation of the Exchange Mode

In this section we give some more examples to demonstrate the different effects of the torques on the transmission spectra. Figure 5.9 (a) shows the color map for a pure antiferromagnetic exchange coupling between the YIG and Co layers. We find an exchange mode at higher frequencies than the Co resonance and symmetric avoided crossings.

In Fig. 5.9 (b) we show the color map for a field-like torque which is substantially smaller than the damping-like torque. We observe a dominant mode locking of the YIG and Co resonances. In metallic systems [185] we expect that the torques are primarily damping-like, as the real part of the spin mixing conductance exceeds the imaginary part. However, for insulating interfaces the amplitudes of the toques is less clear. Here, we cannot reproduce our experiments with a dominant damping-like torque.

In Fig. 5.9 (c) we plot the color map for $\tau_F = -30\,\mathrm{As/m^2}$, $\tau_D = 15\,\mathrm{As/m^2}$ and $J = 0$. Note that this configuration refers to the situation of the YIG/Cu(5)/Co(50) sample from Fig. 5.2 (b, e) with an inverted field-like toque. We find that the intensity symmetry of the avoided crossings is now also inverted compared to the experimental data (inset). Therefore, we know the sign of the field-like torque is positive for the YIG/Cu(5)/Co(50) samples.

In Fig. 5.9 (d) we show the color map for the YIG/Co(50) sample for a positive field-like torque and a strong antiferromagnetic coupling. The avoided crossings are symmetric, as the influence of the field-like torque is much smaller than the exchange torque. When we compare Fig. 5.8 (a, b), and Fig. 5.9 (d), we find that all used parameter combinations produce avoided crossings, with slightly different intensity modifications in the dispersion branches of the coupled systems. Due to the similar effects of the exchange torques and field-like torques, it is challenging to determine the signs of these torques for the YIG/Co samples without an interlayer.

However, taking the interlayer data into account, we can draw the following conclusions: (i) To model the avoided crossings, the field-like torques have to exceed the damping-like torques in both the YIG/Co(50) and the YIG/Cu(5)/Co(50) samples, which is in contrast to the observations in metallic systems metallic systems [185]. (ii) To model the intensity asymmetry in the YIG/Cu(5)/Co(50) sample, the field-like torque needs to be positive. (iii) As the spin diffusion length of Cu is much larger than its thickness, we expect a similar influence of the field-like and damping-like torques in the YIG/Co(50) without any interlayer. (iv) The SQUID magnetometry measurements speak for an interlayer exchange coupling in the order of 4 mT which translates into $|J| \approx 400\,\mu\mathrm{J}$. Using this value in our numerical simulations allow to model the avoided crossings in the YIG/Co(50) sample. We thus have a consistent picture of our sample set with only three different parameters.

5.5 Conclusion

In conclusion, we investigate the dynamic magnetization coupling in YIG/Co heterostructures using broadband ferromagnetic resonance spectroscopy. We find exchange dominated PSSWs in the YIG, excited by spin currents from the Co layer, and static interfacial exchange coupling of YIG and Co magnetizations. An efficient excitation of YIG PSSWs, even with a homogeneous external magnetic driving field, occurs in YIG/Co(35), YIG/Co(50) and YIG/Cu(5)/Co(50) samples, but is suppressed completely in YIG/AlOx(1.5)/Co(50) samples. We model our observations with a modified Landau-Lifshitz-Gilbert equation, which takes field-like and damping-like torques as well as direct exchange coupling into account.

Our findings pave the way for magnonic devices which operate in the exchange spin-wave regime. This allows utilizing the isotropic spin-wave dispersion relations in 2D magnonic structures. An excitation of short-wavelength spin waves by an interfacial spin torque does not require any micro structuring of excitation antennas but is in operation in simple magnetic bilayers. The coupling shown in this chapter might even be enhanced using spin conductance matching [207], through a careful variation of the Cu and Co resistivities. Remarkably, this spin torque scheme allows for the coupling of spin dynamics in a ferrimagnetic insulator to that in a ferromagnetic metal, although the magnetization is carried by itinerant electrons in the insulator and by conduction electrons in the ferromagnetic metal. The coupling is qualitatively different to that found for all-metallic heterostructures [185], where only damping-like torques have been observed.

Furthermore, the excitation of magnetization dynamics by interfacial torques should allow for efficient manipulation of microscopic magnetic textures, such as magnetic Skyrmions. Our findings are also relevant for studying macroscopic quantum phenomena (such as Bose-Einstein condensates [208] and magnon supercurrents [209]) in YIG, where we can use the spin torques to realize a coupling to an adjacent ferromagnet.

6 Optical Investigation of Magnon-Photon Coupling

The interaction between light and magnetic matter is of long-standing and fundamental interest. In recent years, the coupling of elementary excitations of the light field (photons) to those of the spin system (magnons) regained is intensively studied due to potential applications in quantum information processing [210–212]. For example, hybrid quantum systems are discussed as potential candidates for the up- and down-conversion of quantum signals from the optical to the microwave domain and vice versa. One possible hybrid quantum system consists of spin ensembles coupled to microwave resonators [102, 213–216]. The prerequisite for information transfer on the quantum level is to realize a large coupling strength exceeding the loss rates of the resonators [213, 216, 217], *viz.* here, the microwave resonator and the spin ensemble. However, the single spin coupling rate is only in the order of 0.1 Hz to 10 Hz [102, 213] which makes it hard to overcome the resonator loss rates which are in the order of 1 MHz. In ferromagnets the coupling rate is proportional to the square root of the number of participating spins [213,218], hence, ferromagnets with a high spin density are ideal for the creation of strongly coupled, hybridized magnon-photon modes [218, 219].

Magnon-photon coupling has been investigated in several experiments where a microwave cavity was loaded with yttrium iron garnet (YIG) and the microwave transmission and/or reflection was measured as a function of the applied magnetic field [213–216]. Furthermore, spin pumping in combination with the dc inverse spin Hall effect has been employed as a detection scheme for sensing the magnonic part of magnon-photon polaritons in magnetic thin film heterostructures [102, 215]. which is effectively a down-conversion of the coupling to dc. Recently, Hisatomi *et al.* detected the GHz-frequency Faraday rotation of light polarization in a hybrid system consisting of a YIG sphere and a 3D cavity [220]. Osada *et al.* investigated the coupling of optical whispering gallery modes to the magnetic resonance mode of a YIG sphere [221].

Here, we report on the optical observation of strong coupling of microwave photons in a micro patterned split-ring resonator [222, 223] (SRR) and magnons in a 1 μm-thick LPE YIG film. We simultaneously use Brillouin light scattering (BLS) spectroscopy and microwave absorption (MA) measurements to probe both magnonic and photonic excitations in the SRR/YIG film system. We find a clear avoided mode crossing indicating a hybridization of the magnon and microwave photon modes in the strong coupling regime with a coupling strength of $g_{\mathrm{eff}}/2\pi = 63$ MHz. Our findings represent an up-conversion of the hybridized mode frequencies to optical frequencies by inelastic optical photon-magnon scatter-

ing. The combined BLS and MA data allows us to study the continuous transition of the hybridized modes from a purely magnonic to a purely photonic mode by varying the applied magnetic field and microwave frequency. Furthermore, light-polarization dependent measurements give insight into the nature of inelastic scattering of optical-frequency photons by the hybridized microwave frequency photon-magnon mode.

Some of the figures and parts of the text in this chapter have been published in S. Klingler, H. Maier-Flaig, R. Gross, C.M. Hu, H. Huebl, S.T.B. Goennenwein, M. Weiler, *Combined Brillouin light scattering and microwave absorption study of magnon-photon coupling in a split-ring resonator/YIG film system*, Applied Physics Letters **109**, 072402 (2016).

6.1 Magnon-Photon Coupling

The narrow resonances of a resonator system can be used for short-term storage of information. Hereby the maximum storage time is inversely proportional to the linewidth of the resonance, see Eq. (2.57). By exciting an eigenmode (eigen-resonance) of a resonator A we can thus store information in the resonance. If resonator A is coupled to a resonator B, this information can be transferred into resonator B, and vice versa. A prototypical example for this type of effect are two classical pendulums which are coupled by a spring. When we excite the first pendulum (resonator A) it starts to oscillate, but the spring transfers its energy to the second pendulum (resonator B), until the first stops moving and the second pendulum oscillates. Afterwards, the energy transfer goes into the opposite direction. The rate of energy transfer from one pendulum to the other is given by the coupling rate g_{eff}, which is inversely proportional to the time the energy transfer needs to take place.

However, all real resonators have a certain decay rate, which is due to energy dissipation processes. To observe the coupling effect mentioned above, the energy transfer between the resonators has to be faster than the energy dissipation of each resonator. If the coupling rate exceeds the decay rates of both resonators we are in the regime of strong coupling, where the resonators are not independent anymore. We can thus exchange information between both resonators before loosing it due to dissipation and dephasing.

The coupling of the resonators is accompanied by a specific change of the resonator dispersions, known as avoided crossing, where we find an hybridization of the modes when the eigenfrequencies coincide. Note that we have already seen a magnetostatic mode (MSM) hybridization in Fig. 4.5. Furthermore, the mode hybridization between two different magnonic resonators is discussed extensively in Chap. 5. In contrast, we will here discuss the coupling of a photonic and a magnonic system (a photonic and a magnonic resonator), instead of two magnonic systems.

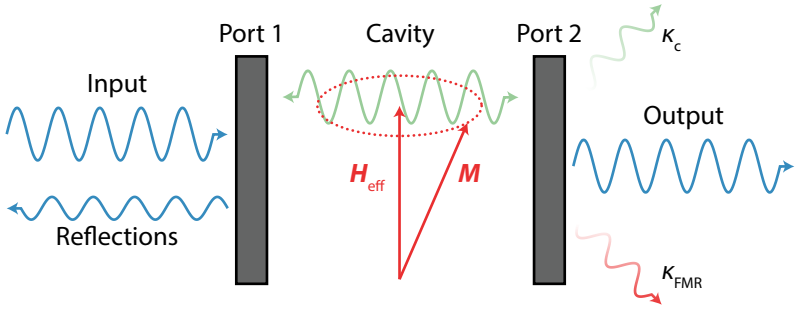

Fig. 6.1. – Sketch of the input-output model. We feed microwaves through port 1 to the cavity (blue), where we excite the cavity mode (green), which is accompanied with the cavity losses κ_c. The cavity mode couples to the FMR mode (red), which is accompanied with the FMR losses κ_{FMR}. The recorded output microwave signal through port 2 contains information about all coupling and loss processes.

To this end, we use a split-ring resonator (SRR) which is loaded with a magnetic YIG sample. The SRR is a two-dimensional LRC-circuit, as shown below and its resonance frequency is independent of the applied magnetic field. However, the magnetic FMR frequency of the YIG sample depends on the applied magnetic field. Hence, we can tune the magnetic subsystem to be in resonance with the SRR by tuning the field. At the crossing of dispersions, the subsystems hybridize and the coupled system exchanges energy between a pure photon and a pure magnon like excitation.

In quantum mechanics, the physics of a coupled resonator system can be described by the so-called Tavis-Cummings-Hamiltonian [225, 226]:

$$\mathcal{H}_{TC} = \hbar\omega_c b^\dagger b + \hbar\omega_s a^\dagger a + \hbar g_{eff}\left(a^\dagger b + a b^\dagger\right), \tag{6.1}$$

where $b^\dagger$ and b are creation and annihilation operators of the resonator excitation with a resonance frequency ω_c. The operators $a^\dagger$ and a describe the creation and annihilation of spin excitations in the spin system, i.e., our magnetic film. The interaction between the resonator system and the spin system is given by the terms in the brackets: When a spin excitation is created, a resonator excitation is annihilated, and vice versa. The prefactor $g_{eff} = \sqrt{\sum_i^N g_i} = \sqrt{N g_0}$ is the total coupling strength to which all coupled spins contribute, where we assume an identical coupling strength of all spins: $g_i = g_0$. From the Tavis-Cummings-Hamiltonian we can find the energy spectrum $E = \hbar\omega_\pm$ with [226]:

$$\omega_\pm = \frac{1}{2}\left(\omega_c + \omega_{FMR} \pm \sqrt{(\omega_c - \omega_{FMR})^2 + 4g_{eff}^2}\right). \tag{6.2}$$

The resonances $\omega_\pm$ are the eigenfrequencies of the coupled system. For a vanishing coupling strength $g_{eff} = 0$ the eigenfrequencies are those of the uncoupled resonators: $\omega_+ = \omega_c$ and $\omega_- = \omega_{FMR}$. In contrast to that, we find a mutual dependence of the eigenfrequencies for a non-vanishing coupling strength.

Using $\omega_c = \omega_{\mathrm{FMR}}$ in Eq. (6.2) the eigenfrequencies show a finite difference $\omega_+ - \omega_- = 2g_{\mathrm{eff}}$. This frequency splitting determines the time scale for energy transfer between the resonators and shows up as a so called avoided crossing of the resonator dispersions (see below). Note that the eigenspectrum is completely analogous to the resonance frequencies of two coupled harmonic oscillators [213,215,222]. From the Tavis-Cummings-Hamiltonian it is possible to calculate the transmission coefficients of a vector network analyzer measurement of the loaded SRR using the input-output-model, of which we show a sketch in Fig. 6.1. For this we use the Heisenberg picture to obtain the time evolution of the microwave and magnetic excitations [225, 227]. The transmission coefficient is given by [225, 227]:

$$S_{21} = \frac{\kappa_c}{i(\omega - \omega_c) - \kappa_c - ig_{\mathrm{eff}}^2(\omega - \omega_{\mathrm{FMR}} + i\kappa_{\mathrm{FMR}})^{-1}}, \tag{6.3}$$

whereas the number of magnetic excitations in the resonator is proportional to [227]:

$$N_{\mathrm{ex}} = a^\dagger a \propto \left| \frac{1}{(i(\omega - \omega_c) - \kappa_c)\,(i(\omega - \omega_{\mathrm{FMR}}) - \kappa_{\mathrm{FMR}}) + g_{\mathrm{eff}}^2} \right|^2. \tag{6.4}$$

It is also possible to calculate the transmission coefficient by modeling the resonator as a cavity consisting of two parallel mirrors using the Maxwell equations [228]. The input and the output ports of the cavity are then modeled using specific transmission and reflection coefficients, where we require specific electromagnetic boundary conditions in the resonator and the sample.

In Fig. 6.2 (a) we show the real part of the transmission coefficient S_{21} calculated from Eq. (6.3) as a function of the excitation frequency and the magnetic field. We furthermore use the dispersion of an in-plane magnetized film with $k = 0$ from Eq. (2.45) to model the behavior of the spin system. The plot parameters are $\mu_0 M_s = 0.18\,\mathrm{T}$, $\gamma/2\pi = 28\,\mathrm{GHz/T}$, $\kappa_c/2\pi = 25\,\mathrm{MHz}$, $\kappa_{\mathrm{FMR}}/2\pi = 4\,\mathrm{MHz}$, $\omega_c = 5\,\mathrm{GHz}$ and $g_{\mathrm{eff}}/2\pi = 100\,\mathrm{MHz}$. For small and large fields we find a strong absorption of microwave power at the resonator frequency ω_c, which is shown by the small microwave transmission (blue color). However, for a medium field strength of about $\mu_0 H = 0.11\,\mathrm{T}$ the resonance frequency of the YIG film is tuned to the resonator frequency ω_c and we find a strong perturbation of the field-independent resonator mode. In this case, the resonator mode hybridizes with the magnetic excitation in the magnetic film. Figure 6.2 (b) shows the normalized number of magnetic excitations in the magnetic film, calculated using Eq. (6.4). In contrast to Fig. 6.2 (a) we cannot find any magnetic excitations for a large detuning from the ferromagnetic resonance field and frequency. However, right at the center of the avoided crossings we see an increased number of magnetic excitations, which vanishes again for larger detuning. To explain this behavior we plot in Fig. 6.2 (c) the microwave absorption and in Fig. 6.2 (d) the number of magnetic

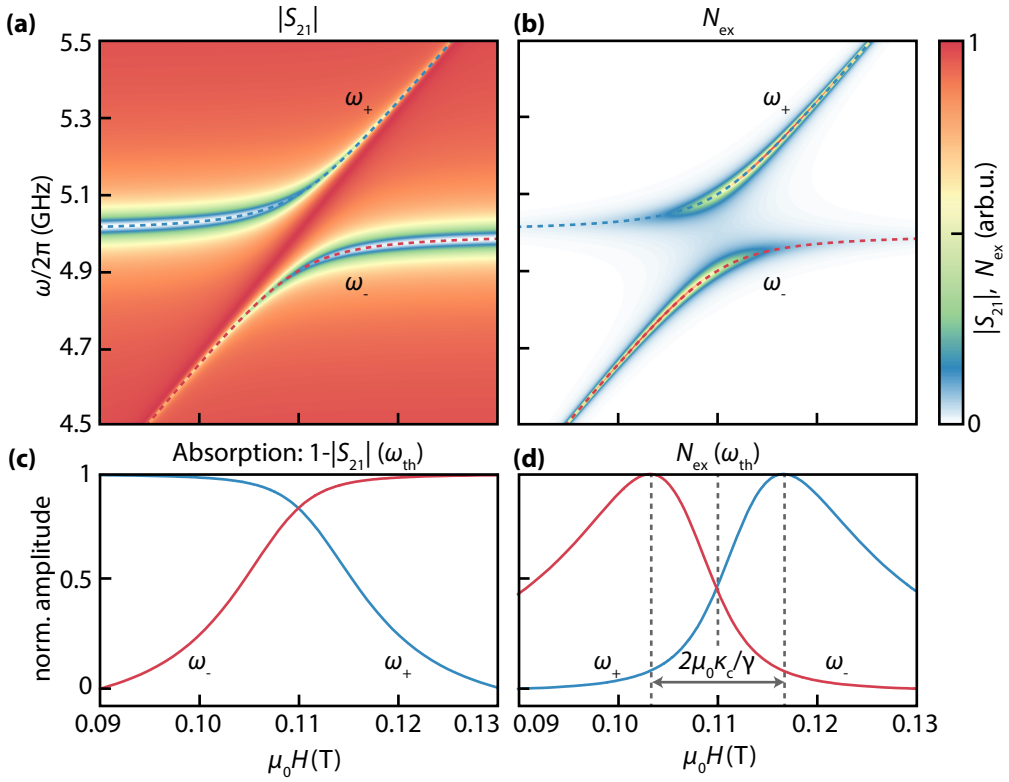

Fig. 6.2. – (a) The calculated microwave transmission S_{21} through a loaded cavity. The red color indicates a low absorption, whereas blue indicates a high absorption. (b) The spin excitation of a spin ensemble in a loaded cavity. The spin excitations N_{ex} are limited to the frequency range where the cavity resonance mode exists. The red color indicated a high spin excitation, whereas blue indicates a small spin excitation. (c) Microwave absorption in the cavity along $\omega_{\pm}$. (d) Spin excitations along $\omega_{\pm}$.

excitations as a function of the coupled resonance frequencies $\omega_{\pm}$. In the following, we only discuss the behavior along ω_{+}, but the discussion along ω_{-} is completely analogous. For small applied magnetic fields mainly the photonic mode of the cavity is excited which leads to a high absorption of microwave power at the resonator frequency, but a vanishing number of magnetic excitations. For increasing magnetic field, ω_{FMR} approaches ω_{c} and the photon and magnon modes become increasingly hybridized. This leads to a drop-off of the microwave absorption and an increasing number of magnetic excitations, as now the magnon modes can be populated and energy is transferred form the photon to the magnon mode. At about $\mu_0 H = \mu_0 H_{\mathrm{res,c}} = 0.11\,\mathrm{T}$ where $\omega_{\mathrm{c}} = \omega_{\mathrm{FMR}}$ the photonic and magnonic character have equal weight, and we find the same number of excitations in the ω_{+} and ω_{-} branches. Increasing the field further detunes the ferromagnetic resonance frequency from the cavity resonance, and the modes are not hybridized anymore. In the case of the transmission parameter we get a perfect transmission for a large detuning. However, in the picture of the magnetic excitations we find again a decrease. This decrease is connected to the linewidth of the resonator, as only

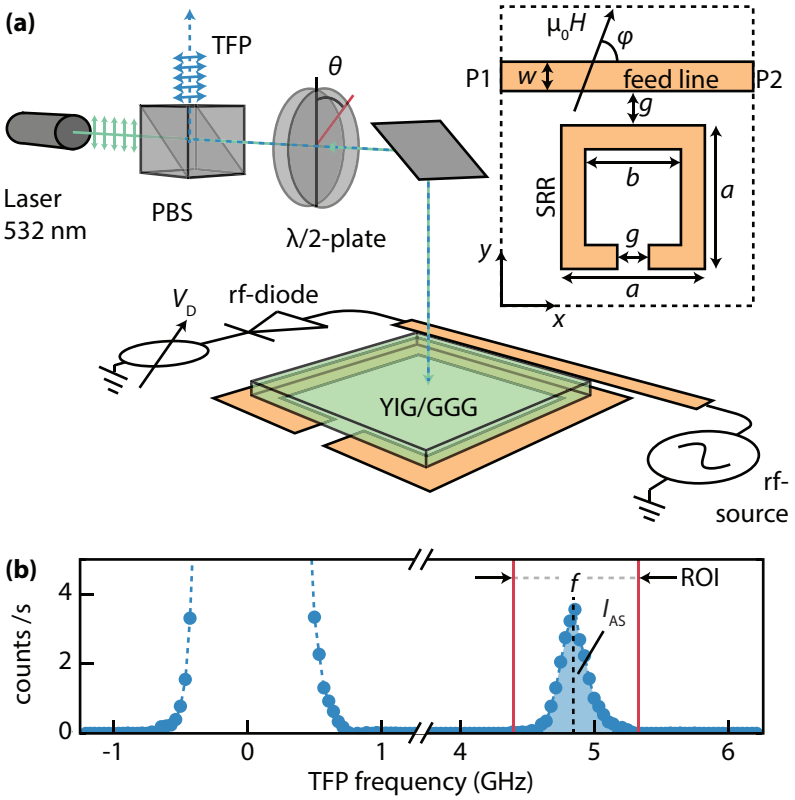

Fig. 6.3. – (a) Experimental setup: A microwave signal with frequency ω is applied to the feedline which is inductively coupled to the SRR. The YIG film is placed onto the SRR. The microwave transmission through the feedline is detected with a diode and a voltmeter as V_D. A polarized laser beam which passes a polarizing beam splitter (PBS) and a $\lambda/2$-plate and is focused on the surface of the YIG film by a microscope objective lens (not shown). The backscattered light passes again the $\lambda/2$-plate and the PBS, before it reaches the Tandem-Fabry-Pérot interferometer (TFP). The polarization of the backscattered light is determined by changing ϑ. Inset: Sketch of the SRR system. (b) Typical BLS spectrum (100 averages) as a function of the detuning from the laser line, with the reference laser peak at 0 GHz and the anti-Stokes signal at frequency ω.

in this range a excitation of the magnetization can occur. For a resonator with infinite linewidth (i.e. free space) we do not observe any drop off below and above $\mu_0(H_{\mathrm{res,c}} \pm 2\kappa_c/\gamma)$. In the next section we introduce our experimental setup which is able to probe both the shown microwave absorption and the magnetic excitations simultaneously.

6.2 Experimental Methods

A sketch of the experimental setup is shown in Fig. 6.3 (a). The setup consists of three parts: (i) the SRR/YIG film system where the coupled magnon-photon dynamics take place, (ii) the microwave absorption setup to investigate the photonic excitations, and (iii) the Brillouin light scattering (BLS) setup to analyze the magnonic excitations. In the following, we present the split-ring resonator in detail,

as well as the Brillouin light scattering setup. The discussion of the microwave absorption measurement is analogous to the theory presented in Chap. 2.4.3.

6.2.1 The Split-Ring Resonator System

A split-ring (SRR) resonator is a lithographically designed metallic ring with a slit in it. The SRR can be described as an *LRC*-circuit [222, 223] which can absorb energy from an external microwave field with a frequency close to its resonance frequency. In this case, a current flows in the SRR structure and strongly modifies its electromagnetic properties, such as the magnetic permeability [229], which can even be negative in the vicinity of the resonance.

The SRR system used in this chapter is fabricated by optical lithography on a 508 μm-thick Rogers RT/duroid 5870 substrate with a double-sided 35 μm copper coating. It consists of a 50 Ω impedance matched feedline with a width of $w = 1.4\,\mathrm{mm}$ inductively coupled to the SRR [222,223]. The square SRR has an outer edge length of $a = 6.5\,\mathrm{mm}$ while the inner edge length is $b = 3.5\,\mathrm{mm}$. The gap width and distance to the feedline are both $g = 0.2\,\mathrm{mm}$. The geometric properties lead to a resonance frequency of $\omega_c/2\pi = 4.96\,\mathrm{GHz}$. Note that the resonant wavelength of the SRR is in the order of 6 cm, whereas the spatial dimensions are in the order of 6 mm. The reason for this is the small gap which increases the capacity of the *LRC*-circuit and thus lowers the resonance frequency [223, 230]. This results in small microwave losses and high quality factors (lumped element approach) and make the SRR ideal candidates to investigate magnon-photon coupling. Here, we employ the rf microwave field in the SRR to excite the magnetization precession in the YIG film [222].

The YIG/Gadolinium Gallium Garnet (GGG) bilayer has a lateral size of $5\times5\,\mathrm{mm}$ and a YIG (GGG) thickness of 1 μm (500 μm). The YIG film is grown by liquid phase epitaxy on a (111)-oriented GGG substrate by a commercial supplier. We position the unmetallized YIG/GGG heterostructure with the GGG side down in the center of the SRR. In this way, the YIG film is optically accessible from above for the BLS measurements. An external magnetic field $40\,\mathrm{mT} \leq \mu_0 H \leq 200\,\mathrm{mT}$ is applied in the film plane at an angle $\varphi = 20^\circ$ relative to the feedline (y-axis). We chose this angle to comply with geometrical restrictions of the BLS setup.

The microwave absorption is recorded by connecting port 1 (P1) and port 2 (P2) of the feedline to a microwave source and a microwave diode, respectively. The SRR is excited with microwave radiation in the frequency range $4.8\,\mathrm{GHz} \leq \omega/2\pi \leq 5.2\,\mathrm{GHz}$ with a fixed microwave power of $P_{\mathrm{rf}} = 20\,\mathrm{dBm}$. The diode voltage:

$$V_{\mathrm{D}} \propto P_{\mathrm{rf}} - P_{\mathrm{abs}}, \tag{6.5}$$

is recorded with a voltmeter and used as a measure for the field- and frequency-dependent microwave power absorption P_{abs} in the device.

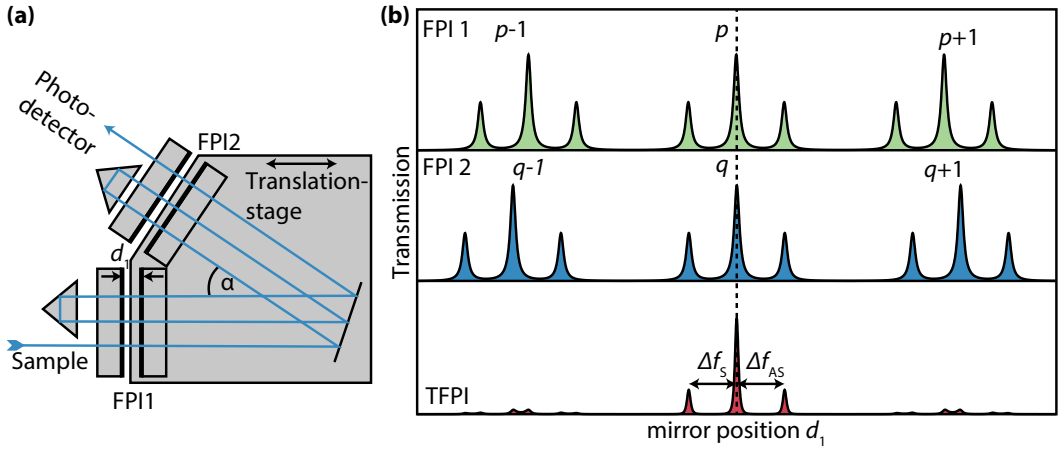

Fig. 6.4. – (a) Sketch of the six-path Tandem-Fabry-Pérot interferometer. (b) The upper curve shows the transmission around the transmission order p of the FP1. The panel in the middle shows the transmission around the transmission order q of the FP2. The bottom panel shows the combined transmission of the TFP. The higher transmission orders are strongly suppressed if the transmission orders p and q can pass through the TFP for the same mirror spacing d_1. Picture adapted from Ref. [3].

6.2.2 Brillouin Light Scattering Spectroscopy

The BLS optical setup employs a continuous wave single frequency laser with a wavelength of 532 nm. The laser beam passes a polarizing beam splitter (PBS) and a $\lambda/2$-plate before it is focused onto the surface of the YIG film using a microscope objective lens with a focal length of 4 mm (not shown in Fig. 6.3 (a)). The focused laser spot is positioned in the center of the SRR, where CST microwave studio [231] simulations of the unloaded SRR predict the most homogeneous microwave magnetic field. This is also confirmed by simulations of the SRR in Ref. [222]. The incident laser photons are inelastically scattered by the magnonic excitations in the SRR/YIG film system. Hereby, the frequency of the inelastically scattered light is shifted by $\pm\omega$ in anti-Stokes (AS) and Stokes processes, respectively, where ω is the magnon frequency. The polarization of the inelastically scattered light is rotated by the scattering event by an angle β with respect to the incident polarization direction [232]. In contrast, the elastically scattered light retains its incident energy and polarization [233, 234]. The scattered and collected light passes again the $\lambda/2$-plate before it reaches the PBS. The PBS is then used to selectively direct the inelastically scattered photons (which underwent a polarization rotation) to a Tandem-Fabry-Pérot interferometer (TFP). The scattering cross-section of the magnons, and thus the polarization of the scattered light, is strongly dependent on the incident light polarization [232, 235]. The $\lambda/2$-plate allows to simultaneously rotate the polarization of the incident and backscattered light by changing the angle ϑ of its fast optical axis relative to the polarization axis of the incoming light. In combination with the PBS, it is possible to analyze the polarization of the backscattered light with respect to the incoming light polarization.

A sketch of the TFP is shown in Fig. 6.4 (a). The incident light which is scattered elastically and inelastically from the sample passes through the first Fabry-Pérot interferometer (FP1) and is subsequently reflected to a second Fabry-Pérot interferometer (FP2) where it is reflected back. The light can only pass both FPs if the mirror distances are exactly the same. As the light needs to pass six times through the interferometer, the contrast and the finesse of the TFP is very high. A translation stage allows to change the mirror spacing of the FP1 and FP2 simultaneously with high accuracy, which allows to detect the absolute frequency shift of the scattered light. If the translation stage is moved by Δd_1, the mirror distance of FP1 is also changed by Δd_1. However, the mirror spacing of the FP2 is changed by $\Delta d_2 = \Delta d_1 \cos\alpha$, where α is the angle of the light beam shown in Fig. 6.4 (a). The different mirror spacings lead to a different free spectral range as shown in Fig. 6.4 (b). In blue we show the transmission spectra through FP1. At Δd_1 we find the transmission of the p-th transmission order, whereas we find in green the q-th transmission order of FP2. If now the mirror spacing is changed by moving the translation stage, the next higher transmission order of both FP do not overlap. Hence the transmission of the $q+1$-maximum of FP2 is blocked by FP1 and vice versa. However, for the p-th and q-th transmission order the transmission through both FP is possible and we get a net transmission signal through the TFP, shown in orange. This is also the case for the Brillouin sidebands as they only have a very small frequency offset from the central maximum. With this we can detect the absolute frequency shift of the sidebands, as they do not overlap with other transmission orders of the different interferometers. The frequency shift for the Stokes processes is denoted as $\Delta\omega_S$, whereas the frequency shift through the anti-Stokes processes is denoted as $\Delta\omega_{AS}$.

Figure 6.3 (b) shows a typical BLS spectrum of the YIG film as function of the detuning $\omega/2\pi$ from the laser line. At $\omega/2\pi = 0\,\text{GHz}$ the photons from the elastic scattering process are observed while at $\omega/2\pi = 4.9\,\text{GHz}$ photons inelastically scattered by magnons in an anti-Stokes process are detected. The total intensity of the anti-Stokes peak I_{AS} is proportional to the number of magnons present in the system [236, 237], given by Eq. (6.4) in the case of magnon-photon coupling. It is obtained by numerical integration of the counts in the region of interest ($\omega/2\pi \pm 100\,\text{MHz}$), see ROI in Fig. 6.3 (b). The frequency offset of the BLS spectra is corrected with respect to the microwave source.

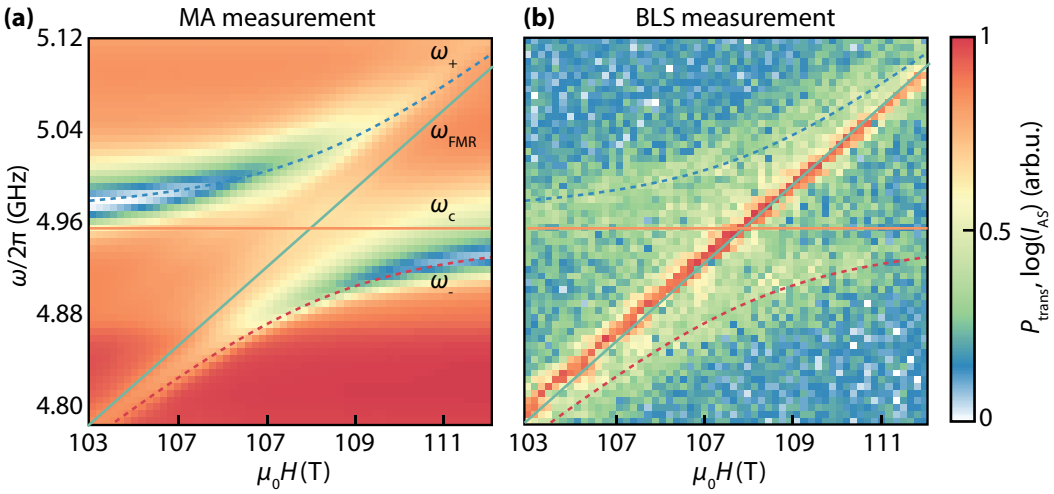

Fig. 6.5. – (a) Diode voltage as a measure for the microwave transmission versus applied magnetic field and microwave frequency. The avoided crossing is clearly visible. (b) BLS anti-Stokes intensity as a measure for the spin excitations as a function of field and microwave frequency. In addition to the avoided crossing, the uncoupled FMR mode of the YIG film is clearly visible. The dashed lines in (a) and (b) were obtained by simultaneously fitting the avoided crossing from (a) and the FMR mode from (b) to Eq. (6.2). The solid lines show the uncoupled modes.

6.3 Experimental Results

6.3.1 Magnon-Photon Up-Conversion

Firstly, the measurements without the $\lambda/2$-plate (corresponding to $\vartheta = 0°$) are discussed, hence the light polarization is not rotated before reaching the YIG film. The YIG thin film and the SRR couple electromagnetically with an effective coupling strength g_{eff}. If g_{eff} exceeds the intrinsic loss rates of the YIG and the SRR, an clear avoided crossing of the magnon and photon modes is expected [210, 211, 213]. To get information about both the photons in the SRR and the magnons in the YIG, we simultaneously record the microwave absorption and the BLS signal as function of the applied magnetic field and microwave frequency. In Fig. 6.5 (a) the microwave absorption from the diode voltage V_{D}, cf. Eq. (6.5), is plotted versus the applied magnetic field and microwave frequency. This measurement probes the purely photonic character of the coupled system. For $\mu_0 H \leq 103\,\text{mT}$ and $\mu_0 H \geq 112\,\text{mT}$, a single strong resonance at ω_{c} occurs. This is the pure microwave eigenmode of the loaded SRR. For magnetic fields around 108 mT, where the detuning between the photon and magnon modes is zero, the mode coupling results in two hybridized modes with frequencies ω_+ and ω_-. Since the effective coupling strength g_{eff} is larger than the relevant loss rates, the mode coupling is observed as a pronounced avoided crossing. It is evident from Fig. 6.5 (a) that the ω_+ and ω_- modes approach the purely photon and magnon modes for large detuning.

Figure 6.5 (b) shows the simultaneously recorded BLS anti-Stokes signal I_{AS}. This measurement probes the purely magnonic character of the coupled system. Here, three different modes are visible: (i) The most prominent mode appears at a frequency which depends almost linearly on the applied magnetic field. This mode is attributed to the detection of the ferromagnetic resonance at frequency ω_{FMR} excited directly by the feedline.[4] (ii) The two faint modes at ω_+ and ω_- resemble the hybridized modes of the magnon-photon system. Their field and frequency dependence is identical to that of the hybridized modes detected in the microwave absorption experiments. The low intensity of these modes in the BLS measurement indicates a small BLS scattering cross-section. Note that BLS does not detect the pure photon modes of the SRR.

For a quantitative analysis of the hybridized mode frequencies we use Eq. (6.2). Here, the SRR resonance frequency ω_c is assumed to be independent of the applied magnetic field. The ferromagnetic resonance frequency ω_{FMR} is modeled by the in-plane Kittel equation (2.45):

$$\omega_{FMR} = \gamma\mu_0\sqrt{H\,(H + M_{eff})}. \tag{6.6}$$

An excellent agreement of $\omega_\pm$ with the MA and BLS data is obtained, as can be seen by the dashed fit curves in Figs. 6.5 (a, b). From the fits $g_{eff}/2\pi = 63(1)\,\text{MHz}$, $\mu_0 M_{eff} = 182(5)\,\text{mT}$ and $g_J = 2.003(4)$ are obtained. The extracted values of M_{eff} and g_J agree well to previously reported observations for similar YIG films [23, 99, 238, 239]. The loss rate of the loaded resonator $\kappa_c/2\pi = 25\,\text{MHz}$ is determined from the half width at half maximum (HWHM) of the resonance at $\mu_0 H = 40\,\text{mT}$, where the magnon and photon systems are well decoupled. The loss rate of the spin system $\kappa_{FMR}/2\pi = 4.1\,\text{MHz}$ (HWHM) is obtained from the BLS measurement, as detailed below. Taken together, both $g_{eff}/\kappa_c > 1$ and $g_{eff}/\kappa_{FMR} > 1$, and thus the system is well in the strong coupling regime [214].

Figure 6.6 (a, b) shows both I_{AS} (full dots) and $P_{abs} \propto -V_D$ (open squares) of the coupled system normalized to $[0, 1]$ along $\omega_\pm$ in Figs. 6.5 (a, b). Note that I_{AS} was averaged in a frequency and magnetic field range of $\pm 3\,\text{MHz}$ and $\pm 0.25\,\text{mT}$, respectively, to improve the signal-to-noise ratio of the BLS measurements. The error bars show the standard deviation. Figure 6.6 (a) shows a decrease of P_{abs} along ω_+ for increasing H, while I_{AS} simultaneously increases. Along ω_-, shown in Fig. 6.6 (b), both P_{abs} and I_{AS} show the reversed trend.

In the following, only the behavior along $\omega_+(H)$ is discussed for simplicity. The discussion of the ω_- mode is completely analogous. For small applied magnetic field mainly the photonic mode of the SRR is excited which leads to a high P_{abs} and vanishing I_{AS}. For increasing magnetic field, ω_{FMR} approaches ω_c and the photon and magnon modes become increasingly hybridized. Since the

[4] Depending on the position of the YIG film relative to the feedline, the uncoupled mode can also be observed in the MW transmission as shown in Ref. [222]

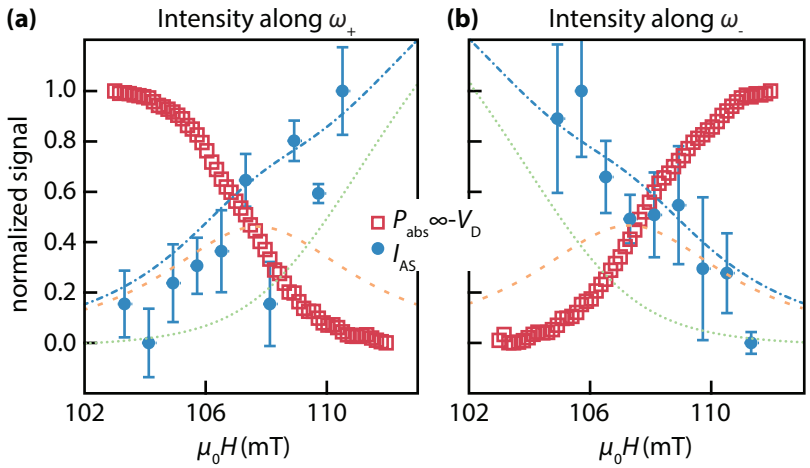

Fig. 6.6. – Absorbed microwave power P_{abs} and anti-Stokes intensity I_{AS} from Fig 6.5 along ω_+ in (a) and ω_- in (b). For ω_+ and ω_- close to ω_{FMR}, large I_{AS} and small P_{abs} is observed. Far away from ω_{FMR}, I_{AS} vanishes and P_{abs} becomes maximal. The lines indicate the contribution of the magnonic (orange dashed) and of the uncoupled FMR (green dotted) to the total BLS signal (blue dash-dotted).

photonic and magnonic character of the hybridized mode decreases and increases with increasing field, respectively, the same is expected for P_{abs} and I_{AS} probing the respective character of the hybridized mode. At about 108 mT ($\omega_{\mathrm{FMR}} = \omega_{\mathrm{c}}$) the photonic and magnonic character have equal weight and a drop of P_{abs} to 0.5 as well as an increase of I_{AS} to 0.5 is expected in good agreement with the experimental data. Increasing the applied field further reduces the photonic character of the ω_+ mode and P_{abs} is expected to drop to zero for $\mu_0 H \gg 108$ mT, where the ω_+ mode is purely magnonic. Again, this is in good agreement with the experimental data of Fig. 6.5 (c). Accordingly, I_{AS}, which is probing the magnonic character of the ω_+ mode, is expected to increase to unity. Although this also seems to be in good agreement with the data, the situation is more complicated here and has to be discussed in more detail. Due to the limited linewidth κ of the SRR, the amplitude of the excited FMR mode is expected to rapidly decrease for $|\omega_{\mathrm{FMR}} - \omega| > \kappa$ and vanish for $|\omega_{\mathrm{FMR}} - \omega| \gg \kappa$ as indicated by the dashed orange line in Fig. 6.5 (c) [227]. The resulting I_{AS} is expected to follow the orange line since it reflects the amplitude of the magnetic excitations [227, 240]. The fact that this is not observed in the experiment is attributed to the excitation of the FMR mode by the microwave field from the feedline. The signal expected from this uncoupled mode is shown by the dotted green line in Fig. 6.5 (c, d). Evidently, the dash-dotted blue line representing the sum of both contributions describes the measured BLS intensity reasonably well.

In summary, the signals from the MA and BLS measurements give complementary pictures of the magnon-photon coupling process. We find in both measurements the same characteristic avoided-crossing. This is an important results, as the MA measurement only probes the photonic character of the coupled

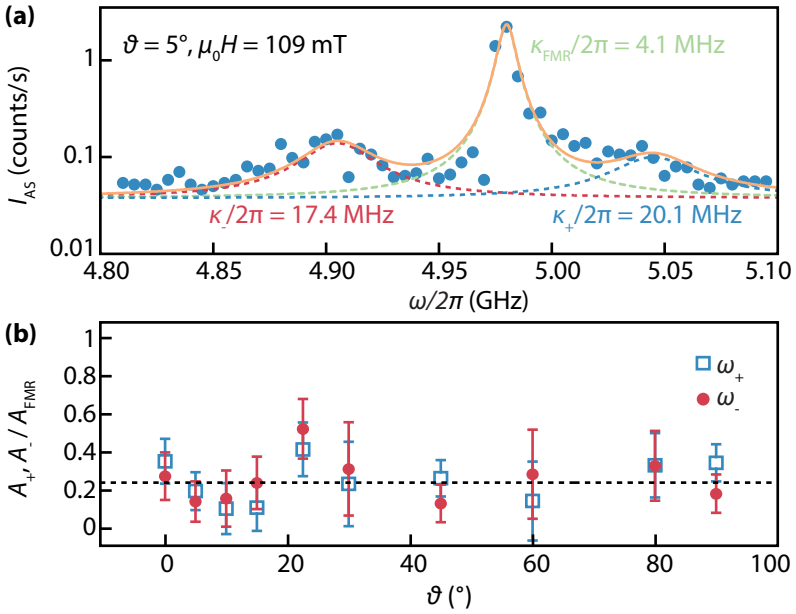

Fig. 6.7. – (a) Anti-Stokes intensity plotted versus microwave frequency for $\vartheta = 5°$ and $\mu_0 H = 109\,\mathrm{mT}$. The solid line represents the sum of three Lorentzian curves (dashed). (b) The ratios A_+ / A_{FMR} and A_- / A_{FMR} are plotted as a function of ϑ. The black dashed line marks the average ratio of 0.23.

system, whereas the BLS probes the magnonic character. Furthermore, the BLS intensity is closely connected to the MA absorption, as our qualitative analysis shows. With the BLS anti-Stokes process an up-conversion from the microwave SRR signal to the optical BLS signal is possible. Hereby the term up-conversion emphasizes, that the GHz-signal of the coupled system can be transferred to a carrier wave with frequencies in the order of 10^{14} Hz. This allows for a long-range transport of the coupled signal. On the other hand a down-conversion of the transported signal can be realized using the BLS Stokes process.

6.3.2 Polarization Dependence

In a further set of experiments, the polarization of the inelastically scattered light is investigated to gain a deeper understanding of the magnetic coupling phenomena. For example, we know that a magnetic field can split the degeneracy of quantum states (Zeeman effect) [21]. The optical transitions between the split levels of the quantum system can then be probed by light of a specific polarization, depending on the viewing angle relative to the magnetic field lines [21].

In our experiment, we vary the polarization of the incoming light, and record the intensity of the Stokes and anti-Stokes signals. For this we insert a $\lambda/2$-plate into the optical path as shown in Fig. 6.3 (a). These measurements correspond to fixed-field cuts through Fig. 6.5 (b). From the recorded data we can then conclude if Stokes and anti-Stokes processes are sensitive to the incoming light polarization.

Figure 6.7 (a) shows I_{AS} vs. ω obtained with $\vartheta = 5°$ and $\mu_0 H = 109\,\mathrm{mT}$. I_{AS} is fitted with the sum of three Lorentzian curves (solid line) corresponding to the hybridized modes in Eq. (6.2). For the fit, the resonance frequencies are fixed at $\omega_-/2\pi = 4.905\,\mathrm{GHz}$ (red dashed), $\omega_+/2\pi = 5.045\,\mathrm{GHz}$ (blue dashed) and the pure FMR mode at $\omega_{FMR}/2\pi = 4.98\,\mathrm{GHz}$ (green dashed). The areas A_+, A_- and A_{FMR} under the Lorentzian curves, an global offset and the HWHM loss rates are free parameters. For the loss rates we obtain $\kappa_+/2\pi = 20.1\,\mathrm{MHz}$, $\kappa_-/2\pi = 17.4\,\mathrm{MHz}$ and $\kappa_{FMR}/2\pi = 4.1\,\mathrm{MHz}$. The loss rate of the pure FMR line is smaller than the loss rates of the coupled resonances, as the pure FMR line in the BLS signal is not coupled to the SRR.

To investigate the polarization dependence of the BLS signal, we fit all fixed-field measurements recorded for various rotation angles of the $\lambda/2$-plate. To reduce the number of free parameters in the fit, the loss rates κ_+, κ_- and κ_{FMR} are fixed to the values discussed above. Figure 6.7 (b) shows the ratios A_+/A_{FMR} and A_-/A_{FMR} as a function of ϑ for constant $\mu_0 H = 109\,\mathrm{mT}$. The error bars are calculated from the fitting errors of A_+, A_- and A_{FMR} and depict the maximum fitting error. The average value of $A_+, A_-/A_{FMR}$ is 0.23 as shown by the black dashed line. Within error bars, A_+/A_{FMR} and A_-/A_{FMR} are independent of ϑ. This is consistent with the notion that all photons inelastically scattered off the hybridized modes and the pure FMR mode undergo the same polarization rotation. This indicates that only the magnonic part of the hybridized mode is accessible in the BLS measurement. The photonic part does not change the BLS process, suggesting a vanishing photon-photon scattering probability.

6.4 Conclusion

In conclusion, the presented microwave absorption and BLS measurements reveal strong magnon-photon coupling and its up-conversion to optical frequencies in a system consisting of a micropatterned split-ring resonator and a YIG film. We find a coupling constant of $g_{eff}/2\pi = 63\,\mathrm{MHz}$, which exceeds the loss rates of both the pure spin system $\kappa_{FMR}/2\pi = 4.1\,\mathrm{MHz}$ and the split-ring resonator $\kappa_c/2\pi = 25\,\mathrm{MHz}$. With this the formal criteria of strong coupling is fulfilled. The combined analysis of the microwave absorption and BLS intensities strongly indicates a continuous transition from a photonic to a magnonic mode with varying applied microwave frequency and magnetic field. The measurements show that the BLS and MA techniques are complimentary by sensing the magnonic and photonic character of the hybridized excitations, respectively.

In the center of the avoided-crossing the coupled mode oscillates between the magnonic and the photonic state. Hence, the experiments presented here provide a powerful platform for the study of time-dependent oscillations of the coupled system in between the purely magnonic and photonic states during coherent magnon-photon exchange, as well as limiting decoherence processes. Such Rabi

oscillations have previously been observed in microwave measurements [214], but the periodic conversion between magnons and photons have not. The measurement of such Rabi oscillations would not only open up a way to measure the time-dependence of coherent conversion processes, but we would also gain insight into the phase relations between magnons and photons.

Furthermore, the BLS technique opens the path to study macroscopic quantum phenomena, such as magnon Bose-Einstein condensates (BECs) [208] and magnonic supercurrents [241] which are coupled to photonic resonators. As the BEC forms at wavevectors $k \neq 0$ with vanishing group velocity, a resonator with a matched periodicity has to be invented to guarantee for an efficient population of the magnon gas with finite microwave powers. From the electrical measurement of a coupled BEC we could then achieve an further insight into the spontaneous coherence of thermal BECs [242, 243]. The BLS measurement on the other hand would allow for the observation of a possible splitting of the BEC frequency (similar to the FMR frequency). The coexistence of two BECs with different frequencies and hence different wavevectors could then result in a net BEC transport in the YIG film [241].

7 Summary

This thesis deals with coupling phenomena in the framework of magnonics and spintronics, where the spin degree of freedom of the electron is used for information processing, instead of its charge. We investigated several coupling mechanisms which can be used to read, write and transport information, or which are at least a step towards such applications. This thesis thereby covers a broad range of experiments which can be employed and combined with different modern information technology approaches: We used spin pumping to transfer spin information from a ferromagnet to Si-based semiconductors; we discovered a novel spin-torque approach to couple magnetic layers, which allows for the excitation of isotropic exchange spin waves; and we presented a procedure to transport and analyze the pure spin information originating from a hybrid magnon-polariton. For most of our experiments we used the ferrimagnetic insulator yttrium iron garnet. In retrospective this material was the ideal choice, as it obeys a saturation magnetization and an exchange stiffness, which shift all the observed phenomena to a frequency range which is suitable for our standard vector network analyzer measurements. Nevertheless, alone the broad spectrum of experiments done with YIG show its high potential for various novel technology fields. For a clear overview we structured this thesis into chapters, which successively complete our current understanding of the reported observations.

In Chap. 2 we summarized the theoretical foundations for this thesis. We introduced the reader to the theory of ferromagnetic resonances and spin waves, and gave an overview of different relevant damping mechanisms, such as the viscous Gilbert damping, as well as radiative and eddy-current damping. Additionally, we described our used experimental setups and derived expressions for the exact measurement signals of lock-in-based and VNA-based FMR measurements.

In Chap. 3 we used the spin pumping effect in permalloy/silicon heterostructures to inject spin angular momentum into the silicon layer. To proof this, we employed various silicon substrates with different resistance, and various permalloy thicknesses. The results show an increase of the spin pumping efficiency with decreasing permalloy thickness and decreasing silicon resistance. Both phenomena can be understood in the framework of the well known spin pumping theory, put forward by Tserkovnyak *et al.* Although the spin pumping effect from ferromagnets into semiconductors is well known, this work provides the first systematic study on the doping- and hence the resistivity of the silicon layer. The experiments in this chapter highlight a link between novel spintronic devices and common silicon-based CMOS technology. With the published results, one has now the chance to

optimize spin transport in semiconductors and to realize a fully CMOS-compatible spin-based technology, which unifies the advantages of both worlds.

In Chap. 4 we used sensitive ferromagnetic resonance spectroscopy to investigate the complex damping behavior of a YIG sphere. We find a record low Gilbert damping which is the same for all observed modes in the sphere. In contrast, we observe that the inhomogeneous line broadening depends strongly on the mode-specific distribution of the dynamic magnetization in the sphere. The first finding is explained with the Kasuya-LeCraw processes, where the damping process is the same for all modes. This result is also in agreement with the notion, that the Gilbert damping is a global material parameter. However, the second effect is explained and modeled with two-magnon scattering processes at the surface of the YIG. The inhomogeneous linebroadening depends strongly on the spatial distribution of the dynamic magnetization in the YIG sphere, such that we have a sensitive measure for the surface quality of our spherical sample. The results from this chapter might be used to improve the bandpass of YIG tuned filters, which are up to 40 MHz at 2 GHz [142]. The resonances observed here, are in he order of 2 MHz at a comparable frequencies. However, the more interesting application of our results would be to populate certain modes for quantum coupling experiments, where the relatively high volume of the sphere should guarantee for a large coupling parameter.

In Chap. 5 we discovered a spin torque effect at the interface of YIG/Co heterostructures. These torques still exist if we insert an conducting interlayer between the YIG and the Co, but they vanish for an insulating interlayer. Surprisingly, these spin torques allow for the excitation of sub-100 nm spin waves, which are already deep in the exchange dominated wavelength regime. We model our findings using a theory of mutual spin pumping and exchange torques at the interface, and we find an excellent agreement between the theory and the experimental data. Due to the coupled boundary conditions of the ferromagnets at the interface, the spin torques act as strongly localized excitation fields, which is the reason for the observed spin-wave wavelength range. It is interesting to see, that this coupling mechanism works at an insulator/metal interface, although the magnetization is carried by itinerant electrons in the insulator and by conduction electrons in the metallic ferromagnet. Even more noteworthy is the occurrence of large field-like torques, which are connected with the imaginary part of the spin-mixing conductance. However, the microscopic mechanisms behind this phenomena are not yet resolved. Our observed interfacial spin torques can be used to easily excite exchange-dominated spin waves with extended microwave fields, so that a micro structuring of the excitation antennas is not required. This paves the way for exchange magnonics, where we can exploit the isotropic spin-wave dispersions. With the excitation of dozens of spin wave modes, it is possible to realize a parallel and coherent transfer of information between the coupled subsystems. For example one could imagine a propagating carrier spin waves with

several higher order resonances, where each resonance carries a different logic input value.

In Chap. 6 we used Brillouin light scattering for the upconversion of the spin information from a magnon-polariton to optical frequencies. For this we employed a dipolar coupling mechanism between the dynamic magnetization of the YIG film and the out-of-plane dynamic magnetic field of a split-ring resonator. The coupling is evidenced by avoided crossings of the resonator and the YIG FMR mode dispersions in the optical BLS measurements. We simultaneously performed microwave absorption measurements of the YIG/SRR system. With this we were able to detect the purely photonic part of the magnon-polariton. In our first experiments we find that both measurement methods are complementary to each other, *viz.* both measurements show the same avoided crossing and coupling efficiency. The light scattering technique allows us to transfer the magnonic information processed at a speeds of gigahertz to optical frequencies. In principle this method can be used to transport the information of the coupled YIG/SRR system over long distances using laser beams. A next step would be a time-resolved experiment to observe the Rabi oscillations optically between the coupled subsystems. This would give a new insight into the coupling mechanism, as we could gain the phase information between the magnonic and the photonic part of the coupled YIG/SRR signal. However, also the observation of thermal spin waves would be interesting, as the detection of these waves is only possible with Brillouin light scattering.

All in all our findings help to understand the complex behavior of hybrid systems coupled by magnetic and spin excitations. And in the end we hope that our experiments and observations encourage the application of spin information in tomorrow's information technology.

Spin torques in YIG/Co heterostructures: Theory

A

In this appendix we present the full theory used in Chap. 5, which explains the interfacial spin torque coupling of the YIG and the Co layers by mutual spin pumping and exchange torques. The theoretical work was mainly done by V. Amin, M. Stiles and R. McMichael from the National Institute for Standards and Technology in Gaithersburg, USA, and we here try to give an edited compendium of their ideas and calculations. Some of the figures and parts of the text in this chapter have been published in S. Klingler, V. Amin, S. Geprägs, K. Ganzhorn, H. Maier-Flaig, M. Althammer, H. Huebl, R. Gross, R.D. McMichael, M.D. Stiles, S.T.B. Goennenwein, M. Weiler, *Spin-torque excitation of perpendicular standing spin waves in coupled YIG/Co heterostructures*, Physical Review Letters **120** (2018).

As the coupling consists of basically two contributions, we introduce in Chap. A.1 the mechanism of mutual spin pumping in a $FM_1/NM/FM_2$ system. For this, we derive expressions for the effective spin current which flows between the coupled layers, and subsequently find expressions for the spin torques. In Chap. A.2 we then introduce theses mutual spin pumping torques, as well as the exchange coupling, to the Landau-Lifshitz-Gilbert equation, from which we then calculate the magnetic susceptibility. The magnetic susceptibility can then be used to simulate the microwave transmission spectra, as shown in Chap. 5.4, or to derive the macrospin model used in Chap. 5.3.

A.1 Spin Pumping in a $FM_1/NM/FM_2$ System

In Chap. 3.1 we have introduced the spin pumping mechanism, which allows for the transport of angular momentum across an interface. We have already shown that the spin pumping mechanism leads to an increase of the Gilbert damping in an ferromagnet when the high frequency magnetization excitation is transferred into and absorbed in an adjacent metal. However, in our material system which consists of two adjacent ferromagnets, the spin current transports energy and angular momentum across the interface, which can be used to excite a magnetic resonance. If both magnetic subsystems share the same eigenfrequency at a given magnetic field, this results in a resonant transport of angular momentum under energy conservation. The coherent absorption of angular momentum in one ferromagnetic layer, and the emission of angular momentum from the other ferromagnetic layer then couples the dynamic magnetizations, similar to the magnon-photon coupling presented in Chap. 6. We now want to calculate the

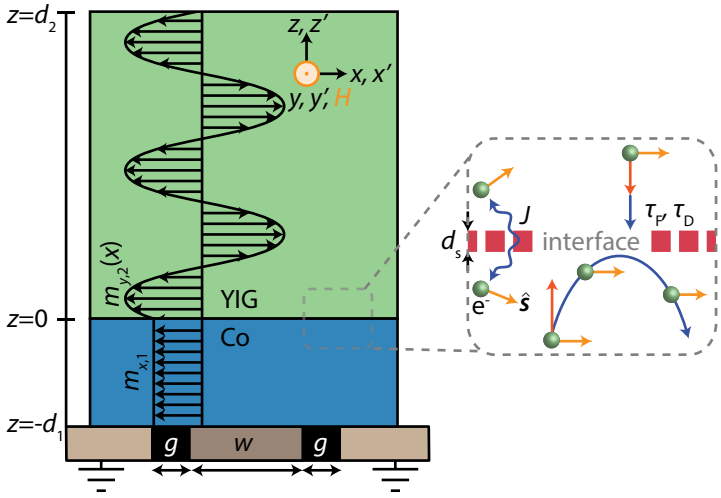

Fig. A.1. – Sketch of the physical problem. The YIG/Co samples are modeled using a z-dependent dynamic magnetization in the YIG films, whereas we assume a uniform precession in the Co film. The interface (inset) allows for different coupling mechanisms, such as a direct exchange coupling and a coupling via mutual spin pumping.

spin torques acting on the different magnetic layers, which is the result of the absorption of spin currents.

A.1.1 Notation and Units

A.1.1.1 Coordinate System, Approximations and Assumptions

We start by modeling the mutual spin pumping process of two adjacent ferromagnets. Figure A.1 shows a sketch of the physical problem. We consider a ferromagnet/normal metal/ferromagnet ($FM_1/NM/FM_2$) heterostructure, where the normal metal layer of thickness d_s is thick compared to its mean free path but thin compared to the spin diffusion length. The first assumption allows us to use the drift-diffusion approach to treat the transport, instead of the full Boltzmann transport equation. The second assumption allows us to neglect spin-flip scattering in the NM spacer layer, in which case the spin accumulation varies linearly across the spacer layer. We furthermore apply a large applied field in the y'-direction which aligns the magnetization. The film lies in the $x' - y'$-plane, whereas the film normal points along the z'-direction. Hence, in this chapter the coordinate systems of the magnetization and the sample-ellipsoid coincide, see Fig. 2.1 for comparison. We thus drop the prime superscript in the following. We furthermore assume that the transverse magnetization is small compared to the static magnetization, which allows us to concentrate on the transverse parts only in the following.

A.1.1.2 Complex Vector Notation

It is convenient (in retroperspective) to write the equations of motion in terms of complex numbers made up of the transverse components. Thus we express a vector $\boldsymbol{f} = (f_x, 1, f_z)$ as follows:

$$f_\perp^\star = f_z + i f_x \leftrightarrow \begin{pmatrix} \mathrm{Re}\,[f_\perp^\star] \\ \mathrm{Im}\,[f_\perp^\star] \end{pmatrix} = \begin{pmatrix} f_z \\ f_x \end{pmatrix}. \tag{A.1}$$

In this notation, the cross product operation $(0,1,0) \times (f_x, 1, f_z) = (f_z, 0, -f_x)$ can be represented as multiplication with the imaginary unit i:

$$(\hat{\boldsymbol{y}} \times \boldsymbol{f})_\perp \rightarrow -f_x + i f_z = i(f_z + i f_x) = i f_\perp^\star. \tag{A.2}$$

The definition would include another minus sign if we would have chosen a different vector definition. In the following we drop the subscript $\perp$ from the complex representation of vectors for simplicity.

A.1.2 Mutual spin pumping

The spin current density which flows across the interface is given by $\boldsymbol{I}_\mathrm{s}$ from Eq. (3.5):

$$\boldsymbol{I}_\mathrm{s} = \frac{\hbar}{4\pi}\left(\mathrm{Re}\left[G^{\uparrow\downarrow}\right]\hat{\boldsymbol{y}} \times \dot{\boldsymbol{m}} - \mathrm{Im}\left[G^{\uparrow\downarrow}\right]\dot{\boldsymbol{m}}\right). \tag{A.3}$$

Note that the spin mixing conductance in the main text is units of $[\mathrm{m}^{-2}]$, whereas the spin current is in units of $[\mathrm{J/m}^2]$. When we multiply the spin current with $(2e/h)$, we convert the spin current density into a charge current density in units of $[\mathrm{A/m}^2]$, as every electron carries an angular momentum of $\hbar/2$. As the flow of angular momentum is then carried by a flow of electrons, the conversion from a spin current to a charge current equivalent is justified [244]. We furthermore rewrite the spin mixing conductance in units of $[\Omega^{-1}\ \mathrm{m}^{-2}]$, which is obtained by dividing the above equation by the Klitzing constant $(e^2/2\pi\hbar)$:

$$\boldsymbol{I}_\mathrm{c} = \frac{2\pi\hbar}{e^2}\frac{2e}{\hbar}\boldsymbol{I}_\mathrm{s} = \frac{\hbar}{e}\left(\mathrm{Re}\left[G^{\uparrow\downarrow}\right]\hat{\boldsymbol{y}} \times \dot{\boldsymbol{m}} - \mathrm{Im}\left[G^{\uparrow\downarrow}\right]\dot{\boldsymbol{m}}\right). \tag{A.4}$$

In our complex notation we can rewrite the above term into:

$$I_\mathrm{c}^\star = \frac{\hbar}{e} G^\star i\dot{m}^\star \tag{A.5}$$

where the real part gives the z-component and the imaginary part gives the x-component.

In the normal metal spacer layer, the spin transport can be described by magnetoelectric circuit theory [245]. When a spin current is injected from the

ferromagnet into the normal metal, this results in a spin accumulation $\mu^\star(z) = (\mu_\uparrow^\star - \mu_\downarrow^\star)/e$ in units of [V], which is the imbalance of the electrochemical potential of majority $\mu_\uparrow^\star$ and minority $\mu_\downarrow^\star$ electrons. The spin accumulation then relaxes into the normal metal layer over a spin diffusion length. For copper the spin diffusion length is in the order of 500 nm, which is much larger than our layer thickness. We can then write the spin current in the normal metal as the product of the normal metal conductance D and the spin voltage $\mu^\star(z)$ [245], which looks as a one-dimensional spin diffusion equation [244]:

$$I_c^\star(z) = -D\nabla\mu^\star(z) = -D\nabla(\mu_0^\star + \mu'^\star z) = -D\mu'^\star. \tag{A.6}$$

Here, $D = \sigma_{NM}/2 = \sigma^\uparrow = \sigma^\downarrow$ in units of $[\Omega^{-1}m^{-1}]$), where σ_{NM} is the bulk electrical conductivity of the normal metal, which has the same electrical conductivities for both majority $\sigma^\uparrow$ and minority $\sigma^\downarrow$ electrons. Note that we have used a Taylor approximation where $\mu'^\star = \partial\mu^\star/\partial z$ in the second step. This is justified, as the spin relaxation varies linearly over the spacer layer thickness, when the spin diffusion length is much larger than the layer thickness [246]. We find that the spatially-constant spin current density is proportional to the gradient of the spin accumulation.

A.1.2.1 Spin Current Boundary Conditions

We assume the spacer layer has thickness d_s, running from $z = -d_s/2$ to $z = d_s/2$. For the boundary conditions at the first interface ($z = -d_s/2$), we consider the spin current which penetrates the normal metal to be the sum of a dc spin current and the pumped spin current Eq. (A.5). The magneto electronic circuit theory causes that the spin accumulation just within the normal metal layer leads to a spin current via reflection of carriers at the interface [247]. Hence the dc spin current is generated by the voltage drop due to the spin accumulation and the spin mixing constant $G^\star$. For this reasons first boundary condition reads [247]:

$$\begin{aligned} I_c^\star(-d_s/2) &= -D\mu'^\star = -G_1^\star\mu^\star + \frac{\hbar}{4\pi e}G_1^\star i\dot{m}_1^\star \\ &= -G_1^\star(\mu_0^\star - \mu'^\star d_s/2) + \frac{\hbar}{4\pi e}G_1^\star i\dot{m}_1^\star. \end{aligned} \tag{A.7}$$

Here, $G_1^\star$ is the complex spin mixing conductance of the first interface, and $m_i^\star = (m_{z,i}^\star, m_{x,i}^\star)$ is the transverse magnetization.

The boundary condition at the other interface ($z = d_s/2$) is the same except that the signs change because the direction of the interface normal changes:

$$I_c^\star(d_s/2) = -D\mu'^\star = G_2^\star(\mu_0^\star + \mu'^\star d_s/2) - \frac{\hbar}{4\pi e}G_2^\star i\dot{m}_2^\star. \tag{A.8}$$

The boundary conditions then give us four equations in four unknowns (μ_{0z}, μ_{0x} μ'_z, μ'_x), or two complex equations Eq. (A.7) and Eq. (A.8) in two complex unknowns (μ_0, μ').

A.1.2.2 Determination of the Spin Currents

We take the boundary conditions Eq. (A.7) and Eq. (A.8) and solve them for the two complex unknowns (μ_0, μ'). From this we find the spin accumulation in the normal metal layer, which connects both ferromagnetic layers with each other. The spin accumulation reads:

$$\begin{aligned}\mu_0 &= \frac{i\hbar}{4\pi e}\frac{2D(G_1^\star \dot{m}_1^\star + G_2^\star \dot{m}_2^\star) + d_s G_1^\star G_2^\star(\dot{m}_1^\star + \dot{m}_2^\star)}{2(D(G_1^\star + G_2^\star) + d_s G_1^\star G_2^\star)},\\ \mu' &= -\frac{iG_1^\star G_2^\star \hbar(\dot{m}_1^\star - \dot{m}_2^\star)}{4\pi e(D(G_1^\star + G_2^\star) + d_s G_1^\star G_2^\star)},\end{aligned} \tag{A.9}$$

from which we can derive the spin current:

$$j^\star(-d_s/2) = -i\frac{\hbar}{4\pi e}G^\star(\dot{m}_1^\star - \dot{m}_2^\star). \tag{A.10}$$

Here we have defined an effective mixing conductance that describes the coupled system:

$$G^\star = \frac{G_1^\star G_2^\star}{G_1^\star + G_2^\star + G_1^\star G_2^\star d_s/D} \approx \frac{G_1^\star G_2^\star}{G_1^\star + G_2^\star}, \tag{A.11}$$

where we have used the small d_s limit in the second step in the denominator, as the conductance of a thin Cu layer is much greater than either mixing conductance (the Cu interlayer is much thinner than the spin-diffusion length of Cu). Note that in this limit the amplitudes of the spin currents persist, when we remove the Cu layer. However, in this case the exchange coupling starts to play a major role, as shown in the main text.

A.1.2.3 Calculation of the Spin Torques

The calculated spin currents transport angular momentum. If this angular momentum is propagated through the normal metal and absorbed in one of the ferromagnets, it exerts a torque. In the absence of spin-orbit coupling, the spin torque exerted on one of the ferromagnets equals the difference between the spin currents at the boundaries of that ferromagnet, as both ferromagnets pump spin current into each other. The transverse spin current just inside the ferromagnets vanish due to dephasing [248], on a length-scale of about one nanometer [249–251], i.e. $j^\star(-d_s/2 - \epsilon) = 0$ and $j^\star(d_s/2 + \epsilon) = 0$. The physical reason for the dephasing becomes clear in the view point of the conduction electrons of the normal metal at the Fermi energy. In the normal metal both spin-up and spin-down electrons have identical Fermi spheres. In the ferromagnet however, the spin-up and spin down-

electrons degeneracy is lifted, due to the spin-dependent band structure. When the electrons in the normal metal penetrate the ferromagnet, the spin-degeneracy is lifted and the electrons are scattered into different k-vectors at different energies. Thus we find a pairwise dephasing of the conduction electrons in the ferromagnet, which leads to a vanishing transverse spin current [244, 245, 248].

The spin torque τ_1, also a complex number representing the two transverse components, at the first interface is given by:

$$\tau_1^\star = \Delta j^\star = j^\star(-d_s/2+\epsilon) - j^\star(-d_s/2-\epsilon) = j^\star(-d_s/2+\epsilon), \tag{A.12}$$

where the x and z components are extracted according to the prescription given in Eq. (A.1):

$$\tau_{1,z} = \mathrm{Re}[j^\star], \tag{A.13}$$
$$\tau_{1,x} = \mathrm{Im}[j^\star]. \tag{A.14}$$

Since the interface normal flips between the two interfaces, the torques on the two magnetizations have the same magnitude but the opposite sign, i.e. $\tau_1 = -\tau_2$. Note that here, the torques have still the same units as the charge current density.

We now want show how the spin torques are included in the Landau-Lifshitz-Gilbert equation. Assuming a time dependence of the magnetization:

$$m_i^\star = (m_{i,z}, m_{i,x}) \exp(-i\omega t), \tag{A.15}$$

the spin torque on the first ferromagnet is given by:

$$\tau_1^\star = -i\frac{\hbar}{4\pi e} G^\star(-i\omega)(m_1^\star - m_2^\star) = -\omega\frac{\hbar}{4\pi e} G^\star(m_1^\star - m_2^\star), \tag{A.16}$$

and similarly the spin torque on the second ferromagnet is given by:

$$\tau_2^\star = \omega\frac{\hbar}{4\pi e} G^\star(m_1^\star - m_2^\star) = -\tau_1^\star. \tag{A.17}$$

Hence, the torques depend on the real and imaginary parts of the effective mixing conductance $G^\star$. Unfortunately, extracting the mixing conductances for each interface is impossible unless one mixing conductance is already known. We use a complex multiplication to obtain the spin torques from Eq. (A.16) and Eq. (A.17):

$$\begin{aligned}\tau_{1,z} = \mathrm{Re}[\tau_1^\star] &= -\omega\frac{\hbar}{4\pi e}\Big(\mathrm{Re}[G^\star]\mathrm{Re}[m_1^\star - m_2^\star] - \mathrm{Im}[G^\star]\mathrm{Im}[m_1^\star - m_2^\star]\Big) \\ &= -\omega\Big(\tau_D(m_{1,z} - m_{2,z}) - \tau_F(m_{1,x} - m_{2,x})\Big)\end{aligned} \tag{A.18}$$

$$\begin{aligned}\tau_{1,x} = \mathrm{Im}[\tau_1^\star] &= -\omega\frac{\hbar}{4\pi e}\Big(\mathrm{Im}[G^\star]\mathrm{Re}[m_1^\star - m_2^\star] + \mathrm{Re}[G^\star]\mathrm{Im}[m_1^\star - m_2^\star]\Big) \\ &= -\omega\Big(\tau_F(m_{1,z} - m_{2,z}) + \tau_D(m_{1,x} - m_{2,x})\Big),\end{aligned} \tag{A.19}$$

and analogously:

$$\tau_{2,z} = \mathrm{Re}[\tau_2^\star] = \omega\Big(\tau_\mathrm{D}(m_{1,z} - m_{2,z}) - \tau_\mathrm{F}(m_{1,x} - m_{2,x})\Big) \tag{A.20}$$

$$\tau_{2,x} = \mathrm{Im}[\tau_2^\star] = \omega\Big(\tau_\mathrm{F}(m_{1,z} - m_{2,z}) + \tau_\mathrm{D}(m_{1,x} - m_{2,x})\Big), \tag{A.21}$$

where we have defined the torque strengths, in units of [Asm^{-2}], as:

$$\tau_\mathrm{D} = \frac{\hbar}{4\pi e}\mathrm{Re}[G^\star], \tag{A.22}$$

$$\tau_\mathrm{F} = \frac{\hbar}{4\pi e}\mathrm{Im}[G^\star]. \tag{A.23}$$

Note that multiplying a torque strength ($\tau_{\mathrm{D/F}}$) by the time derivative of a magnetization unit vector gives a torque in units of [Am^{-2}]. The torque on the second interface ($\boldsymbol{\tau}_2$) is obtained in a similar manner. We rewrite the expressions Eq. (A.18) to Eq. (A.21):

$$\begin{pmatrix} \tau_{1,z} \\ \tau_{1,x} \\ \tau_{2,z} \\ \tau_{2,x} \end{pmatrix} = -\omega \begin{pmatrix} \tau_\mathrm{D} & -\tau_\mathrm{F} & -\tau_\mathrm{D} & \tau_\mathrm{F} \\ \tau_\mathrm{F} & \tau_\mathrm{D} & -\tau_\mathrm{F} & -\tau_\mathrm{D} \\ -\tau_\mathrm{D} & \tau_\mathrm{F} & \tau_\mathrm{D} & -\tau_\mathrm{F} \\ -\tau_\mathrm{F} & -\tau_\mathrm{D} & \tau_\mathrm{F} & \tau_\mathrm{D} \end{pmatrix} \begin{pmatrix} m_{1,z} \\ m_{1,x} \\ m_{2,z} \\ m_{2,x} \end{pmatrix}. \tag{A.24}$$

Here the torques still have units of charge current density [Am^{-2}]. To convert the torque strengths into a form consistent with the LLG equations, where all torques have the unit of [s^{-1}], we multiply them by [252]:

$$-\frac{\hbar\gamma_i}{ed_iM_{s,i}}, \tag{A.25}$$

where $i \in [1,2]$ denotes the material, γ_i is the gyromagnetic ratio, $M_{s,i}$ is the saturation magnetization, and d_i is the magnetic film thickness. Note that we use $i = 1$ for Co and $i = 2$ for YIG. The torque term that we add to the LLG is then given by:

$$\tau_i = -\frac{\hbar\gamma_i}{ed_iM_{s,i}}\left[(\tau_\mathrm{F} - \tau_\mathrm{D}\hat{\boldsymbol{y}}\times)(\dot{\boldsymbol{m}}_i - \dot{\boldsymbol{m}}_j)\right]. \tag{A.26}$$

Note that the damping-like torque is proportional again to the $\boldsymbol{y} \times \dot{\boldsymbol{m}}$, whereas the field-like torque is proportional to $\dot{\boldsymbol{m}}$, as already seen in Eq. (3.1).

A.2 The Interfacial Spin Torque Model

In the previous section we have calculated the torque on the ferromagnets due to the mutual spin pumping across the normal metal interface. Now, we calculate the torques due to the direct exchange coupling, if the YIG and the Co is in direct contact to each other. For this we use a macrospin approximation for the Co magnetization ($\boldsymbol{M}_1$), as we only consider the first cobalt mode. However, we assume that the unit vector of YIG magnetization direction ($\boldsymbol{M}_2(z)$) varies spatially. In Chap. A.1, a real-valued two-vector was represented as a single complex number. Here, we adopt a notation of using lower case bold letters to indicate the transverse components. In addition, to capture the phases of the precessing moments, we allow these vectors to be complex. In this case, we get the physical quantities from the real part of the vectors. Upper case bold characters indicate three-dimensional vectors, as in the other chapters of this thesis.

For the transverse magnetization, the energy per unit area[5,6] of the coupled heterostructure reads [33, 247]:

$$\begin{aligned} E/A = \int_0^{d_2} dz \left[A_{\mathrm{ex}} \left(\partial_z \boldsymbol{m}_2\right)^2 + \frac{\mu_0 H M_{\mathrm{s},2}}{2} \boldsymbol{m}_2 \cdot \boldsymbol{m}_2 + \frac{\mu_0 M_{\mathrm{s},2}^2}{2} m_{2,z}^2 \right] \\ + \frac{\mu_0 H M_{\mathrm{s},1} d_1}{2} \boldsymbol{m}_1 \cdot \boldsymbol{m}_1 + \frac{\mu_0 M_{\mathrm{s},1}^2 d_1}{2} m_{1,z}^2 + \frac{1}{2} J \left[\boldsymbol{m}_1 - \boldsymbol{m}_2(0)\right]^2 . \end{aligned} \tag{A.27}$$

Here, the integrand describes the energy contribution of the YIG film and $\hat{\boldsymbol{z}}$ is the unit vector in z-direction. The first term of the integrand is the YIG exchange energy of the PSSWs [19, 33]. The second term is the energy of the YIG magnetization in the applied external field [33]. The third term is the demagnetization energy of the YIG [33]. The first term in the second line is the energy of the Co magnetization in the applied magnetic field [33], and the second term is the demagnetization energy of the Co [33]. The exchange coupling constant between the YIG and the Co is given by the exchange integral J [19, 21, 205]. The YIG magnetization direction at the YIG/Co interface is given by $\boldsymbol{m}_2(0)$. We obtain the effective field of the Co by using the magnetic energy which is normalized by the Co thickness and

5 Note that we have normalized the energy by the area rather than the volume, as in Chap. 2. The reason is, that we start here from an integral over the complete sample volume. However, as the area of the YIG and the Co film are the same, we can normalize on the parameter A. This is also the reason why we find a parameter d_1 in the energy terms of the Co film; As the Co magnetization is a macrospin we can integrate over the full Co volume, including the thickness. This is not possible for the YIG film, as the z-dependence is not yet resolved. Furthermore, we note that the direct exchange is a delta function at the interface $\int dV J[\boldsymbol{m}_1 - \boldsymbol{m}_2(z)]^2 \delta(z) = JA[\boldsymbol{m}_1 - \boldsymbol{m}_2(0)]^2$, hence it is not multiplied with the volume but the area, which is subsequently normalized out.

6 The energy contributions are chosen in such a way that they directly lead to the linearized form of the LLG. E.g. the exchange torque $\tau_{\mathrm{ex},1} = \gamma_1 \hat{\boldsymbol{y}} \times \nabla_{\boldsymbol{m}_1} J[\boldsymbol{m}_1 - \boldsymbol{m}_2(z)]^2/2 = \gamma_1 \hat{\boldsymbol{y}} \times J[\boldsymbol{m}_1 - \boldsymbol{m}_2(z)]$. This expression is similar to the exchange torque which we have found in Eq. (5.16) for the macrospin model.

saturation magnetization: $\mu_0 H_{\text{eff},1} = -\nabla E/(M_{s,1} d_1)$. We can hence write down the linearized Landau-Lifshitz-Gilbert equation for the Co film:

$$\begin{aligned}\dot{\boldsymbol{m}}_1 = &-\gamma_1 \hat{\boldsymbol{y}} \times \Bigg[-\mu_0 H \boldsymbol{m}_1 - \frac{\alpha_1}{\gamma_1}\dot{\boldsymbol{m}}_1 - \mu_0 M_{s,1} M_{1,z}\hat{\boldsymbol{z}} \\ &- \frac{J}{d_1 M_{s,1}}\left(\boldsymbol{m}_1 - \boldsymbol{m}_2(0)\right) + \mu_0 \boldsymbol{h}\Bigg] \\ &- \frac{\hbar \gamma_1}{e d_1 M_{s,1}}\left[(\tau_{\text{F}} - \tau_{\text{D}}\hat{\boldsymbol{y}}\times)(\dot{\boldsymbol{m}}_1 - \dot{\boldsymbol{m}}_2(0))\right].\end{aligned} \tag{A.28}$$

Here we have used that the static magnetization lies in the film plane, parallel to the external magnetic field along the y-direction. The magnetic driving field from the CPW is denoted by $\boldsymbol{h}$. Note that, in the model, $\boldsymbol{h}$ is assumed to be spatially uniform, to reflect the experimental situation where the CPW center conductor width is much larger than either YIG or Co thickness, cf. Chap.2.4.1. Analogously, we derive the equation of motion for the YIG away from the interface:

$$\begin{aligned}\dot{\boldsymbol{m}}_2 = &-\gamma_2 \hat{\boldsymbol{y}} \times \Bigg[-\mu_0 H \boldsymbol{m}_2 - \frac{\alpha_2}{\gamma_2}\dot{\boldsymbol{m}}_2 \\ &- \mu_0 M_{\text{s},2} m_{2,z}\hat{\boldsymbol{z}} + \frac{2A_{\text{ex}}}{M_{\text{s},2}}\partial_z^2 \boldsymbol{m}_2 + \mu_0 \boldsymbol{h}\Bigg],\end{aligned} \tag{A.29}$$

where the definitions of the variables is analogous to the Co variables, except of the index 2 instead of 1. The exchange constant of the YIG is given by A_{ex}. We treat the coupling terms as boundary conditions as shown below.

A.2.1 Determination of the Eigenvectors

To solve the coupled LLG of the Co film, we have to determine the interfacial value of the YIG magnetization $\boldsymbol{m}_2(0)$. For this, we derive the eigenmodes of the undisturbed YIG film, as we can express every excitation in the YIG as a superposition of those modes. We use a complex ansatz for the transverse magnetization components:

$$\boldsymbol{m}_2 = \exp(ikz)\exp(-i\omega t)\begin{pmatrix} m_{2,z} \\ m_{2,x}\end{pmatrix}, \tag{A.30}$$

where k is a complex wavevector. From Eq. (A.29) we obtain a system of equations including the YIG susceptibility $\tilde{\chi}_2^{-1}$, which describes the response of the transverse YIG magnetization perpendicular to external magnetic fields:

$$0 = \underbrace{\begin{pmatrix} -\frac{2A_{\text{ex}}k^2}{M_{\text{s},2}} - \mu_0 H - \mu_0 M_{\text{s},2} + \frac{i\alpha_2\omega}{\gamma_2} & -\frac{i\omega}{\gamma_2} \\ \frac{i\omega}{\gamma_2} & -\frac{2A_{\text{ex}}k^2}{M_{\text{s},2}} - \mu_0 H + \frac{i\alpha_2\omega}{\gamma_2}\end{pmatrix}}_{\tilde{\chi}_2^{-1}} \begin{pmatrix} m_{2,z} \\ m_{2,x}\end{pmatrix}. \tag{A.31}$$

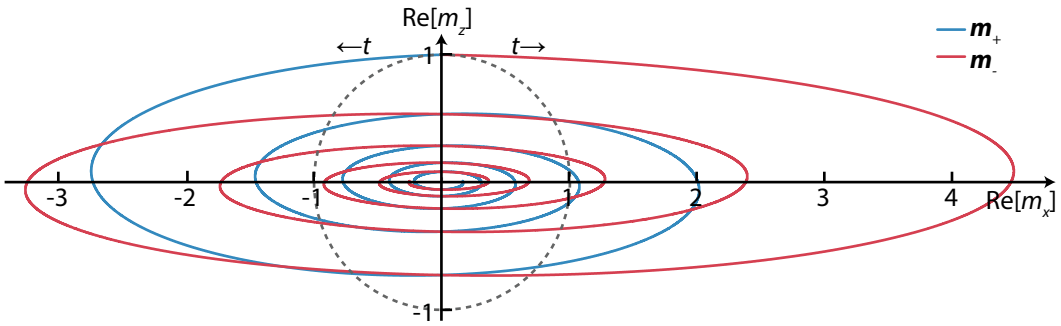

Fig. A.2. – Precessional motion of the different magnetization eigenvectors. $\boldsymbol{m}_+$ precesses counter-clockwise, whereas $\boldsymbol{m}_-$ precesses clockwise. The precession is elliptical as $\omega_{M,2}/2\pi = 4.9\,\mathrm{GHz}$. For a vanishing demagnetization field the precession is circular (dashed line).

The system of equations is solved for $\det \tilde{\chi}_2^{-1} = 0$ by two different wavevectors:

$$k_\pm = \frac{1}{2}\sqrt{\frac{M_{s,2}\left(2i\alpha_2\omega - 2\gamma_2\mu_0 H - \omega_{M,2} \pm \sqrt{\omega_{M,2}^2 + 4\omega^2}\right)}{A_{ex}\gamma_2}}, \tag{A.32}$$

where we have used $\omega_{M,2} = \gamma_2\mu_2 M_{s,2}$. The wavevector k_+ describes an harmonic oscillation of the magnetization along the z-direction. The wavevector k_- on the other side describes an evanescent behavior of the YIG magnetization, with a decay length in the order of 10 nm. We now use the obtained wavevectors $k_\pm$ in Eq. (A.31) to derive the eigenvectors of the dynamic YIG magnetization:

$$k_\pm : \; 0 = \begin{pmatrix} \frac{1}{2}\left(-\omega_{M,2} \mp \sqrt{\omega_{M,2}^2 + 4\omega^2}\right) & -i\omega \\ i\omega & \frac{1}{2}\left(\omega_{M,2} \mp \sqrt{\omega_{M,2}^2 + 4\omega^2}\right) \end{pmatrix} \begin{pmatrix} m_{2,z} \\ m_{2,x} \end{pmatrix}, \tag{A.33}$$

The system of equation has several solutions, however, we restrict our model to the zero eigenvalue of both systems, as this refers to our resonance condition $\det \tilde{\chi}_2^{-1} = 0$. We find from the different wavevectors:

$$k_\pm : \; \boldsymbol{m}_{2_\pm} = \begin{pmatrix} \frac{i\left(\mp\sqrt{\omega_{M,2}^2+4\omega^2}+\omega_{M,2}\right)}{2\omega} \\ 1 \end{pmatrix}. \tag{A.34}$$

In Fig. A.2 we sketch the time evolution of the real parts of the magnetization components for both eigenvectors $\boldsymbol{m}_{2\pm}$. For this we calculate $\mathrm{Re}[\boldsymbol{m}_\pm \exp(i(-\omega + i\alpha)t)]$, with the material parameters of YIG, given in the main text. We find an elliptical precession, as the demagnetization field increases the magnetostatic energy along the z-direction. Hence we find a larger precession amplitude in the x-direction than in the z-direction. For a vanishing demagnetization field, we obtain a circular precession (dashed lines). Note furthermore that the magnetization

eigenvectors precess counter-clockwise $\boldsymbol{m}_+$ and clockwise $\boldsymbol{m}_-$. It is obvious that the eigenvectors are thus linear independent, and span a vector space with which we can model all possible solutions of the YIG magnetization.

A.2.2 Boundary Conditions and Solution of the Problem

We model the YIG/Co interface as an infinitesimally thin surface layer. While the magnetization is not pinned at the interface, the infinitesimally thin layer has no volume, an hence no angular momentum. As a consequence, the total torque acting on the interface has to vanish [203–205]:

$$\begin{aligned} 0 =& 2A_{\mathrm{ex}}\hat{\boldsymbol{y}} \times \partial_z \boldsymbol{m}_2(z)|_{z=0} - J\hat{\boldsymbol{y}} \times (\boldsymbol{m}_1 - \boldsymbol{m}_2(0)) \\ &+ (\hbar/e)(\tau_{\mathrm{F}} - \tau_{\mathrm{D}}\hat{\boldsymbol{y}}\times)\,(\dot{\boldsymbol{m}}_1 - \dot{\boldsymbol{m}}_2(0))\,. \end{aligned} \tag{A.35}$$

On the YIG/substrate interface, we assume an uncoupled boundary condition, where the torques vanish as well:

$$0 = 2A_{\mathrm{ex}}\hat{\boldsymbol{y}} \times \partial_z \boldsymbol{m}_2(z)|_{z=d_2}. \tag{A.36}$$

As stated previously we model the YIG magnetization as a space-dependent variable, which is a superposition of the YIG magnetization eigenvectors. The ansatz for the dynamic YIG magnetization thus reads:

$$\boldsymbol{m}_2 = [c_-\boldsymbol{m}_{2-}\cos(k_-z) + c_+\boldsymbol{m}_{2+}\cos(k_+z)]\exp(-i\omega t), \tag{A.37}$$

where $c_\pm$ are complex coefficients. We model the Co magnetization in a macrospin approximation, without any space dependence:

$$\boldsymbol{m}_1 = \begin{pmatrix} m_{z,1} \\ m_{x,1} \end{pmatrix} \exp(-i\omega t). \tag{A.38}$$

Here, $m_{x,1}, m_{z,1}$ are complex coefficients. Note that the real behavior of the dynamic magnetization can be found in the real parts of Eq. (A.37) and Eq. (A.38).

In a first step we insert the ansatz Eq. (A.37) and Eq. (A.38) into the boundary condition Eq. (A.35):

$$\begin{aligned} 0 =& +2A_{\mathrm{ex}}(-c_-k_-\boldsymbol{m}_{2-}\sin(k_-z) - c_+k\boldsymbol{m}_{2+}\sin(k_+z)) \\ &- (\hbar/e)\tau_{\mathrm{F}}\hat{\boldsymbol{y}} \times (ic_-\boldsymbol{m}_{2-}\omega\cos(k_-z) + ic_+\boldsymbol{m}_{2+}\omega\cos(k_+z) - i\boldsymbol{m}_{1,0}\omega) \\ &+ (\hbar/e)\tau_{\mathrm{D}}(ic_-\boldsymbol{m}_{2-}\omega\cos(k_-z) + ic_+\boldsymbol{m}_{2+}\omega\cos(k_+z) - i\boldsymbol{m}_{1,0}\omega) \\ &- J(-c_-\boldsymbol{m}_{2-}\cos(k_-z) - c_+\boldsymbol{m}_{2+}\cos(k_+z) + \boldsymbol{m}_{1,0}) \end{aligned} \tag{A.39}$$

where we have used $\hat{\boldsymbol{y}} \times (\hat{\boldsymbol{y}} \times \boldsymbol{m}_i) = -\boldsymbol{m}_i$ in the first step. In the second step we have used Eq. (A.37), and the fact that the dynamic YIG magnetization must obey the boundary conditions for all times t. To solve for the coefficients $c_\pm$, we

multiply the above equation with the complex conjugates of the YIG magnetization eigenvectors $\boldsymbol{m}_{2\pm}^*$, which obey the special orthogonality relations $\boldsymbol{m}_{2\mp}\boldsymbol{m}_{2\pm}^* = 0$. From the multiplication of $\boldsymbol{m}_{2+}^*$ we obtain:

$$\begin{aligned} 0 = \boldsymbol{m}_{2+}^* \big[& -2A_{\mathrm{ex}} c_+ k \boldsymbol{m}_{2+} \sin(k_+ z) \\ & - (\hbar/e)\tau_{\mathrm{F}} \hat{\boldsymbol{y}} \times (i c_- \boldsymbol{m}_{2-} \omega \cos(k_- z) + i c_+ \boldsymbol{m}_{2+} \omega \cos(k_+ z) - i \boldsymbol{m}_{1,0} \omega) \\ & + (\hbar/e)\tau_{\mathrm{D}} (i c_+ \boldsymbol{m}_{2+} \omega \cos(k_+ z) - i \boldsymbol{m}_{1,0} \omega) \\ & - J(-c_+ \boldsymbol{m}_{2+} \cos(k_+ z) + \boldsymbol{m}_{1,0}) \big]. \end{aligned} \tag{A.40}$$

From the multiplication of $\boldsymbol{m}_{2-}^*$ we obtain:

$$\begin{aligned} 0 = \boldsymbol{m}_{2-}^* \big[& -2A_{\mathrm{ex}} c_- k_- \boldsymbol{m}_{2-} \sin(k_- z) \\ & - (\hbar/e)\tau_{\mathrm{F}} \hat{\boldsymbol{y}} \times (i c_- \boldsymbol{m}_{2-} \omega \cos(k_- z) + i c_+ \boldsymbol{m}_{2+} \omega \cos(k_+ z) - i \boldsymbol{m}_{1,0} \omega) \\ & + (\hbar/e)\tau_{\mathrm{D}} (i c_- \boldsymbol{m}_{2-} \omega \cos(k_- z) - i \boldsymbol{m}_{1,0} \omega) \\ & - J(-c_- \boldsymbol{m}_{2-} \cos(k_- z) + \boldsymbol{m}_{1,0}) \big]. \end{aligned} \tag{A.41}$$

We now can solve the system of equations consisting of Eq. (A.40) and Eq. (A.41) to obtain the complex coefficients $c_\pm$ as a function of the four variables $\boldsymbol{m}_1(\hat{\boldsymbol{y}} \times \boldsymbol{m}_{2\pm})$ and $\boldsymbol{m}_{2\mp}(\hat{\boldsymbol{y}} \times \boldsymbol{m}_{2\pm})$:

$$\begin{aligned} c_\pm = \frac{\pm 1}{c} \Big(& + 2A_{\mathrm{ex}} k_- \sin(dk_-) \big\{ \boldsymbol{m}_{1,0} (\hat{\boldsymbol{y}} \times \boldsymbol{m}_{2\mp}) \\ & - i(\hbar/e)\omega \left[\boldsymbol{m}_{1,0} \boldsymbol{m}_{2\mp} \tau_{\mathrm{F}} + \boldsymbol{m}_{1,0} (\hat{\boldsymbol{y}} \times \boldsymbol{m}_{2\mp}) \tau_{\mathrm{D}} \right] \big\} \\ & + \boldsymbol{m}_{1,0} (\hat{\boldsymbol{y}} \times \boldsymbol{m}_{2\mp}) \cos(dk_-) \left[(\hbar/e)^2 \omega^2 \left(\tau_{\mathrm{D}}^2 + \tau_{\mathrm{F}}^2 \right) + 2i(\hbar/e) J \tau_{\mathrm{D}} \omega - J^2 \right] \Big) \end{aligned} \tag{A.42}$$

where the prefactor c is given by:

$$\begin{aligned} c = \cos(dk_+) \Big(& 2A_{\mathrm{ex}} k_- \sin(dk_-) \big\{ J \boldsymbol{m}_{2+} (\hat{\boldsymbol{y}} \times \boldsymbol{m}_{2-}) \\ & + i(\hbar/e)\omega \left[\boldsymbol{m}_{2-} (\hat{\boldsymbol{y}} \times \boldsymbol{m}_{2+}) \tau_{\mathrm{D}} - \boldsymbol{m}_{2-} \boldsymbol{m}_{2+} \tau_{\mathrm{F}} \right] \big\} \\ & + \boldsymbol{m}_{2+} (\hat{\boldsymbol{y}} \times \boldsymbol{m}_{2-}) \cos(dk_-) \left[(\hbar/e)^2 \omega^2 \left(\tau_{\mathrm{D}}^2 + \tau_{\mathrm{F}}^2 \right) + 2i(\hbar/e) J \tau_{\mathrm{D}} \omega - J^2 \right] \Big) \\ & + 2A_{\mathrm{ex}} k \sin(dk_+) \Big(- 2A_{\mathrm{ex}} k_- \boldsymbol{m}_{2+} (\hat{\boldsymbol{y}} \times \boldsymbol{m}_{2-}) \sin(dk_-) + \cos(dk_-) \big\{ J \boldsymbol{m}_{2+} (\hat{\boldsymbol{y}} \times \boldsymbol{m}_{2-}) \\ & + i(\hbar/e)\omega \left[\boldsymbol{m}_{2-} \boldsymbol{m}_{2+} \tau_{\mathrm{F}} + \boldsymbol{m}_{2-} (\hat{\boldsymbol{y}} \times \boldsymbol{m}_{2+}) \tau_{\mathrm{D}} \right] \big\} \Big). \end{aligned} \tag{A.43}$$

The complex coefficients $c_\pm$ now specify the YIG solution and contain the influence of the Co layer. Using the eigenvectors Eq. (A.34) together with the wavevectors Eq. (A.32) and and the complex coefficients Eq. (A.43) and Eq. (A.42) in the ansatz Eq. (A.37) yields the spatially-dependent YIG magnetization. Using subsequently the ansatz Eq. (A.37) and Eq. (A.38) in the modified LLG Eq. (A.28) allows to extract the Co susceptibility $\tilde{\chi}_1$ by sorting the resulting expression by the transverse Co magnetization components $(m_{1,z}, m_{1,x})$. We find:

$$\begin{aligned} \tilde{\chi}_1^{-1} &= \begin{pmatrix} \chi_{1,zz}^{-1} & \chi_{1,xz}^{-1} \\ \chi_{1,zx}^{-1} & \chi_{1,xx}^{-1} \end{pmatrix} \\ \Longleftrightarrow \tilde{\chi}_1 &= \frac{1}{\chi_{1,zz}^{-1}\chi_{1,xx}^{-1} - \chi_{1,zx}^{-1}\chi_{1,xz}^{-1}} \begin{pmatrix} \chi_{1,xx}^{-1} & -\chi_{1,zx}^{-1} \\ -\chi_{1,xz}^{-1} & \chi_{1,zz}^{-1} \end{pmatrix}, \end{aligned} \tag{A.44}$$

where the entries of the inverse susceptibility are:

$$\begin{aligned} \chi_{1,zz}^{-1} =& \frac{i\alpha_1\omega}{\gamma_1} + \boldsymbol{m}_2(0)\frac{-i(\hbar/e)\tau_\mathrm{D}\omega + i(\hbar/e)\tau_\mathrm{F}\omega + J}{d_1 M_{\mathrm{s},1}} \\ &+ \frac{i(\hbar/e)\tau_\mathrm{D}\omega - J}{d_1 M_{\mathrm{s},1}} - \mu_0(H + M_{\mathrm{s},1}), \end{aligned} \tag{A.45}$$

$$\chi_{1,zx}^{-1} = -\frac{i\omega}{\gamma_1} + \boldsymbol{m}_2(0)\frac{-i(\hbar/e)\tau_\mathrm{D}\omega + i(\hbar/e)\tau_\mathrm{F}\omega + J}{d_1 M_{\mathrm{s},1}} - \frac{i(\hbar/e)\tau_\mathrm{F}\omega}{d_1 M_{\mathrm{s},1}}, \tag{A.46}$$

$$\chi_{1,xz}^{-1} = \frac{i\omega}{\gamma_1} + \boldsymbol{m}_2(0)\frac{-i(\hbar/e)\tau_\mathrm{D}\omega - i(\hbar/e)\tau_\mathrm{F}\omega + J}{d_1 M_{\mathrm{s},1}} + \frac{i(\hbar/e)\tau_\mathrm{F}\omega}{d_1 M_{\mathrm{s},1}}, \tag{A.47}$$

$$\begin{aligned} \chi_{1,xx}^{-1} =& \frac{i\alpha_1\omega}{\gamma_1} + \boldsymbol{m}_2(0)\frac{-i(\hbar/e)\tau_\mathrm{D}\omega - i(\hbar/e)\tau_\mathrm{F}\omega + J}{d_1 M_{\mathrm{s},1}} \\ &+ \frac{i(\hbar/e)\tau_\mathrm{D}\omega - J}{d_1 M_{\mathrm{s},1}} - \mu_0 H. \end{aligned} \tag{A.48}$$

While an analytical solution of the resonance condition $\det \tilde{\chi}_1^{-1} = 0$ is not possible, we can use Eq. (A.44) to calculate $\tilde{\chi}_1$ and plot it as a function of H and ω, as shown in Chap. 5.4. To discuss the influences of the different torques on the magnetization we develop a simplified macrospin model in Chap. 5.3, which contains all salient features of the microscopic solution.

List of publications

- S. Klingler, V. Amin, S. Geprägs, K. Ganzhorn, H. Maier-Flaig, M. Althammer, H. Huebl, R. Gross, R.D. McMichael, M.D. Stiles, S.T.B. Goennenwein, M. Weiler, *Spin-torque excitation of perpendicular standing spin waves in coupled YIG/Co heterostructures*, Physical Review Letters **120** (2018).

- H. Maier-Flaig, S. Klingler, C. Dubs, O. Surzhenko, R. Gross, M. Weiler, H. Huebl, S.T.B. Goennenwein, *Temperature-dependent magnetic damping of yttrium iron garnet spheres*, Physical Review B **95**, 214423 (2017).

- R. Ohshima, S. Klingler, S. Dushenko, Y. Ando, M. Weiler, H. Huebl, T. Shinjo, S.T.B. Goennenwein, M. Shiraishi, *Spin injection into silicon detected by broadband ferromagnetic resonance spectroscopy*, Applied Physics Letters **110**, 182402 (2017).

- H. Maier-Flaig, M. Harder, S. Klingler, Z. Qiu, E. Saitoh, M. Weiler, S. Geprägs, R. Gross, S.T.B. Goennenwein, H. Huebl, *Tunable magnon-photon coupling in a compensating ferrimagnet - from weak to strong coupling*, Applied Physics Letters **110**, 132401 (2017).

- S. Klingler, H. Maier-Flaig, C. Dubs, O. Surzhenko, R. Gross, H. Huebl, S.T.B. Goennenwein, M. Weiler, *Gilbert damping of magnetostatic modes in a yttrium iron garnet sphere*, Applied Physics Letters **110**, 092409 (2017).

- R. Ohshima, Y. Ando, K. Matsuzaki, T. Susaki, M. Weiler, S. Klingler, H. Huebl, E. Shikoh, T. Shinjo, S.T.B. Goennenwein, M. Shiraishi, *Strong evidence for d-electron spin transport at room temperature at a LaAlO3/SrTiO3 interface*, Nature Materials **16**, 609 (2017).

- S. Klingler, H. Maier-Flaig, R. Gross, C.M. Hu, H. Huebl, S.T.B. Goennenwein, M. Weiler, *Combined Brillouin light scattering and microwave absorption study of magnon-photon coupling in a split-ring resonator/YIG film system*, Applied Physics Letters **109**, 072402 (2016).

- K. Ganzhorn, S. Klingler, T. Wimmer, S. Geprägs, R. Gross, H. Huebl, S.T.B. Goennenwein, *Magnon-based logic in a multi-terminal YIG/Pt nanostructure*, Applied Physics Letters **109**, 022405 (2016).

- S. Klingler, P. Pirro, T. Brächer, B. Leven, B. Hillebrands, A.V. Chumak, *Spin-wave logic devices based on isotropic forward volume magnetostatic waves*, Applied Physics Letters **106**, 212406 (2015).
- S. Klingler, A.V. Chumak, T. Mewes, B. Khodadadi, C. Mewes, C. Dubs, O. Surzhenko, B. Hillebrands, A. Conca, *Measurements of the exchange stiffness of YIG films using broadband ferromagnetic resonance techniques*, Journal of Physics D: Applied Physics **48**, 15001 (2015).
- S. Klingler, P. Pirro, T. Brächer, B. Leven, B. Hillebrands, A.V. Chumak, *Design of a spin-wave majority gate employing mode selection*, Applied Physics Letters **105**, 152410 (2014).
- A. Conca, E.T. Papaioannou, S. Klingler, J. Greser, T. Sebastian, B. Leven, J. Lösch, B. Hillebrands, *Annealing influence on the Gilbert damping parameter and the exchange constant of CoFeB thin films*, Applied Physics Letters **104**, 182407 (2014).
- A. Conca, J. Greser, T. Sebastian, S. Klingler, B. Obry, B. Leven, B. Hillebrands, *Low spin-wave damping in amorphous $Co_{40}Fe_{40}B_{20}$ thin films*, Journal of Applied Physics **113**, 213909 (2013).

Bibliography

[1] M.M. Waldrop, *The chips are down for Moore's law*, Nature **530**, 144 (2016).

[2] R. Landauer, *Irreversibility and heat generation in the computing process*, IBM Journal of Research and Development **5**, 183 (1961).

[3] S. Klingler, *Spinwellendynamik in mikrostrukturiertem Yttrium-Eisen-Granat*, Diplomarbeit, Technische Universität Kaiserslautern (2014).

[4] C. Papadimitriou, *Computational complexity*, in *Encyclopedia of computer science*, Wiley, Chichester, 4. Ed. (2003).

[5] D.J. Moylett, N. Linden, A. Montanaro, *Quantum speedup of the traveling-salesman problem for bounded-degree graphs*, Physical Review A **95**, 032323 (2017).

[6] F.D. Natterer, K. Yang, W. Paul, P. Willke, T. Choi, T. Greber, A.J. Heinrich, C.P. Lutz, *Reading and writing single-atom magnets*, Nature **543**, 226 (2017).

[7] A. Fert, *The origin, development and future of spintronics*, Nobel Lecture 59–80 (2007).

[8] M.N. Baibich, J.M. Broto, A. Fert, F.N.V. Dau, *Giant magnetoresistance of (001)Fe/\-(001)Cr magnetic superlattices*, Physical Review Letters **61**, 2472 (1988).

[9] P.A. Grünberg, *From spinwaves to giant magnetoresistance (GMR) and beyond*, Nobel Lecture 92–108 (2007).

[10] G. Binasch, P. Grünberg, F. Saurenbach, W. Zinn, *Enhanced magnetoresistance in layered magnetic structures with antiferromagnetic interlayer exchange*, Physical Review B **39**, 4828 (1989).

[11] A.A. Serga, A.V. Chumak, B. Hillebrands, *YIG magnonics*, Journal of Physics D: Applied Physics **43**, 264002 (2010).

[12] A.V. Chumak, A.A. Serga, B. Hillebrands, *Magnon transistor for all-magnon data processing*, Nature Communications **5**, 4700 (2014).

[13] S. Klingler, P. Pirro, T. Brächer, B. Leven, B. Hillebrands, A.V. Chumak, *Spin-wave logic devices based on isotropic forward volume magnetostatic waves*, Applied Physics Letters **106**, 212406 (2015).

[14] K. Ganzhorn, S. Klingler, T. Wimmer, S. Geprägs, R. Gross, H. Huebl, S.T.B. Goennenwein, *Magnon-based logic in a multi-terminal YIG/Pt nanostructure*, Applied Physics Letters **109**, 022405 (2016).

[15] K. Uchida, S. Takahashi, K. Harii, J. Ieda, W. Koshibae, K. Ando, S. Maekawa, E. Saitoh, *Observation of the spin Seebeck effect*, Nature **455**, 778 (2008).

[16] J. Xiao, G.E.W. Bauer, K.C. Uchida, E. Saitoh, S. Maekawa, *Theory of magnon-driven spin Seebeck effect*, Physical Review B **81**, 214418 (2010).

[17] J.H.E. Griffiths, *Anomalous high-frequency resistance of ferromagnetic metals*, Nature **158**, 670 (1946).

[18] A.V. Chumak, V.I. Vasyuchka, A.A. Serga, B. Hillebrands, *Magnon spintronics*, Nature Physics **11**, 453 (2015).

[19] S. Chikazumi, *Physics of ferromagnetism*, Oxford University Press, Oxford, 2. Ed. (1997).

[20] R. Gross, A. Marx, *Festkörperphysik*, DE De Gruyter, Berlin, 2. Ed. (2014).

[21] H. Haken, H.C. Wolf, *Atom- und Quantenphysik: Einführung in die experimentellen und theoretischen Grundlagen*, Springer, Berlin, 8. Ed. (2000).

[22] R.C. O'Handley, *Modern magnetic materials: Principles and applications*, Wiley, New York, 1. Ed. (2000).

[23] S. Klingler, A.V. Chumak, T. Mewes, B. Khodadadi, C. Mewes, C. Dubs, O. Surzhenko, B. Hillebrands, A. Conca, *Measurements of the exchange stiffness of YIG films using broadband ferromagnetic resonance techniques*, Journal of Physics D: Applied Physics **48**, 15001 (2015).

[24] L. Bergmann, C. Schaefer, *Lehrbuch der Experimentalphysik: Festkörper*, De Gruyter, Berlin, 2. Ed. (2005).

[25] J.D. Jackson, *Klassische Elektrodynamik*, De Gruyter, Berlin, 3. Ed. (2002).

[26] R.I. Joseph, E. Schlömann, *Demagnetizing field in nonellipsoidal bodies*, Journal of Applied Physics **36**, 1579 (1965).

[27] J.A. Osborn, *Demagnetizing factors of the general ellipsoid*, Physical Review **67**, 351 (1945).

[28] E. Schlömann, *A sum rule concerning the inhomogeneous demagnetizing field in nonellipsoidal samples*, Journal of Applied Physics **33**, 2825 (1962).

[29] C. Kittel, *On the theory of ferromagnetic resonance absorption*, Physical Review **73**, 155 (1948).

[30] D.D. Stancil, A. Prabhakar, *Spin waves: Theory and applications*, Springer, Berlin, 1. Ed. (2009).

[31] L.D. Landau, E. Lifshitz, *On the theory of the dispersion of magnetic permeability in ferromagnetic bodies*, Physikalische Zeitschrift der Sowjetunion **5**, 153 (1935).

[32] T.L. Gilbert, *Classics in magnetics: A phenomenological theory of damping in ferromagnetic materials*, IEEE Transactions on Magnetics **40**, 3443 (2004).

[33] L. Dreher, M. Weiler, M. Pernpeintner, H. Huebl, R. Gross, M.S. Brandt, S.T.B. Goennenwein, *Surface acoustic wave driven ferromagnetic resonance in nickel thin films: Theory and experiment*, Physical Review B **86**, 134415 (2012).

[34] B.A. Kalinikos, A.N. Slavin, *Theory of dipole-exchange spin wave spectrum for ferromagnetic films with mixed exchange boundary conditions*, Journal of Physics C: Solid State Physics **19**, 7013 (1986).

[35] H. Goldstein, *Klassische Mechanik*, Wiley-VCH, Berlin, 3. Ed. (2006).

[36] S. Klingler, H. Maier-Flaig, C. Dubs, O. Surzhenko, R. Gross, H. Huebl, S.T.B. Goennenwein, M. Weiler, *Gilbert damping of magnetostatic modes in a yttrium iron garnet sphere*, Applied Physics Letters **110**, 092409 (2017).

[37] H. Maier-Flaig, S. Klingler, C. Dubs, O. Surzhenko, R. Gross, M. Weiler, H. Huebl, S.T.B. Goennenwein, *Temperature-dependent magnetic damping of yttrium iron garnet spheres*, Physical Review B **95**, 214423 (2017).

[38] S. Klingler, P. Pirro, T. Brächer, B. Leven, B. Hillebrands, A.V. Chumak, *Design of a spin-wave majority gate employing mode selection*, Applied Physics Letters **105**, 152410 (2014).

[39] M.P. Kostylev, A.A. Serga, T. Schneider, B. Leven, B. Hillebrands, *Spin-wave logical gates*, Applied Physics Letters **87**, 153501 (2005).

[40] A. Khitun, K.L. Wang, *Spin wave magnetic nanofabric: A new approach to spin-based logic circuitry*, IEEE Transactions on Magnetics **44**, 2141 (2008).

[41] T. Fischer, M. Kewenig, D.A. Bozhko, A.A. Serga, I.I. Syvorotka, F. Ciubotaru, C. Adelmann, B. Hillebrands, A.V. Chumak, *Experimental prototype of a spin-wave majority gate*, Applied Physics Letters **110**, 152401 (2017).

[42] A.V. Chumak, A.A. Serha, B. Hillebrands, *Magnonic crystals for data processing*, Journal of Physics D: Applied Physics **50**, 244001 (2017).

[43] M.B. Jungfleisch, *Spin pumping and inverse spin Hall effect in yttrium iron garnet/platinum heterostructures Dissertation*, Dissertation, Technische Universität Kaiserslautern (2013).

[44] J. Stigloher, M. Decker, H.S. Körner, K. Tanabe, T. Moriyama, T. Taniguchi, H. Hata, M. Madami, G. Gubbiotti, K. Kobayashi, T. Ono, C.H. Back, *Snell's law for spin waves*, Physical Review Letters **117**, 1 (2016).

[45] M. Vogel, R. Aßmann, P. Pirro, A.V. Chumak, B. Hillebrands, G. von Freymann, *Control of spin-wave propagation using magnetisation gradients*, Scientific Reports **8**, 1 (2018).

[46] T. Kasuya, R.C. LeCraw, *Relaxation mechanisms in ferromagnetic resonance*, Physical Review Letters **6**, 223 (1961).

[47] V. Kambersky, C.E. Patton, *Spin-wave relaxation and phenomenological damping in ferromagnetic resonance*, Physical Review B **11** (1975).

[48] P. Röschmann, *Separation of anisotropy and porosity contributions to inhomogeneous broadened FMR linewidth in polycrystalline YIG*, IEEE Transactions on Magnetics **11**, 1247 (1975).

[49] M. Hickey, J. Moodera, *Origin of intrinsic Gilbert damping*, Physical Review Letters **102**, 137601 (2009).

[50] C. Liu, C.K.A. Mewes, M. Chshiev, T. Mewes, W.H. Butler, *Origin of low Gilbert damping in half metals*, Applied Physics Letters **95**, 22509 (2009).

[51] M. Körner, K. Lenz, R.A. Gallardo, M. Fritzsche, A. Mücklich, S. Facsko, J. Lindner, P. Landeros, J. Fassbender, *Two-magnon scattering in permalloy thin films due to rippled substrates*, Physical Review B **88**, 054405 (2013).

[52] B. Heinrich, J.F. Cochran, R. Hasegawa, *FMR linebroadening in metals due to two-magnon scattering*, Journal of Applied Physics **57**, 3690 (1985).

[53] M.J. Hurben, C.E. Patton, *Theory of two magnon scattering microwave relaxation and ferromagnetic resonance linewidth in magnetic thin films*, Journal of Applied Physics **83**, 4344 (1998).

[54] K. Lenz, H. Wende, W. Kuch, K. Baberschke, K. Nagy, A. Jánossy, *Two-magnon scattering and viscous Gilbert damping in ultrathin ferromagnets*, Physical Review B **73**, 144424 (2006).

[55] P. Krivosik, N. Mo, S. Kalarickal, C.E. Patton, *Hamiltonian formalism for two magnon scattering microwave relaxation: Theory and applications*, Journal of Applied Physics **101**, 83901 (2007).

[56] M.C. Weber, H. Nembach, B. Hillebrands, M.J. Carey, J. Fassbender, *Real-time evidence of two-magnon scattering in exchange-coupled bilayers*, Journal of Applied Physics **99**, 08J308 (2006).

[57] J. Nemarich, *Contribution of the two-magnon process to magnetostatic-mode relaxation*, Physical Review **136**, A1657 (1964).

[58] R.D. McMichael, M.D. Stiles, P.J. Chen, W.F. Egelhoff, *Ferromagnetic resonance linewidth in thin films coupled to NiO*, Journal of Applied Physics **83**, 7037 (1998).

[59] R. Arias, D.L. Mills, *Extrinsic contributions to the ferromagnetic resonance response of ultrathin films*, Physical Review B **60**, 7395 (1999).

[60] S.S. Kalarickal, P. Krivosik, M. Wu, C.E. Patton, M.L. Schneider, P. Kabos, T.J. Silva, J.P. Nibarger, *Ferromagnetic resonance linewidth in metallic thin films: Comparison of measurement methods*, Journal of Applied Physics **99**, 093909 (2006).

[61] P. Röschmann, *Annealing effects of FMR linewidth in substituted YIG*, IEEE Transactions on Magnetics **17**, 2973 (1981).

[62] G. Woltersdorf, *Spin-pumping and two-magnon scattering in magnetic multilayers*, Phd thesis, Simon Fraser University (2004).

[63] J. Lindner, I. Barsukov, C. Raeder, C. Hassel, O. Posth, R. Meckenstock, P. Landeros, D.L. Mills, *Two-magnon damping in thin films in case of canted magnetization: Theory versus experiment*, Physical Review B **80**, 224421 (2009).

[64] D.L. Mills, S.M. Rezende, *Spin damping in ultrathin magnetic films*, in B. Hillebrands, K. Ounadjela (Eds.), *Spin dynamics in confined magnetic structures II*, Vol. 87, Springer, Berlin, 1. Ed. (2003).

[65] C. Wen, *Coplanar waveguide: A surface strip transmission line suitable for nonreciprocal gyromagnetic device applications*, IEEE Transactions on Microwave Theory and Techniques **17**, 1087 (1969).

[66] H.B. Maier-Flaig, *Magnetic resonance of ferrimagnetic insulators*, Dissertation, Technische Universität München (2017).

[67] M.A. Schoen, J.M. Shaw, H.T. Nembach, M. Weiler, T.J. Silva, *Radiative damping in waveguide-based ferromagnetic resonance measured via analysis of perpendicular standing spin waves in sputtered permalloy films*, Physical Review B **92**, 184417 (2015).

[68] T.J. Silva, C.S. Lee, T.M. Crawford, C.T. Rogers, *Inductive measurement of ultrafast magnetization dynamics in thin-film Permalloy*, Journal of Applied Physics **85**, 7849 (1999).

[69] J.C. Mallinson, *The foundations of magnetic recording*, Academic Press, Cambridge, 2. Ed. (1993).

[70] O. Karlqvist, *Calculation of the magnetic field in the ferromagnetic layer of a magnetic drum*, Transactions of the Royal Institute of Technology Stockholm, Stockholm, 1. Ed. (1954).

[71] A.J. Berger, E.R.J. Edwards, H.T. Nembach, A.D. Karenowska, M. Weiler, T.J. Silva, *Inductive detection of fieldlike and dampinglike ac inverse spin-orbit torques in ferromagnet/normal-metal bilayers*, Physical Review B **97** (2018).

[72] Stanford Research Systems, *About lock-in amplifiers: Application note #3* (2017).

[73] A.M. Tyryshkin, S.A. Lyon, A.V. Astashkin, A.M. Raitsimring, *Electron spin relaxation times of phosphorus donors in silicon*, Physical Review B **68**, 193207 (2003).

[74] P.R. Hammar, B.R. Bennett, M.J. Yang, M. Johnson, *Observation of spin injection at a ferromagnet-semiconductor interface*, Physical Review Letters **83**, 203 (1999).

[75] A. Fert, H. Jaffrès, *Conditions for efficient spin injection from a ferromagnetic metal into a semiconductor*, Physical Review B **64**, 184420 (2001).

[76] G. Schmidt, D. Ferrand, L.W. Molenkamp, A.T. Filip, B.J. van Wees, *Fundamental obstacle for electrical spin injection from a ferromagnetic metal into a diffusive semiconductor*, Physical Review B **62**, R4790 (2000).

[77] E.I. Rashba, *Theory of electrical spin injection: Tunnel contacts as a solution of the conductivity mismatch problem*, Physical Review B **62**, R16267 (2000).

[78] V.F. Motsnyi, J. De Boeck, J. Das, W. Van Roy, G. Borghs, E. Goovaerts, V.I. Safarov, *Electrical spin injection in a ferromagnet/tunnel barrier/semiconductor heterostructure*, Applied Physics Letters **81**, 265 (2002).

[79] Y. Tserkovnyak, A. Brataas, G.E.W. Bauer, *Enhanced Gilbert damping in thin ferromagnetic films*, Physical Review Letters **88**, 117601 (2002).

[80] S. Mizukami, Y. Ando, T. Miyazaki, *Effect of spin diffusion on Gilbert damping for a very thin permalloy layer in Cu/permalloy/Cu/Pt films*, Physical Review B **66**, 1044131 (2002).

[81] K. Ando, S. Takahashi, J. Ieda, H. Kurebayashi, T. Trypiniotis, C.H.W. Barnes, S. Maekawa, E. Saitoh, *Electrically tunable spin injector free from the impedance mismatch problem*, Nature Materials **10**, 655 (2011).

[82] K. Ando, E. Saitoh, *Observation of the inverse spin Hall effect in silicon*, Nature Communications **3**, 629 (2012).

[83] E. Shikoh, K. Ando, K. Kubo, E. Saitoh, T. Shinjo, M. Shiraishi, *Spin-pump-induced spin transport in p-type Si at room temperature*, Physical Review Letters **110**, 1 (2013).

[84] A. Yamamoto, Y. Ando, T. Shinjo, T. Uemura, M. Shiraishi, *Spin transport and spin conversion in compound semiconductor with non-negligible spin-orbit interaction*, Physical Review B **91**, 1 (2015).

[85] S. Dushenko, M. Koike, Y. Ando, T. Shinjo, M. Myronov, M. Shiraishi, *Experimental demonstration of room-temperature spin transport in n -type germanium epilayers*, Physical Review Letters **114**, 1 (2015).

[86] Y. Pu, P.M. Odenthal, R. Adur, J. Beardsley, A.G. Swartz, D.V. Pelekhov, M.E. Flatte, R.K. Kawakami, J. Pelz, P.C. Hammel, E. Johnston-Halperin, *Ferromagnetic resonance spin pumping and electrical spin injection in silicon-based metal-oxide-semiconductor heterostructures*, Physical Review Letters **115**, 1 (2015).

[87] C. Du, H. Wang, P.C. Hammel, F. Yang, *Y3Fe5O12 spin pumping for quantitative understanding of pure spin transport and spin Hall effect in a broad range of materials*, Journal of Applied Physics **117**, 172603 (2015).

[88] M. Jamali, J.S. Lee, J.S. Jeong, F. Mahfouzi, Y. Lv, Z. Zhao, B.K. Nikolić, K.A. Mkhoyan, N. Samarth, J.P. Wang, *Giant spin pumping and inverse spin Hall effect in the presence of surface and bulk spin-orbit coupling of topological insulator Bi2Se3*, Nano Letters **15**, 7126 (2015).

[89] A.A. Baker, A.I. Figueroa, L.J. Collins-Mcintyre, G. Van Der Laan, T. Hesjedal, *Spin pumping in ferromagnet-topological insulator-ferromagnet heterostructures*, Scientific Reports **5**, 1 (2015).

[90] A.R. Mellnik, J.S. Lee, A. Richardella, J.L. Grab, P.J. Mintun, M.H. Fischer, A. Vaezi, A. Manchon, E.A. Kim, N. Samarth, D.C. Ralph, *Spin-transfer torque generated by a topological insulator*, Nature **511**, 449 (2014).

[91] J.C. Rojas-Sánchez, S. Oyarzún, Y. Fu, A. Marty, C. Vergnaud, S. Gambarelli, L. Vila, M. Jamet, Y. Ohtsubo, A. Taleb-Ibrahimi, P. Le Fèvre, F. Bertran, N. Reyren, J.M. George, A. Fert, *Spin to charge conversion at room temperature by spin pumping into a new type of topological insulator: α-Sn films*, Physical Review Letters **116**, 096602 (2016).

[92] S. Klingler, V. Amin, S. Geprägs, K. Ganzhorn, H. Maier-Flaig, M. Althammer, H. Huebl, R. Gross, R.D. McMichael, M.D. Stiles, S.T.B. Goennenwein, M. Weiler, *Spin-torque excitation of perpendicular standing spin waves in coupled YIG/Co heterostructures*, Physical Review Letters **120** (2018).

[93] R. Ohshima, Y. Ando, K. Matsuzaki, T. Susaki, M. Weiler, S. Klingler, H. Huebl, E. Shikoh, T. Shinjo, S.T.B. Goennenwein, M. Shiraishi, *Strong evidence for d-electron spin transport at room temperature at a LaAlO3/SrTiO3 interface*, Nature Materials **16**, 609 (2017).

[94] R. Ohshima, S. Klingler, S. Dushenko, Y. Ando, M. Weiler, H. Huebl, T. Shinjo, S.T.B. Goennenwein, M. Shiraishi, *Spin injection into silicon detected by broadband ferromagnetic resonance spectroscopy*, Applied Physics Letters **110**, 182402 (2017).

[95] G. Bauer, Y. Tserkovnyak, *Spin-magnon transmutation*, Physics **4**, 40 (2011).

[96] M. Weiler, *Magnon-phonon interactions in ferromagnetic thin films*, Dissertation, Technische Universität München (2012).

[97] M. Haertinger, C.H. Back, J. Lotze, M. Weiler, S. Geprägs, H. Huebl, S.T.B. Goennenwein, G. Woltersdorf, *Spin pumping in YIG/Pt bilayers as a function of layer thickness*, Physical Review B **92**, 054437 (2015).

[98] W. Gannett, M.W. Keller, H.T. Nembach, T.J. Silva, A.N. Chiaramonti, *Suppression of spin pumping between Ni80Fe20 and Cu by a graphene interlayer*, Journal of Applied Physics **117**, 213907 (2015).

[99] B. Heinrich, C. Burrowes, E. Montoya, B. Kardasz, E. Girt, Y.Y. Song, Y. Sun, M. Wu, *Spin pumping at the magnetic insulator (YIG)/normal metal (Au) interfaces*, Physical Review Letters **107**, 066604 (2011).

[100] P. Pirro, T. Brächer, A.V. Chumak, B. Lägel, C. Dubs, O. Surzhenko, P. Görnert, B. Leven, B. Hillebrands, *Spin-wave excitation and propagation in microstructured waveguides of yttrium iron garnet/Pt bilayers*, Applied Physics Letters **104**, 12402 (2014).

[101] H. Nakayama, K. Ando, K. Harii, T. Yoshino, R. Takahashi, Y. Kajiwara, K. Uchida, Y. Fujikawa, E. Saitoh, *Geometry dependence on inverse spin Hall effect induced by spin pumping in Ni81Fe19/Pt films*, Physical Review B **85**, 144408 (2012).

[102] H. Maier-Flaig, M. Harder, R. Gross, H. Huebl, S.T.B. Goennenwein, *Spin pumping in strongly coupled magnon-photon systems*, Physical Review B **94**, 054433 (2016).

[103] F.D. Czeschka, L. Dreher, M.S. Brandt, M. Weiler, M. Althammer, I.M. Imort, G. Reiss, A. Thomas, W. Schoch, W. Limmer, H. Huebl, R. Gross, S.T.B. Goennenwein, *Scaling behavior of the spin pumping effect in ferromagnet-platinum bilayers*, Physical Review Letters **107**, 1 (2011).

[104] O. Mosendz, J.E. Pearson, F.Y. Fradin, G.E.W. Bauer, S.D. Bader, A. Hoffmann, *Quantifying spin Hall angles from spin pumping: Experiments and theory*, Physical Review Letters **104**, 046601 (2010).

[105] C.W. Sandweg, Y. Kajiwara, K. Ando, E. Saitoh, B. Hillebrands, *Enhancement of the spin pumping efficiency by spin wave mode selection*, Applied Physics Letters **97**, 2013 (2010).

[106] E. Saitoh, M. Ueda, H. Miyajima, G. Tatara, *Conversion of spin current into charge current at room temperature: Inverse spin-Hall effect*, Applied Physics Letters **88**, 1 (2006).

[107] M. Weiler, J.M. Shaw, H.T. Nembach, T.J. Silva, *Phase-sensitive detection of spin pumping via the ac inverse spin Hall effect*, Physical Review Letters **113**, 157204 (2014).

[108] Y. Tserkovnyak, A. Brataas, G.E.W. Bauer, *Spin pumping and magnetization dynamics in metallic multilayers*, Physical Review B **66**, 224403 (2002).

[109] Y. Tserkovnyak, A. Brataas, G.E. Bauer, B.I. Halperin, *Nonlocal magnetization dynamics in ferromagnetic heterostructures*, Reviews of Modern Physics **77**, 1375 (2005).

[110] O. d'Allivy Kelly, A. Anane, R. Bernard, J. Ben Youssef, C. Hahn, A.H. Molpeceres, C. Carretero, E. Jacquet, C. Deranlot, P. Bortolotti, R. Lebourgeois, J.C. Mage, G. de Loubens, O. Klein, V. Cros, A. Fert, *Inverse spin Hall effect in nanometer-thick yttrium iron garnet/Pt system*, Applied Physics Letters **103**, 082408 (2013).

[111] M.B. Jungfleisch, V. Lauer, R. Neb, A.V. Chumak, B. Hillebrands, *Improvement of the yttrium iron garnet/platinum interface for spin pumping-based applications*, Applied Physics Letters **103**, 022411 (2013).

[112] S.S.L. Zhang, S. Zhang, *Spin convertance at magnetic interfaces*, Physical Review B **86**, 214424 (2012).

[113] X. Jia, K. Liu, K. Xia, G.E.W. Bauer, *Spin transfer torque on magnetic insulators*, Epl **96**, 0 (2011).

[114] M. Weiler, M. Althammer, M. Schreier, J. Lotze, M. Pernpeintner, S. Meyer, H. Huebl, R. Gross, A. Kamra, J. Xiao, Y.T. Chen, H. Jiao, G.E.W. Bauer, S.T.B. Goennenwein, *Experimental test of the spin mixing interface conductivity concept*, Physical Review Letters **111**, 176601 (2013).

[115] H. Jiao, G.E.W. Bauer, *Spin backflow and ac voltage generation by spin pumping and the inverse spin Hall effect*, Physical Review Letters **110**, 217602 (2013).

[116] M. Althammer, M. Weiler, H. Huebl, S.T.B. Goennenwein, *Spin pumping*, in K. Sato, E. Saitoh (Eds.), *Spintronics for next generation innovative devices*, Wiley, Chichester, 1. Ed. (2015).

[117] O. Mosendz, J.E. Pearson, F.Y. Fradin, S.D. Bader, A. Hoffmann, *Suppression of spin-pumping by a MgO tunnel-barrier*, Applied Physics Letters **96**, 1 (2010).

[118] L. Mihalceanu, S. Keller, J. Greser, D. Karfaridis, K. Simeonidis, G. Vourlias, T. Kehagias, A. Conca, B. Hillebrands, E.T. Papaioannou, *Spin-pumping through a varying-thickness MgO interlayer in Fe/Pt system*, Applied Physics Letters **110**, 252406 (2017).

[119] J. Evertsson, F. Bertram, F. Zhang, L. Rullik, L. Merte, M. Shipilin, M. Soldemo, S. Ahmadi, N. Vinogradov, F. Carlà, J. Weissenrieder, M. Göthelid, J. Pan, A. Mikkelsen, J.O. Nilsson, E. Lundgren, *The thickness of native oxides on aluminum alloys and single crystals*, Applied Surface Science **349**, 826 (2015).

[120] K. Zakeri, J. Lindner, I. Barsukov, R. Meckenstock, M. Farle, U. Von Hörsten, H. Wende, W. Keune, J. Rocker, S.S. Kalarickal, K. Lenz, W. Kuch, K. Baberschke, Z. Frait, *Spin dynamics in ferromagnets: Gilbert damping and two-magnon scattering*, Physical Review B **76**, 1 (2007).

[121] J.M. Shaw, H.T. Nembach, T.J. Silva, C.T. Boone, *Precise determination of the spectroscopic g-factor by use of broadband ferromagnetic resonance spectroscopy*, Journal of Applied Physics **114** (2013).

[122] J.M. Shaw, H.T. Nembach, T.J. Silva, *Measurement of orbital asymmetry and strain in Co90Fe10/Ni multilayers and alloys: Origins of perpendicular anisotropy*, Physical Review B **87**, 1 (2013).

[123] H.T. Nembach, T.J. Silva, J.M. Shaw, M.L. Schneider, M.J. Carey, S. Maat, J.R. Childress, *Perpendicular ferromagnetic resonance measurements of damping and Lande g- factor in sputtered (Co2Mn)1-xGe x thin films*, Physical Review B **84**, 1 (2011).

[124] J.M. Gallego, J.M. García, J. Alvarez, R. Miranda, *Metallization-induced spontaneous silicide formation at room temperature: The Fe/Si case*, Physical Review B **46**, 13339 (1992).

[125] N. Kuratani, Y. Murakami, O. Imai, A. Ebe, S. Nishiyama, K. Ogata, *Study on the internal stress in nickel films deposited onto silicon substrates by ion beam and vapor deposition (IVD)*, Thin Solid Films **281-282**, 352 (1996).

[126] Y. Li, W. Bailey, *Wave-number-dependent Gilbert damping in metallic ferromagnets*, Physical Review Letters **116**, 117602 (2016).

[127] V. Zarifis, T. Castner, *Observation of the conduction-electron spin resonance from metallic antimony-doped silicon*, Physical Review B **57**, 14600 (1998).

[128] R.J. Elliott, *Theory of the effect of spin-Orbit coupling on magnetic resonance in some semiconductors*, Physical Review **96**, 266 (1954).

[129] Y. Yafet, *Conduction electron spin relaxation in the superconducting state*, Physics Letters A **98**, 287 (1983).

[130] A.J. Berger, E.R.J. Edwards, H.T. Nembach, O. Karis, M. Weiler, T.J. Silva, *Determination of spin Hall effect and spin diffusion length of Pt from self-consistent fitting of damping enhancement and inverse spin-orbit torque measurements*, Physical Review B **98** (2018).

[131] N.W. Ashcroft, D.N. Mermin, *Festkörperphysik*, Oldenbourg Wissenschaftsverlag, Berlin, 4. Ed. (2001).

[132] A.N. Anisimov, M. Farle, P. Poulopoulos, W. Platow, K. Baberschke, P. Isberg, R. Wäppling, A.M.N. Niklasson, O. Eriksson, *Orbital magnetism and magnetic anisotropy probed with ferromagnetic resonance*, Physical Review Letters **82**, 2390 (1999).

[133] Y. Ohno, D.K. Young, B. Beschoten, F. Matsukura, H. Ohno, D.D. Awschalom, *Electrical spin injection in a ferromagnetic semiconductor heterostructure*, Nature **402**, 790 (1999).

[134] R. Fiederling, M. Keim, G. Reuscher, W. Ossau, G. Schmidt, A. Waag, L.W. Molenkamp, *Injection and detection of a spin-polarized current in a light-emitting diode*, Nature **402**, 787 (1999).

[135] V.E. Demidov, S. Urazhdin, A. Zholud, A.V. Sadovnikov, A.N. Slavin, S.O. Demokritov, *Spin-current nano-oscillator based on nonlocal spin injection*, Scientific Reports **5**, 8578 (2015).

[136] V.E. Demidov, S. Urazhdin, R. Liu, B. Divinskiy, A. Telegin, S.O. Demokritov, *Excitation of coherent propagating spin waves by pure spin currents*, Nature Communications **7**, 1 (2016).

[137] Y. Au, M. Dvornik, O. Dmytriiev, V.V. Kruglyak, *Nanoscale spin wave valve and phase shifter*, Applied Physics Letters **100**, 172408 (2012).

[138] U.H. Hansen, V.E. Demidov, S.O. Demokritov, *Dual-function phase shifter for spin-wave logic applications*, Applied Physics Letters **94**, 10 (2009).

[139] V.E. Demidov, S. Urazhdin, S.O. Demokritov, *Control of spin-wave phase and wavelength by electric current on the microscopic scale*, Applied Physics Letters **95**, 262509 (2009).

[140] K. Ando, S. Takahashi, J. Ieda, Y. Kajiwara, H. Nakayama, T. Yoshino, K. Harii, Y. Fujikawa, M. Matsuo, S. Maekawa, E. Saitoh, *Inverse spin-Hall effect induced by spin pumping in metallic system*, Journal of Applied Physics **109** (2011).

[141] T. Brächer, M. Fabre, T. Meyer, T. Fischer, S. Auffret, O. Boulle, U. Ebels, P. Pirro, G. Gaudin, *Detection of short-waved spin waves in individual microscopic spin-wave waveguides using the inverse spin Hall effect*, Nano Letters **17**, 7234 (2017).

[142] Micro Lambda Wireless Inc., *Technology description: YIG tuned filters* (2017).

[143] Micro Lambda Wireless Inc., *Technology description: YIG tuned oscillators* (2017).

[144] S. Geller, *Crystal chemistry of the garnets*, Zeitschrift für Kristallographie **125**, 1 (1967).

[145] S.C. Abrahams, S. Geller, *Refinement of the structure of a grossularite garnet*, Acta Crystallographica **11**, 437 (1958).

[146] S. Geller, M. Gilleo, *The crystal structure and ferrimagnetism of yttrium-iron garnet, Y3Fe2(FeO4)3*, Journal of Physics and Chemistry of Solids **3**, 30 (1957).

[147] P. Hansen, *Saturation magnetization of gallium-substituted yttrium iron garnet*, Journal of Applied Physics **45**, 2728 (1974).

[148] G. Winkler, *Magnetic garnets*, Vieweg, Braunschweig, 5. Ed. (1981).

[149] Y. Lam, *Magnetostatic-mode linewidths in yttrium-iron Garnet*, Solid-State Electronics **8**, 923 (1965).

[150] D. Hölzer, *Landau-Lifshitz-damping for Walker modes*, Physics Letters A **170**, 45 (1992).

[151] L.R. Walker, *Magnetostatic modes in ferromagnetic resonance*, Physical Review **105**, 390 (1957).

[152] P.C. Fletcher, R.O. Bell, *Ferrimagnetic resonance modes in spheres*, Journal of Applied Physics **30**, 687 (1959).

[153] P. Röschmann, H. Dötsch, *Properties of magnetostatic modes in ferrimagnetic spheroids*, Physica Status Solidi (b) **82**, 11 (1977).

[154] A. Berk, B. Lengyel, *Magnetic fields in small ferrite bodies with applications to microwave cavities containing such bodies*, Proceedings of the IRE **43**, 1587 (1955).

[155] G. Wiese, *Parametric excitation of spherical modes in ferromagnetic spheres by perpendicular and parallel pumping*, Zeitschrift für Physik B - Condensed Matter **82**, 453 (1991).

[156] P. Fletcher, I.H. Solt, R. Bell, *Identification of the magnetostatic modes of ferrimagnetic resonant spheres*, Physical Review **114**, 739 (1959).

[157] M. Sparks, R. Loudon, C. Kittel, *Ferromagnetic relaxation: I. Theory of the relaxation of the uniform precession and the degenerate spectrum in insulators at low temperatures*, Physical Review **122**, 791 (1961).

[158] R.L. White, *Observations on line width in ferrimagnetic resonance*, Journal of Applied Physics **30**, S182 (1959).

[159] R.L. White, *Use of magnetostatic modes as a research tool*, Journal of Applied Physics **31**, S86 (1960).

[160] S. Bornmann, R. Gluche, P. Görnert, R. Hergt, C. Becker, *Preparation and properties of YIG single crystals*, Kristall und Technik **9**, 895 (1974).

[161] C.P. Poole, *Electron spin resonance*, Dover Publications, Mineola, 2. Ed. (1996).

[162] J.F. Dillon, *Ferrimagnetic resonance in yttrium iron garnet*, Physical Review **105**, 759 (1957).

[163] P. Hansen, *Anisotropy and magnetostriction of gallium-substituted yttrium iron garnet*, Journal of Applied Physics **45**, 3638 (1974).

[164] P. Röschmann, W. Tolksdorf, *Epitaxial growth and annealing control of FMR properties of thick homogeneous Ga substituted yttrium iron garnet films*, Materials Research Bulletin **18**, 449 (1983).

[165] M. Sparks, *Ferromagnetic relaxation theory*, McGraw-Hill, New York, 1. Ed. (1964).

[166] C. Hauser, T. Richter, N. Homonnay, C. Eisenschmidt, M. Qaid, H. Deniz, D. Hesse, M. Sawicki, S.G. Ebbinghaus, G. Schmidt, *Yttrium iron garnet thin films with very low damping obtained by recrystallization of amorphous material*, Scientific Reports **6**, 20827 (2016).

[167] Y. Sun, Y.Y. Song, H. Chang, M. Kabatek, M. Jantz, W. Schneider, M. Wu, H. Schultheiss, A. Hoffmann, *Growth and ferromagnetic resonance properties of nanometer-thick yttrium iron garnet films*, Applied Physics Letters **101**, 152405 (2012).

[168] C. Hahn, V.V. Naletov, G. de Loubens, O. Klein, O. d'Allivy Kelly, A. Anane, R. Bernard, E. Jacquet, P. Bortolotti, V. Cros, J.L. Prieto, M. Muñoz, *Measurement of the intrinsic damping constant in individual nanodisks of $Y_3Fe_5O_{12}$ and $Y_3Fe_5O_{12}/Pt$*, Applied Physics Letters **104**, 152410 (2014).

[169] C. Dubs, O. Surzhenko, R. Linke, A. Danilewsky, U. Brückner, J. Dellith, *Sub-micrometer yttrium iron garnet LPE films with low ferromagnetic resonance losses*, Journal of Physics D: Applied Physics **50**, 204005 (2017).

[170] M. Vogel, A.V. Chumak, E.H. Waller, T. Langner, V.I. Vasyuchka, B. Hillebrands, G. von Freymann, *Optically reconfigurable magnetic materials*, Nature Physics **11**, 487 (2015).

[171] K. Wagner, A. Kákay, K. Schultheiss, A. Henschke, T. Sebastian, H. Schultheiss, *Magnetic domain walls as reconfigurable spin-wave nanochannels*, Nature Nanotechnology **11**, 432 (2016).

[172] K. Vogt, F.Y. Fradin, J.E. Pearson, T. Sebastian, S.D. Bader, B. Hillebrands, A. Hoffmann, H. Schultheiss, *Realization of a spin-wave multiplexer*, Nature Communications **5**, 3727 (2014).

[173] F. Heussner, A.A. Serga, T. Brächer, B. Hillebrands, P. Pirro, *A switchable spin-wave signal splitter for magnonic networks*, Applied Physics Letters **111**, 122401 (2017).

[174] M. Weiler, M. Althammer, F.D. Czeschka, H. Huebl, M.S. Wagner, M. Opel, I.M. Imort, G. Reiss, A. Thomas, R. Gross, S.T.B. Goennenwein, *Local charge and spin currents in magnetothermal landscapes*, Physical Review Letters **108**, 1 (2012).

[175] I.S. Maksymov, M. Kostylev, *Broadband stripline ferromagnetic resonance spectroscopy of ferromagnetic films, multilayers and nanostructures*, Physica E: Low-dimensional Systems and Nanostructures **69**, 253 (2015).

[176] H. Yu, O. d' Allivy Kelly, V. Cros, R. Bernard, P. Bortolotti, A. Anane, F. Brandl, F. Heimbach, D. Grundler, *Approaching soft X-ray wavelengths in nanomagnet-based microwave technology*, Nature Communications **7**, 11255 (2016).

[177] A.G. Gurevich, A.N. Anisimov, *Intrinsic spin wave relaxation process in yttrium iron garnet*, Journal of Experimental and Theoretical Physics **41**, 336 (1975).

[178] T. Brächer, P. Pirro, B. Hillebrands, *Parallel pumping for magnon spintronics: Amplification and manipulation of magnon spin currents on the micron-scale*, Physics Reports **699**, 1 (2017).

[179] C.S. Davies, V.D. Poimanov, V.V. Kruglyak, *Mapping the magnonic landscape in patterned magnetic structures*, Physical Review B **96**, 094430 (2017).

[180] F.B. Mushenok, R. Dost, C.S. Davies, D.A. Allwood, B.J. Inkson, G. Hrkac, V.V. Kruglyak, *Broadband conversion of microwaves into propagating spin waves in patterned magnetic structures*, Applied Physics Letters **111**, 042404 (2017).

[181] M. Collet, X. de Milly, O. d'Allivy Kelly, V.V. Naletov, R. Bernard, P. Bortolotti, J. Ben Youssef, V.E. Demidov, S.O. Demokritov, J.L. Prieto, M. Muñoz, V. Cros, A. Anane, G. de Loubens, O. Klein, *Generation of coherent spin-wave modes in*

yttrium iron garnet microdiscs by spin–orbit torque, Nature Communications **7**, 10377 (2016).

[182] M. van Kampen, C. Jozsa, J.T. Kohlhepp, P. LeClair, L. Lagae, W.J.M. de Jonge, B. Koopmans, *All-optical probe of coherent spin waves*, Physical Review Letters **88**, 227201 (2002).

[183] T. Satoh, Y. Terui, R. Moriya, B.A. Ivanov, K. Ando, E. Saitoh, T. Shimura, K. Kuroda, *Directional control of spin-wave emission by spatially shaped light*, Nature Photonics **6**, 662 (2012).

[184] G. Dieterle, J. Förster, H. Stoll, A.S. Semisalova, S. Finizio, A. Gangwar, M. Weigand, M. Noske, M. Fähnle, I. Bykova, J. Gräfe, D.A. Bozhko, H.Y. Musiienko-Shmarova, V. Tiberkevich, A.N. Slavin, C.H. Back, J. Raabe, G. Schütz, S. Wintz, *Coherent excitation of heterosymmetric spin waves with ultrashort wavelengths* (2017).

[185] B. Heinrich, Y. Tserkovnyak, G. Woltersdorf, A. Brataas, R. Urban, G.E.W. Bauer, *Dynamic exchange coupling in magnetic bilayers*, Physical Review Letters **90**, 187601 (2003).

[186] S. Pütter, S. Geprägs, R. Schlitz, M. Althammer, A. Erb, R. Gross, S.T.B. Goennenwein, *Impact of the interface quality of Pt/YIG(111) hybrids on their spin Hall magnetoresistance*, Applied Physics Letters **110**, 012403 (2017).

[187] H. Maier-Flaig, S.T.B. Goennenwein, R. Ohshima, M. Shiraishi, R. Gross, H. Huebl, M. Weiler, *Note: Derivative divide, a method for the analysis of broadband ferromagnetic resonance in the frequency domain*, Review of Scientific Instruments **89**, 076101 (2018).

[188] D.C. Crew, K.J. Kennewell, M.J. Lwin, R.C. Woodward, S. Prasad, R.L. Stamps, *Optic and acoustic modes measured in a cobalt/Permalloy exchange spring bilayer using inductive magnetometry*, Journal of Applied Physics **97** (2005).

[189] M. Belmeguenai, T. Martin, G. Woltersdorf, M. Maier, G. Bayreuther, *Frequency- and time-domain investigation of the dynamic properties of interlayer-exchange- coupled Ni81Fe19/Ru/Ni81Fe19 thin films*, Physical Review B **76**, 104414 (2007).

[190] J. Li, Y. Xu, M. Aldosary, C. Tang, Z. Lin, S. Zhang, R. Lake, J. Shi, *Observation of magnon-mediated current drag in Pt/yttrium iron garnet/Pt(Ta) trilayers*, Nature Communications **7**, 10858 (2016).

[191] D.C. Crew, R.L. Stamps, *Ferromagnetic resonance in exchange spring thin films*, Journal of Applied Physics **93**, 6483 (2003).

[192] K.L. Livesey, D.C. Crew, R.L. Stamps, *Spin wave valve in an exchange spring bilayer*, Physical Review B **73**, 184432 (2006).

[193] H. Luo, D. Wang, J. He, Y. Lu, *Magnetic cobalt nanowire thin films*, The Journal of Physical Chemistry B **109**, 1919 (2005).

[194] G. Carlotti, G. Gubbiotti, L. Pareti, G. Socino, G. Turilli, *Elastic and magnetic properties of Co/Cu multilayers studied by Brillouin spectroscopy*, Journal of Magnetism and Magnetic Materials **165**, 424 (1997).

[195] J. Cantu-Valle, I. Betancourt, J.E. Sanchez, F. Ruiz-Zepeda, M.M. Maqableh, F. Mendoza-Santoyo, B.J.H. Stadler, A. Ponce, *Mapping the magnetic and crystal structure in cobalt nanowires*, Journal of Applied Physics **118**, 024302 (2015).

[196] P.F. Herskind, A. Dantan, J.P. Marler, M. Albert, M. Drewsen, *Realization of collective strong coupling with ion Coulomb crystals in an optical cavity*, Nature Physics **5**, 494 (2009).

[197] P. Landeros, D.L. Mills, *Spin waves in periodically perturbed films*, Physical Review B **85**, 054424 (2012).

[198] M. Krawczyk, S. Mamica, M. Mruczkiewicz, J.W. Klos, S. Tacchi, M. Madami, G. Gubbiotti, G. Duerr, D. Grundler, *Magnonic band structures in two-dimensional bi-component magnonic crystals with in-plane magnetization*, Journal of Physics D: Applied Physics **46**, 495003 (2013).

[199] R.A. Gallardo, A. Banholzer, K. Wagner, M. Körner, K. Lenz, M. Farle, J. Lindner, J. Fassbender, P. Landeros, *Splitting of spin-wave modes in thin films with arrays of periodic perturbations: theory and experiment*, New Journal of Physics **16**, 023015 (2014).

[200] R. McMichael, P. Krivosik, *Classical model of extrinsic ferromagnetic resonance linewidth in ultrathin films*, IEEE Transactions on Magnetics **40**, 2 (2004).

[201] R.D. McMichael, *A mean-field model of extrinsic line broadening in ferromagnetic resonance*, Journal of Applied Physics **103**, 07B114 (2008).

[202] M. Tokaç, S.A. Bunyaev, G.N. Kakazei, D.S. Schmool, D. Atkinson, A.T. Hindmarch, *Interfacial structure dependent spin mixing conductance in cobalt thin films*, Physical Review Letters **115**, 056601 (2015).

[203] M. Vohl, J. Barnaś, P. Grünberg, *Effect of interlayer exchange coupling on spin-wave spectra in magnetic double layers: Theory and experiment*, Physical Review B **39**, 12003 (1989).

[204] J. Xiao, G.E.W. Bauer, *Spin-wave excitation in magnetic insulators by spin-transfer torque*, Physical Review Letters **108**, 217204 (2012).

[205] G. Rado, J. Weertman, *Spin-wave resonance in a ferromagnetic metal*, Journal of Physics and Chemistry of Solids **11**, 315 (1959).

[206] S. Yakata, Y. Ando, T. Miyazaki, S. Mizukami, *Temperature dependences of spin-diffusion lengths of Cu and Ru layers*, Japanese Journal of Applied Physics **45**, 3892 (2006).

[207] C. Du, H. Wang, F. Yang, P.C. Hammel, *Enhancement of pure spin currents in spin pumping Y3Fe5O12/Cu/Metal trilayers through spin conductance matching*, Physical Review Applied **1**, 044004 (2014).

[208] S.O. Demokritov, V.E. Demidov, O. Dzyapko, G.A. Melkov, A.A. Serga, B. Hillebrands, A.N. Slavin, *Bose-Einstein condensation of quasi-equilibrium magnons at room temperature under pumping*, Nature **443**, 430 (2006).

[209] D.A. Bozhko, A.A. Serga, P. Clausen, V.I. Vasyuchka, F. Heussner, G.A. Melkov, A. Pomyalov, S.L. Victor, B. Hillebrands, *Supercurrent in a room temperature Bose-Einstein magnon condensate*, Nature Physics (2016).

[210] A. Imamoğlu, *Cavity QED based on collective magnetic dipole coupling: Spin ensembles as hybrid two-level systems*, Physical Review Letters **102**, 83602 (2009).

[211] J.H. Wesenberg, A. Ardavan, G.A.D. Briggs, J.J.L. Morton, R.J. Schoelkopf, D.I. Schuster, K. Mølmer, *Quantum computing with an electron spin ensemble*, Physical Review Letters **103**, 070502 (2009).

[212] Z.Z.L. Xiang, S. Ashhab, J.J. You, F. Nori, *Hybrid quantum circuits: Superconducting circuits interacting with other quantum systems*, Reviews of Modern Physics **85**, 623 (2013).

[213] H. Huebl, C.W. Zollitsch, J. Lotze, F. Hocke, M. Greifenstein, A. Marx, R. Gross, S.T.B. Goennenwein, *High cooperativity in coupled microwave resonator ferrimagnetic insulator hybrids*, Physical Review Letters **111**, 127003 (2013).

[214] X. Zhang, C.l. Zou, L. Jiang, H.X. Tang, *Strongly coupled magnons and cavity microwave photons*, Physical Review Letters **113**, 156401 (2014).

[215] L. Bai, M. Harder, Y. Chen, X. Fan, J. Xiao, C.M. Hu, *spin pumping in electrodynamically coupled magnon-photon systems*, Physical Review Letters **114**, 227201 (2015).

[216] N.J. Lambert, J.A. Haigh, S. Langenfeld, A.C. Doherty, A.J. Ferguson, *Cavity-mediated coherent coupling of magnetic moments*, Physical Review A **93**, 021803 (2016).

[217] Y. Tabuchi, S. Ishino, A. Noguchi, T. Ishikawa, R. Yamazaki, K. Usami, Y. Nakamura, *Coherent coupling between a ferromagnetic magnon and a superconducting qubit*, Science **349**, 405 (2015).

[218] Ö.O. Soykal, M.E. Flatté, *Strong field interactions between a nanomagnet and a photonic cavity*, Physical Review Letters **104**, 077202 (2010).

[219] Ö.O. Soykal, M.E. Flatté, *Size dependence of strong coupling between nanomagnets and photonic cavities*, Physical Review B **82**, 104413 (2010).

[220] R. Hisatomi, A. Osada, Y. Tabuchi, T. Ishikawa, A. Noguchi, R. Yamazaki, K. Usami, Y. Nakamura, *Bidirectional conversion between microwave and light via ferromagnetic magnons*, Physical Review B **93**, 174427 (2016).

[221] A. Osada, R. Hisatomi, A. Noguchi, Y. Tabuchi, R. Yamazaki, K. Usami, M. Sadgrove, R. Yalla, M. Nomura, Y. Nakamura, *Cavity optomagnonics with spin-orbit coupled photons*, Physical Review Letters **116**, 223601 (2016).

[222] B. Bhoi, T. Cliff, I.S. Maksymov, M. Kostylev, R. Aiyar, N. Venkataramani, S. Prasad, R.L. Stamps, *Study of photon-magnon coupling in a YIG-film split-ring resonant system*, Journal of Applied Physics **116**, 243906 (2014).

[223] P. Gay-Balmaz, O.J.F. Martin, *Electromagnetic resonances in individual and coupled split-ring resonators*, Journal of Applied Physics **92**, 2929 (2002).

[224] S. Klingler, H. Maier-Flaig, R. Gross, C.M. Hu, H. Huebl, S.T.B. Goennenwein, M. Weiler, *Combined Brillouin light scattering and microwave absorption study of magnon-photon coupling in a split-ring resonator/YIG film system*, Applied Physics Letters **109**, 072402 (2016).

[225] G.J. Milburn, D. Walls, *Quantum optics*, Springer, Berlin, 2. Ed. (2008).

[226] C.W. Zollitsch, *Single excitation transfer in the quantum regime: A spin-based solid-state approach*, Dissertation, Technische Universität München (2016).

[227] J. Lotze, *Spin pumping in ferrimagnet/normal metal bilayers*, Dissertation, Technische Universität München (2015).

[228] Y. Cao, P. Yan, H. Huebl, S.T.B. Goennenwein, G.E.W. Bauer, *Exchange magnon-polaritons in microwave cavities*, Physical Review B **91**, 094423 (2015).

[229] J. Pendry, A. Holden, D. Robbins, W. Stewart, *Magnetism from conductors and enhanced nonlinear phenomena*, IEEE Transactions on Microwave Theory and Techniques **47**, 2075 (1999).

[230] J. Baena, J. Bonache, F. Martin, R. Sillero, F. Falcone, T. Lopetegi, M. Laso, J. Garcia-Garcia, I. Gil, M. Portillo, M. Sorolla, *Equivalent-circuit models for split-ring resonators and complementary split-ring resonators coupled to planar transmission lines*, IEEE Transactions on Microwave Theory and Techniques **53**, 1451 (2005).

[231] CST Computer Simulation Technology AG, *CST Studio Suite* (2016).

[232] J.F. Cochran, J.R. Dutcher, *Calculation of the intensity of light scattered from magnons in thin films*, Journal of Magnetism and Magnetic Materials **73**, 299 (1988).

[233] V.E. Demidov, S.O. Demokritov, B. Hillebrands, M. Laufenberg, P.P. Freitas, *Radiation of spin waves by a single micrometer-sized magnetic element*, Applied Physics Letters **85**, 2866 (2004).

[234] T. Sebastian, K. Schultheiss, B. Obry, B. Hillebrands, H. Schultheiss, *Micro-focused Brillouin light scattering: Imaging spin waves at the nanoscale*, Frontiers in Physics **3**, 1 (2015).

[235] H. Le Gall, T.K. Vien, B. Desormière, *Theory of the elastic and inelastic scattering of light by magnetic crystals. II. Second-order processes*, Physica Status Solidi (b) **47**, 591 (1971).

[236] S.O. Demokritov, B. Hillebrands, A.N. Slavin, *Brillouin light scattering studies of confined spin waves: linear and nonlinear confinement*, Physics Reports **348**, 441 (2001).

[237] C.W. Sandweg, Y. Kajiwara, A.V. Chumak, A.A. Serga, V.I. Vasyuchka, M.B. Jungfleisch, E. Saitoh, B. Hillebrands, *Spin pumping by parametrically excited exchange magnons*, Physical Review Letters **106**, 1 (2011).

[238] H.A. Algra, P. Hansen, *Temperature dependence of the saturation magnetization of ion-implanted YIG films*, Applied Physics A **86**, 83 (1982).

[239] M.A. Popov, I.V. Zavislyak, *Mechanism of electric frequency tuning in composite resonators based on epitaxial ferrite films*, Technical Physics Letters **38**, 865 (2012).

[240] M. Buchmeier, H. Dassow, D.E. Bürgler, C.M. Schneider, *Intensity of Brillouin light scattering from spin waves in magnetic multilayers with noncollinear spin configurations: Theory and experiment*, Physical Review B **75**, 184436 (2007).

[241] D.A. Bozhko, A.A. Serga, P. Clausen, V.I. Vasyuchka, F. Heussner, G.A. Melkov, A. Pomyalov, V.S. L'vov, B. Hillebrands, *Supercurrent in a room-temperature Bose-Einstein magnon condensate*, Nature Physics **12**, 1057 (2016).

[242] V.E. Demidov, O. Dzyapko, S.O. Demokritov, G.A. Melkov, A.N. Slavin, *Observation of spontaneous coherence in Bose-Einstein condensate of magnons*, Physical Review Letters **100**, 1 (2008).

[243] S.M. Rezende, *Theory of coherence in Bose-Einstein condensation phenomena in a microwave-driven interacting magnon gas*, Physical Review B **79**, 174411 (2009).

[244] S. Maekawa, S.O. Valenzuela, E. Saitoh, *Spin current*, Oxford University Press, Oxford, 1. Ed. (2012).

[245] A. Brataas, G. Bauer, P. Kelly, *Non-collinear magnetoelectronics*, Physics Reports **427**, 157 (2006).

[246] F.D. Czeschka, *Spin currents in metallic nanostructures*, Dissertation, Technische Universität München (2011).

[247] V. Amin, M.D. Stiles, R. McMichael, *Private communication* (2017).

[248] M.D. Stiles, A. Zangwill, *Anatomy of spin-transfer torque*, Physical Review B **66**, 144071 (2002).

[249] T. Taniguchi, S. Yakata, H. Imamura, Y. Ando, *Penetration depth of transverse spin current in ferromagnetic metals*, IEEE Transactions on Magnetics **44**, 2636 (2008).

[250] S. Nonoguchi, T. Nomura, T. Kimura, *Longitudinal and transverse spin current absorptions in a lateral spin-valve structure*, Physical Review B **86**, 1 (2012).

[251] A. Ghosh, S. Auffret, U. Ebels, W.E. Bailey, *Penetration depth of transverse spin current in ultrathin ferromagnets*, Physical Review Letters **109**, 127202 (2012).

[252] V.P. Amin, M.D. Stiles, *Spin transport at interfaces with spin-orbit coupling: Phenomenology*, Physical Review B **94**, 1 (2016).

[253] H. Maier-Flaig, M. Harder, S. Klingler, Z. Qiu, E. Saitoh, M. Weiler, S. Geprägs, R. Gross, S.T.B. Goennenwein, H. Huebl, *Tunable magnon-photon coupling in a compensating ferrimagnet - from weak to strong coupling*, Applied Physics Letters **110**, 132401 (2017).

[254] A. Conca, E.T. Papaioannou, S. Klingler, J. Greser, T. Sebastian, B. Leven, J. Lösch, B. Hillebrands, *Annealing influence on the Gilbert damping parameter and the exchange constant of CoFeB thin films*, Applied Physics Letters **104**, 182407 (2014).

[255] A. Conca, J. Greser, T. Sebastian, S. Klingler, B. Obry, B. Leven, B. Hillebrands, *Low spin-wave damping in amorphous $Co_{40}Fe_{40}B_{20}$ thin films*, Journal of Applied Physics **113**, 213909 (2013).

Acknowledgements

Diese Dissertation wäre ohne die Hilfe und die Unterstützung diverser Personen nicht möglich gewesen. Sei es wegen der gemeinsamen und spannenden Zeit im Labor, wegen wichtigen, zahlreichen und interessanten Diskussionen oder wegen der Stunden, die ich außerhalb meiner regelmäßigen Arbeitszeiten mit euch verbringen durfte.

Ich bedanke mich bei meinem Doktorvater *Sebastian Gönnenwein* für die Möglichkeit am WMI forschen zu dürfen. Danke für das Korrekturlesen meiner Doktorarbeit und diverser Manuskripte und für die richtigen und wichtigen physikalischen Fragen zur richtigen Zeit.

Vielen Dank *Mathias Weiler* für deine intensive Betreuung und deine Hartnäckigkeit, wenn es darum ging Messdaten auszuquetschen oder vermeintlich gesichertes Wissen zu hinterfragen. Danke auch dafür, dass du immer ein offenes Ohr für mich und meine Fragen hattest, sowie für deine vielen Ideen und Diskussionen, die mir stets weitergeholfen haben.

Mein Dank geht auch an *Rudolf Gross*, der mit seinem sehr breiten physikalischen Wissen und diverser Anekdoten, beispielsweise von der Ferienakademie, immer zu unterhalten und zu lehren wusste. Außerdem möchte ich mich für die Unterstützung, sowie für alle Möglichkeiten und Freiheiten am WMI bedanken, die Grundvorausetzung für diese Doktorarbeit waren.

Ohne *Matthias Althammer* wäre ich vermutlich nie nach München gekommen. Danke, dass du damals in Alabama meine Kontaktperson warst und mir später während unserer gemeinsam Zeit am WMI immer mit Rat (und manchmal Tat) zur Seite gestanden hast.

Ich bedanke mich außerdem bei *Stephan Geprägs* dafür, dass er immer über meine Witze lacht und außerdem auch tolle Proben für mich hergestellt hat.

Mein Dank geht weiter an die gesamte Magnetismus-Gruppe für die konsequente Durchsetzung diverser Geburstags-, Einstands- und Ausstandskuchen, sowie für die unkomplizierte Zusammenarbeit. Besonders möchte ich mich auch bei *Tobias Wimmer* und *Daniel Schwienbacher* für die Zeit im gemeinsamen Büro bedanken! Generell gebührt mein Dank dem gesamten WMI für die immer kurzfristige Unterstützung in Sachen Feinmechanik und IT, für die Organisation vor Ort an sich, und für die Organisation der WMI Wiesn im Speziellen.

Ich bedanke mich außerdem bei meinen Mitstreitern der letzten Jahre am WMI für die gute gemeinsame Zeit. Besonderer Dank geht an *Hannes Maier-Flaig* für die vielen gemeinsamen Diskussionen, die produktive Zeit im Labor, sowie die tolle Zusammenarbeit. Dank gebührt außerdem *Jan Goetz* und *Philipp Schmidt* für gemeinsame Unternehmungen, euer Durchhaltevermögen und die interessanten Einblicke in und über das Nachtleben Münchens... Da wir keine gemeinsamen Themen am WMI hatten, konnten wir unsere gemeinsame Zeit stets den schönen Dingen des Lebens widmen! In diesem Zusammenhang möchte ich mich natürlich auch bei *Jan Naundorf* dafür bedanken, dass er immer der Fels in der Brandung jeder WMI Feierlichkeit war und hoffentlich auch bleibt.

Vielen Dank auch für die internationale Unterstützung von *Mark Stiles*, *Vivek Amin* und *Robert McMichael*. Danke, dass ihr mir mit viel Ruhe und Geduld eure Sicht der Dinge verständlich gemacht habt und ich viel Physik von euch lernen durfte. Außerdem möchte ich mich bei unserem WMI Gast *Ryo Ohshima* bedanken, der in zwei Wochen knapp einhundert Proben mit unserem FMR Setup vermessen hat. Danke für diese sehr produktive und unterhaltsame Zusammenarbeit, die ich jedem nur empfehlen kann!

Aber natürlich haben nicht nur die Kollegen und Freunde vom WMI zum Gelingen dieser Arbeit beigetragen, sondern auch viele andere wichtige Personen in meinem Leben. Zuallererst möchte ich mich bei *Meike* bedanken. Danke, dass du immer und schon so lange zu mir hältst, danke für deine Unterstützung und danke für deine Art, mit der du mein Leben so viel besser machst!

Danke auch an meine ganze Familie die mir immer eine große Unterstützung ist und (gefragt oder nicht) viele gute Tipps und Ratschläge auf Lager hat. Danke an meine Eltern *Petra* und *Thomas* für euren Rückhalt und dafür, dass ihr mir immer alles ermöglicht habt. In diesem Zusammenhang geht ein großer Dank natürlich auch an meine zahlreichen Brüder und größten Fans *Andreas*, *Michael* und *Felix*.

Und zum Schluss noch ein ganz herzlicher Dank an meine Freunde aus Idar-Oberstein und München, sowie an meine Studienkollegen aus Kaiserslautern, die stets für umfangreiche Erdung (und Zündung) sorgen. Do kannste nix sah'n!